The population of ultracompact binaries and their progenitors

Proefschrift

ter verkrijging van de graad van doctor
aan de Radboud Universiteit Nijmegen
op gezag van de rector magnificus prof. dr. Th. L. M. Engelen,
volgens besluit van het college van decanen
in het openbaar te verdedigen op donderdag 16 juli 2015
om 10:30 uur precies

door

Thomas Kupfer

geboren op 1 april 1984
te Grimma, Germany

PROMOTOR: Prof. dr. P. J. Groot

MANUSCRIPTCOMMISSIE: Prof. dr. D. H. Parker
                           Prof. dr. F. W. M. Verbunt
                           Prof. dr. B. Gänsicke   (University of Warwick, Verenigd Koninkrijk)
                           Prof. dr. T. A. Prince   (California Institute of Technology, Verenigde Staten)
                           Dr. E. G. Körding

*All truths are easy to understand
once they are discovered;
the point is to discover them.*
-Galileo Galilei

CONTENTS

CHAPTER 1

INTRODUCTION

1.1 Compact binary evolution

In the year 1617 Benedetto Castelli was the first to observe a binary star with a telescope. He was able to resolve two of the components in the Mizar system. Today, we know that $\sim 30\,\%$ are not born as single stars but are rather born in binary or multiple systems (Lada, 2006). The most important parameters that determine the evolution of the two components in a binary system, and the system as a binary itself, are the two component masses and the orbital period. Binaries show a wide range of component masses and orbital periods. Most binaries have orbital periods so long that the evolution of each stellar component will proceed independently from its companion, and in a similar way to single star evolution, i.e. the components will never interact.

If the initial period of the system is short enough ($P_{\mathrm{orb}} \lesssim 30\,\mathrm{yr}$) both components can come into contact (Eggleton, 2006). An important process by which stars can transfer mass in a binary system is Roche lobe overflow (RLOF). The Roche lobe is the region around a star in a binary system where material is gravitationally bound to that star. The gravitational Roche potential, shown in Fig. 1.1, is the effective potential in a co-rotating frame that includes the gravitational potential of the two stars and the centrifugal force which acts on a test particle moving in the potential (e.g. Kopal, 1959). If the radius of one star exceeds its Roche lobe due to expansion or if the Roche lobe becomes smaller than the radius of the star due to a decreasing orbital separation, mass will flow to the other star through the inner Lagrangian point. The inner Lagrangian point is defined as the point between the two stars where a test particle feels no net force in a co-rotating frame. RLOF can occur stably or unstably depending on the mass ratio of the system and the structure of the stars. Stable mass transfer occurs when the donor can stay inside its Roche lobe and remain in thermal equilibrium, e.g. when the Roche lobe expansion/contraction because of the changing mass ratio and the expansion/contraction of the star (upon mass loss or due to nuclear evolution) is smaller/larger than the Roche lobe expansion/contraction. If the mass ratio $q = \frac{M_2}{M_1} > 1.2$, where M_2 is the Roche lobe filling star, RLOF is unstable (Han et al., 2002b). Dynamically unstable mass transfer occurs when the donor is not able to keep its radius smaller than its Roche lobe. The runaway mass transfer will produce an envelope surrounding the two stars: a so-called common envelope. Both stellar
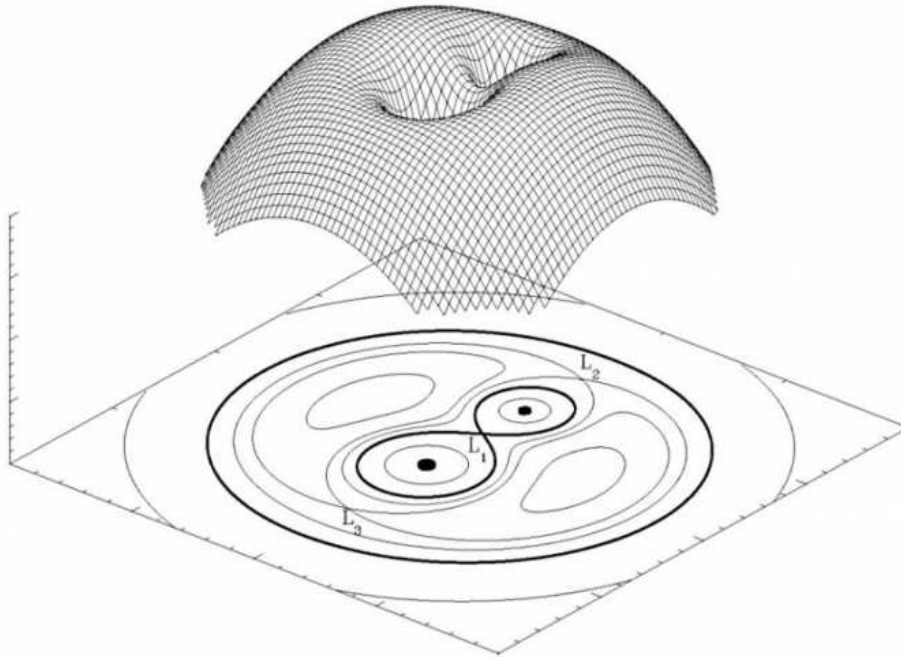
Figure 1.1: A 3-D representation of a dimensionless Roche potential in the co-rotating frame for a binary with a mass ratio of components $q = 2$. Courtesy Martin Heemskerk

cores move inside the common envelope, and orbital energy is deposited in the envelope due to friction, which causes the orbit to shrink significantly and eventually expel the envelope (Paczynski, 1976; Ivanova et al., 2013).

Compact binaries are binary systems where the evolution of the components is affected by the transfer of matter between them (Paczyński, 1971). A schematic overview of the evolutionary paths discussed in the following sections is shown in Fig. 1.2. The following discussion is based on, e.g. Paczyński (1971), Eggleton (2006) and Postnov & Yungelson (2014). To form a compact binary, two main sequence stars with different masses evolve in a binary system. The more massive star evolves faster, reaches the red giant phase first and fills its Roche lobe. If the mass transfer onto the companion is dynamically unstable a common envelope is formed. In the simplest description, the common envelope phase leaves a much closer binary with an orbital period typically between ∼0.1 and a few days. If the mass transfer is dynamically stable, no common envelope is formed and the companion will slowly accrete material from the more massive star. The loss of angular momentum is less effective compared to a common envelope, and the system ends up with a period of hundreds of days. However, our understanding of the onset of instability, of the development and outcome of a common envelope, and even of the amount of loss go mass and angular momentum during stable RLOF are all subject to large uncertainty, and thus our understanding of the formation of compact binaries is limited as well. If the core of the evolved star is degenerate a helium white dwarf is formed directly. If the envelope is removed of a star which has a non-degenerate core, the central burning in the core continues and a helium star is formed which will further evolve to become a carbon/oxygen

(C/O) white dwarf. The companion is still a main sequence star.

If the more massive star fills its Roche lobe on the asymptotic giant branch, the mass transfer onto the companion is unstable and a common envelope is formed. The core of the evolved star has already turned into a C/O white dwarf. This results in a system containing a C/O white dwarf with a main sequence star companion in an orbit between $\sim$0.1 and 10 days.

When the less massive star evolves to become a red giant, a second phase of mass transfer will remove the envelope and shrink the orbit which can lead to separations less than the radius of the sun. Depending on whether the core of the secondary is degenerate or non-degenerate, the system ends up as a double degenerate binary or a white dwarf + helium star binary in a close orbit.

We are now left with a compact double white dwarf or a helium star + white dwarf system in a compact binary with an orbital period of up to a few days. The following evolution is governed by the loss of angular momentum due to the radiation of gravitational waves, which decreases the orbit. The loss of angular momentum ($\dot{J}_{\mathrm{GR}}$) can be calculated as follows, with a being the orbital separation of the stars and $M = M_1 + M_2$ being the total mass of the system and M_1 and M_2 the masses of the two stars and J_{orb} the initial orbital angular momentum:

$$\dot{J}_{\mathrm{GR}} = -\frac{32}{5}\frac{G^3}{c^5}\frac{M_1 M_2 M}{a^4}J_{\mathrm{orb}} \qquad (1.1)$$

If the orbital period after the last common envelope phase is only a few hours the orbital shrinkage due to the radiation of gravitational waves will bring both components into contact within a time span shorter than a Hubble time (equation 9 in Paczyński, 1967 with M_1 and M_1 in $M_\odot$ and P_{orb} in sec):

$$T_0(\text{years}) = 3.22 \cdot 10^{-3}\frac{(M_1 + M_2)^{1/3}}{M_1 M_2}P_{\mathrm{orb}}^{8/3} \qquad (1.2)$$

Once the larger of the stellar remnants fills its Roche lobe, mass is transferred onto the primary (accretor). The larger of the stellar remnants is either the lower mass white dwarf in a double white dwarf system or the helium star in a helium star + white dwarf system. Depending on the structure of the donor star, mass transfer starts at different periods (Nelemans, 2005). A helium white dwarf donor stars fill its Roche lobe at an orbital period of 3-5 min whereas a helium star donor will start transferring mass at an orbital period above ten minutes. If some hydrogen is left in the donor the star will fill its Roche lobe at an orbital period larger than 20 min (Nelemans, 2005). For the most compact systems ($P_{\mathrm{orb}} \lesssim 10$ min) the mass transfer stream hits the accretor directly. This is called the direct impact phase.

Nelemans et al. (2001a) found that the fraction of compact double white dwarfs that survive the direct impact phase and continue their evolution as AM CVn stars is only 0.2%, assuming an absence of an effective coupling between the accretor spin and the orbital motion. However, the survival rate will increase up to 21% in the case of effective spin-orbit coupling (Nelemans et al., 2001a). In the systems that do not form AM CVn stars, the orbit will shrink further. Either the system merges to become an R CrB star if the core reignites, or forms a massive white dwarf if the core does not reignite, or explodes as a supernova Ia if the total mass exceeds the Chandrashekar mass of $1.4\,M_\odot$. For double white dwarf systems, commonly in the literature

(super)giant + main sequence (MS) star

stable roche lobe overflow (RLOF)   unstable RLOF: common envelope phase

He-star + MS star

evolved MS donor
AM CVn star   C/O white dwarf (WD) + MS star

unstable RLOF: common envelope phase

white dwarf + He-star   double white dwarf

He-star donor   Type   R CrB star   He-WD donor
AM CVn star   Ia supernova   C/O WD   AM CVn star
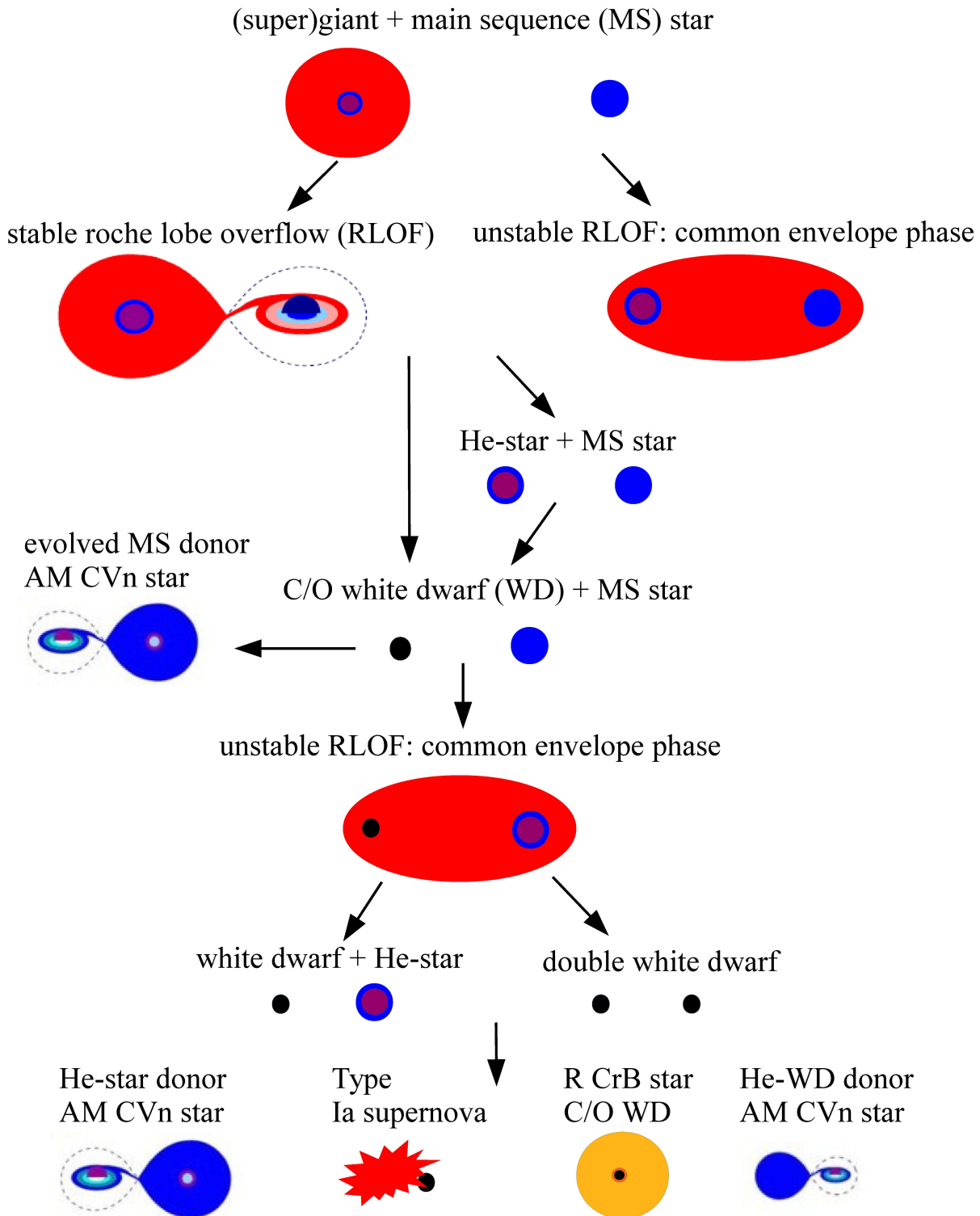
Figure 1.2: Formation of compact binaries.
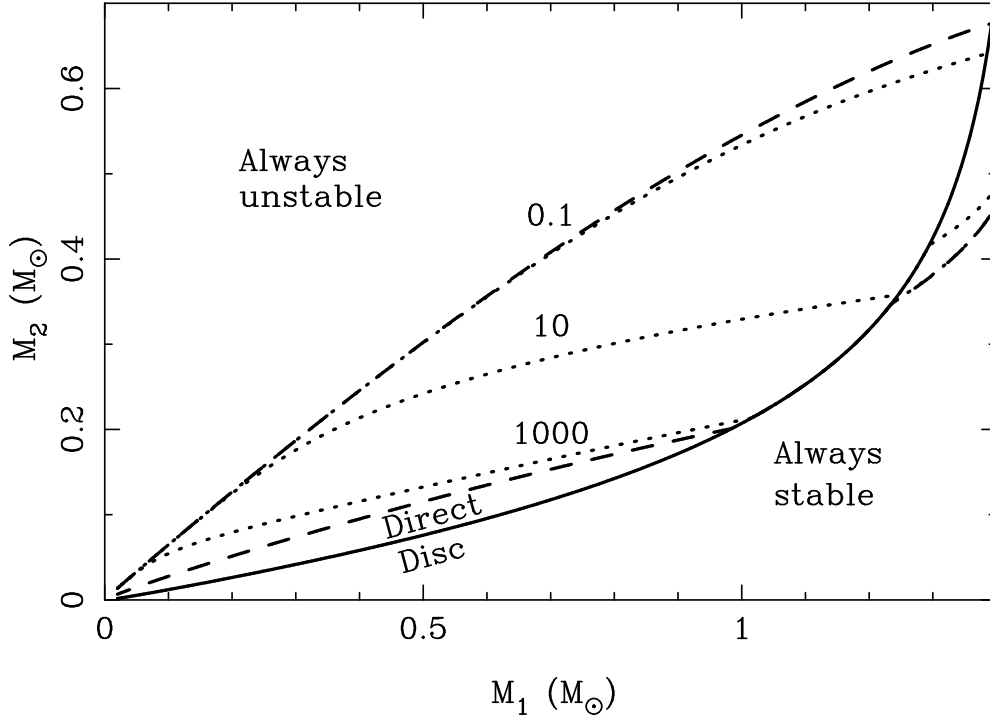
Figure 1.3: The upper dashed line shows the dynamical stability limit $q > 2/3$, while the lower dashed line assumes no feedback of the angular momentum of the accreted material to the orbit. The solid line shows the transition between disc and direct impact accretion. The three dotted lines show how the strict stability limit is relaxed when dissipative torques feed angular momentum from the accretor back to the orbit. The three lines are labelled by the synchronisation timescale (τ_1) in years. Taken from Marsh et al. (2004).

a system with a mass ratio $q = M_2/M_1 < 2/3$, M_1 being the mass of the accretor, is assumed to form an AM CVn type system. Systems with larger mass ratios will merge. This criterion holds if the angular momentum in the spin of the binary components is neglected and all the angular momentum contained in the mass transfer stream is returned to the orbit by tides.

Marsh et al. (2004) and Gokhale et al. (2007) studied the effect of coupling of the accretor's and donor's spin to the orbit. They found that a strong coupling and therefore a strong feedback of angular momentum to the orbit can destabilize systems with mass ratios lower than $2/3$. The rate of change in orbital separation can be written as follows:

$$\frac{\dot{a}}{2a} = \frac{\dot{J}_{GR}}{J_{orb}} + \frac{k_1 M_1 R_1^2}{\tau_1 J_{orb}}\omega_1 + \frac{k_2 M_2 R_2^2}{\tau_2 J_{orb}}\omega_2 - [1 - q - \sqrt{(1+q)r_h}]\frac{\dot{M}_2}{M_1}, \qquad (1.3)$$

with $k_1 M_1 R_1^2$ and $k_2 M_2 R_2^2$ being the moment of inertia of the accretor and the donor star, $\tau_{1,2}$ being the synchronization timescales for the stars, and $\omega_{1,2} = \Omega_{1,2} - \Omega_{orbit}$ being the spin difference between the star(s) and the orbit, $r_h = R_h/a$, where R_h is the radius of an orbit around the accretor which has the same angular momentum as the transferred mass. The first term is always negative and describes the loss of angular momentum due to gravitational wave radiation (Eq. 1.1). The second and the third term describe the dissipative coupling between
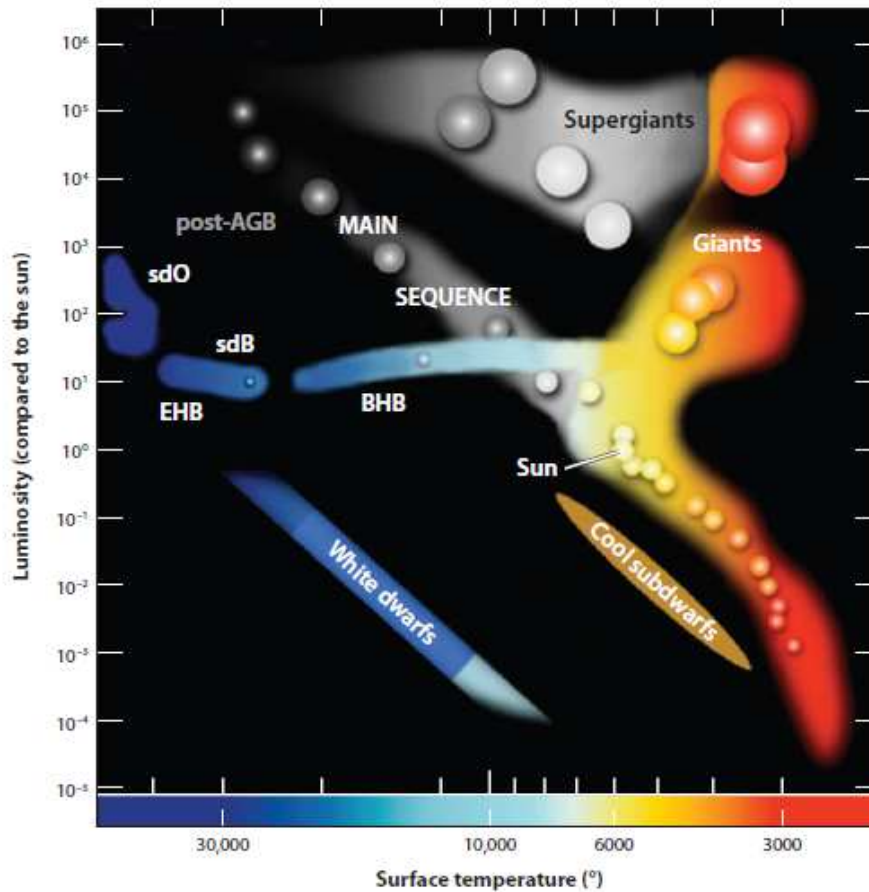
Figure 1.4: Sketch of a Hertzsprung-Russell diagram highlighting the position of hot subdwarf (sdB and sdO) stars and the extreme horizontal branch (EHB) located to the left and below the hot end of the main sequence but above the white dwarf cooling sequence. The EHB is separated from the blue horizontal branch (BHB). Taken from (Heber, 2009).

the accretor/donor and the orbit. The terms are positive if the accretor/donor spins faster than the orbit ($\omega_{1,2} > 0$). The last term can make the mass transfer unstable, because it can lead to a runaway where mass transfer causes the separation to decrease, which in turn causes the mass-transfer rate to increase. Marsh et al. (2004) showed that the critical parameter is the synchronisation timescale (τ_1). The shorter this timscale is, the higher is the survival rate of the direct impact phase, which means that more systems will evolve to become AM CVn type systems and prevent the merger (Fig. 1.3).

1.2   Hot subdwarf stars

Humason & Zwicky (1947) conducted the first survey for faint blue stars in the Northern hemisphere. The Hale telescope on Mount Palomar was used for spectroscopic follow-up where the first hot subdwarf star (HZ 44) was discovered (Greenstein, 1954). Hot subdwarf B stars have little in common with traditional subdwarfs. They are defined as being less luminous

than main-sequence stars of similar spectral type and are situated between the main sequence and the white-dwarf sequence in the Hertzsprung-Russell-Diagram. On the main sequence stars fuse hydrogen in their cores. Once hydrogen is depleted in the core, stars evolve off the main sequence towards lower surface temperatures. Hot subdwarf B stars have evolved far beyond the main sequence (see Fig. 1.4). Therefore these stars do not fuse hydrogen in their cores.

It has been found that hot subdwarf B stars (sdBs) are core helium-fusing stars with masses around $0.5\,M_\odot$ and thin hydrogen envelopes (Heber, 1986; for a recent review see Heber, 2009). Usually core-helium burning stars have also a hydrogen burning layer above the core (so called horizontal branch stars). Once the helium is exhausted, these stars evolve up the asymptotic giant branch when they have two shell burning layers. However, the structure of hot subdwarf stars is distinctively different from ordinary horizontal-branch stars, because their hydrogen envelopes are too thin ($M_{\mathrm{envelope}} < 0.005\,M_\odot$) to sustain hydrogen shell burning, which means that they evolve directly to the white dwarf cooling sequence and avoid the asymptotic giant branch. The question is how the progenitor can remove all but a tiny fraction of the hydrogen envelope at about the same time as the helium core has attained the mass ($0.5\,M_\odot$) required for the He flash, which is a phase of unstable helium burning under degenerate conditions, happening when the star is at the tip of the red-giant branch.

Already more than 40 years ago Mengel et al. (1976) showed that binary interaction can cause strong mass loss. Indeed, Maxted et al. (2001) found that about two-thirds of the sdBs are members of short period binaries with periods below $\sim 10\,$days (Maxted et al., 2001). More recent investigations indicate that half of the sdBs reside in such close binaries (Napiwotzki et al., 2004a; Copperwheat et al., 2011) which is still a very high fraction. This shows that binary interaction must play an important role in the process of formation and evolution of hot subdwarf stars. Han et al. (2002a) and Han et al. (2003) discuss different formation channels to form compact hot subdwarf binaries in detail. In all scenarios, the sdB progenitor fills its Roche lobe close to the tip of the red giant branch. Mass transfer can either be unstable or stable. Fig. 1.5 shows a schematic overview of the evolutionary paths to form compact sdB binaries.

Unstable mass transfer leads to a common envelope and a spiral-in, typically leaving a compact binary containing an sdB with main sequence companion. Stable mass transfer leads to a stable Roche lobe overflow resulting in an sdB or white dwarf with a main sequence companion with an orbital period up to 2000 days. In a second phase of mass transfer, which is unstable, the companion to the sdB progenitor has already turned into a white dwarf. This results, after the common envelope is ejected, in a compact system containing an sdB with a white dwarf (WD) companion.

Fontaine et al. (2012) derived the average sdB mass observationally. They collected sdB masses of a sample of 22 sdBs (15 derived from asteroseismology and 7 from resolved binaries), and found a sharp peak at $M_{\mathrm{sdB}} = 0.47\,M_\odot$. The result is consistent with calculations done with binary population synthesis codes. Han et al. (2003) discussed the sdB mass distribution formed via different phases of mass transfer. They found a sharp peak at $M_{\mathrm{sdB}} = 0.46\,M_\odot$ for sdBs formed after a common envelope phase.
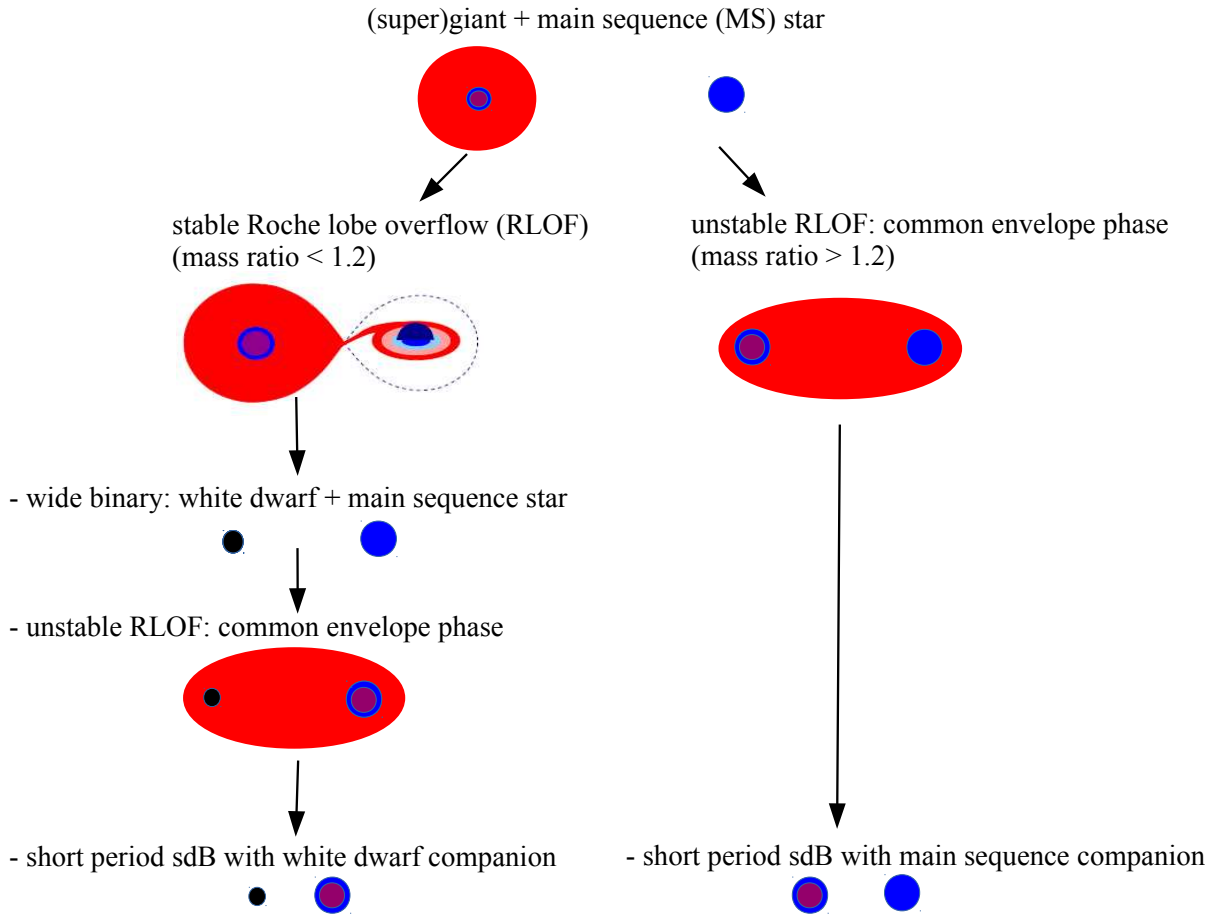
Figure 1.5: Evolutionary channels for the production of compact sdB binaries with white dwarf or main sequence companion.

Several studies were undertaken to determine the orbital parameters of subdwarf binaries (e.g. Edelmann et al. 2005; Green et al. 2008; Morales-Rueda et al. 2003b; Geier et al. 2011b). The orbital periods range from 0.07 to more than 10 days with a peak at 0.5-1.0 days. The number of known systems increased significantly over the last years to 142 compact hot subdwarf binaries with known orbital periods and constrains on the mass function (chapter 2).

The companions to sdBs in radial-velocity-variable close binary systems are white dwarfs (37%), late type main sequence stars (19%) or, in three cases, brown dwarfs (2%). In the remaining 42% of the systems the companion type remains unclassified. Two of the known systems with white dwarf companion are candidates for supernovae Ia (Maxted et al., 2000a; Geier et al., 2007; Vennes et al., 2012; Geier et al., 2013b). Almost all close sdB binaries appear to be single-lined. Therefore, only the binary mass function can be calculated.

The binary mass function can be derived (Eq. 1.4) from Kepler's third law, which depends only on two observable quantities: the orbital period P and the radial velocity (RV) semi-amplitude K_{sdb}. If the inclination of the system and the mass of one star in the binary is known, the mass of the other star can be calculated.

$$f_{\mathrm{m}} = \frac{M_{\mathrm{comp}}^3 \sin^3 i}{(M_{\mathrm{comp}} + M_{\mathrm{sdB}})^2} = \frac{PK_{\mathrm{sdb}}^3}{2\pi G}. \tag{1.4}$$

The orbital period P and the RV semi-amplitude K_{sdb} can be measured from spectroscopy. Hence, the mass of the sdB (M_{sdB}) and the companion (M_{comp}) as well as the inclination angle i remain free parameters. Assuming a canonical mass for the sdB $M_{\mathrm{sdB}} = 0.47\,\mathrm{M_\odot}$ (see Fontaine et al., 2012 and references therein) and an inclination angle $i < 90°$, a minimum mass for the companion can be determined by solving the cubic equation:

$$\frac{2\pi G \sin^3 i}{PK^3} M_{\mathrm{comp}}^3 - M_{\mathrm{comp}}^2 - 2M_{\mathrm{sdB}} M_{\mathrm{comp}} - M_{\mathrm{sdB}}^2 = 0 \tag{1.5}$$

If time resolved photometry for the short-period sdB binaries is available, further constraints can be put even if the companion mass is inconclusive. The hemisphere of a cool low-mass main sequence companion facing the sdB is heated up by the significantly hotter sdB star. This causes a sinusoidal variation in the light curve. More (less) flux is emitted if the irradiated hemisphere of the cool companion is faced towards (away) from the observer. If this so-called reflection effect is detected, a compact companion can be excluded and a cool companion, either a low-mass main sequence star of spectral type M or a brown dwarf, is most likely. However, if the light curve of the short-period system shows no variation, a compact object like a WD is most likely to be the companion.

1.2.1   The MUCHFUSS project

The existence of a neutron star or black hole companion to sdB stars is predicted by theory (Podsiadlowski et al., 2003; Pfahl et al., 2003). About 1% of the compact sdB binaries are expected to have a neutron star companion (Yungelson & Tutukov, 2005; Nelemans, 2010). To search for such rare systems with either massive white dwarfs ($M_{\mathrm{WD}} > 1.0\,\mathrm{M_\odot}$), neutron stars or black holes the radial velocity survey MUCHFUSS (Massive Unseen Companions to Hot Faint Underluminous Stars from the Sloan Digital Sky Survey) was started (Geier et al., 2011a).

The Sloan Digital Sky Survey (SDSS) is a multi-color imaging and spectroscopic survey using a 2.5-m wide-angle optical telescope at Apache Point Observatory (York et al., 2000). About 1100 hot subdwarf stars from SDSS were selected by colour selection and visual inspection of their spectra. Stars with high velocities (heliocentric radial velocities $> \pm 100\,\mathrm{km\,s^{-1}}$) have been re-observed and individual SDSS spectra have been analysed. The sample of promising targets consists of 69 objects: 52 stars show significant RV shifts ($> 30\,\mathrm{km\,s^{-1}}$) within 0.02 - 0.07 days, while 17 stars show high RV shifts (100 - 300 $\mathrm{km\,s^{-1}}$) over more than one day. A detailed overview of the strategy and target selection is given in Geier et al. (2011a).

Up to now a total of 22 systems from the MUCHFUSS sample have their orbital periods and mass functions measured. Originally designed as a project to find the most massive companions, MUCHFUSS has now discovered the least massive companions to hot subdwarf stars: two systems host brown dwarf companions (Geier et al., 2011d; Schaffenroth et al., 2014b).

However, no neutron star or black hole companion to a hot subdwarf star has yet been detected unambiguously.

1.3   AM CVn type binaries

A specific type of object discussed in this thesis are the AM Canum Venaticorum stars, named after the prototype AM Canum Venaticorum (AM CVn), which is a variable star in the constellation Canum Venatici (Hunting Dog). AM CVn itself was first recognized as a blue star by Malmquist (1936). In the first survey for faint blue stars in the Northern hemisphere, done by Humason & Zwicky (1947), AM CVn became HZ 29. The first spectrum of AM CVn was taken at the Hale telescope on Mount Palomar, and Greenstein & Matthews (1957) recognized a large number of He I absorption lines and the absence of hydrogen. Smak (1967) discovered an 18 min variability in AM CVn and suggested a binary nature for the system. Faulkner et al. (1972) proposed an ultracompact nature of the system with a degenerate helium star donor with a mass of $M \sim 0.041\,\mathrm{M_\odot}$. Although, the binary nature of AM CVn was known very early, it took until the new millennium before the true orbital period of $1028.7\,\mathrm{s}$ was discovered (Nelemans et al., 2001b).

Fifteen years ago, fewer than 10 systems were known. Mainly due to two very successful surveys the known sample of AM CVn systems increased significantly. Sixteen systems were discovered by the Sloan Digital Sky Survey (e.g. Roelofs et al., 2005; Anderson et al., 2005, 2008; Rau et al., 2010; Carter et al., 2012, 2014a) and another seven systems by the Palomar Transient Factory (Levitan et al., 2011, 2013, 2014). Together with smaller scale surveys, this quadrupled the number of known systems over the last 15 years to the 43 AM CVn type binaries known today. An overview of the known systems is given in Tab. 1.1.

AM CVn systems are ultracompact binaries consisting of a white dwarf accretor and a low mass (semi-)degenerate helium star secondary (Nelemans et al., 2001a, see Solheim (2010) for a recent review). The accretor is believed to be a C/O white dwarf with a mass around 0.5-$1.0\,\mathrm{M_\odot}$. The accretion disc and the accretor contribute significantly to the luminosity of the system (Bildsten et al., 2006). The donor was never observed in an AM CVn type system with $P_{\mathrm{orb}} > 10\,\mathrm{min}$ because of its low luminosity. Depending on the evolutionary history, three different donor types are discussed in the literature.

1) White dwarf: The first discussed donor type is a white dwarf (Nelemans et al., 2001a; Tutukov & Yungelson, 1996). In this scenario the companion is a degenerate helium white dwarf with a mass below $M_2 \sim 0.3\,\mathrm{M_\odot}$ to prevent helium ignition in the core. The degenerate donor increases in size upon mass loss, and therefore the system is only stable as an AM CVn system when the Roche Lobe of the donor increases. In order to increase the Roche Lobe, the orbit has to widen. The composition of the donor is dominated by helium with CNO abundances according to the equilibrium of the CNO cycle. In the CNO cycle nitrogen is enhanced and carbon and oxygen is depleted. Therefore, a high N/O and N/C ratio is expected for a helium white dwarf donor (Nelemans et al., 2010).

2) Semi-degenerate He-star: The second possible donor is a semi-degenerate helium star (Iben & Tutukov, 1991; Nelemans et al., 2001a; Yungelson, 2008). In this scenario the
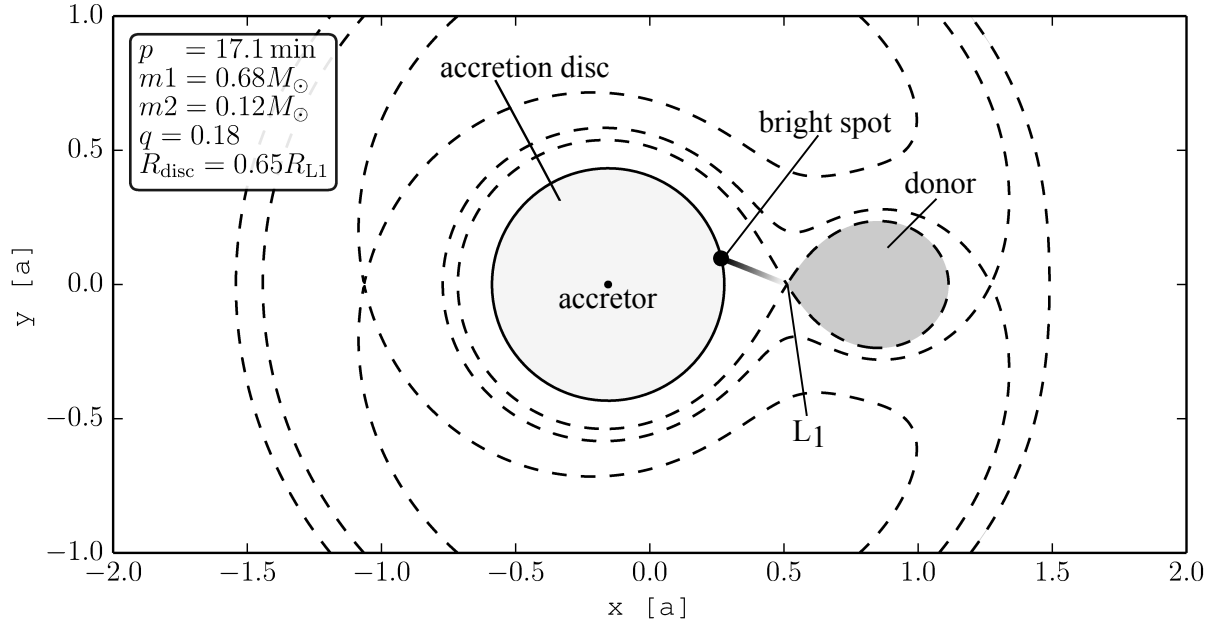
Figure 1.6: Model of an AM CVn type system using the system parameter found for AM CVn itself (Roelofs et al., 2006b). The donor star (teardrop-shaped) fills its Roche lobe and material leaves the donor star though the L_1 point. The accretion stream hits the disc in the bright spot. Accretion onto the primary white dwarf occurs through the accretion disc. Indicated is also the Roche potential.

companion is a helium star with a mass above $M \sim 0.3\,\mathrm{M_\odot}$ to allow helium ignition in the core. A non-degenerate helium star shrinks upon mass loss, therefore the Roche lobe has to shrink to sustain accretion. In order to decrease the Roche lobe, the orbit has to shrink. Once the helium envelope is stripped enough, helium burning will stop and the donor star turns into a semi-degenerate object where the evolution occurs in a similar way as for the white dwarf donor. The minimum orbital period for a system with a semi-degenerate helium star donor is around 10 min. During the helium burning phase the composition in the core of the donor has changed. Helium burns into carbon and oxygen which increases the carbon and oxygen abundance. Therefore, a lower N/O and N/C ratio is expected for a semi-degenerate donor compared to the white dwarf donor (Nelemans et al., 2010).

3) Evolved main sequence star: The last discussed scenario is the evolved main-sequence star donor (Podsiadlowski et al., 2003; Tutukov et al., 1985). This scenario needs a lot of fine tuning. The initial orbital period of the system has to be such that the progenitor donor star fills its Roche lobe close to the end of the main sequence. At this point the core of the donor star reaches a high level of hydrogen depletion. When accretion starts, the evolution occurs in a similar way as for a helium star and the orbit shrinks further. Once the mass loss has progressed into the helium rich core the donor star turns into a semi-degenerate object, the orbit starts to widen and the evolution occurs in a similar way as in the other two scenarios. The system can reach a minimum orbital period of ~ 7 min (Podsiadlowski et al., 2003). Most of these systems will have some hydrogen left which can be detected in the spectrum. Only systems which evolved to very short periods get rid of all their hydrogen and may look like

helium white dwarf donors because helium never ignited in these systems (Nelemans et al., 2010).

The currently known population of AM CVn type binaries shows orbital periods in a range of 5.4 - 65 min. As these systems evolve from a short orbital period, their mass transfer rate decreases by several orders of magnitude as the orbit widens.

The AM CVn objects can be divided into four groups:

1. $P_{orb} < 10$ min: Ultrashort period systems where no or only a very small disc is present, and accretion occurs through direct impact onto the surface of the accretor

2. 10 min $< P_{orb} < 20$ min: High state systems with an optically thick disc with helium spectral lines in absorption. These systems show no outburst behaviour photometrically

3. 20 min $\leq P_{orb} < 40$ min: Variable systems that show regular photometric outbursts when the systems switch from a low state accretion disc spectroscopically dominated by helium emission lines, to a high state, where helium lines in absorption dominate the spectrum. The outburst frequency decreases with increasing orbital period (Levitan et al., 2015)

4. $P_{orb} \geq 40$ min: Low state systems with strong helium emission lines in their spectra. They have optically thin accretion discs, which were thought to show no outburst until recently (Tsugawa & Osaki, 1997; Nelemans, 2005). Only recently three systems with periods well above 40 min were detected in outburst (Woudt et al., 2013; Kato et al., 2014; Rixon et al., 2014)

The material leaving the donor is transferred through a free falling accretion stream towards the accretor. The stream hits the disc in the so-called 'bright spot'. This small area of increased luminosity on the side of the accretion disc is crucial when analysing AM CVn type binaries. The radial velocity changes of light emitted by this 'bright spot' can be detected, and the orbital period can therefore be measured spectroscopically. A schematic view of an AM CVn type system is shown in Fig. 1.6.

Table 1.1: Overview of the known AM CVn systems

System[a]	Outbursting	Period (min)	Quiescence (g)	Discovery year	References
HM Cnc	N	5.36	20.7	1999	1
V407 Vul	N	9.48	19.7	1995	2
ES Ceti	N	10.3	17.1	2002	3
AM CVn	N	17.1	14.2	1967	5
KIC 004547333	N	18.2	16.1	2010	4
HP Lib	N	18.4	13.5	1994	6
PTF1 J191905.19+481506.2	Y	22.5	21.5	2011	7
ASASSN-14cc	Y	22.5[sh]	19.0	2014	35
CR Boo	Y	24.5	17.4	1985	8, 9
KL Dra	Y	25.0	19.1	1998	10

Overview of the known AM CVn systems - continued

System	Outbursting	Period (min)	Quiescence (g)	Discovery year	References
V803 Cen	Y	26.6	16.9	1987	6, 11, 12
PTF1 J071912.13+485834.0	Y	26.8	19.4	2010	13
SDSS J092638.71+362402.4	Y	28.3	19.0	2005	14, 15
CP Eri	Y	28.7	20.3	1992	16
PTF1 J094329.59+102957.6	Y	30.4	20.7	2011	17
V406 Hya	Y	33.8	20.5	2003	18
PTF1 J043517.73+002940.7	Y	34.3	22.3	2011	17
SDSS J173047.59+554518.5	N	35.2	20.1	2011	19, 20
2QZ J142701.6–012310	Y	36.6	20.3	2005	21
SDSS J124058.03–015919.2	Y	37.4	19.7	2005	22
SDSS J012940.05+384210.4	Y	37.6	19.8	2005	14, 23, 24
SDSS J172102.48+273301.2	Y	38.1	20.1	2009	25, 26
SDSS J152509.57+360054.5	N	44.3	19.8	2009	24, 25
SDSS J080449.49+161624.8	N	44.5	18.2	2009	27
SDSS J141118.31+481257.6	N	46.0	19.4	2005	14
GP Com	N	46.5	15.9	1972	28
CRTS J045020.8–093113	Y	47.3	20.5	2012	29
SDSS J090221.35+381941.9	Y	48.3	20.2	2009	25
Gaia14aae	Y	48.7	18.5	2014	36
SDSS J120841.96+355025.2	N	52.6	18.8	2008	24, 30
SDSS J164228.06+193410.0	N	54.2	20.3	2009	24, 25
SDSS J155252.48+320150.9	N	56.3	20.2	2005	31
SDSS J113732.32+405458.3	N	59.6	19.0	2013	32
V396 Hya	N	65.1	17.3	2001	33
SDSS J150551.58+065948.7	N		19.1	2013	32
CRTS J084413.6–012807	Y		20.3	2014	34
SDSS J104325.08+563258.1	Y		20.3	2012	19
PTF1 J221910.09+313523.1	Y		20.6	2011	17
CRTS J074419.7+325448	Y		21.1	2014	34
PTF1 J085724.27+072946.7	Y		21.8	2011	17
PTF1 J163239.39+351107.3	Y		23.0	2011	17
PTF1 J152310.71+184558.2	Y		23.5	2011	17
SDSS J204739.40+000840.1	Y		24.0	2008	31

[sh] superhump period

References: (1) Roelofs et al. (2010); (2) Steeghs et al. (2006); (3) Espaillat et al. (2005); (4) Kupfer et al. submitted; (5) Roelofs et al. (2006b); (6) Roelofs et al. (2007b); (7) Levitan et al. (2014); (8) Patterson et al. (1997); (9) Kato et al. (2000); (10) Wood et al. (2002); (11) Patterson et al. (2000); (12) Kato et al. (2004); (13) Levitan et al. (2011); (14) Anderson et al. (2005); (15) Copperwheat et al. (2011); (16) Groot et al. (2001); (17) Levitan et al. (2013); (18) Roelofs et al. (2006a); (19) Carter et al.

(2013); (20) Carter et al. (2014b); (21) Woudt et al. (2005); (22) Roelofs et al. (2005); (23) Shears et al. (2011); (24) Kupfer et al. (2013); (25) Rau et al. (2010); (26) Augusteijn, T, private communication; (27) Roelofs et al. (2009); (28) Nather et al. (1981); (29) Woudt et al. (2013); (30) Anderson et al. (2008); (31) Roelofs et al. (2007c); (32) Carter et al. (2014a); (33) Ruiz et al. (2001); (34) Breedt et al. (2014); (35) Kato et al. (2015); (36) Rixon et al. (2014)

1.4 Techniques

In this thesis, I make extensive use of phase resolved spectroscopy and Doppler tomography to derive orbital periods, velocity amplitudes and phases in order to put constraints on system parameters.

1.4.1 Phase resolved spectroscopy

Spectroscopy has been used to study stellar objects for more than 200 years. William Hyde Wollaston was the first who recognized dark features in the spectrum of the Sun. Twelve years later Joseph von Fraunhofer rediscovered these dark lines independently and mapped over 570 lines systematically, the so called Fraunhofer lines. However, he could not explain the origin of these lines. It took until the year 1860 when Gustav Kirchhoff and Robert Bunsen noticed that several of the Fraunhofer lines are coincident with emission lines identified in the spectra of heated elements. Kirchhoff (1860) correctly concluded that the dark lines in the solar spectrum are caused by absorption of different elements in the atmosphere of the Sun.

Today, about 150 years later, spectroscopy is not just used to identify elements in the stars but also to determine stellar parameters such as effective temperatures, surface gravity, rotational velocities and surface abundances. In a binary system spectroscopy is a powerful tool for determining binary parameters. The components in a binary star move around the centre of mass of the binary and thus their observed spectral features will be shifted in wavelength due to the Doppler effect. This shift will correspond to the radial velocity, the projected velocity in the line of sight of the observer, of the star. The velocity of a star can be determined by measuring the central wavelength, λ_{obs} of a line emitted by it, and comparing it to the line's rest wavelength λ_{rest}. The measured non-relativistic velocity is then:

$$v = c\frac{\lambda_{\mathrm{obs}} - \lambda_{\mathrm{rest}}}{\lambda_{\mathrm{rest}}} \tag{1.6}$$

From one single velocity measurement the binary parameters cannot be constrained. Several spectra covering at least one full orbital period are needed to measure a radial velocity curve and obtain system parameters, such as the radial velocity amplitude of the stars and the orbital period. It is important that the exposure time of one individual spectrum does not exceed $\sim 1/10$ of the orbital period because the spectrum will be smeared over the orbit and the measured velocity does not correspond to the real velocity. This is particularly important for the ultracompact AM CVn type binaries because of their short orbital periods.
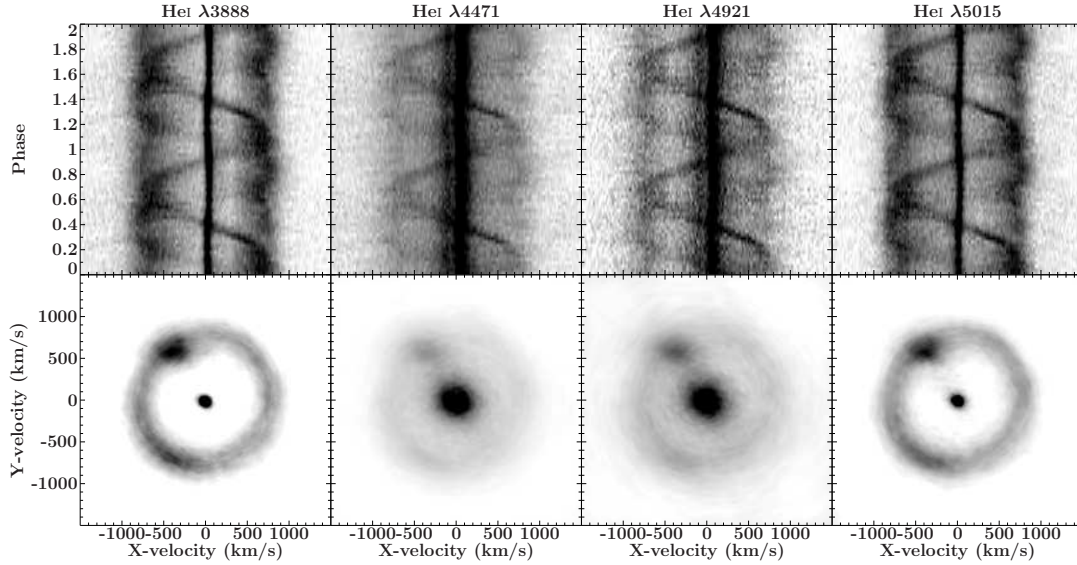
Figure 1.7: Trailed spectra (top row) and maximum-entropy Doppler tomograms (bottom row) of four He I lines from GP Com (chapter 4).

Given the typical orbital periods in AM CVn stars, the maximum exposure time is a couple of minutes in most cases. This results in poor signal-to-noise ratio (SNR) individual spectra (SNR∼ 1-5). Phase resolved spectroscopy is the tool to address this issue. Here, many short exposures are taken consecutively covering several binary orbits. Once the orbital period is known the spectra are folded on this period which means that the orbit is divided into several phase bins and the spectra taken at the same orbital phase are co-added to increase the signal to noise ratio per phase bin. If enough orbits are covered the signal per phase bin is high enough to show spectral signatures which can then be analysed in full detail. The upper row in Fig. 1.7 shows the phase folded spectra around four example helium lines in the AM CVn system GP Com (chapter 4).

1.4.2 Doppler tomography

Doppler tomography (Marsh & Horne, 1988) is a powerful tool for representing 2-dimensional velocity fields of unresolved point sources such as compact binaries. At a distance of 100 parsec and a typical separation of the components in an ultracompact binary of about 100 000 km, the angular separation on the sky is 10^{-6} arcseconds. The Hubble Space Telescope has a angular resolution worse than 10^{-2} arcseconds and even the European Extremely Large Telescope (E-ELT) will have a maximum angular resolution of 10^{-3} arcseconds, three orders of magnitude worse than needed to resolve a close-by ultracompact binary. Therefore, indirect techniques are the only suitable tool to study the structure of these binaries.

The stellar components revolve in a binary system around the center of mass (Fig. 1.6), hence a specific point in the system is redshifted when it moves towards us and blueshifted when it moves away from us during one orbit. Doppler tomography uses this information to reconstruct the binary system in velocity coordinates. Emission features that are stationary

in the binary frame add up constructively in a Doppler tomogram while emission that is not stationary in the binary frame or moves on a period different from the orbital period will be spread out over the Doppler tomogram.

Although a Doppler tomogram does not contain more information than phase folded spectra and is just a different way of showing the data compared to a trail of the phase resolved spectroscopy, it is useful to measure velocity amplitudes and phases and to separate out features that move with a different velocity and/or different phase (e.g. bright spot and central spike). In particular, this is very important if the data are noisy and the profiles show a complicated structure. In such a case, Doppler tomography is important to concentrate the signal of features, and makes it possible to measure velocity amplitudes and phases. Fig. 1.7 shows an example of a trail and the corresponding Doppler tomograms. Usually, in a trail the accretion disc, an S-wave and a central spike is visible. The S-wave corresponds to the motion of the bright spot. The central spike is an emission feature which is connected to the primary white dwarf and has so far only been detected in AM CVn type systems. In the trail two S-waves, as well as the central spike, intersect and overlap with each other. In the Doppler tomograms the signals of the two S-waves and the central spike are well separated from each other, and phases and velocity amplitudes can be measured independently.

1.5   Overview of the thesis

The main questions discussed in this thesis are:

1. How does the population of compact hot subdwarf binaries look in different stellar populations and how can we link them to other post-common envelope type binaries, such as compact detached double degenerate systems, white dwarf + main sequence systems and AM CVn type binaries?

2. What is the Galactic population and evolutionary history of ultracompact AM CVn type binaries?

In chapter 2 atmospheric and orbital parameters of 12 new close sdB binaries discovered by the MUCHFUSS project are presented in detail. This study brings the number of sdB binaries with orbital periods of less than 30 days and measured mass functions to 142. We present an analysis of the minimum companion mass distribution and the orbital period distribution. The full sample was compared to the known population of extremely low-mass white dwarf binaries as well as short-period white dwarfs with main sequence companions and the future evolution of the full sample was calculated.

Chapter 3 discusses the results obtained from phase resolved spectroscopy of four AM CVn type systems. Orbital periods for the four systems are derived and spectral signatures of the individual systems are discussed. For one system a mass ratio was constrained. For the first time, flux ratios for several helium lines were extracted from the Doppler tomograms for the disc and bright spot region, and compared with single-slab LTE models with variable electron densities and path lengths to estimate the disc and bright spot temperature.

In chapter 4 *Kepler* satellite photometry obtained in short cadence mode as well as phase-resolved spectroscopy of the ultracompact AM CVn type binary SDSS J190817.07+394036.4 is presented. The orbital period was derived. Velocity amplitudes and phases are obtained and the spectral features are discussed in detail. A Fourier analysis, O-C diagrams and a discrete Fourier analysis of the *Kepler* data is presented. Models of the system were constructed to compare the phases of the radial velocity curves and the lightcurve variation.

Chapter 5 presents high- and medium-resolution UVES and X-Shooter phase-resolved spectroscopy of the AM CVn type binaries GP Com and V396 Hya. The spectral signatures found in the full optical/near-infrared range covered by X-Shooter is shown. Velocity amplitudes of the central spikes as well as the metal emission and absorption lines are measured, and from the results, system parameter are deduced. The central spikes are compared to Stark broadened synthetic models and the electron density in the plasma is determined. Rotational velocities of the narrow emission lines are derived.

In chapter 6 medium-resolution X-Shooter spectroscopy of seven AM CVn type binaries is presented. The spectral signatures found in the full optical/near-infrared range of every individual system is shown and discussed in detail. An overview of the different elements detected in the X-Shooter spectra of the various systems is presented. From the detected elements constrains on the donor types are given.

CHAPTER 2

HOT SUBDWARF BINARIES FROM THE MUCHFUSS PROJECT - ANALYSIS OF 12 NEW SYSTEMS AND A STUDY OF THE SHORT-PERIOD BINARY POPULATION

T. Kupfer, S. Geier, U. Heber, R. H. Østensen, B. N. Barlow, P. F. L. Maxted, C. Heuser, V. Schaffenroth and B. T. Gänsicke

Abstract. The project Massive Unseen Companions to Hot Faint Underluminous Stars from SDSS (MUCHFUSS) aims at finding hot subdwarf stars with massive compact companions like massive white dwarfs ($M > 1.0\,\mathrm{M_\odot}$), neutron stars, or stellar-mass black holes. The existence of such systems is predicted by binary evolution theory, and recent discoveries indicate that they exist in our Galaxy.

We present orbital and atmospheric parameters and put constraints on the nature of the companions of 12 close hot subdwarf B star (sdB) binaries found in the course of the MUCHFUSS project. The systems show periods between 0.14 and 7.4 days. In nine cases the nature of the companions cannot be constrained unambiguously whereas three systems most likely have white dwarf companions. We find that the companion to SDSS J083006.17+475150.3 is likely to be a rare example of a low-mass helium-core white dwarf. SDSS J095101.28+034757.0 shows an excess in the infrared that probably originates from a third companion in a wide orbit, which makes this system the second candidate hierarchical triple system containing an sdB star. SDSS J113241.58−063652.8 is the first helium deficient sdO star with a confirmed close companion.

This study brings to 142 the number of sdB binaries with orbital periods of less than 30 days and with measured mass functions. We present an analysis of the minimum companion mass

distribution and show that it is bimodal. One peak around $0.1\,\mathrm{M_\odot}$ corresponds to the low-mass main sequence (dM) and substellar companions. The other peak around $0.4\,\mathrm{M_\odot}$ corresponds to the white dwarf companions. The derived masses for the white dwarf companions are significantly lower than the average mass for single carbon-oxygen white dwarfs. In a T_{eff} $-\log g$ diagram of sdB+dM companions, we find signs that the sdB components are more massive than the rest of the sample. The full sample was compared to the known population of extremely low-mass white dwarf binaries as well as short-period white dwarfs with main sequence companions. Both samples show a significantly different companion mass distribution indicating either different selection effects or different evolutionary paths. We identified 16 systems where the dM companion will fill its Roche Lobe within a Hubble time and will evolve into a cataclysmic variable; two of them will have a brown dwarf as donor star. Twelve systems with confirmed white dwarf companions will merge within a Hubble time, two of them having a mass ratio to evolve into a stable AM CVn-type binary and another two which are potential supernova Ia progenitor systems. The remaining eight systems will most likely merge and form RCrB stars or massive C/O white dwarfs depending on the structure of the white dwarf companion.

2.1 Introduction

Hot subdwarf B stars (sdBs) are hot core helium-burning stars with masses around $0.5\,\mathrm{M_\odot}$ and thin hydrogen layers (Heber, 1986; for a recent review see Heber, 2009). It has been shown that a large fraction of sdBs are members of short-period binaries with periods below ~ 10 days (Maxted et al., 2001; Napiwotzki et al., 2004a). For such short-period sdB binaries common envelope (CE) ejection is the only likely formation channel. One possible scenario is that two main sequence stars (MS) evolve in a binary system. The more massive one will evolve faster to become a red giant. Unstable mass transfer from the red giant to the companion will lead to a CE phase. Because of the friction in this phase, the two stellar cores lose orbital energy and angular momentum, which leads to a shrinkage of the orbit. This energy is deposited in the envelope which will finally be ejected. If the core reaches the mass required for the core-helium flash before the envelope is lost, a binary consisting of a core-helium burning sdB star and a main sequence companion is formed. In another possible scenario the more massive star evolves to become a white dwarf (WD) either through a CE phase or stable mass transfer onto the less massive companion. The less massive star evolves then to become a red giant. Unstable mass transfer will lead to a CE and once the envelope is ejected the red giant remnant starts burning helium, and a system consisting of an sdB with a WD companion is formed (Han et al., 2002a, 2003).

If the red giant loses enough mass that the remnant is not massive enough to ignite helium the star will evolve directly to become a helium-core white dwarf. Helium-core white dwarfs with masses below $0.3\,\mathrm{M_\odot}$ are called extremely low-mass (ELM) white dwarfs (Brown et al., 2010). According to single star evolution, ELM-WDs should not exist as the evolutionary timescale to form them is much longer than the age of the universe. Therefore, significant mass transfer during the evolution is needed and most of the observed ELM-WDs indeed

reside in close binary systems, usually with WD companions. Those systems are formed through the same CE-ejection process as the short-period sdB binaries, except that the envelope is ejected before the core reaches the mass required to ignite helium (Brown et al., 2010). Recent studies have increased the number of known ELM-WDs significantly (Brown et al., 2013 and references therein). During their evolution they can spectroscopically appear as sdBs. However, they have lower masses compared to helium core-burning sdBs. Three low-mass sdBs, which evolve directly towards the ELM-WD phase are known so far. All have WD companions and lie below the Zero-Age Extreme Horizontal Branch (Heber et al., 2003; O'Toole et al., 2006; Silvotti et al., 2012). Furthermore, hot He-WD progenitors in an earlier stage of evolution have been recently found orbiting intermediate-mass main sequence stars (EL CVn systems, Maxted et al., 2013).

Hot subdwarf binaries, as well as WDs with massive WD companions, turned out to be good candidates for SN Ia progenitors. Because of gravitational wave radiation, the orbit will shrink further and mass transfer from the sdB onto the WD will start once the sdB fills its Roche lobe. The Chandrasekhar limit might be reached either trough He accretion on the WD (e.g. Yoon & Langer, 2004 and references therein) or a subsequent merger of the sdB+WD system (Tutukov & Yungelson, 1981; Webbink, 1984). Two sdBs with massive WD companions have been identified to be good candidates for being SN Ia progenitors. KPD 1930+2752 has a total mass of $1.47\,M_\odot$ exceeding the Chandrasekhar limit and will merge within about 200 million years (Maxted et al., 2000a; Geier et al., 2007). CD$-30°$ 11223 has the shortest known orbital period of all sdB binaries ($P_{orb} = 0.048979$ days) and is a good candidate to explode as an underluminous helium double-detonation SN Ia (Vennes et al., 2012; Geier et al., 2013b). The explosion of the massive WD companion in the eclipsing sdO+WD system HD 49798 on the other hand may be triggered by stable mass transfer (Mereghetti et al., 2009).

Neutron star (NS) or even black hole (BH) companions are predicted by theory as well (Podsiadlowski et al., 2002; Pfahl et al., 2003). In this scenario two phases of unstable mass transfer are needed and the NS or the BH is formed in a supernova explosion. Yungelson & Tutukov (2005) predicted that about 0.8% of the short-period sdBs should have NS companions. In an independent study, Nelemans (2010) showed that about 1% of these systems should have NS companions whereas about 0.1% should have BH companions.

However, no NS/BH companion to an sdB has yet been detected unambiguously whereas a few candidates have been identified (Geier et al., 2010b). Follow-up observations have been conducted with radio and X-ray telescopes. Coenen et al. (2011) did not detect any radio signals of a pulsar companion at the positions of four candidate systems from Geier et al. (2010b). Mereghetti et al. (2011, 2014) searched for X-rays powered by wind accretion onto compact companions to sdBs using the *Swift* and *XMM* satellites, but did not detect any of those targets.

NS+WD systems have been discovered amongst pulsars. Ferdman et al. (2010) showed that the peculiar system PSR J1802-2124 contains a millisecond pulsar and a low-mass C/O WD. This system may have evolved from an sdB+NS system. Most recently, Kaplan et al. (2013) discovered the close companion to the pulsar PSR J1816+4510 to be a He-WD progenitor with atmospheric parameters close to an sdB star ($T_{eff} = 16\,000$ K, $\log g = 4.9$).

Many studies have been performed to identify short-period sdB binaries with periods from a few hours to more than ten days. Up to now, 142 short-period sdB binaries have measured radial velocity curves and mass functions with a peak in the period distribution between 0.5 to 1.0 days (e.g. Morales-Rueda et al., 2003b; Geier et al., 2011b; Copperwheat et al., 2011). In most cases it is hard to constrain the nature of the companion as most sdB binaries are single-lined systems. From the radial-velocity (RV) curve only lower mass limits can be derived. Most of the companions are either dMs or WDs. Only in a few examples could strong constraints be put on the nature of the companion.

SdBs with main sequence companions are potential progenitors of detached WD+dM binaries, which possibly further evolve to become cataclysmic variables (CVs). Hence, there should be correlations between those two types of systems, even though a compact WD+dM system can be formed directly and does not necessarily evolve from an sdB+dM binary. Recent studies have increased the number of known WD+dMs significantly and population studies have been carried out (Nebot Gómez-Morán et al., 2011 and references therein).

In addition to the short-period sdB binaries, long period sdBs formed via stable Roche lobe overflow have been postulated (Han et al., 2002a, 2003). Between one third and half of sdB stars are found to show spectroscopic signature of a main sequence type F/G/K companion and associated infrared excess (Reed & Stiening, 2004). Because of their long periods, these systems show only small radial velocity variations and radial velocity curves have not been measured for years. Just recently the first systems with orbits of several hundreds days were discovered (Deca et al., 2012; Østensen & Van Winckel, 2012; Vos et al., 2012, 2013). Eventually, these systems will evolve to become WD+main sequence binaries with periods of hundreds of days and might experience another phase of mass transfer, when the main sequence companion turns into a red giant.

PG 1253+284, the first triple system containing an sdB with a close companion and a wide main sequence companion was discovered by Heber et al. (2002). This system shows an infrared excess caused by the wide component. However, the wide component is not involved in the formation of the sdB. The unseen close companion expelled the envelope of the sdB progenitor.

Here we present orbital solutions for 12 new sdB binaries discovered in the course of the MUCHFUSS project. Sec. 2.2 describes the status of the MUCHFUSS project. Sec. 2.3 gives an overview of the observations and the data reduction. The derived orbital parameters, as well as the atmospheric parameters of the sdBs, are described in Sec. 2.4 and 2.5. In Sec. 2.6, we determine the minimum masses and put constraints on the nature of the unseen companions when no light variations were detected by searching for an infrared excess in a two-colour diagram. In addition, in Sec. 2.7 we study the full population of sdBs in close binaries, discuss the period distributions, the companion mass distributions, as well as selection effects of the whole sample of sdB binaries with derived mass function. Sec. 2.8 compares the full sample with the samples of known ELM-WD binaries and WD+dM binaries to gain insight in the formation history of hot subdwarfs. Summary and conclusions are given in Sec. 2.9.

Table 2.1: Overview of the solved binary systems.

Short name	SDSS name	Other names
J01185−00254	SDSS J011857.20−002546.5	PB 6373
J03213+05384	SDSS J032138.67+053840.0	PG 0319+055
J08233+11364	SDSS J082332.08+113641.8	−
J08300+47515	SDSS J083006.17+475150.3	PG 0826+480
J09523+62581	SDSS J095238.93+625818.9	PG 0948+632
J09510+03475	SDSS J095101.28+034757.0	PG 0948+041
J10215+30101	SDSS J102151.64+301011.9	−
J11324+06365	SDSS J113241.58−063652.8	PG 1130−063
J13463+28172	SDSS J134632.65+281722.7	TON 168
J15082+49405	SDSS J150829.02+494050.9	SBSS 1506+498
J15222−01301	SDSS J152222.14−013018.3	−
J18324+63091	SDSS J183249.03+630910.5	FBS 1832+631

2.2   The MUCHFUSS project

The project Massive Unseen Companions to Hot Faint Underluminous Stars from SDSS (MUCHFUSS) aims at finding hot subdwarf stars with massive compact companions like massive white dwarfs ($M > 1.0\,\mathrm{M_\odot}$), neutron stars or stellar-mass black holes. Hot subdwarf stars were selected from the Sloan Digital Sky Survey by colour and visual inspection of the spectra. Objects with high radial velocity variations were selected as candidates for follow-up spectroscopy to derive the radial velocity curve and the mass function of the system. [1]

Geier et al. (2011a, 2012b) discuss the target selection and the follow-up strategy. A detailed analysis of seven sdB binaries discovered in the course of this project is presented in Geier et al. (2011b). In addition, three eclipsing systems were detected, two of which host brown-dwarf companions. These are the first confirmed brown-dwarf companions to sdB stars (Geier et al., 2011d; Schaffenroth et al., 2014b). One sdB+dM system contains a hybrid pulsator and shows a strong reflection effect (Østensen et al., 2013). Results from a photometric follow-up campaign of the MUCHFUSS targets will be described in detail in Schaffenroth et al. (in prep). During dedicated spectroscopic MUCHFUSS follow-up runs with unfavourable weather conditions, bright sdB binary candidates were observed (Geier et al., 2013b, 2014). A full catalogue of all RV measurements is presented in Geier et al. (2015)

---

[1]Hot subdwarfs with a large but constant radial velocity were studied in the Hyper-MUCHFUSS project (Tillich et al., 2011).

Table 2.2: Summary of the follow-up observations in the course of the MUCHFUSS project.

Date	Telescope & Instrument	Resolution [$\lambda/\Delta\lambda$]	Coverage [Å]
2009-May-27 – 2009-May-31	CAHA-3.5m+TWIN	4000	3460 – 5630
2009-Nov-08 – 2009-Nov-12	ESO-NTT+EFOSC2	2200	4450 – 5110
2010-Feb-12 – 2010-Feb-15	SOAR+Goodman	7000	3500 – 6160
2010-Aug-02 – 2010-Aug-03	SOAR+Goodman	7000	3500 – 6160
February – July 2011	Gemini-North+GMOS-N	1200	3610 – 5000
February – July 2011	Gemini-South+GMOS-S	1200	3610 – 5000
2011-Nov-15 – 2011-Nov-19	CAHA-3.5m+TWIN	4000	3460 – 5630
February – July 2012	Gemini-North+GMOS-N	1200	3610 – 5000
February – July 2012	Gemini-South+GMOS-S	1200	3610 – 5000
2012-May-25 – 2012-May-27	CAHA-3.5m+TWIN	4000	3460 – 5630
2012-Jul-09 – 2012-Jul-12	ING-WHT+ISIS	4000	3440 – 5270
2012-Oct-21 – 2012-Oct-24	SOAR+Goodman	7000	3500 – 6160
2012-Dec-14 – 2012-Dec-18	ING-WHT+ISIS	4000	3440 – 5270
2013-Jun-02 – 2012-Jun-05	ING-WHT+ISIS	4000	3440 – 5270
2013-Aug-11 – 2013-Aug-13	ING-WHT+ISIS	4000	3440 – 5270
2014-Feb-01 – 2014-Feb-05	ESO-NTT+EFOSC2	2200	4450 – 5110

2.3   Observations and data reduction

Follow-up medium resolution spectroscopy of 12 sdB binaries (see Table 2.1 for an overview) was obtained using different instruments including the CAHA-3.5m telescope with the TWIN spectrograph, the ESO-NTT telescope with the EFOSC2 spectrograph, the SOAR telescope with the Goodman spectrograph, the Gemini-North/South telescopes with the GMOS-N/S spectrographs and the William Herschel telescope (WHT) with the ISIS spectrograph. Table 2.2 gives an overview of all follow-up runs and the instrumental set-ups.

All spectra were corrected with an average bias frame constructed from several individual bias frames as well as an average flat field constructed from several flat field lamps. Reduction was done either with the MIDAS[2], IRAF[3] or PAMELA[4] and MOLLY[4] packages.

---

[2]The ESO-MIDAS system provides general tools for data reduction with emphasis on astronomical applications including imaging and special reduction packages for ESO instrumentation at La Silla and the VLT at Paranal

[3]IRAF is distributed by the National Optical Astronomy Observatories, which are operated by the Association of Universities for Research in Astronomy, Inc., under cooperative agreement with the National Science Foundation

[4]http://www2.warwick.ac.uk/fac/sci/physics/research/astro/people/marsh/software
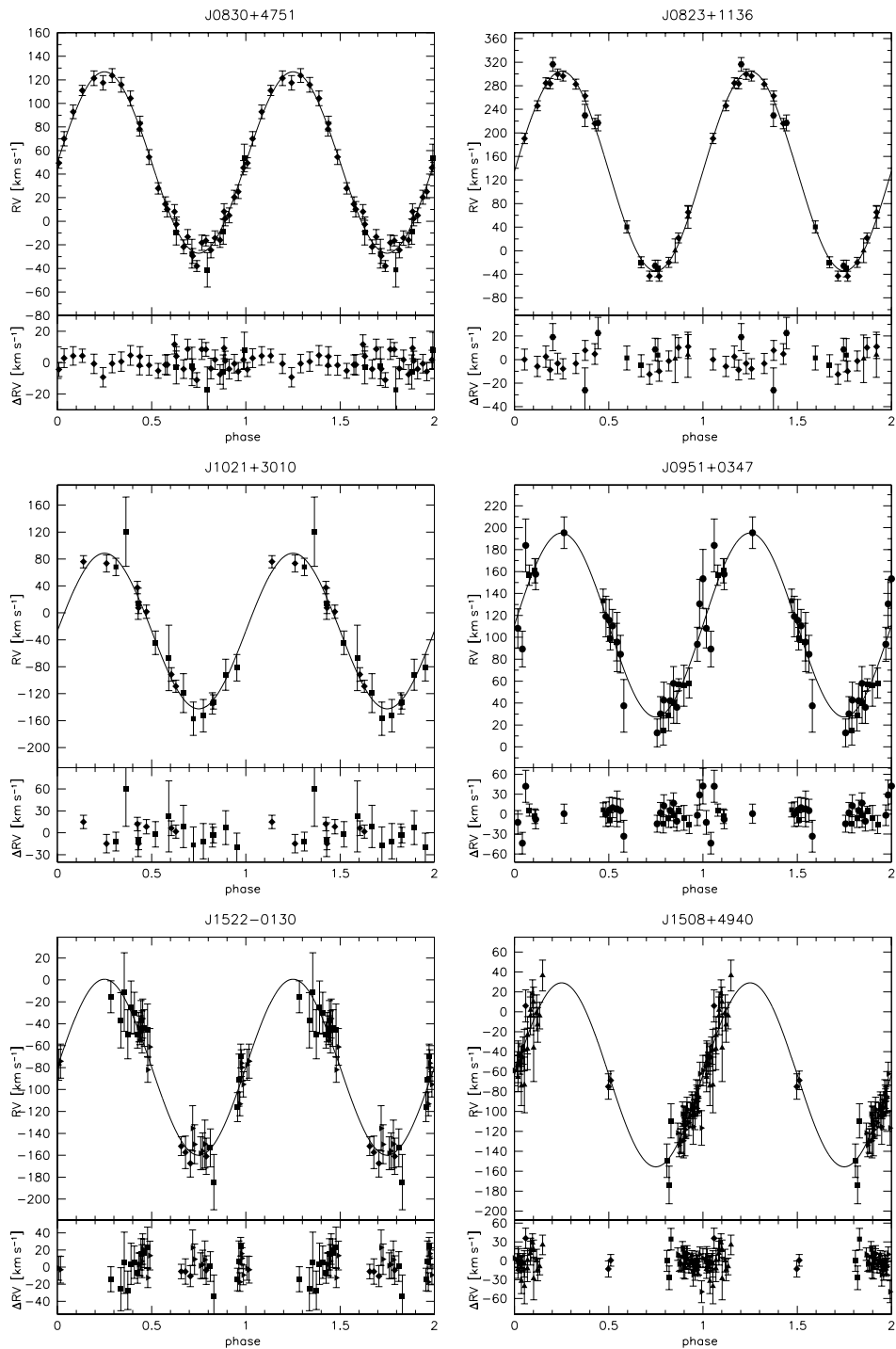
Figure 2.1: Radial velocity plotted against orbital phase. The RV data were phase folded with the most likely orbital periods and are plotted twice for better visualisation. The residuals are plotted below. The RVs were measured from spectra obtained with SDSS (squares), CAHA3.5m/TWIN (upward triangles), WHT/ISIS (diamonds), Gemini/GMOS (triangles turned to the right), ESO-NTT/EFOSC2 (circles), and SOAR/Goodman (pentagons).
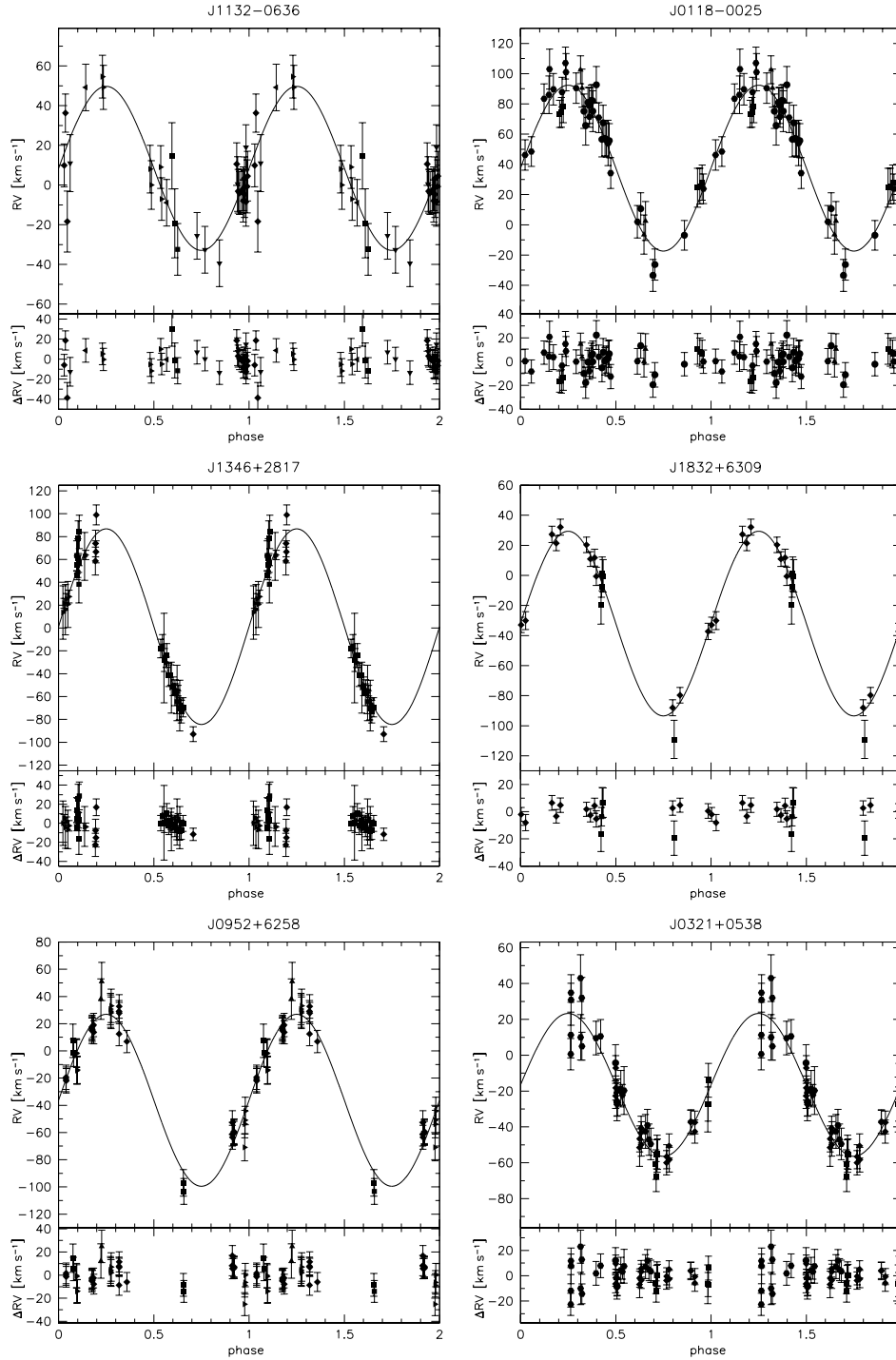
Figure 2.2: Radial velocity plotted against orbital phase (see Fig 2.1).

2.4 Orbital parameters

The radial velocities (RVs) were measured by fitting a set of mathematical functions matching the individual line shapes to the hydrogen Balmer lines as well as helium lines if present using the FITSB2 routine (Napiwotzki et al., 2004b). Polynomials were used to match the continua
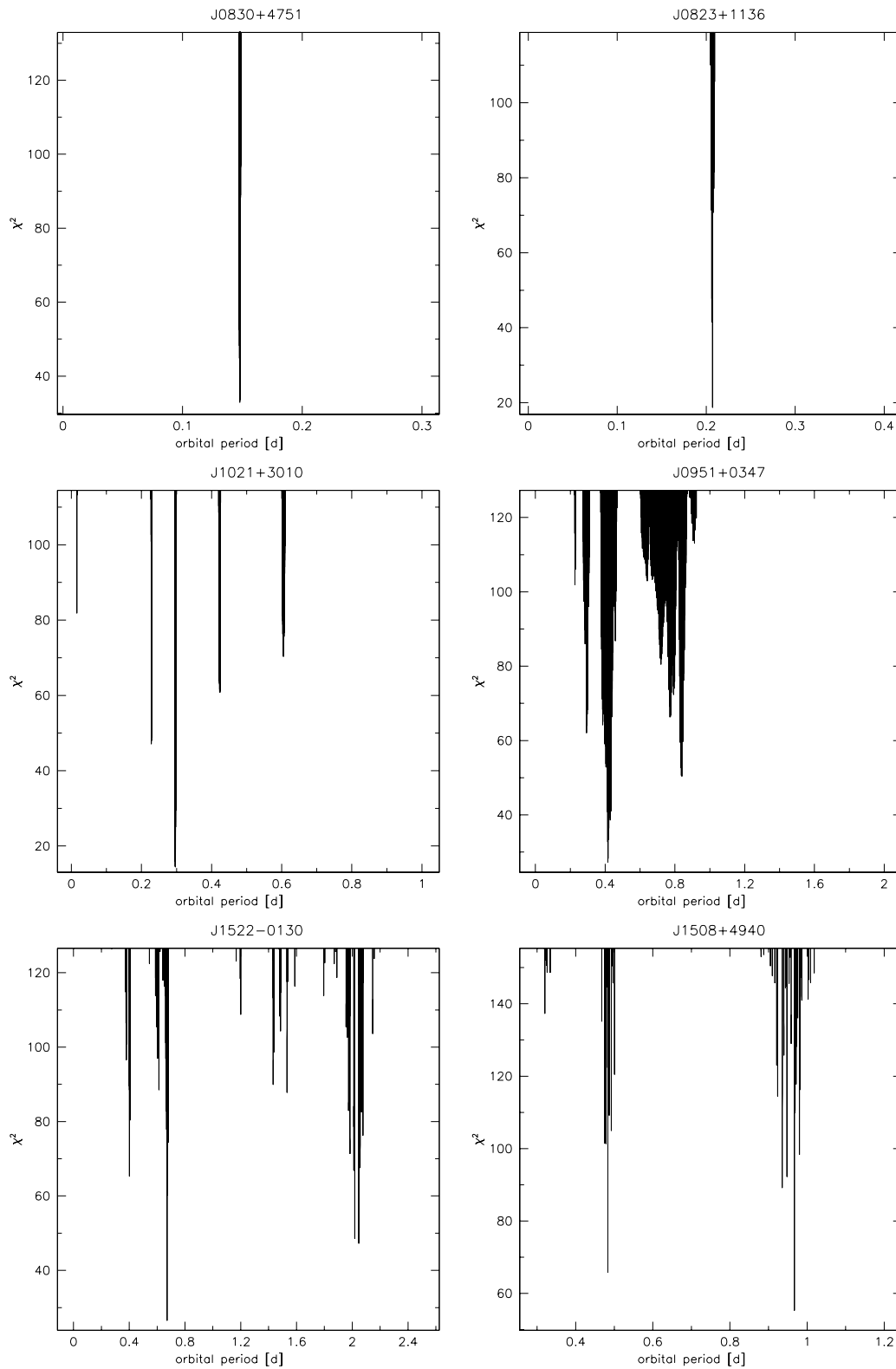
Figure 2.3: χ^2 plotted against orbital period. The lowest peak corresponds to the most likely solution.
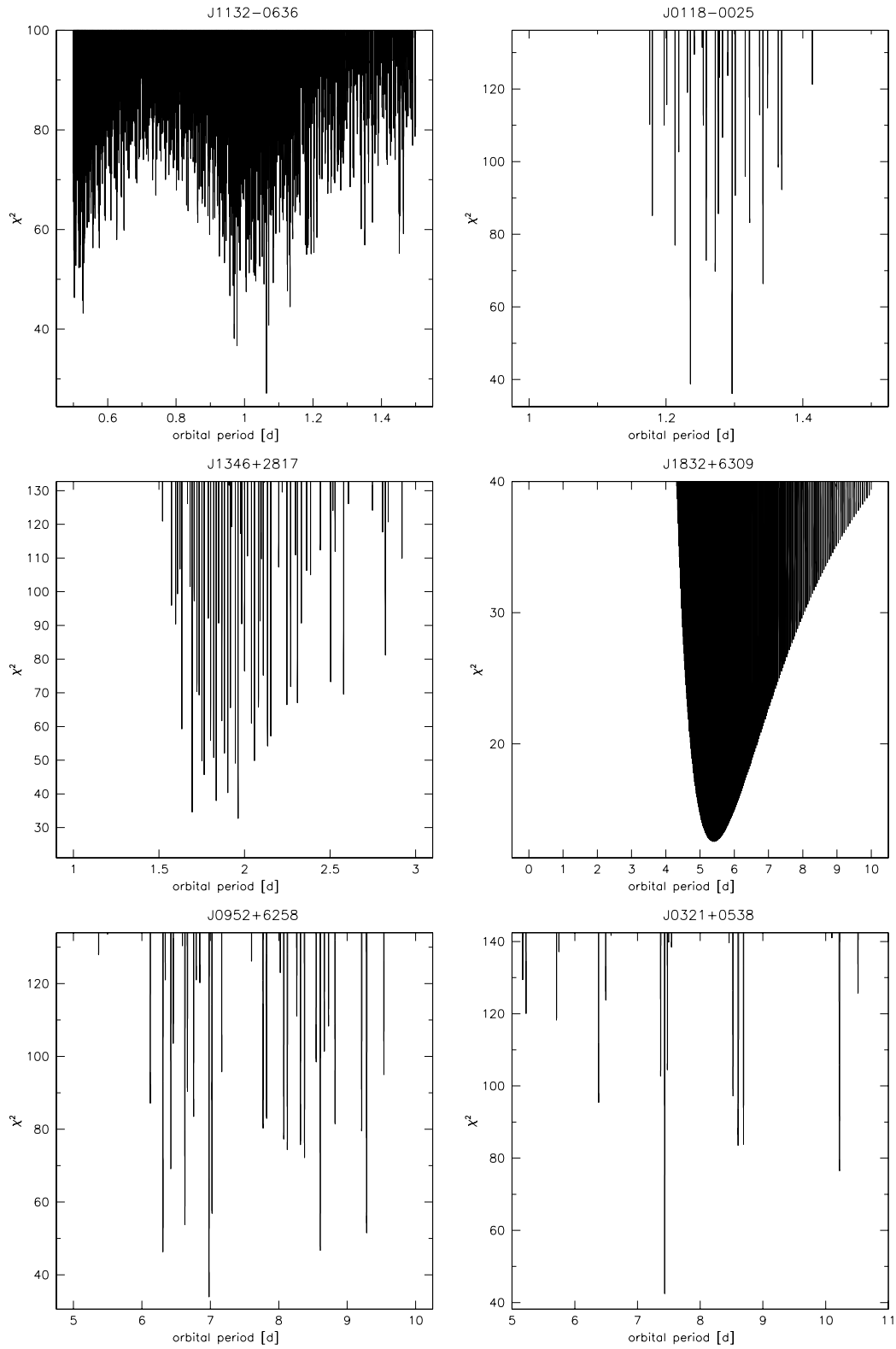
Figure 2.4: χ^2 plotted against orbital period (see Fig 2.3).

and a combination of Lorentzian and Gaussian functions to match cores and wings of the lines.

The orbital parameter (orbital phase T_0[5], period P, system velocity γ, and RV-semiamplitude K), as well as their uncertainties and associated false-alarm probabilities ($p_{\text{false}}[1\%]$, $p_{\text{false}}[10\%]$) are determined as described in Geier et al. (2011b, 2014). To calculate the significance of the orbital solutions and to estimate contribution of systematic effects to the error budget, we modified the χ^2 of the best solution by adding systematic errors e_{norm} in quadrature until the reduced χ^2 reached ~ 1.0. The phased RV curves for the best solutions are given in Fig. 2.1 and 2.2, the χ^2-values plotted against orbital period in Fig. 2.3 and Fig. 2.4. The minimum in χ^2 corresponds to the most likely solution. The adopted systematic errors and false-alarm probabilities are given in Table 2.3. The probabilities that the adopted orbital periods are correct to within 10% range from 80% to $> 99.99\%$.

2.5 Atmospheric parameters

Atmospheric parameters have been determined by fitting appropriate model spectra to the hydrogen Balmer and helium lines in the way described in Geier et al. (2007). For the hydrogen-rich and helium-poor ($\log y = \log(n(\text{He})/n(\text{H})) < -1.0$) sdBs with effective temperatures below $30\,000\,\text{K}$, a grid of metal line blanketed LTE atmospheres with solar metallicity was used (Heber et al., 2000). Helium-poor sdBs and sdOBs with temperatures ranging from $30\,000\,\text{K}$ to $40\,000\,\text{K}$ were analysed using LTE models with enhanced metal line blanketing (O'Toole & Heber, 2006). Metal-free NLTE models were used for the hydrogen-rich sdO J1132$-$0636 (Stroeer et al., 2007).

Each spectrum was velocity corrected according to the orbital solution and co-added for the atmospheric fit. To account for systematic shifts introduced by the different instruments, atmospheric parameters for each star were derived separately from spectra taken with each instrument. Weighted means were calculated and adopted as the final solutions (see Table 2.7).

2.6 The nature of the unseen companion

All our objects appear to be single-lined. Therefore, only the binary mass function can be calculated:

$$f_{\text{m}} = \frac{M_{\text{comp}}^3 \sin^3 i}{(M_{\text{comp}} + M_{\text{sdB}})^2} = \frac{PK^3}{2\pi G}. \tag{2.1}$$

From spectroscopy the orbital period P and the RV semi-amplitude K can be derived. Hence, the mass of the sdB (M_{sdB}) and the companion (M_{comp}) as well as the inclination angle i remain free parameters. Assuming a canonical mass for the sdB $M_{\text{sdB}} = 0.47\,\text{M}_\odot$ (see Fontaine et al., 2012 and references therein) and an inclination angle $i < 90°$, a minimum mass for the companion can be determined. If the derived minimum companion mass is higher than the Chandrasekhar limit, the NS/BH nature of the companion is proven without further constraints

---

[5]T_0 corresponds to the minimum distance of the sdB star from our Solar System

Chapter 2. Hot subdwarf binaries from the MUCHFUSS project - Analysis of 12 new systems and a study of the short-period binary population

30

Table 2.3: Derived orbital parameters.

Object	T_0 [$-2\,450\,000$]	P [d]	γ [$\mathrm{km\,s^{-1}}$]	K [$\mathrm{km\,s^{-1}}$]	e_norm [$\mathrm{km\,s^{-1}}$]	$\log p_\mathrm{false}[10\%]$	$\log p_\mathrm{false}[1\%]$
J08300+47515	6279.6067 ± 0.0004	0.14780 ± 0.00007	49.9 ± 0.9	77.0 ± 1.7	4.0	< -4.0	< -4.0
J08233+11364	6278.5729 ± 0.0007	0.20707 ± 0.00002	135.1 ± 2.0	169.4 ± 2.5	7.0	< -4.0	< -4.0
J10215+30101	6277.819 ± 0.003	0.2966 ± 0.0001	-28.4 ± 4.8	114.5 ± 5.2	6.4	-1.9	-1.9
J09510+03475	6693.666 ± 0.003	0.4159 ± 0.0007	111.1 ± 2.5	84.4 ± 4.2	2.8	-2.0	-0.8
J15222$-$01301	6516.632 ± 0.005	0.67162 ± 0.00003	-79.5 ± 2.7	80.1 ± 3.5	$-$	-1.2	-1.2
J15082$-$49405	6518.395 ± 0.02	0.967164 ± 0.000009	-60.0 ± 10.7	93.6 ± 5.8	6.0	-0.9	-0.9
J11324$-$06365	4583.06 ± 0.01	1.06 ± 0.02	8.3 ± 2.2	41.1 ± 4.0	8.6	-1.1	-0.2
J01185$-$00254	5882.000 ± 0.008	1.30 ± 0.02	37.7 ± 1.8	54.8 ± 2.9	6.9	< -4.0	-0.4
J13463+28172	6517.99 ± 0.01	1.96 ± 0.03	1.2 ± 1.2	85.6 ± 3.4	$-$	-0.4	-0.3
J18324$-$63091	6119.58 ± 0.03	5.4 ± 0.2	-32.5 ± 2.1	62.1 ± 3.3	2.7	-0.9	-0.1
J09523+62581	5210.23 ± 0.08	6.98 ± 0.04	-35.4 ± 3.6	62.5 ± 3.4	7.8	-0.7	-0.6
J03213+05384	6280.17 ± 0.05	7.4327 ± 0.0004	-16.7 ± 2.1	39.7 ± 2.8	4.7	-1.8	-1.8
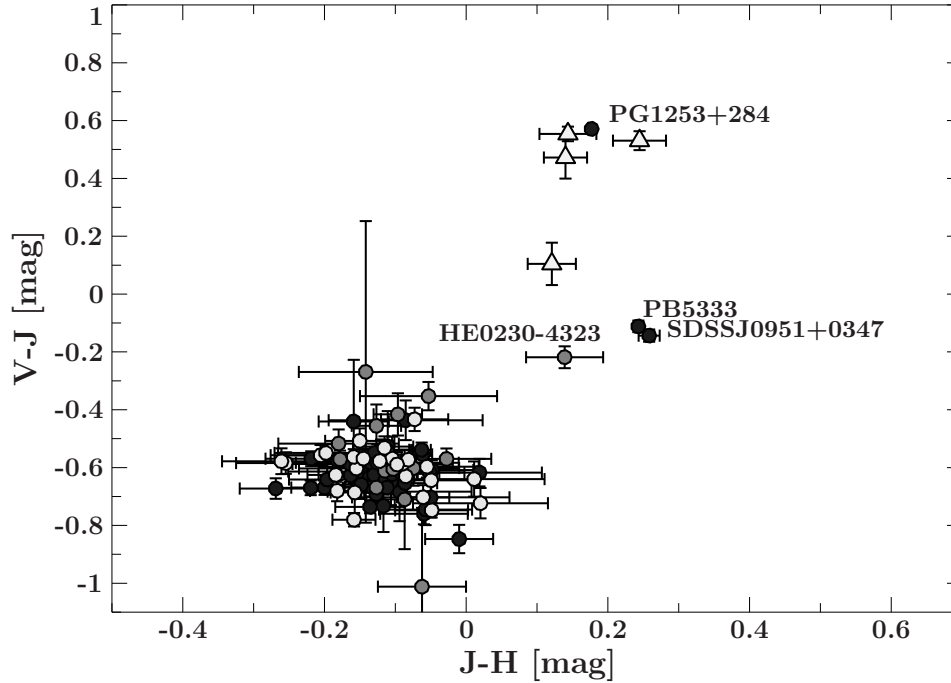
Figure 2.5: Two-colour plots of $V-J$ vs. $J-H$ for all systems in our sample with 2MASS/UKIDSS colours, V magnitudes and low reddening (E(B-V)<0.1; light grey circles: WD companion, grey circles: dM companion, dark grey circles: unknown companion type). Most of the systems show no excess from a companion. The systems showing an infrared excess which indicates a cool companion are named. For comparison, 4 sdB binaries with confirmed G/K-type companions (light grey triangles) are shown (Vos et al., 2012, 2013). All colours were corrected for reddening.

under the assumption that the sdB does not have a mass significantly lower than the canonical mass.

All spectra were checked for contamination by a cool stellar companion. Typically, the Mg I triplet around $5170\,\text{Å}$ and the Ca II triplet around $8650\,\text{Å}$ are the best indicators. None of our programme stars show obvious signs of a companion in the spectrum.

A cool companion of spectral type $\sim M1-M2$ or earlier is detectable from an infrared excess even if the spectra in the optical range are not contaminated with spectral lines from the cool companion. Stark & Wade (2003) showed that two-colour diagrams can be used to detect unresolved late-type stellar companions using optical colours (B and V) in combination with 2MASS colours (J and K_s). Reed & Stiening (2004) convolved Kurucz models with appropriate 2MASS (J, H and K_s) and B-filters and showed that companions of spectral type $M2$ and earlier would be separated from single sdBs in two-colour diagrams. Green et al. (2006, 2008) created two-colour plots from V band and 2MASS photometry (J and H) of single-lined and composite sdB spectra that showed a clear separation between the composites and the single-lined spectra. Hence, the presence of a cool companion can be inferred by its infrared excess.

Table 2.4: Derived minimum masses and most probable nature of the companions.

Object	$f(M)$	$M_{2\text{min}}$	Companion
	$[M_\odot]$	$[M_\odot]$	
J08300+47515	0.007	0.14	WD$^{\text{lc}}$
J08233+11364	0.104	0.44	MS/WD
J09510+03475	0.025	0.23	MS/WD
J15222−01301	0.036	0.27	MS/WD
J10215+30101	0.046	0.30	MS/WD
J15082−49405	0.08	0.39	MS/WD
J11324−06365	0.008	0.14	MS/WD
J01185−00254	0.022	0.22	MS/WD
J13463+28172	0.13	0.49	WD
J18324−63091	0.13	0.50	MS/WD
J09523+62581	0.18	0.58	WD
J03213+05384	0.048	0.31	MS/WD

lc: companion type derived from the lightcurve

We inspected each system with 2MASS/UKIDSS[6] (J and H) and V band colour informa-tion for an infrared excess to put tighter constraints on the nature of the companions. Figure 2.5 shows the two-colour diagram of the whole sample for systems with colour information and small reddening ($E(B-V) < 0.1$). All colours were corrected for Galactic reddening using Table 6 with $R_v = 3.1$ from Schlafly & Finkbeiner (2011). However, if a system does not show an excess in the infrared a cool companion can be excluded only when the minimum companion mass derived from the RV-curve is higher than the mass of a stellar companion which would cause an excess. To calculate the mass of the companion needed to cause an excess we used the following approach.

First, we calculated the distance to each system using the reddening-corrected V magni-tude, effective temperature and surface gravity as described in Ramspeck et al. (2001). The next step is to calculate the apparent magnitude in the J band for different subclasses of dMs using the distance modulus:

$$m = 5\log_{10}(d) - 5 + M, \tag{2.2}$$

where d is the distance in parsec and M the absolute magnitude of the dM taken from Table 5 in Kraus & Hillenbrand (2007). The calculated apparent magnitudes for each subclass in the J band can be compared to the measured J magnitudes of each individual system. Our assumption is that a cool companion would show up in the J band if the calculated magnitude is 3 sigma above the measured J magnitude. The calculated magnitude which would be visible in the J band can be converted to the corresponding mass of the dM from Table 5 in Kraus &

---

[6]for 2MASS; only colours flagged with quality A were used

Hillenbrand (2007) using linear interpolation. If the derived mass is lower than the minimum companion mass derived from the RV-curve, a cool companion can be excluded because it would cause an excess in the infrared. In these systems a compact companion is most likely. If an excess is detected a cool companion is likely.

If time resolved photometry for the short-period sdB binaries is available, further constraints can be put even if the companion mass is inconclusive. The hemisphere of a cool low-mass main sequence companion facing the sdB is heated up by the significantly hotter sdB star. This causes a sinusoidal variation in the light curve. More (less) flux is emitted if the irradiated hemisphere of the cool companion is faced towards (away) from the observer. If this so-called reflection effect is detected, a compact companion can be excluded and a cool companion either a low-mass main sequence star of spectral type M or a brown dwarf is most likely. However, if the light curve of the short-period system shows no variation, a compact object like a WD is most likely to be the companion. Table 2.4 gives an overview on the most likely companions of our sample.

2.6.1   WD companions

J09523+62581 and J13463+28172 have minimum companion masses obtained from the radial velocity curve higher than dM masses which would cause an infrared excess. No sign of a companion is visible in the spectrum nor in the two-colour diagram. Therefore, the companion in both systems is most likely a WD.

2.6.2   J08300+47515 - a system with a possible ELM-WD companion

J08300+47515 is a remarkable system. The minimum companion mass is only $0.14\,\mathrm{M_\odot}$. Therefore, the nature of the companion cannot be constrained unambiguously from spectroscopy. The period of the system is 0.14780 ± 0.00007 days. This means that a cool main sequence companion would show a reflection effect in the light curve. However, a 2.14 h light curve of J08300+47515 obtained with the CAHA-2.2m telescope using BUSCA shows no light variation with a standard deviation of 0.0063 on the normalised lightcurve (see Schaffenroth et. al in prep). The companion might therefore be an ELM-WD. However, the inclination of the system cannot be constrained and it is still possible that the system is seen under low inclination. The maximum mass for an ELM-WD is $\sim 0.3\,\mathrm{M_\odot}$. If the sdB has the canonical mass of $\sim 0.47\,\mathrm{M_\odot}$ and J08300+47515 is seen under an inclination angle of $i < 32.4°$ the companion will be more massive than $\sim 0.3\,\mathrm{M_\odot}$ and not be a new ELM-WD companion. The probability of finding a system with $i < 32.4°$ is $\sim 15\,\%$.

2.6.3   J11324−06365 - the first helium deficient sdO with a close companion

Stroeer et al. (2007) studied the evolutionary status of 58 subdwarf O stars (sdOs) and concluded that the helium deficient sdOs are likely to be evolved sdBs. Indeed, evolution tracks
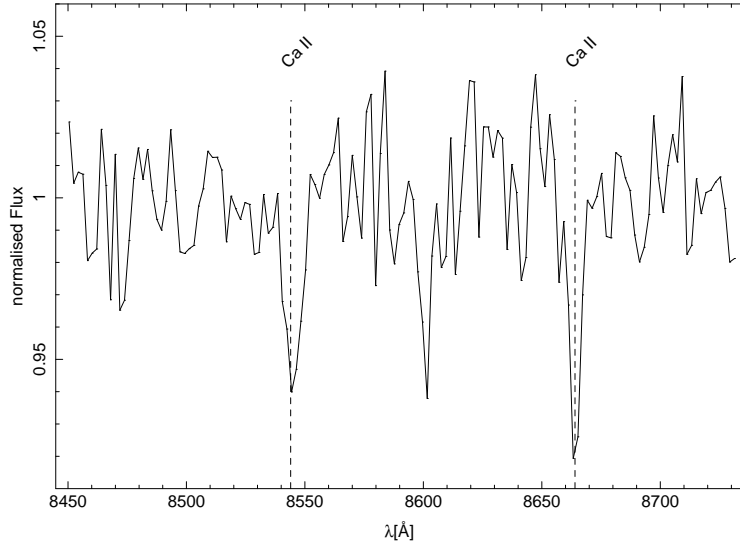
Figure 2.6: Average SDSS spectrum of J09510+03475 showing evidence for weak absorption lines (two strongest components) of the infrared Ca II triplet originating very likely from a wide third component.

by Han et al. (2002a) and Dorman et al. (1993) show that sdBs will become helium deficient sdOs as they evolve to higher temperatures. Since a significant fraction of short-period sdBs is found in compact binaries, helium deficient sdOs should have a similar binary fraction. Although close companions to some helium deficient, evolved sdOBs have been found (Almeida et al., 2012; Klepp & Rauch, 2011), J1132−0636 is the first helium deficient highly evolved sdO with a confirmed close companion. The minimum companion mass derived from the RV-curve is well below the mass which would cause an infrared excess if the companion were a dM. Therefore, the nature of the unseen companion remains unclear.

2.6.4   J09510+03475 - a hierarchical triple

J09510+03475 shows an excess in the J and H bands indicating a cool companion (see Fig. 2.5). In addition, a combination of 7 SDSS spectra from DR9 shows the two strongest components of the Ca II triplet at around 8600 Å (Fig. 2.6). Radial velocity measurements of the hydrogen lines confirm that 4 SDSS spectra were taken when the sdB moved through the minimum of the radial velocity curve. This means that a close companion should be observed in anti-phase around its maximum velocity which is expected to be $\sim 250 \, \mathrm{km \, s^{-1}}$ depending on the mass ratio but certainly higher than the system velocity of $\gamma = 111.1 \pm 2.5 \, \mathrm{km \, s^{-1}}$. Using the same 4 SDSS spectra, an average velocity of $v_{\mathrm{Ca}} = 86 \pm 16 \, \mathrm{km \, s^{-1}}$ for the calcium lines was measured which is just slightly below the system velocity ruling out a close companion. Therefore, the lines originate most likely from a third body in a wide orbit with a low RV amplitude. This makes this system the second candidate for a triple system after PG 1253+284 (Heber et al., 2002) which is an sdB star with one companion in a close orbit and another low-mass main sequence star in a wide orbit which causes the excess in the infrared and the Ca II lines. However,

the nature of the close companion remains unclear.

2.6.5   Unconstrained companions

J18324−63091, J15222−01301, J01185−00254 and J03213+05384 have minimum companion masses derived from the RV-curve well below the mass which would cause an infrared excess. J10215+30101, J15082+49405 and J08233+11364 have no reliable infrared colours. Therefore, the nature of the unseen companion in those seven systems remains ambiguous.

2.6.6   The MUCHFUSS sample

Fig. 2.7 shows the RV semi-amplitudes of all known short-period sdB binaries with orbital solutions plotted against their orbital periods. The dotted, dashed and solid lines mark the regions to the right where the minimum companion masses derived from the binary mass function (assuming $0.47\,\mathrm{M_\odot}$ for the sdBs) exceed $0.08\,\mathrm{M_\odot}$, $0.45\,\mathrm{M_\odot}$ and $1.40\,\mathrm{M_\odot}$.

The MUCHFUSS targets are marked with triangles. Most of the MUCHFUSS targets fall in the region with the highest minimum companion masses detected. However, the MUCH-FUSS campaign discovered not only companions with the highest masses, but also detected the lowest-mass companions to sdBs (Geier et al., 2011d; Schaffenroth et al., 2014b). This shows that our target selection is efficient to find both the most massive companions known to sdB stars with periods of up to a few days and the least massive companions with short orbital periods of less then 3 hours. However, no NS or BH companion has been discovered yet.

2.7   The population of close hot subdwarf binaries

This study extends to 142, the sample of short-period sdB binaries that have measured mass functions. An overview is given in Tables 2.8 and 2.9.

In the following sections a canonical sdB mass of $0.47\,\mathrm{M_\odot}$ will be adopted. All systems have unseen companions, but masses could only be determined for the eclipsing ones. Hence only a minimum companion mass could be derived for most of them. Many systems were pre-selected either from high RV variations between several single exposures or from light variations such as reflection effects, ellipsoidal variations and/or eclipses. Consequently, the distribution is by no means random but biased towards high inclination, both for RV variables (large amplitudes preferred) and light variables (reflection effect and/or eclipses detected). Therefore, statistically, the derived minimum companion masses are expected to be not far from the real companion mass.

We collected orbital and atmospheric parameters as well as V-band and infrared photometry for the full sample from the literature (see Table 2.9). Companion types for 82 systems were identified as described in Sec. 2.6. Thirty low-mass stellar or substellar companions were identified from a reflection effect in the lightcurve. Twenty-three systems show either ellipsoidal variation, eclipses with no additional reflection effect or no light variations at all. For these systems a WD companion is most likely. Additionally, 29 systems could be confirmed
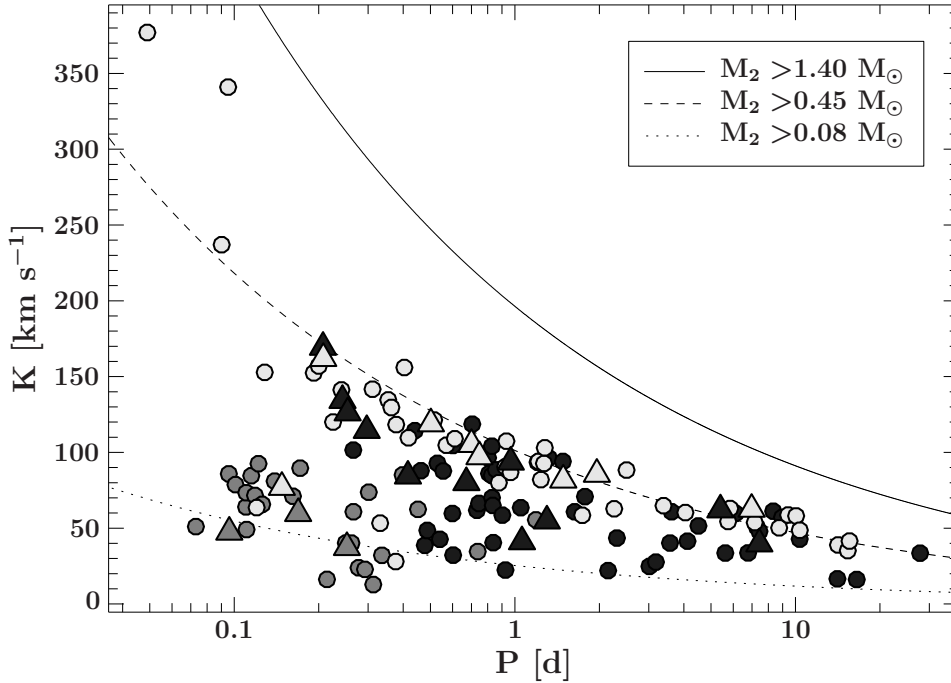
Figure 2.7: The RV semi-amplitudes of all known short-period sdB binaries with spectroscopic solutions plotted against their orbital periods (light grey: WD companions, grey: dM companion, dark grey: unknown companion type). The binaries from the MUCHFUSS programme are marked with triangles, binaries taken from the literature with circles. The lines mark the regions to the right where the minimum companion masses derived from the binary mass function (assuming $0.47\,M_\odot$ for the sdBs) exceed certain values.

as WD companions because the minimum companion mass is higher than the mass for a non-degenerate companion which would cause an infrared excess. None of those show an excess in the J and H band (Fig. 2.5). Therefore, the companions are most likely WDs as well.

Four systems show an excess in the infrared and are good candidates for having a cool companion (see Fig. 2.5). Indeed, HE 0230-4323 shows a reflection effect and a low-mass stellar companion is confirmed.

Some systems may actually be triple as exemplified by PG1253+284, a radial velocity variable sdB with a dwarf companion which causes a strong infrared excess. The components were resolved by HST imaging (Heber et al., 2002), which indicated that the dwarf companion is on a wide orbit. Nevertheless, RV variations of the sdB star were observed, which must stem from another unresolved companion on a short-period orbit. Hence PG1253+284 is a triple system. Additional evidence of multiplicity (triples, quadruples) amongst sdB systems has recently been reported by Barlow et al. (2014). Hence it is worthwhile to search for triples amongst the four systems showing infrared excess. In fact, there is one, J09510+03475, which shows signs that the system actually may be triple (see Sec. 2.6.4 for a detailed discussion), while for HE 0230-4323 and PB5333 there is no hint for a third companion.

In the following we shall discuss the distribution of periods and companion masses, compare the stars' positions in the $T_{\mathrm{eff}} - \log g$ plane to predictions from stellar evolution models,
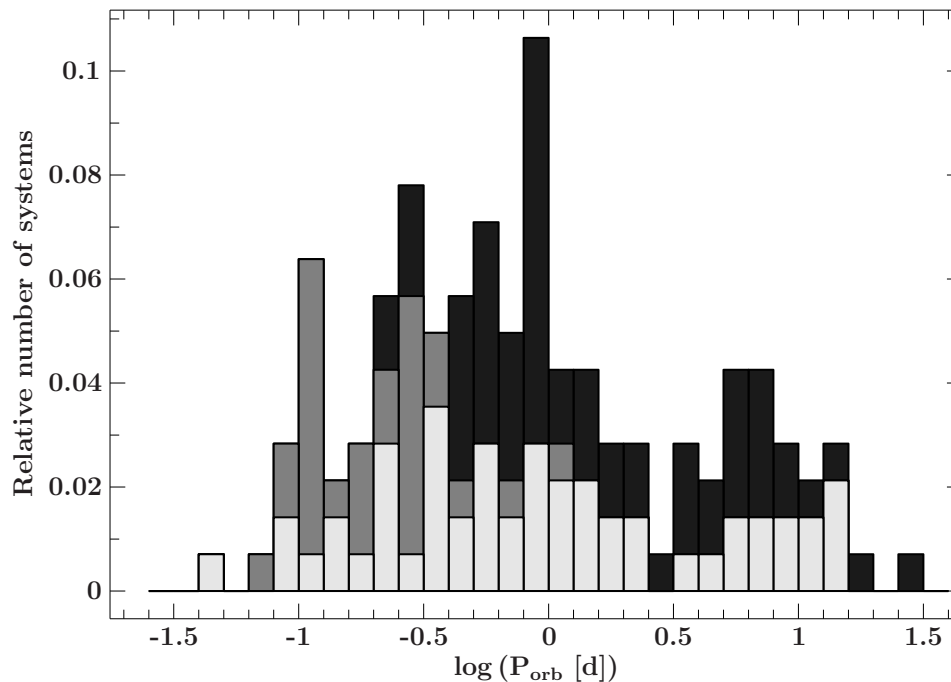
Figure 2.8: Period histogram of the full sample. Light grey: WD companions, grey: dM companion, dark grey: unknown companion type.

and discuss selection bias.

2.7.1 Distribution of orbital periods and minimum companion masses

Fig. 2.8 shows the period distribution of the full sample.

A wide peak near $P_{\mathrm{orb}} = 0.3$ days is found in the full sample. The majority of systems in this group are dM companions detected from reflection effects in the lightcurves. Beyond half a day the contribution from the confirmed dM companions decreases significantly, most likely because a reflection effect is much weaker and not easy to detect. Another peak can be found at around $0.8 - 0.9$ days. Most of the systems here have unidentified companion type. At longer periods the number of systems goes down, but in this region the selection effects are stronger.

Many of the WD companions were confirmed not only by the systems' lightcurves but also by the non-detection of an excess in the infrared (see Sec. 2.6) which is period independent. Therefore, in contrast to the dM companions, we find WD companions almost over the full period range. However, a gap near 3 days appears. We have no explanation for this but at the same time, with the present statistics, we cannot be sure that this gap is real.

The distribution of the minimum masses of the companions is displayed in Fig. 2.9.

We identify three separate populations.

1) The first population has an average minimum companion mass around $0.1\,\mathrm{M_\odot}$, close to the hydrogen burning limit. Most of them were identified as either dMs or brown dwarfs from the observation of their reflection effect. Only four WDs were found in this period regime,
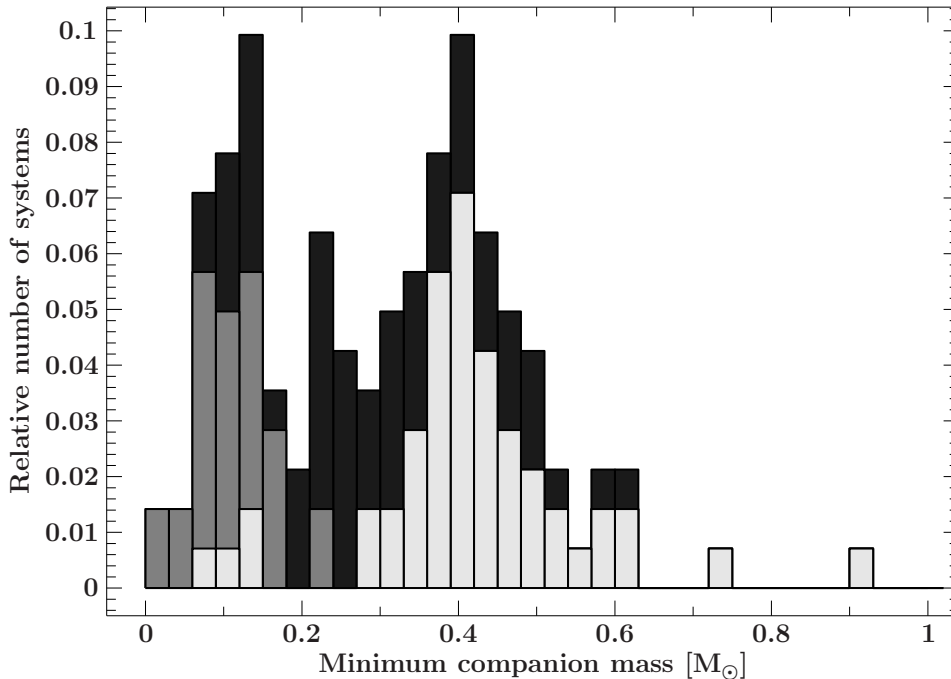
Figure 2.9: Histogram of minimum companion masses (light grey: WD companions, grey: dM companion, dark grey: unknown companion type). Clearly visible are at least two separated populations. The first population peaks at around $0.1\,M_\odot$ and consists mainly of low mass main sequence companions. The second population peaks at around $0.4\,M_\odot$ and consists mainly of WD companions. The two high mass outliers belong to a population of massive WD companions.

which could be ELM-WDs (M<0.3 $M_\odot$, see Sec. 2.8.1).

2) The second population peaks around $0.4\,M_\odot$. Our analysis showed that the majority of this population are most likely WDs with an average minimum mass around $0.4\,M_\odot$, lower than the average mass of single WDs (see discussion in Sec. 2.9.2).

3) The third group are the high mass WD companions ($M_{WD} > 0.7\,M_\odot$). Systems with high companion masses stand out in radial velocity selected samples as they show higher RV variations compared to low-mass companions. However, only the eclipsing systems KPD1930 +2752 and CPD-30°11223 have confirmed companion masses above $0.7\,M_\odot$. This means that in our sample less than 2% of the binaries with measured RV curves have such high mass WD companions.

2.7.2 $T_{\rm eff} - \log g$ diagram

Fig. 2.10 shows the $T_{\rm eff} - \log g$ diagram of the full sample with accurate atmospheric parameters. The size of the symbols represent the companion mass. Most of the stars populate the extreme horizontal branch (EHB) band all the way down to the helium main sequence while about 10% of the sdB sample has already evolved off the EHB. The total evolution time on the EHB is $100\,$Myr, whereas post-EHB evolutionary timescales are lower by a factor of about 10. The theoretical tracks show a linear time-luminosity-relation while the star is in the EHB strip
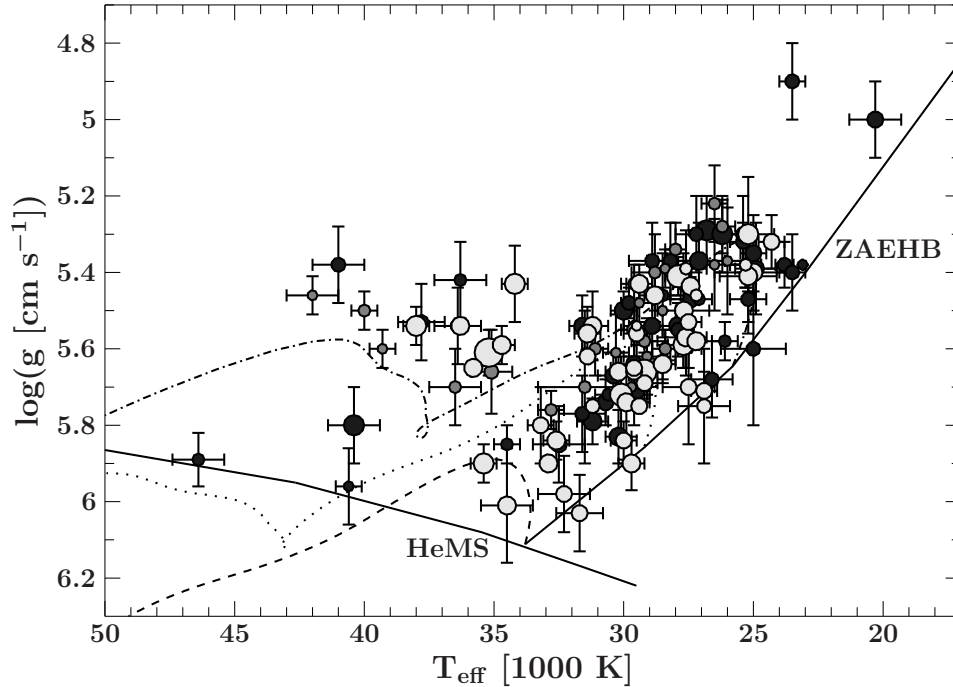
Figure 2.10: $T_{\text{eff}} - \log g$ diagram of the full sample of binary sdB stars (light grey: WD companions, grey: M-dwarf companion, dark grey: unknown companion type). The size of the symbols corresponds to the minimum companion mass. The helium main sequence (HeMS) and the zero-age EHB (ZAEHB) are superimposed with EHB evolutionary tracks by Han et al. (2002a) (dashed lines: $m_{\text{env}} = 0.000\,M_\odot$, dotted lines: $m_{\text{env}} = 0.001\,M_\odot$, dashed-dotted lines: $m_{\text{env}} = 0.005\,M_\odot$ using $0.45\,M_\odot$ models).

until it comes close to the terminal age EHB (TAEHB), where evolution starts to speed up. Hence, we would expect a homogeneous coverage of the EHB band as it is indeed observed. A more detailed comparison can be made using the cumulative luminosity function (see Lisker et al., 2005 for details).

In the next step we concentrate on the systems for which the companions have been classified and separate the distribution according to companion type, that is dMs and WDs, respectively. For WD companions, the sdBs populate the full EHB band homogeneously with a small fraction of sdBs having evolved off the EHB. For sdB stars with dM companions the ratio of post-EHB to EHB stars is similar to that for sdB+WD systems. However, they appear not to cover the full EHB band. There is a lack of hot, high gravity sdBs close to the helium main sequence (Fig. 2.11).

Most striking is that the width of the distribution of the sdB+dM systems is narrower than that of sdB+WD ones, in particular none of the sdB stars is found close to the zero age EHB (ZAEHB) if a sdB mass of $0.45\,M_\odot$ is assumed. Because of the contamination of the sdB spectrum by light from the companion, their gravities could have been systematically overestimated and their effective temperatures could have been systematically underestimated (Schaffenroth et al., 2013), which would shift them even further away from the ZAEHB. The location of the EHB band in the $T_{\text{eff}} - \log g$ diagram depends on the adopted core mass. By increasing it, the EHB stars become more luminous and therefore the EHB band is shifted to
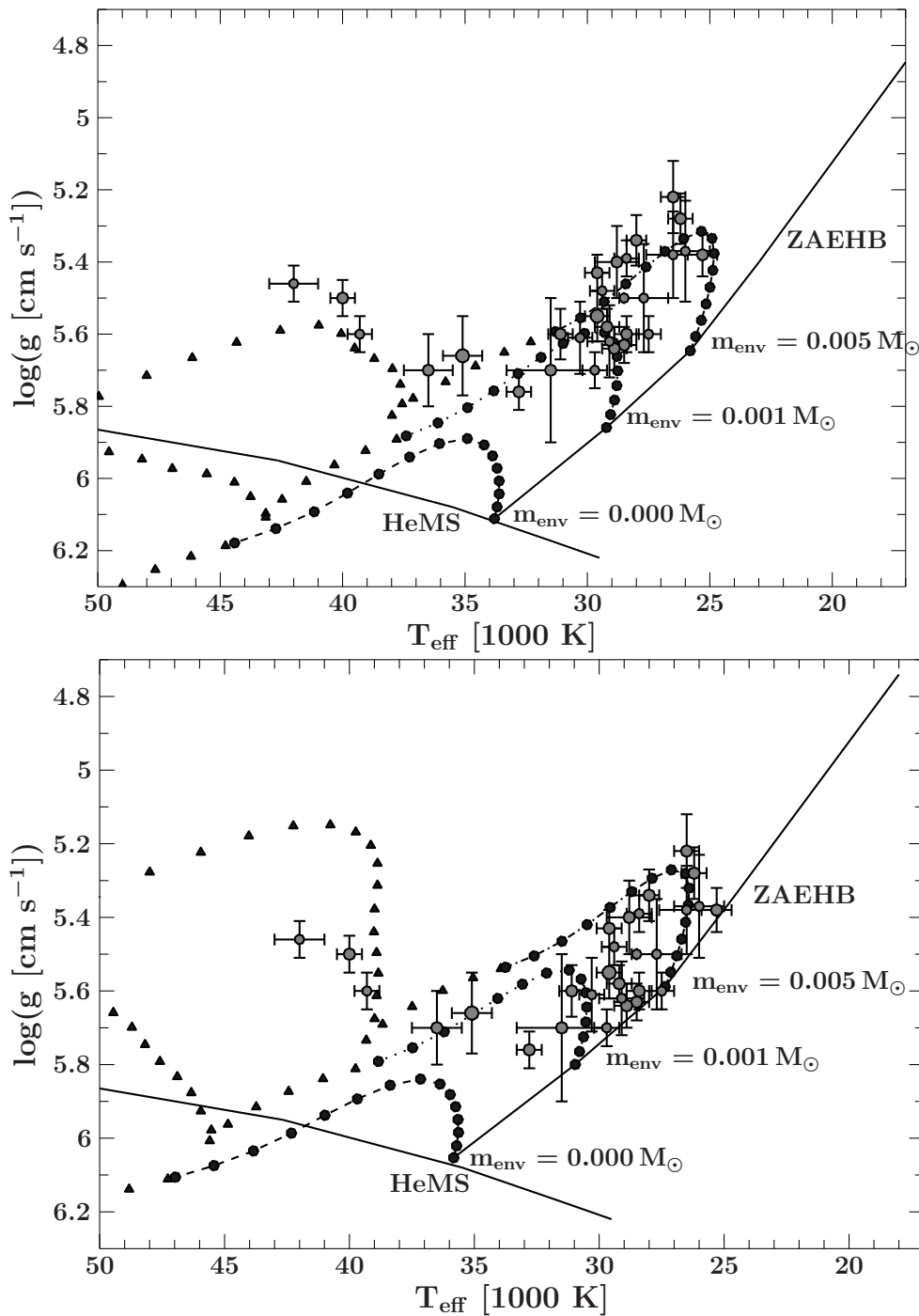
Figure 2.11: $T_{\mathrm{eff}} - \log g$ diagram of sdB stars with confirmed M-dwarf companions. The size of the symbols corresponds to the minimum companion mass. The helium main sequence (HeMS) and the zero-age EHB (ZAEHB) are superimposed with EHB evolutionary tracks by Han et al. (2002a) using $0.45 \, M_{\odot}$ (upper panel) and $0.50 \, M_{\odot}$ (lower panel) models. The space between black symbols corresponds to equal times and shows that the sdB evolution speeds up once the sdB reaches its lowest gravity. Circles mark the region where the sdB star contains helium in the center of the core whereas triangles mark the region where the helium in the center of the core is completely burned.
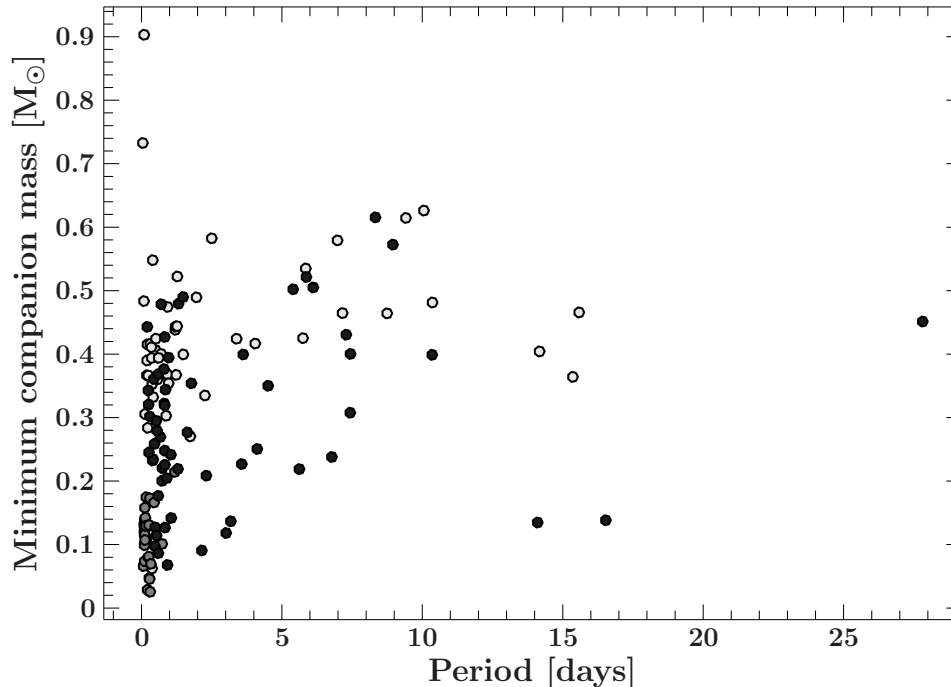
Figure 2.12: Minimum companion masses plotted against the period of the systems (light grey: WD companions, grey: M-dwarf companion, dark grey: unknown companion type).

lower gravities. This is demonstrated in Fig. 2.11 by indicating the ZAEHB for a higher core mass of $0.5\,\mathrm{M_\odot}$ in addition to that of $0.45\,\mathrm{M_\odot}$ shown in all panels. The observed distribution of sdB stars is consistent with the $0.5\,\mathrm{M_\odot}$ ZAEHB, for which the EHB evolution timescales are shorter. Hence, adopting a higher core mass gives better agreement between observations and evolutionary tracks.

2.7.3 Separation of the systems

The details of the common envelope (CE) phase are still poorly understood (Ivanova et al., 2013). In a rather simplistic picture the orbital energy of the binary, which scales with the mass of the companion, is deposited in the envelope. If a more massive companion ejects the common envelope earlier, and therefore at a wider orbit than a less massive companion, a correlation between orbital period and minimum companion mass would the expected. Figure 2.12 shows the minimum companion masses plotted over the period of the systems: however, no obvious correlation can be seen in the sample with WD as well as dM companions (see Sec. 2.9.5 for further discussion).

We also note that, even if the core masses of the sdB progenitors were very similar, their total masses (core + envelope) might have been quite different, implying different energies to expel the envelope and different final orbital separations. This may partially explain why we do not see any correlation between minimum companion mass and orbital period in Fig. 2.12.
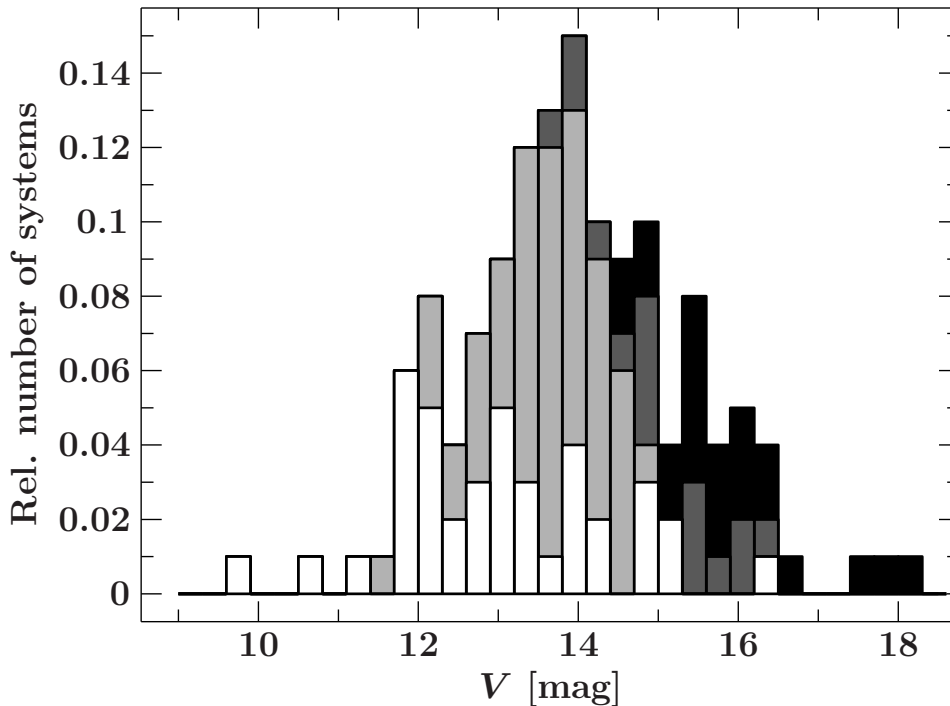
Figure 2.13: Histogram of the magnitudes of the full sample. The systems selected from the SDSS surveys are marked in black and from the Hamburg/ESO (HE), Hamburg Schmidt (HS) are marked in dark grey. The systems selected from the Palomar Green (PG), Edinburgh Cape (EC) and Kitt Peak Downes (KPD) surveys are marked in light grey. The systems selected from smaller scale surveys (e.g. Feige...) are marked in white.

2.7.4   Selection effects

In order to compare the observed sample of close binary sdBs to population synthesis models (e.g. Han et al., 2002a, 2003; Clausen et al., 2012) selection effects have to be taken into account. For the MUCHFUSS sample the target selection is well defined (Geier et al., 2011a). However, since the 142 solved binaries studied here are drawn from several different samples, it is impossible to come up with an unified description of selection bias.

All the sdBs studied here were initially discovered as faint blue stars from multi-band photometric survey data. However, spectral classification had to follow and the brighter limits of those spectroscopic observations have to be taken into account.

In the brightness distribution (V-band, Fig. 2.13) of the whole sample, we can identify two sub-samples. One peaks around $14 \, \mathrm{mag}$ and consists of binaries mostly discovered in the Palomar Green (PG, Green et al., 1986), Edinburgh Cape (EC, Stobie et al., 1997), Kitt Peak Downes (KPD, Downes, 1986) and some smaller scale surveys. The fainter subsample peaks around $15 \, \mathrm{mag}$ and was selected mostly from the Hamburg/ESO (HE, Wisotzki et al., 1996), the Hamburg Schmidt (HS, Hagen et al., 1995) surveys and the SDSS (York et al., 2000).

For 127 binaries we calculated the z-distances from the Galactic plane[7] assuming a canon-

---

[7]We included near-Galactic plane objects neglecting reddening corrections as reddening is of little influence for calculating their z-distance.
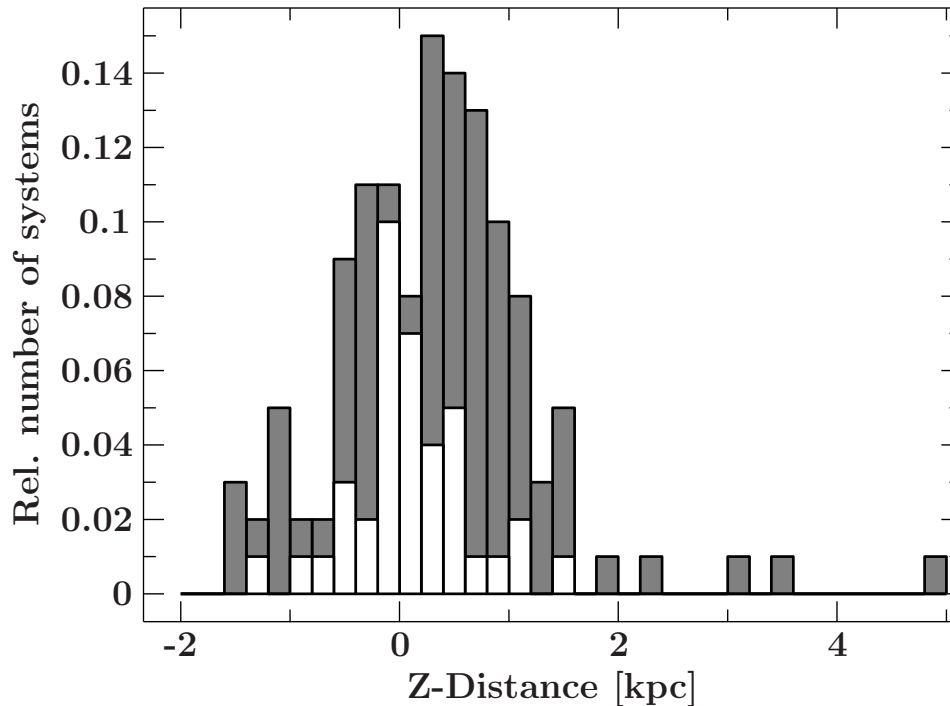
Figure 2.14: Histogram of the spectroscopic z-distances above the Galactic plane. White are systems with a Galactic latitude $|b| < 30°$. Grey marked are the systems with $|b| > 30°$.

ical sdB mass of 0.47 $M_\odot$ (Fig. 2.14) and for 118 systems with sufficient data we calculated also the spectroscopic distances.

Except for four distant stars (at 2 to 5 kpc above the Galactic plane) all stars lie within 2 kpc below or above the Galactic plane. Their distribution is asymmetric, with an excess of objects in the northern Galactic hemisphere. The deficit of near-Galactic plane stars, as well as those below the Galactic plane, is due to the insufficient depth of near-plane and southern surveys. The most distant systems are likely to be halo stars and may be considerably older than the bulk. A significant fraction belongs to the thick disc, which on average is older than the thin disc. Because the age of the progenitor population is an important ingredient for binary population synthesis, it is crucial to assign each system to one of the stellar populations via an investigation of its kinematic and thus derive age estimates.

The search for binarity of the targets has either been done by photometric or spectroscopic follow-up observations. Either the star shows light variations indicative of a close companion or the star RV shifts become apparent. Both discovery methods introduce different selection effects.

Only 20 of the binaries in the sample have been discovered photometrically (see Table 2.9). Short-period sdB stars with cool dM or BD companions show a reflection effect and often also eclipses. 14 binaries with periods of less than 0.3-0.4 d and a peak period of 0.1 d have been discovered in this way. Close sdB+WD binaries can show ellipsoidal variations and sometimes very shallow eclipses. Of the six binaries discovered in this way, two have periods of less than 0.09 d and one has a period of 0.3 d. The remaining three long-period systems (> 3 d) have been discovered by the Kepler mission, which has a much higher sensitivity
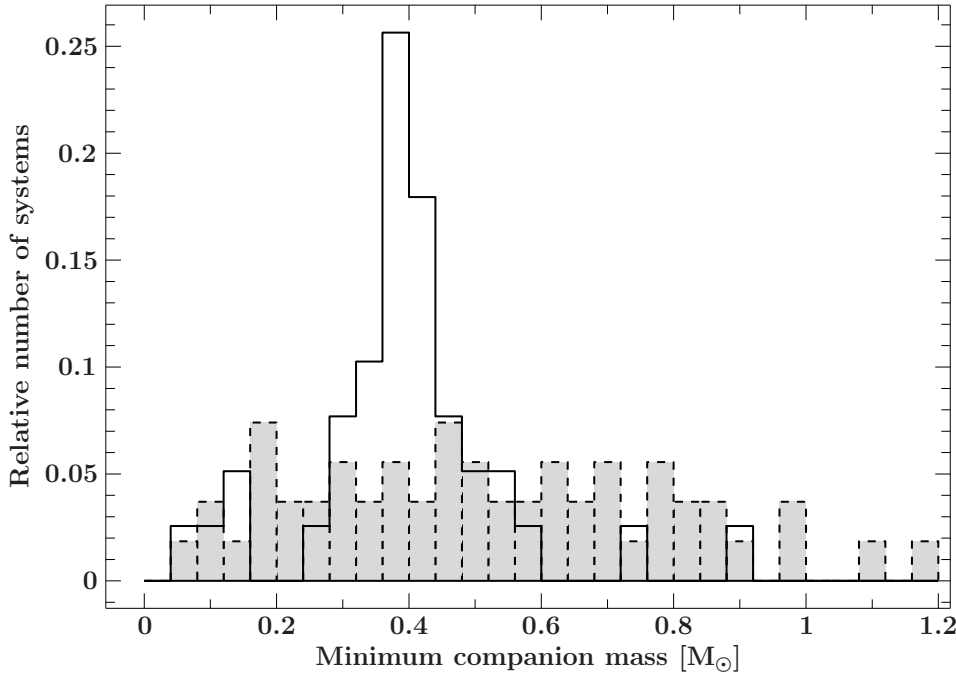
Figure 2.15: Comparison of minimum companion masses of sdB binaries with confirmed WD companions to the ELM-WD binaries (grey shaded area) taken from Gianninas et al. (2014).

than ground-based telescopes. In general, photometric selection is clearly biased towards the shortest-period systems at high inclinations.

The remaining 122 systems have been discovered from RV shifts, most of them from medium-resolution spectra with an RV accuracy of $\sim$ 10-20 km s^{-1} (e.g. Maxted et al., 2001). The binaries studied by Edelmann et al. (2005) and in the course of the ESO Supernova Ia Progenitor Survey (SPY, Napiwotzki et al., 2001a; Karl et al., 2006; Geier et al., 2010a, 2011c) have been discovered using high-resolution spectra with an RV accuracy better than 5 km s^{-1}.

To our knowledge, well-defined cuts of RV-shifts were only used in the MUCHFUSS target selection (see Geier et al., 2011a). In general, short-period systems with high RV shifts and therefore high inclinations are the easiest ones to solve within a few nights of observations. This introduces a selection in favour of such systems. It is unlikely that a significant population of binaries with periods longer than one day and RV semi-amplitudes higher than 100 km s^{-1} has been missed in the high-galactic latitude population of hot subdwarf stars covered by the SDSS. The missing population of close sdB binaries with periods from a few days to a few tens of days most likely consists of systems with small RV semiamplitudes and rather low-mass companions ($< 0.5\,M_\odot$).
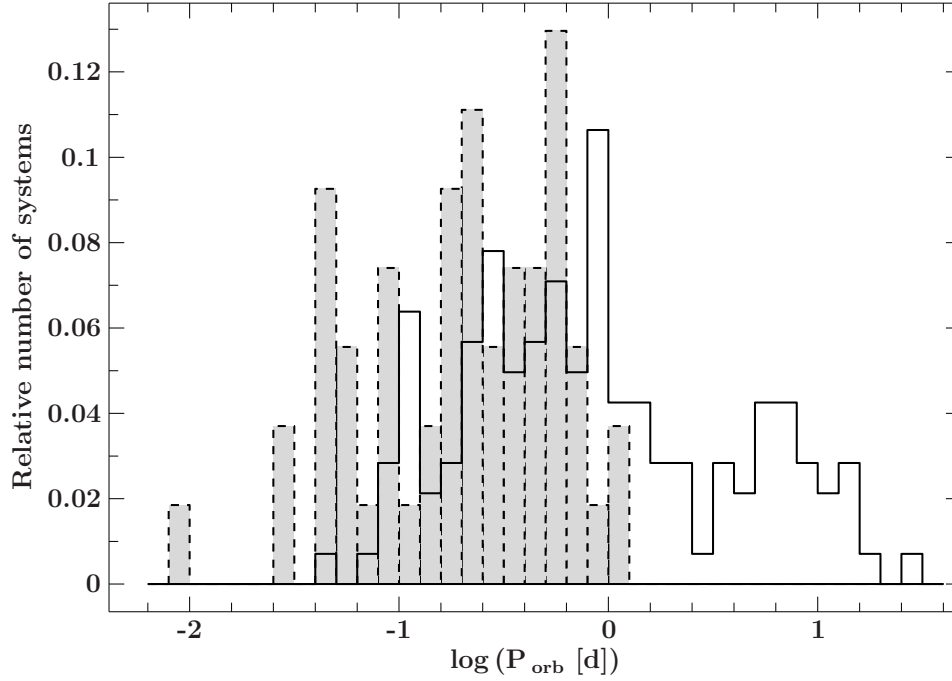
Figure 2.16: Comparison of orbital periods of sdB binaries with confirmed WD companions to the known ELM-WD binaries with orbital solutions (grey shaded area) taken from Gianninas et al. (2014).

2.8   Comparison with related binary populations

2.8.1   The population of helium-core WD binaries

The formation of helium-core WD binaries with masses $< 0.45\,\mathrm{M_\odot}$ is expected to occur in a similar way as the formation of sdB+WD binaries discussed in this paper. Both systems survive two phases of mass transfer with the second phase where the helium-core WD/sdB is formed being a common envelope phase. The helium-core WDs start transferring mass already when the progenitor evolves on the red giant branch (RGB) and lose so much mass that they are not able to ignite helium in the core. The sdBs start mass transfer on or near the tip of the RGB and are massive enough to ignite helium.

Orbital parameters of 55 helium-core WD binaries were selected from Gianninas et al. (2014). All the companions are WDs. Figure 2.15 shows the minimum companion mass histogram of the sample compared to the sdB sample. ELM companions cover a wider range of masses, extending to low as well as high masses and indicating a different evolutionary path. The distribution does not show a clear separate population with a peak at $0.4\,\mathrm{M_\odot}$ like the confirmed WD companions to sdB stars.

Figure 2.16 shows the orbital period distribution of the helium-core WDs compared to our sample. Between an orbital period of 0.1 and 1.0 days both distributions look very similar. However, below 0.25 days helium-core WDs are more numerous compared to the sdB+WD systems. On the other hand at longer periods sdB+WD systems are more numerous which indicates that helium-core WD binaries are formed preferentially with shorter periods.
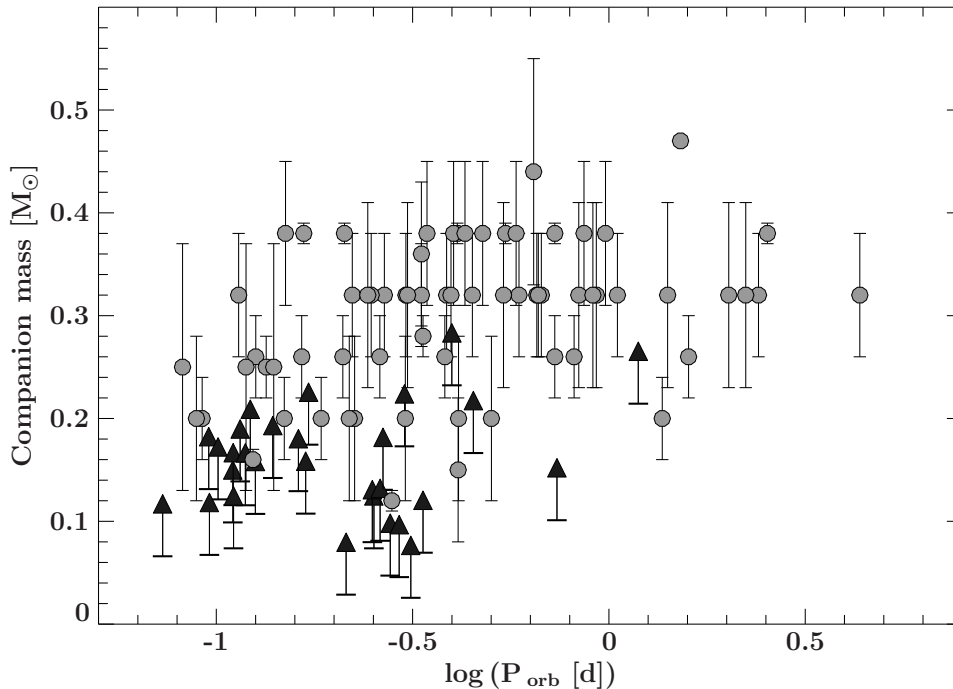
Figure 2.17: Companion mass plotted against the orbital period. Grey circles mark derived companion masses of known WD+dM binaries with orbital solutions taken from Zorotovic et al. (2011), Nebot Gómez-Morán et al. (2011), Pyrzas et al. (2012) and Parsons et al. (2012). Black arrows mark minimum companion masses of the known sdB+dM binaries.

2.8.2 The population of compact WD+dM systems

Compact WD+dM binaries are also the product of CE evolution and so we might expect that the properties of these binaries are similar to the sdB+dM binaries. Indeed, some WD+dM systems may have been created as sdB stars with dM companions that have since evolved to become white dwarfs with masses close to $0.47 \, M_\odot$.

Orbital parameters of 68 post-common envelope binaries consisting of a WD+dM were selected from the literature (Zorotovic et al., 2011; Nebot Gómez-Morán et al., 2011; Pyrzas et al., 2012; Parsons et al., 2012). The systems cannot be compared in the same way as the ELM-WD binaries because all WD+dM systems have confirmed companion masses whereas, for sdB+dMs, only minimum companion masses are known. Figure 2.17 shows the orbital period vs. the companion masses of the dM companions to WDs compared to the confirmed dM companions to sdB stars. The plot shows dM companion masses larger than $\sim 0.2 \, M_\odot$ for the WD+dM systems, while the minimum masses of dM companions to sdBs peak well below, near $\sim 0.1 \, M_\odot$. To increase the companion masses of the sdB+dM systems to an sdB mass larger than $0.2 \, M_\odot$ the systems have to be observed with inclination angles below $30°$. This is not very likely as the majority of the systems were selected from photometry by eclipses and/or reflection effects which are hardly detectable in systems with small inclinations.

The WD+dM systems show a wide spread in orbital period whereas the majority of the sdB+dM systems were found with periods below 0.3 days. A possible reason might be that

WD+dM systems are usually identified spectroscopically because features of the dM dominate the red part of the composite spectra. In contrast to that, almost all sdB+dM systems were identified from the reflection effect in the lightcurves. Longer period systems show much weaker reflection effects and therefore are much harder to detect.

2.9 Discussion

2.9.1 Distribution of sdB masses

Several previous studies discussed the sdB mass distribution. Fontaine et al. (2012) collected sdB masses of a sample of 22 sdBs (15 derived from asteroseismology and 7 from resolved binaries), and found a sharp peak at $M_{\mathrm{sdB}} = 0.47\,\mathrm{M}_\odot$. Han et al. (2003) discussed the sdB mass distribution formed via different phases of mass transfer. Figure 12 in Han et al. (2003) showed a sharp peak at $M_{\mathrm{sdB}} = 0.46\,\mathrm{M}_\odot$ for sdBs formed after a common envelope phase.

In our analysis of the companion mass distribution shown in Fig. 2.9 we apply the assumption that the sdBs have all canonical masses of $M_{\mathrm{sdB}} = 0.47\,\mathrm{M}_\odot$ because of the results of previous studies (see Fontaine et al., 2012 and references therein). The distribution of the minimum companion masses (Fig. 2.9) shows two quite narrow peaks. If the distribution of the sdB masses would be much more smeared out than predicted, those two peaks would have to be smeared out as well. We therefore conclude that the width of the sdB mass distribution is of the order of $0.2\,\mathrm{M}_\odot$ at most, which is consistent with the prediction from theory. We note that from our analysis we cannot claim that $M_{\mathrm{sdB}} = 0.47\,\mathrm{M}_\odot$ is the canonical mass for sdBs because adopting a higher (lower) average sdB mass would also increase (decrease) the companion masses but the distinct peaks in the companion mass distribution would persist.

2.9.2 WD companion masses

The majority of minimum companion masses of confirmed WD companions are located around $0.4\,\mathrm{M}_\odot$, which is significantly below the average mass for single (DA) WDs of $\sim 0.59\,\mathrm{M}_\odot$ (e.g. Kleinman et al., 2013). Because of projection effects and selection biases the detection of high inclination systems should be favoured, which means that the derived limits should be on average close to the companion masses. Since the minimum masses of the WD companions are significantly smaller than the average mass of single C/O-WDs, we test this hypothesis by computing the inclination angles for all sdB+WD binaries assuming that all companion WDs have an average mass of $0.6\,\mathrm{M}_\odot$.

Figure 2.18 shows a comparison between the computed distribution of inclination angles and the one expected for randomly distributed inclinations taking into account projection effects. We do not include any selection biases, but want to point out that they would in any case lead to even higher probabilities of seeing the systems at high inclinations. One can clearly see that the inclination distribution is not consistent with the one expected for a population of $0.6\,\mathrm{M}_\odot$ C/O-WD companions. Hence, it is likely that a significant fraction of the sdB binaries host WDs of masses below $0.6\,\mathrm{M}_\odot$.
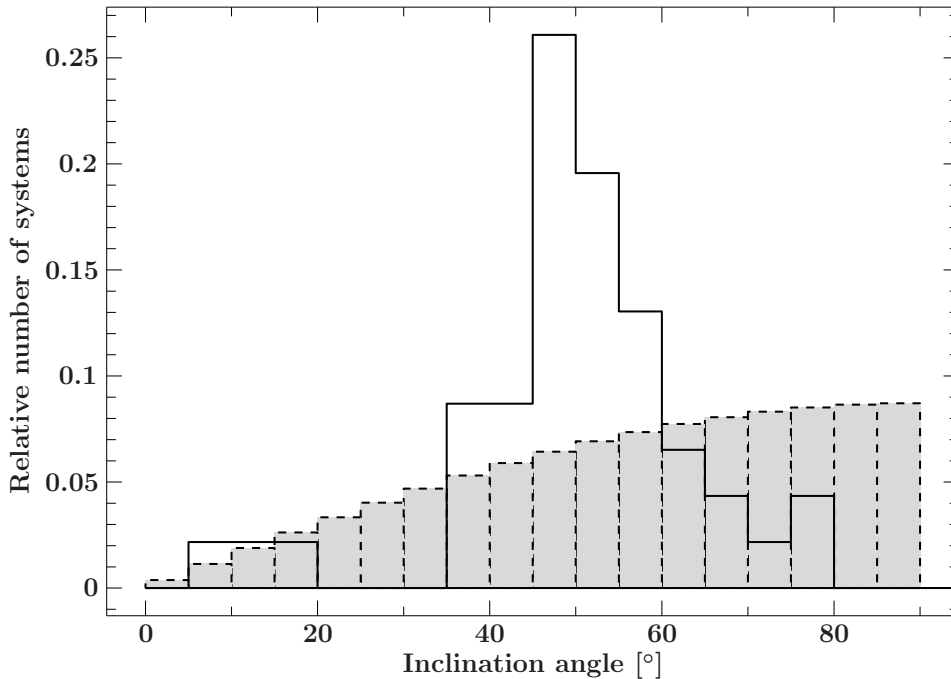
Figure 2.18: Comparison of computed inclination angles of the confirmed sdB+WD systems to match companion masses of $0.6\,M_\odot$ to a theoretical inclination angle distribution assuming randomly distributed inclination angles.

2.9.3 Triple systems

Only one sdB system was known to be triple up to recently. We found another sdB binary, J09510+03475, with a third component in a wide orbit. Barlow et al. (2014) studied 15 sdB binaries to detect long period companions. At least one has a visual companion well separated from the sdB. However, RV measurement show that the orbital period of the system is below 10 days, indicating a close companion in addition to the wide companion.

The properties of J09510+03475 also imply that a fraction of sdB binaries showing an excess in the infrared might be triples systems. If we assume all 3 systems to be triples we find a fraction of $2.1\,\%$ in our sample. However, if the wide companion is too faint to show an excess in the infrared then it would be hidden in our sample and the fraction of triple systems might be significantly higher. Some of the sdB triples might have formed from solar type triples. Raghavan et al. (2010) found a fraction of $9 \pm 2\%$ for solar type triples which is not in disagreement with our findings.

2.9.4 Massive companions

Hot subdwarf + WD binaries are potential supernova Ia progenitors if their masses are sufficiently large. However, only a very small fraction of massive WD companions ($< 2\,\%$) were detected. KPD1930+2752 and CD-30°11223 are the only systems with companion masses $> 0.7\,M_\odot$. This implies that only a specific evolutionary path can form such systems. Wang

et al. (2013) showed that a system like CD-30°11223 is formed from a young stellar population which can only be found in the Galactic disc. Indeed, CD-30°11223 is a confirmed member of the Galactic disc population (Geier et al., 2013b). No NS or BH was detected in our sample but previous studies concentrated on high Galactic latitudes. Based on the non-detection of a NS or BH in our sample with 142 systems, we find that $< 0.7\%$ of the close sdB binaries contain a NS or BH companion which is a small fraction but still consistent with the predictions from binary evolution calculations (Yungelson & Tutukov, 2005; Nelemans, 2010). We encourage a systematic search for compact sdB binaries at low Galactic latitudes.

2.9.5 Implications for the common envelope phase

A remarkable result of our analysis is that we find clearly distinct populations. The majority of confirmed WD companions have minimum companion masses strongly peaked at $\sim 0.4\,M_\odot$. This is much lower than the average mass of single WDs and leads to the conclusion that the WDs need to lose a significant amount of mass during the evolution either during the first phase of mass transfer when the WD is formed or during the common envelope phase when the sdB is formed. The first phase can either be stable Roche lobe overflow or also a common envelope phase depending on the initial separation and the mass ratio of the system. White dwarf masses of $\sim 0.4\,M_\odot$ are on the border between a WD with a helium core and a C/O core and a significant fraction of white dwarf companions might be helium-core WDs.

In comparison, ELM-WD binaries show a much wider companion mass distribution starting at very low masses up to high masses close to the Chandrashekar limit. Either these systems form in a different way or sdB binaries need a special WD companion mass to lose the right amount of mass and form an sdB.

The dM companions were found to have minimum companion masses of $\sim 0.1\,M_\odot$ close to the hydrogen burning limit. These systems have experienced one phase of mass transfer, namely the CE phase when the sdB was formed, and are direct progenitors of WD+dM systems. However, in comparison with the known population of WD+dM systems we find that the main sequence companions in WD systems are significantly more massive than the main sequence companions in sdB systems. This shows on the one hand that only a small number of WD+dM systems evolved from sdB+dM systems and on the other hand that sdBs might be formed preferentially by low mass main sequence companions whereas WD are preferably formed with higher mass main sequence companions. The other possible way to form a compact WD+dM system without forming an sdB first is the formation of the WD directly during a CE phase when the WD progenitor evolves on the asymptotic giant branch.

In addition we found no correlation of the orbital separation of the sdB binaries with companion mass (see Fig. 2.12) which means that the red giant progenitors of the sdB must have had different envelope masses. This could be tested, if we were able to identify systems that had similar envelope masses prior to envelope ejection. In this respect the halo population of sdB binaries would be of great interest because they are expected to form from systems where the sdB progenitor has a mass of $\sim 0.8\,M_\odot$. A detailed kinematic analysis to identify the halo population of compact sdB binaries is crucial. The majority of the MUCHFUSS sample is

Table 2.5: Derived times when the dM will fill its Roche Lobe and start accreting onto the primary to form a cataclysmic variable. The derived M_{Comp} are minimum companion masses which means that the time when the dM fills its Roche Lobe are upper limits

.

Object	Period [days]	M_{Comp} [M$_\odot$]	Time [Gyr]
HS 2333+3927	0.172	0.174	3.44
J192059+372220	0.169	0.107	6.09
2M1533+3759	0.162	0.129	4.21
ASAS102322−3737	0.139	0.142	2.15
2M1938+4603	0.126	0.107	2.38
BULSC16335	0.122	0.158	0.95
EC10246−2707	0.119	0.115	1.70
HW Vir	0.115	0.138	0.97
HS 2231+2441	0.111	0.073	3.05
NSVS14256825	0.110	0.115	1.27
UVEX 0328+5035	0.110	0.098	1.77
PG 1336−018	0.101	0.121	0.72
J082053+000843	0.096	0.067	2.22
HS 0705+6700	0.096	0.131	0.34
PG 1017−086	0.073	0.066	1.01
J162256+473051	0.069	0.060	0.95

faint and therefore they might be the best candidates to be member of the halo population and a good starting point for an extended kinematic analysis of the complete sample of compact sdB binaries.

2.9.6   Future evolution: Pre-CV vs. Merger

For systems with main sequence companions we calculate the time when the dM will fill its Roche Lobe and starts accretion. As approximation for the Roche radius the Eggleton equation was used (Eggleton, 1983), with q being the mass ratio $q = M_{\mathrm{comp}}/M_{\mathrm{sdB}}$:

$$r_L = \frac{0.49q^{2/3}}{0.6q^{2/3} + \ln(1 + q^{1/3})}. \tag{2.3}$$

We used the minimum companion mass for the dM and calculated the corresponding radius using Table 1 in Kaltenegger & Traub (2009) by linear interpolation. Once the companion fills its Roche Lobe mass accretion starts and the systems becomes a cataclysmic variable (CV). We assumed that only gravitational wave radiation brings the to components closer. The time until the system starts accretions was calculated from the gravitational wave timescale, equation 7

Table 2.6: Derived merger timescales of the confirmed sdB+WD systems. The derived M_{Comp} are minimum companion masses which means that the merger timescales are upper limits to merger times.

Object	Period [days]	M_{Comp} [M$_\odot$]	Time [Gyr]	Merger result
PG 0941+280	0.311	0.415	10.27	WD/RCrB
PG 2345+318	0.241	0.366	5.78	WD/RCrB
PG 1432+159	0.225	0.283	6.01	WD/RCrB
J113840−003531	0.208	0.415	3.49	WD/RCrB
HS 1741+2133	0.20	0.389	3.34	WD/RCrB
HE 1414−0309	0.192	0.366	3.16	WD/RCrB
J083006+475150	0.148	0.137	3.77	AM CVn
EC00404−4429	0.128	0.305	1.26	WD/RCrB
PG 1043+760	0.120	0.101	2.88	AM CVn
KPD 1930+2752	0.095	0.903	0.23	SN Ia
KPD 0422+5421	0.090	0.483	0.33	WD/RCrB
CD−30°11223	0.049	0.732	0.05	SN Ia

from Piro (2011):

$$\tau_{\text{GW}} = P \left| \frac{dP}{dt} \right|^{-1} = \frac{5}{96} \frac{c^5}{G^{5/3}} \frac{M_{\text{total}}^{1/3}}{M_{\text{sdb}} M_{\text{dM}}} \left(\frac{P}{2\pi} \right)^{8/3}. \tag{2.4}$$

Table 2.5 shows the 16 systems which will become a CV and start accreting within a Hubble time. J0820+0008 and J1622+4730 have confirmed brown dwarf companions (Geier et al., 2011d; Schaffenroth et al., 2014b). Therefore at least two systems (J0820+0008 and J1622+4730) will have brown dwarf (BD) donor stars. The dM companion in HS0705+6700 will fill its Roche Lobe in about $340\,\text{Myr}$, beeing the first system of our sample. At this stage the sdB is already evolved and turned into a C/O-WD. Therefore, all 16 systems of our sample will appear as WD+dM/BD with a low-mass companion ($M_{\text{Comp}} \lesssim 0.17\,\text{M}_\odot$) before they become a CV. The currently known population of WD+dMs lacks such low-mass main sequence companions (see Fig. 2.17). However, our findings show that low mass dM companions to WDs should exist as well.

Merger timescales were calculated for systems of the full sample which have a confirmed WD companion and will merge within a Hubble time using equation 9 in Paczyński (1967):

$$T_0(\text{years}) = 3.22 \cdot 10^{-3} \frac{(M_{\text{sdB}} + M_{\text{Comp}})^{1/3}}{M_{\text{sdB}} M_{\text{Comp}}} P_{\text{orb}}^{8/3}. \tag{2.5}$$

We identified 12 systems of the full sample which will merge within a Hubble time. Only CD-30°11223 will merge before the sdB turns into a WD. Geier et al. (2013b) showed that this system will most likely explode as a subluminous SN Ia. All other systems will evolve and

turn into a C/O WD before they merge. Depending on the mass ratio the systems either merge ($q >2/3$) or form an AM CVn type binary ($q <2/3$). For a helium-core white dwarf companion the merger might form an RCrB star, whereas a C/O-WD companion forms a massive single C/O-WD. If the system reaches the Chandrashekar mass it might explode as a SN Ia (e.g. Webbink 1984).

PG1043+760 and J0830+4751 have low minimum companion masses and a mass ratio $q <2/3$. The companions in those systems are most likely helium-core white dwarfs. Both systems are therefore good candidates to have stable mass transfer and form an AM CVn type binary. KPD1930+2752 has a massive WD companion. The combined mass is close to the Chandrashekar limit. Thus, this is a good system to explode as a SN Ia. The other 8 systems have mass ratios $q >2/3$ and therefore are potential progenitors for mergers. Depending on the structure of the companion, the merger with a helium-core white dwarf might form an RCrB star, whereas a C/O-WD companion might form a massive single C/O-WD.

This analysis shows that the majority of sdB binaries with white dwarf companions will not merge within a Hubble time and only a small number of systems have periods and companion masses to either merge, form an AM CVn type binary or explode as a supernova Ia.

2.10   Summary

In this paper we have presented atmospheric and orbital parameters of 12 new close sdB binaries discovered by the MUCHFUSS project. Three of them have most likely WD companions. We found the first helium deficient sdO with a compact companion, a good candidate for an ELM-WD companion and confirmed the second known hierarchical triple amongst the known sdBs.

This study increases the number of hot subdwarf binaries with orbital periods less than 30 days and measured mass functions to 142 systems. The companion mass distribution of the full sample shows two separate peaks. The confirmed dM/BD companions are concentrated around $0.1 \, M_\odot$ whereas the majority of the WD companions peak at around $0.4 \, M_\odot$ showing that WDs in compact hot subdwarf binaries have significantly lower masses than single WDs. The $T_{\mathrm{eff}} - \log g$ diagram of the sdB+dM systems indicates that in these systems the sdBs might have higher masses compared to the rest of the sample.

Close hot subdwarf binaries are expected to be formed in a similar way as the compact ELM-WD binaries or the WD+dM pre-CV systems. However, both samples show significantly different companion mass distributions indicating either selection biases or differences in their evolutionary paths.

We discussed possible implications for the common envelope phase, but also found that the progenitor stars of the sdB in our sample might have had a rather broad mass distribution. More insights in the formation process of field sdB stars can be gained, if they can be clearly assigned to their parent populations, either the thin disc, the thick disc or the Galactic halo. Accurate distances and kinematics are crucial for such an analysis. The *GAIA* space mission will provide accurate distances, luminosities and kinematics for most of the known sdB stars and will also cover the Galactic disc region, which has been avoided by previous surveys

because of reddening.

This data will make it possible to derive sdB masses, identify different sdB populations and allow us to put constraints on the evolution history and the common envelope phase which forms the sdBs in close binaries.

2.11   Appendix

Table 2.7: Atmospheric parameters

Object	T_{eff} [K]	$\log g$	$\log y$	Instrument
J01185−00254	26700 ± 1000	5.36 ± 0.15	-3.0	SDSS
	27700 ± 600	5.55 ± 0.09	< -3.0	TWIN
	28000 ± 350	5.55 ± 0.05	< -3.0	Goodman
	27900 ± 600	5.55 ± 0.07	< -3.0	adopted
J03213+05384	30200 ± 500	5.74 ± 0.11	-2.4	SDSS
	30700 ± 100	5.73 ± 0.02	-2.3	ISIS
	31200 ± 300	5.74 ± 0.05	-2.5	Goodman
	30700 ± 500	5.74 ± 0.06	-2.4 ± 0.1	adopted
J08233+11364	31300 ± 600	5.78 ± 0.12	-1.9	SDSS
	31100 ± 200	5.78 ± 0.03	-2.0	ISIS
	31200 ± 400	5.80 ± 0.06	-2.0	Goodman
	31200 ± 600	5.79 ± 0.06	-2.0 ± 0.1	adopted
J08300+47515	25200 ± 500	5.30 ± 0.05	-3.3 ± 0.7	SDSS†
	25400 ± 200	5.45 ± 0.02	< -3.0	ISIS
	25300 ± 600	5.38 ± 0.06	< -3.0	adopted
J09510+03475	29800 ± 300	5.48 ± 0.04	-2.8 ± 0.3	SDSS†
	29800 ± 300	5.48 ± 0.04	-2.8 ± 0.3	adopted
J09523+62581	27800 ± 500	5.61 ± 0.08	-2.6	SDSS†
	27600 ± 200	5.56 ± 0.02	-2.5	ISIS
	27700 ± 600	5.59 ± 0.06	-2.6 ± 0.1	adopted
J10215+30101	30700 ± 500	5.71 ± 0.06	< -3.0	SDSS†
	30000 ± 200	5.63 ± 0.02	-2.5	ISIS
	30400 ± 600	5.67 ± 0.06	-2.6 ± 0.1	adopted
J1132−0636	46400 ± 1900	5.83 ± 0.11	-2.7	SDSS
	46400 ± 500	5.94 ± 0.03	-3.0	ISIS
	46400 ± 1000	5.89 ± 0.07	-2.9 ± 0.2	adopted
J13463+28172	28000 ± 800	5.38 ± 0.12	-2.7	SDSS
	29500 ± 200	5.54 ± 0.02	-2.4	GMOS
	28800 ± 600	5.46 ± 0.07	-2.6 ± 0.2	adopted
J15082+49405	28200 ± 600	5.34 ± 0.09	-2.0 ± 0.2	SDSS†
	27000 ± 1100	5.28 ± 0.19	-2.2	GMOS
	29500 ± 600	5.76 ± 0.10	-2.3	TWIN
	29600 ± 300	5.70 ± 0.05	-2.3	ISIS
	29600 ± 600	5.73 ± 0.07	-2.3 ± 0.1	adopted
J15222−01301	24800 ± 1000	5.52 ± 0.15	-2.6 ± 0.5	SDSS†
	25600 ± 500	5.41 ± 0.07	< -3.0	ISIS
	25200 ± 700	5.47 ± 0.09	< -3.0	adopted
J18324+63091	26700 ± 1100	5.26 ± 0.17	-2.5	SDSS
	26900 ± 200	5.32 ± 0.03	-2.7	ISIS
	26800 ± 700	5.29 ± 0.09	-2.6 ± 0.1	adopted

† Parameters taken from Geier et al. (2011a)

Table 2.8: Orbital parameters of all published helium burning hot subdwarf binaries

Object	T_{eff} [K]	$\log g$	Period [days]	γ [km s^{-1}]	K [km s^{-1}]	References
PG0850+170	27100±1000	5.37±0.10	27.815±0.005	32.2±2.8	33.5±3.3	[1,47]
EGB5	34500±500	5.85±0.05	16.532±0.003	68.5±0.7	16.1±0.8	[2]
PG0919+273	32900	5.90	15.5830±0.00005	-68.6±0.6	41.5±0.8	[3]
PG1619+522	32300±1000	5.98±0.10	15.3578±0.0008	-52.5±1.1	35.2±1.1	[1,47]
KIC7668647	27680±310	5.50±0.03	14.1742±0.0042	-27.4±1.3	38.9±1.9	[4]
CS1246	28500±700	5.46±0.11	14.105±0.011	67.2±1.7	16.6±0.6	[5]
LB1516	25200±1100	5.41±0.12	10.3598±0.00005	14.3±1.1	48.6±1.4	[6]
PG1558-007	20300±1000	5.00±0.10	10.3495±0.00006	-71.9±0.7	42.8±0.8	[3,48]
KIC11558725	27900±500	5.41±0.05	10.0545±0.0048	-66.1±1.4	58.1±1.7	[7]
PG1110+294	30100±1000	5.72±0.10	9.4152±0.0002	-15.2±0.9	58.7±1.2	[1,47]
EC20260-4757	-	-	8.952±0.0002	56.6±1.6	57.1±1.9	[3]
Feige108	34500±1000	6.01±0.15	8.74651±0.00001	45.8±0.6	50.2±1.0	[8,49]
PG0940+068	-	-	8.330±0.003	-16.7±1.4	61.2±1.4	[9]
PHL861	30000±500	5.50±0.05	7.44±0.015	-26.5±0.4	47.9±0.4	[10]
J032138+053840	30700±500	5.74±0.06	7.4327±0.0004	-16.7±2.1	39.7±2.8	This work
HE1448-0510	34700±500	5.59±0.05	7.159±0.005	-45.5±0.8	53.7±1.1	[10
PG1439-013	-	-	7.2914±0.00005	-53.7±1.6	50.7±1.5	[3]
J095238+625818	27700±600	5.59±0.06	6.98±0.04	-35.4±3.6	62.5±3.4	This work
PG1032+406	31600±900	5.77±0.10	6.7791±0.0001	24.5±0.5	33.7±0.5	[1,47]
PG0907+123	26200±900	5.30±0.10	6.11636±0.00006	56.3±1.1	59.8±0.9	[1,47]
HE1115-0631	40400±1000	5.80±0.10	5.87±0.001	87.1±1.3	61.9±1.1	[11,50]
CD-24731	35400±500	5.90±0.05	5.85±0.003	20.0±5.0	63.0±3.0	[12,51]
PG1244+113	36300	5.54	5.75211±0.00009	7.4±0.8	54.4±1.4	[3]
PG0839+399	37800±900	5.53±0.10	5.6222±0.0002	23.2±1.1	33.6±1.5	[1]
J183249+630910	26800±700	5.29±0.09	5.4±0.2	-32.5±2.1	62.1±3.3	This work
EC20369-1804	-	-	4.5095±0.00004	7.2±1.6	51.5±2.3	[3]
TONS135	25000±1250	5.60±0.20	4.1228±0.0008	-3.7±1.1	41.4±1.5	[12,52]
PG0934+186	35800	5.65	4.051±0.001	7.7±3.2	60.3±2.4	[3]
PB7352	25000±500	5.35±0.10	3.62166±0.000005	-2.1±0.3	60.8±0.3	[12,53]
KPD0025+5402	28200±900	5.37±0.10	3.5711±0.0001	-7.8±0.7	40.2±1.1	[1]
KIC10553698	27423±293	5.436±0.024	3.387±0.014	52.1±1.5	64.8±2.2	[65]
PG0958-073	26100±500	5.58±0.05	3.18095±0.000007	90.5±0.8	27.6±1.4	[3,54]
PG1253+284	-	-	3.01634±0.000005	17.8±0.6	24.8±0.9	[3]
TON245	25200±1000	5.30±0.15	2.501±0.000	-	88.3	[1,49]
PG1300+279	29600±900	5.65±0.10	2.25931±0.0001	-3.1±0.9	62.8±1.6	[1,47]
CPD-201123	23500±500	4.90±0.10	2.3098±0.0003	-6.3±1.2	43.5±0.9	[13]
NGC188/II-91	-	-	2.15	-	22.0	[14]
J134632+281722	28800±600	5.46±0.07	1.96±0.03	1.2±1.2	85.6±3.4	This work
V1093Her	27400±800	5.47±0.10	1.77732±0.000005	-3.9±0.8	70.8±1.0	[1,47]
PG1403+316	31200	5.75	1.73846±0.000001	-2.1±0.9	58.5±1.8	[3]
HD171858	27200±800	5.30±0.10	1.63280±0.000005	62.5±0.1	60.8±0.3	[12,53]
J002323-002953	29200±500	5.69±0.05	1.4876±0.0001	16.4±2.1	81.8±2.9	[15]
KPD2040+3955	27900	5.54	1.482860±0.0000004	-16.4±1.0	94.0±1.5	[3]
HE2150-0238	30200±500	5.83±0.07	1.321±0.005	-32.5±0.9	96.3±1.4	[10,55]
J011857-002546	27900±600	5.55±0.07	1.30±0.02	37.7±1.8	54.8±2.9	This work
UVO1735+22	38000±500	5.54±0.05	1.278±0.001	20.6±0.4	103.0±1.5	[12,53]
PG1512+244	29900±900	5.74±0.10	1.26978±0.000002	-2.9±1.0	92.7±1.5	[1,47]
PG0133+114	29600±900	5.66±0.10	1.23787±0.000003	-0.3±0.2	82.0±0.3	[12,1]
HE1047-0436	30200±500	5.66±0.05	1.21325±0.00001	25.0±3.0	94.0±3.0	[16]
PG2331+038	27200	5.58	1.204964±0.0000003	-9.5±1.1	93.5±1.9	[3]
HE1421-1206	29600±500	5.55±0.07	1.188±0.001	-86.2±1.1	55.5±2.0	[17,55]
J113241-063652	46400±000	5.89±0.07	1.06±0.02	8.3±2.2	41.1±4.0	This work
PG1000+408	36400±900	5.54±0.10	1.049343±0.0000005	56.6±3.4	63.5±3.0	[3,47]
J150829+494050	29600±600	5.73±0.07	0.967164±0.000009	-60.0±10.7	93.6±5.8	This work
PG1452+198	29400	5.75	0.96498±0.000004	-9.1±2.1	86.8±1.9	[3]
HS2359+1942	31400±500	5.56±0.07	0.93261±0.00005	-96.1±6.0	107.4±6.8	[6,55]
PB5333	40600±500	5.96±0.10	0.92560±0.0000012	-95.3±1.3	22.4±0.8	[8,54]
HE2135-3749	30000±500	5.84±0.05	0.9240±0.0003	45.0±0.5	90.5±0.6	[10]
EC12408-1427	-	-	0.90243±0.000001	-52.2±1.2	58.6±1.5	[3]
PG0918+029	31700±900	6.03±0.10	0.87679±0.000002	104.4±1.7	80.0±2.6	[1,47]

Table 2.8: continued.

Object	T_{eff}	$\log g$	Period [days]	γ [km s^{-1}]	K [km s^{-1}]	References
PG1116+301	32500±1000	5.85±0.10	0.85621±0.000003	-0.2±1.1	88.5±2.1	[1,47]
PG1230+052	27100	5.47	0.837177±0.0000003	-43.1±0.7	40.4±1.2	[3]
EC21556-5552	-	-	0.8340±0.00007	31.4±2.0	65.0±3.4	[3]
V2579Oph	23500±500	5.40±0.10	0.8292056±0.0000014	-54.16±0.27	70.1±0.13	[18,53]
EC13332-1424	-	-	0.82794±0.000001	-53.2±1.8	104.1±3.0	[3]
TONS183	27600±500	5.43±0.05	0.8277±0.00002	50.5±0.8	84.8±1.0	[12,53]
KPD2215+5037	29600	5.64	0.809146±0.0000002	-7.2±1.0	86.0±1.5	[3]
EC02200-2338	-	-	0.8022±0.00007	20.7±2.3	96.4±1.4	[3]
J150513+110836	33200±500	5.80±0.10	0.747773±0.00005	-77.1±1.2	97.2±1.8	[15]
PG0849+319	28900±900	5.37±0.10	0.74507±0.000001	64.0±1.5	66.3±2.1	[1,47]
JL82	26500±500	5.22±0.10	0.73710±0.00005	-1.6±0.8	34.6±1.0	[12,53]
PG1248+164	26600±800	5.68±0.10	0.73232±0.000002	-16.2±1.3	61.8±1.1	[1,47]
EC22202-1834	-	-	0.70471±0.000005	-5.5±3.9	118.6±5.8	[3]
J225638+065651	28500±500	5.64±0.05	0.7004±0.0001	-7.3±2.1	105.3±3.4	[15]
J152222-013018	25200±700	5.47±0.09	0.67162±0.00003	-79.5±2.7	80.1±3.5	This work
PG1648+536	31400	5.62	0.6109107±0.00000004	-69.9±0.9	109.0±1.3	[3]
PG1247+554	-	-	0.602740±0.000006	13.8±0.6	32.2±1.0	[9]
PG1725+252	28900±900	5.54±0.10	0.601507±0.0000003	-60.0±0.6	104.5±0.7	[1,47]
EC20182-6534	-	-	0.598819±0.0000006	13.5±1.9	59.7±3.2	[3]
PG0101+039	27500±500	5.53±0.07	0.569899±0.000001	7.3±0.2	104.7±0.4	[19]
HE1059-2735	41000±1000	5.38±0.10	0.555624	-44.7±0.6	87.7±0.8	[11,50]
PG1519+640	30600	5.72	0.54029143±0.0000000025	0.1±0.4	42.7±0.6	[8,3]
PG0001+275	25400±500	5.30±0.10	0.529842±0.0000005	-44.7±0.5	92.8±0.7	[12,53]
PG1743+477	27600±800	5.57±0.10	0.515561±0.0000001	-65.8±0.8	121.4±1.0	[1]
J172624+274419	32600±500	5.84±0.05	0.50198±0.00005	-36.7±4.8	118.9±3.7	[15]
HE1318-2111	36300±1000	5.42±0.10	0.487502±0.0000001	48.9±0.7	48.5±1.2	[11,50]
KUV16256+4034	23100	5.38	0.4776±0.00008	-90.9±0.9	38.7±1.2	[3]
GALEXJ2349+3844	23800±350	5.38±0.06	0.462516±0.000005	2.0±1.0	87.9±2.2	[20,56]
HE0230-4323	31100±500	5.60±0.07	0.45152±0.00002	16.6±1.0	62.4±1.6	[12,55]
HE0929-0424	29500±500	5.71±0.05	0.4400±0.0002	41.4±1.0	114.3±1.4	[10]
UVO1419-09	-	-	0.4178±0.00002	42.3±0.3	109.6±0.4	[12]
J095101+034757	29800±300	5.48±0.04	0.4159±0.0007	111.1±2.5	84.4±4.2	This work
KPD1946+4340	34200±500	5.43±0.10	0.403739±0.0000008	-5.5±1.0	156.0±2.0	[21,53]
V1405Ori	35100±800	5.66±0.11	0.398	-33.6±5.5	85.1±8.6	[6]
Feige48	29500±500	5.54±0.05	0.376±0.003	-47.9±0.1	28.0±0.2	[22,51]
GD687	24300±500	5.32±0.07	0.37765±0.00002	32.3±3.0	118.3±3.4	[23,55]
PG1232-136	26900±500	5.71±0.05	0.3630±0.0003	4.1±0.3	129.6±0.04	[12,53]
PG1101+249	29700±500	5.90±0.07	0.35386±0.00006	-0.8±0.9	134.6±1.3	[24,57]
PG1438-029	27700±1000	5.50±0.15	0.336	-	32.1	[25,49]
PG1528+104	27200	5.46	0.331±0.0001	-49.3±1.0	53.3±1.6	[3]
PHL457	26500±1100	5.38±0.12	0.3128±0.0007	-	12.8±0.08	[26,54]
PG0941+280	29400±500	5.43±0.05	0.311	73.7±4.3	141.7±6.3	[6]
HS2043+0615	26200±500	5.28±0.07	0.3015±0.0003	-43.5±3.4	73.7±4.3	[6,55]
J102151+301011	30400±600	5.67±0.06	0.2966±0.0001	-28.4±4.8	114.5±5.2	This work
KBS13	29700±500	5.70±0.05	0.2923±0.0004	7.53±0.08	22.82±0.23	[27,58]
CPD-64481	27500±500	5.60±0.05	0.277263±0.000005	94.1±0.3	23.9±0.05	[26,51]
GALEXJ0321+4727	28000±400	5.34±0.07	0.265856±0.000003	69.6±2.2	60.8±4.5	[20,56]
HE0532-4503	25400±500	5.32±0.05	0.2656±0.0001	8.5±0.1	101.5±0.2	[10]
AADor	42000±1000	5.46±0.05	0.2614±0.0002	1.57±0.09	40.15±0.11	[28,59]
J165404+303701	24900±800	5.39±0.12	0.25357±0.00001	40.5±2.2	126.1±2.6	[15]
J012022+395059	29400±500	5.48±0.05	0.252013±0.000013	-47.3±1.3	37.3±2.8	[44]
PG1329+159	29100±900	5.62±0.10	0.249699±0.0000002	-22.0±1.2	40.2±1.1	[1,47]
J204613-045418	31600±500	5.54±0.08	0.24311±0.00001	87.6±5.7	134.3±7.8	[15]
PG2345+318	27500±1000	5.70±0.15	0.2409458±0.000008	-10.6±1.4	141.2±1.1	[24,49]
PG1432+159	26900±1000	5.75±0.15	0.22489±0.00032	-16.0±1.1	120.0±1.4	[24,49]
BPSCS22169-0001	39300±500	5.60±0.05	0.214	-	16.2	[26,53]
J113840-003531	31200±600	5.54±0.09	0.207536±0.000002	23.3±3.7	162.0±3.8	[15]
J082332+113641	31200±600	5.79±0.06	0.20707±0.00002	135.1±2.0	169.4±2.5	This work
HS1741+2133	-	-	0.20±0.01	-112.8±2.7	157.0±3.4	[29]
HE1414-0309	29500±500	5.56±0.07	0.192±0.004	104.7±9.5	152.4±1.2	[6,55]

Table 2.8: continued.

Object	T_{eff}	log g	Period [days]	γ [km s^{-1}]	K [km s^{-1}]	References
HS2333+3927	36500±1000	5.70±0.10	0.1718023±0.0000009	-31.4±2.1	89.6±3.2	[30]
J192059+372220	27500±1000	5.4±0.1	0.168876±0.00035	16.8±2.0	59.7±2.5	[64]
2M1533+3759	29200±500	5.58±0.05	0.16177042±0.00000001	-3.4±5.2	71.1±1.0	[31]
J083006+475150	25300±600	5.38±0.06	0.14780±0.00007	49.9±0.9	77.0±1.7	This work
ASAS102322-3737	28400±500	5.60±0.05	0.13926940±0.00000004	-	81.0±3.0	[32]
EC00404-4429	-	-	0.12834±0.000004	33.0±2.9	152.8±3.4	[3]
2M1938+4603	29600±500	5.43±0.05	0.1257653±0.000000021	20.1±0.3	65.7±0.6	[33]
BULSC16335	31500±1800	5.70±0.2	0.122	36.4±19.6	92.5±6.2	[6]
PG1043+760	27600±800	5.39±0.1	0.1201506±0.00000003	24.8±1.4	63.6±1.4	[1,47]
EC10246-2707	28900±500	5.64±0.06	0.1185079935±0.00000000091	-	71.6±1.7	[34]
HWVir	28500±500	5.63±0.05	0.115±0.0008	-13.0±0.8	84.6±1.1	[35,60]
HS2231+2441	28400±500	5.39±0.05	0.1105880±0.0000005	-	49.1±3.2	[36]
NSVS14256825	40000±500	5.50±0.05	0.110374230±0.000000002	12.1±1.5	73.4±2.0	[37]
UVEX0328+5035	28500	5.50	0.11017±0.00011	44.9±0.7	64.0±1.5	[29,61]
PG1336-018	32800±500	5.76±0.05	0.101015999±0.00000001	-25.0	78.7±0.6	[38,62]
J082053+000843	26000±1000	5.37±0.14	0.096±0.001	9.5±1.3	47.4±1.9	[45]
HS0705+6700	28800±900	5.40±0.10	0.09564665±0.00000039	-36.4±2.9	85.8±3.6	[39]
KPD1930+2752	35200±500	5.61±0.06	0.0950933±0.0000015	5.0±1.0	341.0±1.0	[40]
KPD0422+5421	25000±1500	5.40±0.10	0.09017945±0.00000012	-57.0±12.0	237.0±8.0	[41,63]
PG1017-086	30300±500	5.61±0.10	0.0729938±0.0000003	-9.1±1.3	51.0±1.7	[42]
J162256+473051	29000±600	5.65±0.06	0.069789	-54.7±1.5	47.0±2.0	[46]
CD-3011223	29200±400	5.66±0.05	0.0489790717±0.0000000038	16.5±0.3	377.0±0.4	[43]

1: Morales-Rueda et al. (2003b); 2: Geier et al. (2011c); 3: Copperwheat et al. (2011); 4: (Telting et al., 2014); 5: Barlow et al. (2011); 6: Geier et al. (2014) 7: Telting et al. (2012); 8: Edelmann et al. (2004); 9: Maxted et al. (2000b); 10: Karl et al. (2006); 11: Napiwotzki et al. (2004a); 12: Edelmann et al. (2005); 13: Naslim et al. (2012); 14: Green et al. (2004); 15: Geier et al. (2011b); 16: Napiwotzki et al. (2001b); 17: Geier et al. (2006); 18: For et al. (2006); 19: Geier et al. (2008); 20: Kawka et al. (2012); 21: Bloemen et al. (2011); 22: O'Toole et al. (2004); 23: Geier et al. (2010a); 24: Moran et al. (1999); 25: Green et al. (2005); 26: Geier et al. (2012a); 27: For et al. (2008); 28: Müller et al. (2010); 29: Kupfer et al. (2014); 30: Heber et al. (2004); 31: For et al. (2010); 32: Schaffenroth et al. (2013); 33: Østensen et al. (2010a); 34: Barlow et al. (2013); 35: Edelmann (2008); 36: Østensen et al. (2007); 37: Almeida et al. (2012); 38: Vučković et al. (2007); 39: Drechsel et al. (2001); 40: Geier et al. (2007); 41: Orosz & Wade (1999); 42: Maxted et al. (2002); 43: Geier et al. (2013b); 44: Østensen et al. (2013); 45: Geier et al. (2011d); 46: Schaffenroth et al. (2014b); 47: Maxted et al. (2001); 48: Heber et al. (2002); 49: Saffer et al. (1994); 50: Stroeer et al. (2007); 51: O'Toole & Heber (2006); 52: Heber (1986); 53: Geier et al. (2010b); 54: Geier et al. (2013a); 55: Lisker et al. (2005); 56: Németh et al. (2012); 57: Edelmann et al. (1999); 58: Østensen et al. (2010b); 59: Klepp & Rauch (2011); 60: Wood & Saffer (1999); 61: Verbeek et al. (2012); 62: Charpinet et al. (2008); 63: Koen et al. (1998); 64: Schaffenroth et al. (2014a); 65: Østensen et al. (2014)

Table 2.9: Photometry, spectroscopic distances and companion types

Object	V [mag]	J [mag]	H [mag]	Distance [kPc]	Comp. Type	References
PG0850+170	13.977±0.000	14.531±0.043	14.624±0.066	$1.04^{+0.16}_{-0.15}$	MS/WD	[1,13]
EGB5	13.808±0.04	14.482±0.036	14.530±0.055	$0.68^{+0.07}_{-0.06}$	MS/WD	[2,13]
PG0919+273	12.765±0.009	13.303±0.021	13.420±0.030	$0.39^{+0.00}_{-0.00}$	WD	[1,13]
PG1619+522	13.297±0.006	13.883±0.027	13.969±0.040	$0.44^{+0.08}_{-0.06}$	WD	[1,13]
KIC7668647	15.218±0.07	15.815±0.066	$16.056±0.201^C$	$1.54^{+0.12}_{-0.12}$	WD^{lc}	[2,13]
CS1246	14.371±0.03	14.013±0.039	14.032±0.058	-	MS/WD^{lc}	[2,13]
LB1516	12.967±0.003	13.520±0.035	13.663±0.054	$0.59^{+0.11}_{-0.10}$	WD	[3,13]
PG1558-007	13.528±0.006	-	-	$0.84^{+0.15}_{-0.12}$	MS/WD^{lc}	[1]
KIC11558725	14.859±0.04	15.379±0.046	15.352±0.088	$1.45^{+0.14}_{-0.13}$	WD^{lc}	[2,13]
PG1110+294	14.086±0.006	14.626±0.037	14.674±0.063	$0.79^{+0.13}_{-0.11}$	WD	[1,13]
EC20260-4757	13.735±0.01	14.424±0.023	14.465±0.046	-	MS/WD	[2,13]
Feige108	12.973±0.000	13.529±0.024	13.704±0.032	$0.39^{+0.08}_{-0.07}$	WD	[4,13]
PG0940+068	-	14.151±0.027	14.147±0.049	-	MS/WD	[13]
PHL861	14.826±0.04	15.375±0.051	15.496±0.103	$1.45^{+0.14}_{-0.13}$	MS/WD	[2,13]
J032138+053840	15.048±0.04	15.148±0.050	$15.402±0.135^B$	$1.02^{+0.11}_{-0.10}$	MS/WD	[2,13]
HE1448-0510	14.611±0.04	15.199±0.056	15.234±0.096	$1.30^{+0.12}_{-0.11}$	WD	[2,13]
PG1439-013	13.943±0.028	14.506±0.035	14.692±0.041	-	MS/WD	[1,13]
J095238+625818	14.693±0.09	15.420±0.067	$15.609±0.147^B$	$1.13^{+0.16}_{-0.14}$	WD	[2,13]
PG1032+406	11.519±0.009	12.166±0.022	12.275±0.018	$0.25^{+0.04}_{-0.04}$	MS/WD	[1,13]
PG0907+123	13.970±0.003	14.474±0.030	14.666±0.066	$1.08^{+0.17}_{-0.15}$	MS/WD	[1,13]
HE1115-0631	-	15.623±0.079	$15.580±0.129^B$	-	MS/WD	[13]
CD-24731	11.748±0.024	12.404±0.027	12.583±0.027	$0.26^{+0.02}_{-0.02}$	WD	[5,13]
PG1244+113	14.197±0.018	14.821±0.004	14.939±0.007	$1.21^{+0.01}_{-0.01}$	WD	[1,14]
PG0839+399	14.389±0.000	14.885±0.035	15.080±0.064	$1.36^{+0.19}_{-0.16}$	MS/WD	[1,13]
J183249+630910	15.695±0.01	16.236±0.096	$16.068±0.176^C$	$2.41^{+0.34}_{-0.30}$	MS/WD	[2,13]
EC20369-1804	13.29 ±0.00	13.937±0.022	14.061±0.044	-	MS/WD	[6,13]
TONS135	13.302±0.042	13.868±0.029	14.017±0.047	$0.54^{+0.19}_{-0.14}$	MS/WD	[5,13]
PG0934+186	13.138±0.001	13.759±0.025	13.972±0.038	$0.66^{+0.00}_{-0.00}$	WD	[1,13]
PB7352	12.261±0.01	12.819±0.026	12.915±0.025	$0.44^{+0.06}_{-0.06}$	MS/WD	[2,13]
KPD0025+5402	13.919±0.015	14.259±0.031	14.361±0.047	-	MS/WD	[1,13]
KIC10553698	14.902±0.08	15.446±0.047	15.538±0.092	-	WD^{lc}	[2,13]
PG0958-073	13.563±0.002	14.098±0.030	14.139±0.039	$0.63^{+0.05}_{-0.05}$	MS/WD	[4,13]
PG1253+284	12.769±0.000	12.182±0.001	12.003±0.001	-	MS/WD	[1,13]
TON245	13.859±0.04	14.312±0.002	14.417±0.005	$0.97^{+0.24}_{-0.20}$	WD	[2,14]
PG1300+279	14.266±0.023	14.894±0.004	15.006±0.007	$0.94^{+0.16}_{-0.13}$	WD	[1,14]
CPD-201123	12.173±0.12	12.565±0.024	12.658±0.027	$0.64^{+0.13}_{-0.11}$	MS/WD	[2,13]
NGC188/II-91	-	-	-	-	MS/WD	[]
J134632+281722	14.908±0.07	15.513±0.007	15.595±0.010	$1.53^{+0.21}_{-0.19}$	WD	[2,14]
V1093Her	13.967±0.008	14.518±0.034	14.677±0.074	$0.93^{+0.14}_{-0.13}$	MS/WD^{lc}	[1,13]
PG1403+316	13.532±0.010	14.179±0.023	14.376±0.041	$0.63^{+0.00}_{-0.00}$	WD	[1,13]
HD171858	9.85±0.04	10.321±0.023	10.432±0.022	-	MS/WD	[7,13]
J002323-002953	15.577±0.02	16.153±0.013	16.275±0.026	$1.60^{+0.14}_{-0.14}$	WD	[2,14]
KPD2040+3955	14.472±0.049	14.560±0.036	14.560±0.065	-	MS/WD	[1,13]
HE2150-0238	-	-	-	-	MS/WD	[]
J011857-002546	14.804±0.05	15.184±0.047	15.262±0.098	$1.25^{+0.16}_{-0.15}$	MS/WD	[2,13]
UVO1735+22	11.861±0.01	12.509±0.021	12.650±0.022	$0.37^{+0.04}_{-0.04}$	WD	[2,13]

Table 2.9: continued.

Object	V[mag]	J [mag]	H [mag]	Distance [kPc]	Comp. Type	References
PG1512+244	13.185±0.04	13.957±0.028	13.957±0.039	$0.50^{+0.09}_{-0.07}$	WD	[2,13]
PG0133+114	12.345±0.000	12.801±0.001	12.918±0.002	$0.37^{+0.05}_{-0.05}$	WD	[1,14]
HE1047-0436	14.796±0.000	15.527±0.060	15.637±0.123[B]	$1.19^{+0.09}_{-0.09}$	WD	[1,13]
PG2331+038	14.974±0.025	15.361±0.005	15.404±0.012	$1.20^{+0.02}_{-0.01}$	WD	[1,14]
HE1421-1206	15.510±0.0	15.891±0.073	15.872±0.165[C]	$1.72^{+0.18}_{-0.16}$	MS	[8,13.15]
J113241-063652	16.273±0.005	16.684±0.142[B]	-	$2.39^{+0.24}_{-0.21}$	MS/WD	[9,13]
PG1000+408	13.327±0.023	13.978±0.027	14.244±0.043	$0.83^{+0.12}_{-0.10}$	MS/WD	[1,13]
J150829+494050	17.516±0.005	-	-	$3.83^{+0.41}_{-0.37}$	MS/WD	[9]
PG1452+198	12.476±0.002	13.055±0.023	13.179±0.025	$0.90^{+0.00}_{-0.00}$	WD	[1,13]
HS2359+1942	15.639±0.06	16.234±0.092	16.227±0.212[C]	$2.02^{+0.26}_{-0.24}$	WD	[2,13]
PB5333	12.874±0.020	12.879±0.001	12.622±0.001	$0.42^{+0.05}_{-0.06}$	MS/WD	[1,14]
HE2135-3749	13.896±0.01	14.598±0.035	14.650±0.051	$0.63^{+0.05}_{-0.05}$	WD	[2,13]
EC12408-1427	12.823±0.02	13.390±0.029	13.465±0.035	-	MS/WD	[2,13]
PG0918+029	13.415±0.080	13.995±0.002	14.092±0.004	$0.43^{+0.08}_{-0.07}$	WD	[1,14]
PG1116+301	14.337±0.019	-	-	$0.84^{+0.14}_{-0.12}$	MS/WD	[1]
PG1230+052	13.287±0.018	13.835±0.002	13.965±0.003	$0.67^{+0.01}_{-0.01}$	MS/WD	[1,14]
EC21556-5552	13.090±0.04	13.718±0.029	13.862±0.047	-	MS/WD	[2,13]
V2579Oph	12.930±0.025	13.369±0.026	13.476±0.030	$0.52^{+0.08}_{-0.07}$	MS/WD[lc]	[1,13]
EC13332-1424	13.380±0.03	13.895±0.030	13.990±0.035	-	MS/WD	[2,13]
TONS183	12.598±0.02	13.232±0.026	13.361±0.028	$0.52^{+0.05}_{-0.04}$	MS/WD	[2,13]
KPD2215+5037	13.739±0.022	14.218±0.040	14.313±0.042	-	MS/WD	[1,13]
EC02200-2338	12.014±0.01	12.616±0.026	12.748±0.021	-	MS/WD	[2,13]
J150513+110836	15.378±0.09	16.043±0.006	16.151±0.015	$1.44^{+0.26}_{-0.23}$	WD	[2,14]
PG0849+319	14.606±0.000	15.177±0.044	15.318±0.095	$1.46^{+0.23}_{-0.19}$	MS/WD	[1,13]
JL82	12.389±0.003	12.857±0.024	12.960±0.025	$0.57^{+0.08}_{-0.07}$	MS	[3,13]
PG1248+164	14.460±0.03	15.037±0.037	15.013±0.080	$0.89^{+0.15}_{-0.13}$	MS/WD	[2,13]
EC22202-1834	13.802±0.03	14.389±0.033	14.431±0.049	-	MS/WD	[2,13]
J225638+065651	15.314±0.01	15.744±0.006	15.789±0.012	$1.39^{+0.12}_{-0.10}$	WD	[2,14]
J152222-013018	17.813±0.02	18.424±0.098	18.202±0.131	-	MS/WD	[9,14]
PG1648+536	14.055±0.017	14.553±0.029	14.587±0.051	$0.88^{+0.01}_{-0.01}$	WD	[1,13]
PG1247+554	12.259±0.01	-	11.087±0.017	-	MS/WD	[2,13]
PG1725+252	13.008±0.018	13.496±0.026	13.641±0.037	$0.54^{+0.09}_{-0.07}$	MS/WD	[1,13]
EC20182-6534	13.29 ±0.0	13.782±0.029	13.877±0.021	-	MS/WD	[6,13]
PG0101+039	12.065±0.000	12.609±0.001	12.724±0.002	$0.36^{+0.04}_{-0.03}$	WD[lc]	[4,14]
HE1059-2735	15.500±0.06	16.051±0.089	16.329±0.206[C]	$2.73^{+0.46}_{-0.43}$	MS/WD	[2,13]
PG1519+640	12.458±0.001	13.007±0.023	13.185±0.026	$0.39^{+0.00}_{-0.00}$	MS/WD	[1,13]
PG0001+275	-	13.833±0.024	13.971±0.041	-	MS/WD	[13]
PG1743+477	13.787±0.009	14.313±0.024	14.526±0.060	$0.76^{+0.12}_{-0.10}$	WD	[1,13]
J172624+274419	15.994±0.01	16.467±0.101	-	$1.76^{+0.15}_{-0.13}$	WD	[2,13]
HE1318-2111	14.718±0.09	15.218±0.049	15.288±0.089	$1.64^{+0.30}_{-0.26}$	MS/WD	[2,13]
KUV16256+4034	12.64 ±0.21	13.067±0.035	13.224±0.035	$0.49^{+0.04}_{-0.05}$	MS/WD	[7,13]
GALEXJ2349+3844	11.73 ±0.13	12.040±0.024	12.156±0.031	-	MS/WD	[7,13]
HE0230-4323	13.768±0.02	13.948±0.032	13.804±0.044	$0.82^{+0.09}_{-0.08}$	MS	[2,13]
HE0929-0424	16.165±0.15	16.646±0.112[B]	-	$2.06^{+0.31}_{-0.28}$	MS/WD	[2,13]
UVO1419-09	12.115±0.09	12.692±0.023	12.835±0.025	-	WD	[2,13]
J095101+034757	15.895±0.02	15.972±0.007	15.705±0.013	$2.37^{+0.17}_{-0.15}$	MS/WD	[2,14]

Table 2.9: continued.

Object	V[mag]	J [mag]	H [mag]	Distance [kPc]	Comp. Type	References
KPD1946+4340	14.299±0.002	14.683±0.031	14.836±0.055	-	WD	[1,13]
V1405Ori	15.142±0.09	14.574±0.031	14.677±0.045	-	MS^{lc}	[2,13]
Feige48	13.456±0.000	13.983±0.027	14.137±0.043	$0.73^{+0.05}_{-0.06}$	WD^{lc}	[1,13]
GD687	14.077±0.03	14.618±0.033	14.874±0.077	$1.04^{+0.12}_{-0.11}$	WD	[2,13]
PG1232-136	13.336±0.033	13.758±0.028	13.897±0.040	$0.50^{+0.05}_{-0.04}$	WD	[1,13]
PG1101+249	12.775±0.03	13.187±0.027	13.257±0.039	$0.36^{+0.03}_{-0.04}$	WD	[2,13]
PG1438-029	-	14.168±0.029	14.240±0.053	-	MS	[13]
PG1528+104	13.569±0.010	14.082±0.002	14.156±0.004	$0.77^{+0.01}_{-0.01}$	WD	[1,14]
PHL457	12.947±0.010	13.499±0.026	13.595±0.021	$0.62^{+0.12}_{-0.11}$	MS	[2,13]
PG0941+280	13.265±0.07	13.799±0.029	13.899±0.042	$0.75^{+0.09}_{-0.07}$	WD^{lc}	[2,13]
HS2043+0615	15.420± 0	16.098±0.093	-	$2.02^{+0.20}_{-0.19}$	MS	[8,13]
J102151+301011	18.218±0.007	-	-	$5.74^{+0.55}_{-0.51}$	MS/WD	[9]
KBS13	13.633±0.01	14.018±0.024	14.063±0.032	-	MS^{lc}	[2,13]
CPD-64481	11.291±0.01	11.878±0.022	11.994±0.028	$0.23^{+0.02}_{-0.02}$	MS	[2,13]
GALEXJ0321+4727	11.73 ±0.15	11.795±0.001	11.923±0.001	-	MS	[7,14]
HE0532-4503	15.98 ±0.0	16.563±0.146^C	-	$2.55^{+0.20}_{-0.18}$	MS/WD	[10,13]
AADor	11.90 ±0.0	11.795±0.028	11.965±0.029	-	MS^{lc}	[2,13]
J165404+303701	15.409±0.04	15.938±0.008	16.030±0.016	$1.78^{+0.37}_{-0.30}$	MS/WD	[2,14]
J012022+395059	15.341±0.07	16.016±0.078	15.925±0.175^C	$1.79^{+0.19}_{-0.18}$	MS	[2,13]
PG1329+159	13.507±0.03	14.047±0.002	14.221±0.004	$0.67^{+0.12}_{-0.10}$	MS	[2,13]
J204613-045418	16.324±0.01	16.677±0.143^B	16.308±0.217^D	$2.81^{+0.33}_{-0.30}$	MS/WD	[2,13]
PG2345+318	14.178±0.005	14.690±0.039	14.833±0.071	$0.19^{+0.05}_{-0.03}$	WD	[1,13]
PG1432+159	13.896±0.013	14.445±0.028	14.530±0.050	$0.64^{+0.15}_{-0.12}$	WD	[1,13]
BPSCS22169-0001	12.848±0.01	13.456±0.023	13.551±0.024	-	MS	[2,13]
J113840-003531	14.467±0.03	15.161±0.043	15.137±0.085	$1.23^{+0.17}_{-0.16}$	WD	[2,13]
J082332+113641	16.658±0.005	-	-	$2.48^{+0.22}_{-0.21}$	MS/WD	[2]
HS1741+2133	13.990±0.01	14.386±0.036	14.616±0.060	-	WD	[2,13]
HE1415-0309	16.487±0.0	-	-	$2.76^{+0.27}_{-0.26}$	WD	[9]
HS2333+3927	14.794±0.01	14.986±0.048	15.018±0.084	$1.25^{+0.17}_{-0.15}$	MS^{lc}	[2,13]
J192059+372220	15.745±0.01	16.186±0.083	16.272±0.224^D	-	MS	[2,13]
2M1533+3759	12.964±0.17	13.652±0.026	13.736±0.031	$0.55^{+0.09}_{-0.08}$	MS^{lc}	[2,13]
J083006+475150	16.043±0.03	16.737±0.143^B	16.477±0.220^D	$2.44^{+0.27}_{-0.24}$	WD	[2,13]
ASAS102322-3737	11.707±0.07	12.028±0.021	12.112±0.027	$0.28^{+0.03}_{-0.03}$	MS^{lc}	[2,13]
EC00404-4429	13.674±0.02	14.220±0.030	14.424±0.052	-	WD	[2,13]
2M1938+4603	12.063±0.01	12.757±0.022	12.889±0.020	-	MS^{lc}	[2,13]
BULSC16335	16.395±0.028	12.868±0.022	12.072±0.021	-	MS^{lc}	[11,13]
PG1043+760	13.768±0.016	14.278±0.030	14.359±0.049	$0.89^{+0.14}_{-0.12}$	WD	[1,13]
EC10246-2707	14.38 ±0.0	14.830±0.036	14.842±0.052	$0.92^{+0.08}_{-0.07}$	MS^{lc}	[12,13]
HWVir	10.577±0.069	10.974±0.027	11.093±0.022	$0.17^{+0.01}_{-0.02}$	MS^{lc}	[1,13]
HS2231+2441	14.153±0.05	14.669±0.035	14.732±0.054	$1.11^{+0.11}_{-0.10}$	MS^{lc}	[2,13]
NSVS14256825	13.389±0.25	13.658±0.026	13.797±0.026	-	MS^{lc}	[2,13]
UVEX0328+5035	14.263±0.02	14.121±0.004	13.915±0.004	-	MS	[2,14]
PG1336-018	13.661±0.27	14.594±0.037	14.646±0.050	$0.61^{+0.07}_{-0.07}$	MS^{lc}	[2,13]
J082053+000843	15.168±0.05	15.712±0.008	15.818±0.014	$1.69^{+0.42}_{-0.33}$	BD	[2,14]
HS0705+6700	14.923±0.52	15.103±0.039	15.233±0.086	$1.58^{+0.74}_{-0.50}$	MS^{lc}	[2,13]
KPD1930+2752	13.833±0.035	13.983±0.029	13.968±0.045	-	WD^{lc}	[1,13]
KPD0422+5421	14.682±0.018	14.425±0.031	14.421±0.046	-	WD^{lc}	[1,13]

Table 2.9: continued.

Object	V[mag]	J [mag]	H [mag]	Distance [kPc]	Comp. Type	References
PG1017-086	14.426±0.025	14.866±0.042	15.036±0.074	$1.05^{+0.16}_{-0.14}$	MS	[1,13]
J162256+473051	16.188±0.02	16.732±0.136^B	-	$2.25^{+0.23}_{-0.21}$	BD	[2,13]
CD-3011223	12.296±0.03	12.886±0.029	12.932±0.023	$0.35^{+0.03}_{-0.03}$	WD	[2,13]

lc: identified photometrically; B,C,D: 2MASS colours of quality B, C or D which were excluded from the analysis

1: Wesemael et al. (1992); 2: UCAC4; 3: Landolt (2007); 4: Landolt (2009); 5: Mermilliod (1992); 6: O'Donoghue et al. (2013) 7: Høg et al. (2000); 8: NOMAD; 9: SDSS, Jester et al. (2005); 10: SPM4.0; 11: Udalski et al. (2002); 12: Kilkenny et al. (1997); 13: 2MASS; 14: UKIDSS; 15: Koen priv. comment

CHAPTER 3

ORBITAL PERIODS AND ACCRETION DISC STRUCTURE OF FOUR AM CVN SYSTEMS

T. Kupfer, P. J. Groot, D. Levitan, D. Steeghs, T. R. Marsh, R. G. M. Rutten and G. Nelemans

Abstract. Phase-resolved spectroscopy of four AM CVn systems obtained with the William Herschel Telescope and the Gran Telescopio de Canarias is presented. SDSS J120841.96+355 025.2 was found to have an orbital period of 52.96±0.40 min and shows the presence of a second bright spot in the accretion disc. The average spectrum contains strong Mg I and Si I/II absorption lines most likely originating in the atmosphere of the accreting white dwarf. SDSS J01 2940.05+384210.4 has an orbital period of 37.555±0.003 min. The average spectrum shows the Stark broadened absorption lines of the DB white dwarf accretor. The orbital period is close to the previously reported superhump period of 37.9 min. Combined, this results in a period excess ϵ=0.0092±0.0054 and a mass ratio q =0.031±0.018. SDSS J164228.06+193410.0 displays an orbital period of 54.20±1.60 min with an alias at 56.35 min. The average spectrum also shows strong Mg I absorption lines, similar to SDSS J120841.96+355025.2. SDSS J15250 9.57+360054.50 displays an period of 44.32±0.18 min. The overall shape of the average spectrum is more indicative of shorter period systems in the 20-35 minute range. The accretor is still clearly visible in the pressure broadened absorption lines most likely indicating a hot donor star and/or a high mass accretor. Flux ratios for several helium lines were extracted from the Doppler tomograms for the disc and bright spot region, and compared with single-slab LTE models with variable electron densities and path lengths to estimate the disc and bright spot temperature. A good agreement between data and the model in three out of four systems was found for the disc region. All three systems show similar disc temperatures of $\sim$10 500 K. In contrast, only weak agreement between observation and models was found for the bright spot region.

3.1   Introduction

AM CVn systems are a small group of mass transferring ultra compact binaries with orbital periods between 5.4 and 65 min (see Solheim, 2010 for a recent review). They consist of a white dwarf (WD) primary, and a WD, or semi-degenerate helium star secondary (e.g. Nelemans et al., 2001a). Spectroscopically these systems are characterized by a high deficiency of hydrogen, indicating an advanced stage of binary evolution.

Over the course of evolution of a close binary consisting of intermediate mass stars, two common envelope phases may produce a detached WD binary system at a period of minutes to hours (see Kilic et al., 2012 and references therein). Gravitational wave radiation will decrease the orbital separation until the low-mass secondary fills its Roche lobe and mass transfer sets in at an orbital period between 3-10 min (e.g.Nelemans, 2005). A fraction of these systems will survive the ensuing direct impact phase, pass through an orbital period minimum and become AM CVn systems (Nelemans et al., 2001a; Marsh et al., 2004). An accretion disc forms at an orbital period of ∼10 min depending on the masses and the entropy of the donor (see e.g. Kaplan et al., 2012). Material transferred from the secondary hits the disc at the so-called bright spot. In the further evolution the system widens, upon loss of angular momentum in gravitational waves, causing the mass-transfer rate to drop. The mass-transfer rate drops as the orbit widens and the system ends up as a more massive WD with an extremely low-mass WD companion (~ 0.001 M$_\odot$) at an orbital period of ∼1 hour. AM CVn systems are important as strong low-frequency Galactic gravitational wave sources (e.g. Nelemans et al., 2004; Roelofs et al., 2007d; Nissanke et al., 2012) and are the source population of the proposed '.Ia' supernovae (Bildsten et al., 2007).

AM CVn systems show three phases during their lifetime based on their photometric behaviour. Systems with periods below 20 min have a high mass-transfer rate resulting in spectra that are dominated by helium absorption lines originating in the optically thick disc. Systems with periods above 40 min are in a low mass-transfer rate state and have spectra dominated by strong helium emission lines from an optically thin accretion disc. The intermediate period systems between 20 and 40 min orbital period undergo dwarf-nova type photometric outbursts and change their spectral behaviour from low state, where emission lines from the disc and Stark-broadened absorption lines from the accretor dominate the spectrum, to a high state, where absorption lines from the optically thick disc dominate the spectra (Groot et al., 2001; Levitan et al., 2011; Ramsay et al., 2012).

In a large campaign using the Sloan Digital Sky Survey (SDSS; York et al., 2000) Roelofs et al. (2005, 2007b); Anderson et al. (2005, 2008); Rau et al. (2010); Carter et al. (2012) built up the population of AM CVn systems and significantly increased the number of known systems over the last ten years. The recent increase in the population from photometric, spectroscopic, and synoptic surveys (e.g. Levitan et al., 2011, 2013, 2014) allows the derivation of population properties such as the orbital period distribution or the presence or absence of spectral features as a function of evolutionary stage. To determine the orbital period, and detect variations in the spectrum over the orbital period, phase-resolved spectroscopy is needed (Roelofs et al., 2005, 2006a), although Levitan et al. (2011) showed that the photometric pe-

Table 3.1: Summary of the observations of SDSS J1208, SDSS J0129, SDSS J1642 and SDSS J1525.

System	Telescope+Instrument	Exp.	Exp. time (s)	Coverage (Å)	Binning	Resolution (Å)
SDSS J1208						
2008/12/25	WHT+ISIS(R300B/R316R)	50	180	3250 - 8119	2x2	1.77 (R300B) 1.75 (R316R)
2008/12/27	WHT+ISIS(R300B/R316R)	50	180	3250 - 8119	2x2	1.77 (R300B) 1.75 (R316R)
2008/12/28	WHT+ISIS(R300B/R316R)	50	210	3250 - 8119	2x2	1.77 (R300B) 1.75 (R316R)
SDSS J0129						
2011/09/25	GTC+Osiris(R1000B)	42	120	3833 - 7877	2x2	2.15 (R1000B)
2011/09/26	GTC+Osiris(R1000B)	40	120	3833 - 7877	2x2	2.15 (R1000B)
2011/09/27	GTC+Osiris(R1000B)	20	120	3833 - 7877	2x2	2.15 (R1000B)
2011/09/28	GTC+Osiris(R1000B)	21	120	3833 - 7877	2x2	2.15 (R1000B)
SDSS J1642						
2011/08/24	GTC+Osiris(R1000B)	32	180	3833 - 7877	2x2	2.15 (R1000B)
2011/08/26	GTC+Osiris(R1000B)	32	180	3833 - 7877	2x2	2.15 (R1000B)
2011/08/27	GTC+Osiris(R1000B)	20	180	3833 - 7877	2x2	2.15 (R1000B)
2012/01/25	Hale+DoubleSpec(600/4000)	1	1200	3500 - 5250	1x1	2.75 (600/4000)
SDSS J1525						
2011/07/24	GTC+Osiris(R1000B)	16	180	3833 - 7877	2x2	2.15 (R1000B)
2011/08/28	GTC+Osiris(R1000B)	22	180	3833 - 7877	2x2	2.15 (R1000B)
2011/08/29	GTC+Osiris(R1000B)	32	180	3833 - 7877	2x2	2.15 (R1000B)

riod may be tied to the spectroscopic period for some systems. This is not valid for all systems. GP Com shows variability in the light curve which is not tied to the orbital motion (Morales-Rueda et al., 2003a).

Here, the results of follow-up phase-resolved spectroscopy of four systems which were originally found in the SDSS spectroscopy or photometry, and confirmed by spectroscopy to be AM CVn systems are presented. SDSS J120841.96+355025.2 (hereafter SDSS J1208) and SDSS J012940.05+384210.4 (hereafter SDSS J0129) were found in the spectral database of SDSS due to their strong helium emission lines and lack of hydrogen (Anderson et al., 2005, 2008). SDSS J164228.06+193410.0 (hereafter SDSS J1642) and SDSS J152509.57+360054.5 (hereafter SDSS J1525) were found during follow-up observations of colour selected AM CVn candidates from SDSS (Rau et al., 2010).

As Doppler tomography (Marsh & Horne, 1988) remaps line intensities from the wavelength-time domain to the binary velocity frame, the technique can also be used to derive line intensities of specific regions in the binary system. Skidmore et al. (2000) used ratioed Doppler maps to study the structure of the accretion disc in the dwarf nova WZ Sge. This ratio-mapping has so far not been applied to Doppler tomograms to derive disc temperatures and densities in AM CVn type binaries. Here, for the first time, this technique is used to limit the characteristics of the accretion disc and bright spot regions under the assumption of an LTE slab model in AM CVn type binaries.

3.2   Observations and Data reduction

Phase-resolved spectroscopy of SDSS J1208 using the William Herschel Telescope (WHT) and the ISIS spectrograph (Carter et al., 1993) was obtained. Table 3.1 gives an overview of all observations and the instrumental set-ups. Each night an average bias frame was made out of 20 individual bias frames and a normalised flat field frame was constructed out of 20 individual

lamp flat fields. CuNeAr arc exposures were taken every hour to correct for instrumental flexure. Each exposure was wavelength calibrated by interpolating between the two closest calibration exposures. A total of about 30 lines could be well fitted in each arc exposure using a Legendre polynomial of order 4 resulting in 0.08 Å root-mean-square residuals.

Feige 34 (Oke, 1990) was used as a spectrophotometric standard to flux calibrate the spectra and correct them for the instrumental response.

For SDSS J0129, SDSS J1642 and SDSS J1525 phase-resolved spectroscopy using the Gran Telescopio de Canarias (GTC) and the Osiris spectrograph (Cepa, 1998) was obtained. 10 to 12 bias frames each night to construct an average bias frame and 5 to 7 individual tungsten lamp flat fields to construct a normalised flat field were obtained. HgArNe calibration were obtained for SDSS J1642 and SDSS J1525 at the end of every night. To check the stability of Osiris the O I 5577 sky line was used. It shows a maximum shift of 0.3Å over the night. This corresponds to $17\,\mathrm{km\,s^{-1}}$ which is acceptable for the velocity fields displayed by our systems. For SDSS J0129, calibrations were obtained directly following a two hour block of the science observations. About 30 lines could be well fitted in each arc exposure using a Legendre function of order 4 resulting in 0.07 Å root-mean-square residuals. The only exception was August 26 on SDSS J1642 when the calibration lamp spectra were stretched by a few pixels. The reason for the stretched image was an incorrect focus position of the spectrograph. This was initially not spotted, and corrected for by adjusting the telescope focus. This produced a focussed spectrum on the detector, but had the side effect of generating a few pixels of stretching. Sky lines could not be used for calibration as to few isolated sky lines are visible in the spectrum in particular in the blue. Calibration lines from a different night could also not be used as the stretching of the spectra is a non-linear effect and variable from night to night. Therefore, the helium emission lines from the target itself were used to calibrate the spectra for this night. To correct for the instrumental response G24–9, L1363–3 and G158–100 (Oke, 1974, 1990) were used as spectrophotometric standards.

All spectra were debiased and flat fielded using IRAF routines. One dimensional spectra were extracted using optimal extraction and were subsequently wavelength and flux calibrated.

SDSS J1642 was also observed on the Hale telescope using the DoubleSpec spectrograph (Oke & Gunn, 1982), which covers wavelengths below 3900 Å. Only data taken with the blue side, using the 600/4000 grating is shown here. An FeAr lamp was used for wavelength calibration and G191-B2B (Oke, 1990) was used as a spectrophotometric standard. STARLINK, PAMELA, and MOLLY were used for reduction and calibration.

3.3   Methods

3.3.1   Period determination

To determine the orbital period the violet-over-red method (V/R) described in Nather et al. (1981) was used following Roelofs et al. (2005, 2006a, 2007c). The normalised emission wings of the helium lines were divided into a red and a violet part and the flux ratio of both wings was calculated. To maximise the SNR the ratios of the strongest emission helium lines

(3888 Å, 4026 Å, 4471 Å, 5015 Å, 5875 Å and 6678 Å) were summed for SDSS J1208, as well as for SDSS J1642 without 3888 Å. For SDSS J0129 and SDSS J1525 the lines which are supposed to be least affected by broad wing absorption from the accretor were used (5875 Å, 6678 Å and 7065 Å). Lomb-Scargle periodograms of the measured violet-over-red-ratio as a function of the heliocentric date were computed (Fig. 3.6) and the strongest peaks are assumed to correspond to the orbital period.

The uncertainty on the derived period for each system was estimated using a simple Monte Carlo simulation, where 1000 periodograms were computed and in each the highest peak was taken as the orbital period (see Roelofs et al., 2006a). For SDSS J1208, 150 spectra were randomly picked out of the full sample of 150 spectra, allowing for a spectrum to be picked more than once. The same was done for SDSS J1029, SDSS J1642 and SDSS J1525 using 123, 84 and 70 spectra respectively. The standard deviation on the distribution of the computed orbital periods is taken as a measure of the accuracy in the derived period.

3.3.2 Analysis of Doppler tomograms

In Doppler tomography (Marsh & Horne, 1988) phase-resolved spectra are projected onto a two-dimensional map in velocity coordinates. We refer to Steeghs (2003) and Marsh (2001) for reviews on Doppler tomography. Emission features that are stationary in the binary frame add up constructively in a Doppler tomogram while emission that is not stationary in the binary frame or moves on a period different from the orbital period will be spread out over the Doppler tomogram. Therefore, Doppler tomograms are useful to separate out features that move with a different velocity and/or different phase (e.g. bright spot and central spike). In this analysis Doppler tomograms were computed using the software package DOPPLER[1], and were used to measure the phase shift between the two bright spots in SDSS J1208 (see Sec. 3.4.4), and to extract fluxes from Doppler tomograms to estimate temperatures of the disc and the bright spot. In the analysis we assume that the disc emission is radially and azimuthally symmetric around the WD and the bright spot emission is concentrated in a single quarter in the Doppler tomogram.

SDSS J1208 shows a prominent second bright spot in several helium lines (see Fig. 3.8). To measure the phase shift between both spots in SDSS J1208, a 2D-Gaussian was fitted to the spots in the Doppler tomograms of the 5875 Å, 6678 Å and 7065 Å lines. The center of every 2D-Gaussian fit $(v_{x,max}, v_{y,max})$ was calculated for each line. The error-weighted mean of the center is taken to be the center of the bright spot. The phase error on the position of the bright spot is calculated as the length of the intersection between the phase angle and the positional error ellipse.

The flux ratios obtained from the line emission strengths in the Doppler tomograms were used to estimate the temperature of the disc and the bright spot. To separate the disc and bright spot region, each Doppler tomogram was divided into two sections. The Doppler tomograms of all systems with only one bright spot were divided into three quarters with only disc emission and one quarter including the bright spot region (see Fig. 3.1). The quarter with the second

---

[1]DOPPLER was written by Marsh and is available at http://www.warwick.ac.uk/go/trmarsh/software/

bright spot was excluded from the disc region in SDSS J1208. For this system only half of the Doppler tomogram was used for the disc region.

Every section was divided into radial bins with a bin size of $60\,\mathrm{km\,s^{-1}}$, starting at the center of the Doppler tomogram (v_x, v_y=0,0). The center of the Doppler tomogram is assumed to be the center of the WD primary due to the extreme mass ratios expected in AM CVn systems where the orbital velocity of the primary in long period systems is expected to be less than $50\,\mathrm{km\,s^{-1}}$ (Morales-Rueda et al., 2003a; Roelofs et al., 2006b). The average flux per radial bin was calculated, which leads to a radial emission profile of the disc and the bright spot. Finally the flux of the radial profile was summed to obtain the full flux in a line.

To isolate the bright spot emission, the radial emission profile of the disc region was subtracted from the radial emission profile of the bright spot region. The innermost radii ($<300\,\mathrm{km\,s^{-1}}$) in SDSS J1208, SDSS J1525 and SDSS J0129 were excluded to avoid contamination from the central spike. In SDSS J1642 the flux was calculated starting from the center ($0\,\mathrm{km\,s^{-1}}$) because no central spike is visible in this system.

The obtained flux ratios were compared to a single slab LTE model with uniform temperature and density. This model is an approximation as temperature and density will change over the disc. Marsh et al. (1991) found overall good agreement between those models and the observations for GP Com. They also found a 25% discrepancy between the models and the observed strengths in the He I 5015 Å line. The same discrepancy is found in all four systems (see upper left panel in Fig. 3.12 without 25% correction and upper right panel in Fig. 3.12 with 25% correction). Therefore, in this analysis a 25% correction is applied to the He I 5015 Å line in all systems. Figure 3.12 shows that excluding the He I 5015 Å line leads to a degeneracy in the derived temperatures because the remaining flux ratios still allows a dual solution. The measured flux ratios with the He I 5015 Å line are needed to break this degeneracy even when including a 25% uncertainty on the He I 5015 Å line itself. Lines further to the blue are not usable as they are either affected by absorption from the accretor or by a very strong central spike. The single slab LTE model is described in full detail in Marsh et al. (1991). For the temperature estimation a fixed electron density ($n_\mathrm{e}=10^{14}\mathrm{cm^{-3}}$) and fixed path length ($l=10^9\mathrm{cm}$) is used, which are values similar to those found in GP Com by Marsh et al. (1991).

To estimate the temperature of the disc and bright spot, six different flux ratios of helium lines were used (7065/6678, 7065/5875, 7065/5015, 6678/5875, 6678/5015 and 5875/5015). The output of every Doppler tomogram is set by the targeted χ^2 value. This value has to be set manually and depends on the number of lines used and the quality of the data. A χ^2 value set too high smears out features, whereas a χ^2 value set too low leads to noise artefacts in the reconstructions. The optimal χ^2 is a compromise between goodness of fit and avoiding overfitting the data. This is a common feature of all maximum entropy reconstruction techniques as, such as e.g. also eclipse mapping (Horne, 1985). Setting the targeted χ^2 turned out to be the dominant uncertainty in our method using actual line fluxes to derive temperatures.

To estimate this uncertainty a simple Monte Carlo simulation was used. For SDSS J1208 a number of 150 spectra were randomly picked out of the full sample of 150 spectra, allowing for a spectrum to be picked more than once and also allowing for randomly distributed χ^2 values in the Doppler tomograms. The allowed range of the target χ^2 value is taken to be
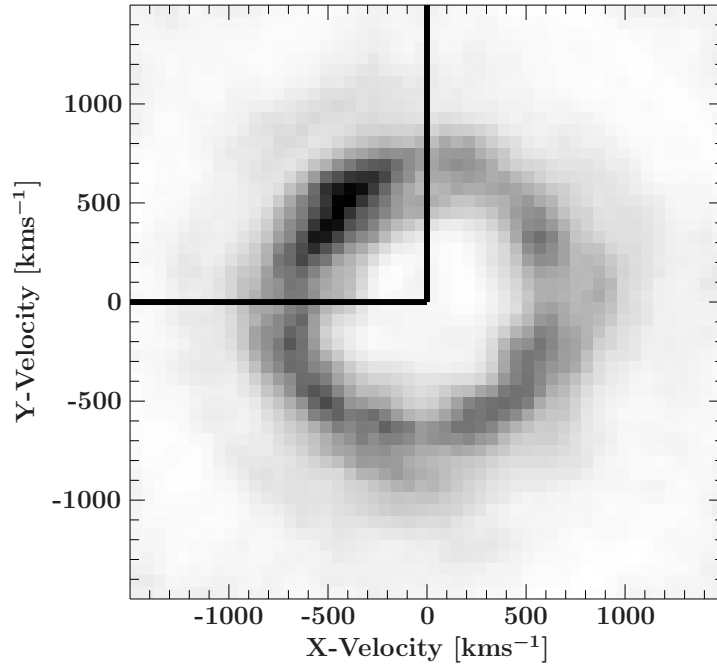
Figure 3.1: Doppler tomogram of the He I 7065 Å line from SDSS J0129 with two distinguished areas used for the temperature estimation. The upper left quarter was taken for the bright spot region, whereas the other three quarter were taken for the disc region.

between half the initial value and the estimated best value. Next, 1000 Doppler tomograms were computed, the flux extracted and the standard deviation of all extracted fluxes taken as the error on the fluxes. The same was done for SDSS J0129, SDSS J1642 and SDSS J1525 using 123, 84 and 70 spectra respectively.

The temperature was calculated taking a weighted mean of all intersection points (see Fig. 3.12). The weighting factor for each intersection point was calculated from the region where the calculated flux ratio from the model lies within the error bars of the measured flux ratio. The error on the temperature estimation was calculated as a weighted error, where the error on each flux ratio was taken as the weighting factor. The obtained error is only the statistical error on the temperatures. The change of the assumed column density leads to a systematic error and is described in Sec. 3.4.7.

3.4   Results

3.4.1   Average spectra

Helium lines in absorption and emission

The average spectrum of SDSS J1208 is shown in Fig. 3.2. The strong emission lines of neutral helium and He II 4685 Å are clearly visible. The spectrum looks very similar to the long-period system GP Com (Marsh, 1999). The emission lines show a double-peaked profile
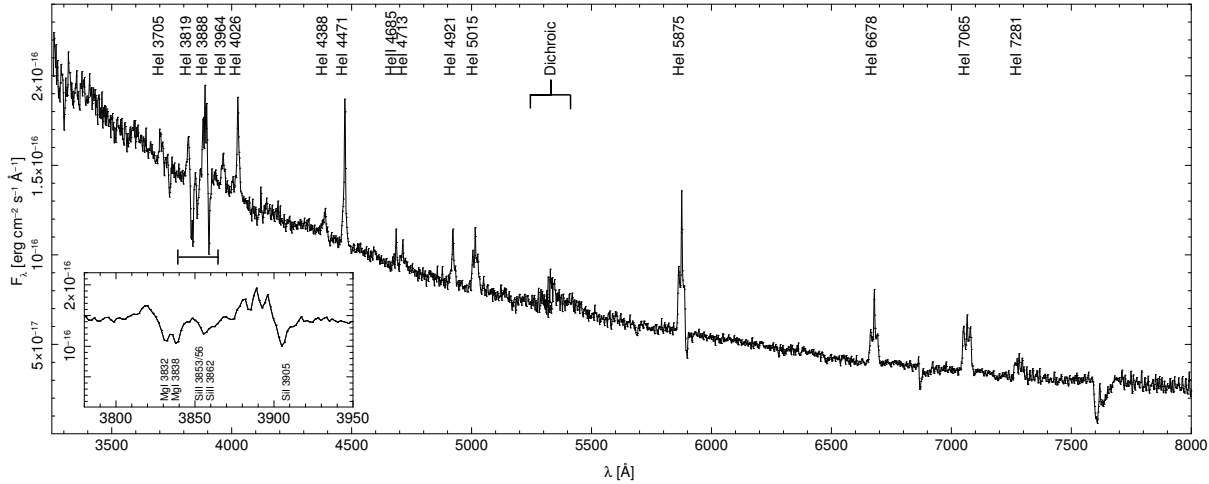
Figure 3.2: Average spectrum of SDSS J1208 obtained with the WHT. The strong absorption lines of Mg I and Si I/II are prominent

originating in the disc, as well as the well-known central-spike feature, which is only observed in AM CVn systems (Marsh, 1999; Morales-Rueda et al., 2003a) and the 65-min orbital period He-rich dwarf nova CSS100603:112253–111037 (Breedt et al., 2012). The He I 4471 Å line only shows emission from the central spike. The central-spike feature is known to move with the accreting white dwarf. Therefore, the strong central spike of SDSS J1208 was used to measure radial velocities of the accretor and is discussed in Sec. 3.4.3.

Figure. 3.3 shows the average spectra of SDSS J1525 and SDSS J0129. The spectra look very similar. The red part of the spectra is dominated by double peaked emission lines with a small central spike feature in He I 5875 Å and no discernible central spike in He I 6678 Å and 7065 Å. The blue helium lines are dominated by the Stark-broadened absorption lines from the WD accretor.

The average spectrum of SDSS J1642 (Fig. 3.3) is different from the previous systems, showing only strong emission lines and no sign of an underlying accretor. The double peaks of the individual helium lines are barely resolved and no central spike is seen in this spectrum.

Emission lines of metals

Emission lines of various metals including calcium, silicon, iron and nitrogen are observed in quiescent spectra of AM CVn systems (Ruiz et al., 2001; Morales-Rueda et al., 2003a; Roelofs et al., 2006a, 2007c, 2009). In particular SDSS J080449.49+161624.8 (hereafter SDSS J0804; Roelofs et al., 2009) shows a very rich emission line spectrum.

Marsh et al. (1991) predicted Si II emission at 6346 Å and 6371 Å and Fe II emission at 5169 Å to be the strongest metal lines in helium-dominated optically-thin accretion discs. In principle, the strength of these lines can be used to determine the initial metallicity since their abundance is not supposed to be affected by nuclear synthesis processes during binary evolution. SDSS J0129 shows emission of Fe II at 5169 Å and Si II at 6347 Å and 6371 Å whereas the similar system SDSS J1525 shows only weak emission of Si II at 6347 Å and 6371 Å.
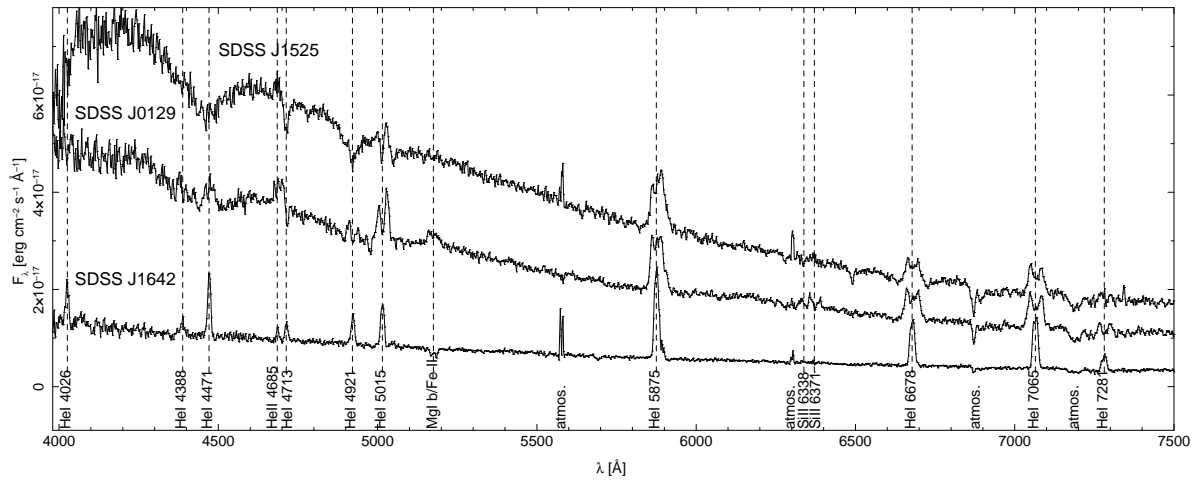
Figure 3.3: Average spectra of SDSS J1525 (top), SDSS J0129 (middle) and SDSS J1642 (bottom) obtained with the GTC. The strongest features are labelled. Each spectrum was flux calibrated but for clarity the flux of SDSS J1525 and SDSS J1642 was multiplied by 1.5 and 1.35 respectively. The flux of SDSS J1642 was divided by a factor of 2.5. Prominent lines are marked with dashed lines.
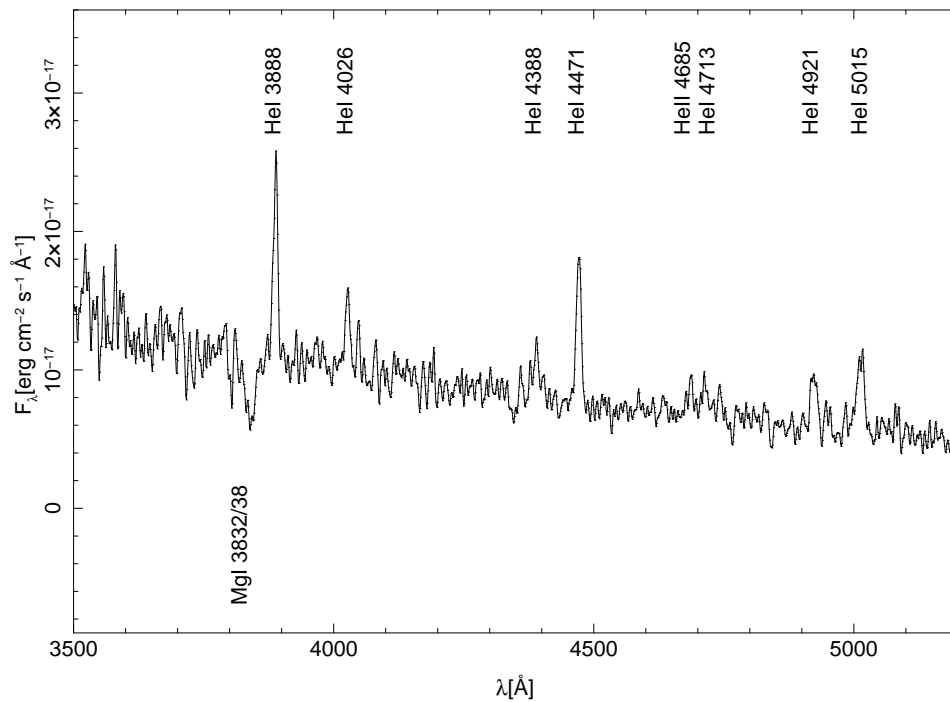

Figure 3.4: Gaussian smoothed spectrum of SDSS J1642 obtained with the Hale telescope. Beside the known helium emission lines also the strong Mg I absorption lines similar to SDSS J1208 are present.
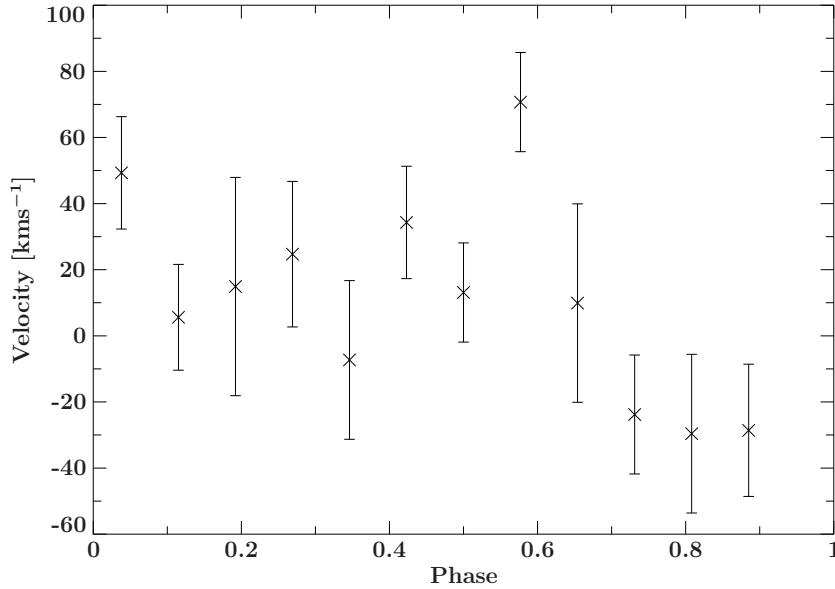
Figure 3.5: Velocity measurement at each phase using a multi-Gaussian fit to the Mg I lines 3832 Å and 3838 Å and the Si I line 3905 Å.

SDSS J1208 and SDSS J1642 show no metal lines in emission (see Tab. 3.2).

Absorption lines of metals

In contrast to metal lines in emission, metal lines in absorption are not common for quiescent spectra of long-period AM CVn systems. The only known long-period system in quiescence that shows metal lines in *absorption* is SDSS J155252.48+320150.9 (hereafter SDSS J1552; Roelofs et al., 2007c).

In the systems discussed here, SDSS J1208 displays strong absorption lines of Mg I 3832 Å and 3838 Å and Si I/II 3853 Å, 3856 Å, 3862 Å and 3905 Å (Fig. 3.2). A single exposure with the Hale telescope revealed the same signature in SDSS J1642: strong Mg I 3832 Å and 3838 Å absorption (Fig. 3.4). Both systems also show the Mg I*b* triplet (Fig. 3.2, 3.3). Roelofs et al. (2007c) found the Mg I absorption lines as well in the 56-min-period system SDSS J1552 but did not detect silicon absorption.

To check the origin of the metal absorption lines in SDSS J1208, the individual spectra were phase-binned into 13 bins, and multi-Gaussian fits to the Mg I 3832 Å and 3838 Å as well as Si I 3905 Å lines were calculated to measure their radial velocity. No periodic shifts are detected within the error bars (Fig. 3.5). In long period systems such as SDSS J1208 the mass ratio is extreme ($M_2/M_1=q \leq 0.01$) and the center of mass is close to the white dwarf. As no periodic velocity shift could be detected (Fig. 3.5), the origin of the metal lines can only be the accreting white dwarf or the disc. The latter one is unlikely because the absorption lines are expected to be broadened due to Keplerian velocities in the disc as seen in high state systems such as AM CVn itself (Roelofs et al., 2006b). Therefore, it is most likely that these lines originate in the accreting WD.

Table 3.2: Measured equivalent widths in (Å) and limits of disc emission and photospheric absorption lines.

Line	EW (Å) SDSS J1208	EW (Å) SDSS J0129	EW (Å) SDSS J1642	EW (Å) SDSS J1525
Disc emission				
He I 3888	–4.8 ± 0.2	...[a]	–7.2 ± 0.3	...[a]
He I 3964	–1.9 ± 0.2	...[a]	–0.3 ± 0.2	...[a]
He I 4026	–4.6 ± 0.3	...[a]	–4.2 ± 0.4	...[a]
He I 4388	–2.3 ± 0.3	4.1 ± 0.7[b,c]	–1.8 ± 0.3	25.4 ± 0.7[b,c]
He I 4471	–7.0 ± 0.2		–13.0 ± 0.5	
He II 4685	–1.0 ± 0.2	–3.5 ± 0.3	–1.5 ± 0.4	–0.8 ± 0.2
He I 4713	–1.2 ± 0.2	0.8 ± 0.3	–3.8 ± 0.4	1.9 ± 0.3
He I 4921	–4.0 ± 0.2	2.4 ± 0.6[b]	–7.8 ± 0.5	6.9 ± 0.5[b]
He I 5015	–7.1 ± 0.3	–7.9 ± 0.4	–13.2 ± 0.5	0.7 ± 0.3[b]
He I 5875	–19.8 ± 0,4	–24.4 ± 0.4	–56.8 ± 0.7	–16.0 ± 0.3
He I 6678	–15.8 ± 0.5	–18.8 ± 0.5	–39.4 ± 0.7	–6.7 ± 0.3
He I 7065	–24.0 ± 0.5	–25.4 ± 0.5	–54.7 ± 0.7	–11.8 ± 0.4
He I 7281	–7.9 ± 0.4	–2.8 ± 0.4	–14.7 ± 0.7	>–1.3
Fe II 5169	X	–2.4 ± 0.4	X	>–0.5
Si II 6347/6371	X	–3.1 ± 0.4	X	–0.6 ±0.2
Absorption lines				
Mg I 3832/3838	3.2 ± 0.2	...[a]	10.2 ± 1.7	...[a]
Ca II 3933[d]	<0.3	...[a]	<0.7	...[a]
Si II 3853/58/62	1.3 ± 0.2	...[a]	<0.7	...[a]
Si I 3905	1.6 ± 0.2	...[a]	<0.7	...[a]
Mg I b	1.2 ± 0.2	...[a]	4.0 ± 0.5	...[a]

Lines marked with an X indicate that this line is not detectable in the spectrum obtained

[a] Spectrum does not extend to this wavelength

[b] Equivalent width is combination between disc emission and absorption from accretor

[c] Combined equivalent width of He I 4388 and He I 4471

[d] Ca II 3968 was excluded because of an He I blend
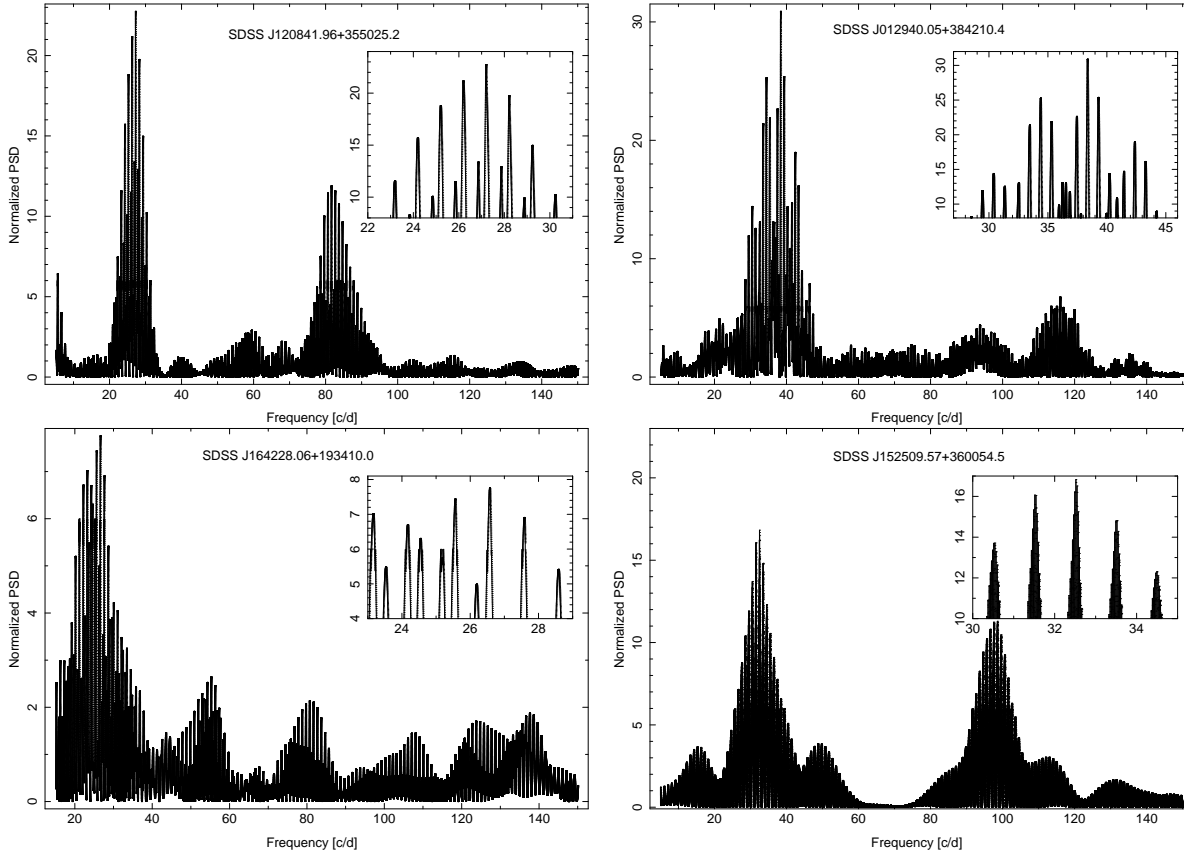
Figure 3.6: Lomb-Scargle periodograms of the red over violet wing flux ratio. The strongest peak was chosen to be the correct period. Top left: SDSS J1208, top right: SDSS J0129, lower left: SDSS J1642 and lower right: SDSS J1525

The presence and strengths of these absorption lines in AM CVns were compared to spectra of DBZ WDs. Absorption features of various metal species are known from DBZ WDs but always occur together with the Ca II H & K lines at 3933.66 Å and 3968.47 Å (e.g. Dufour et al., 2012). In order to set a detection limit in equivalent width for calcium, the calcium absorption lines are simulated with a Voigt profile including the resolution and SNR of the spectrum. For a recent work see Dufour et al. (2012). No sign of calcium in SDSS J1208 exceeding an equivalent width of 0.3 Å and in SDSS J1642 exceeding an equivalent width of 0.7 Å is detected. A summary of measured equivalent widths and detection limits is given in Tab 3.2.

3.4.2 Spectroscopic orbital periods

Using the method described in Sec. 3.3.1 orbital periods of 52.96±0.40 min for SDSS J1208, 37.555±0.003 min for SDSS J0129, 54.20±1.60 min for SDSS J1642 and 44.32±0.18 min for SDSS J1525 are found (see Tab. 3.3 and Fig. 3.6). The spectra for every system were folded onto the obtained period and phase-folded spectra and Doppler tomograms were computed. These are discussed in Section 3.4.4.

All systems, with the exception of SDSS J1642, show significant peaks in the periodogram
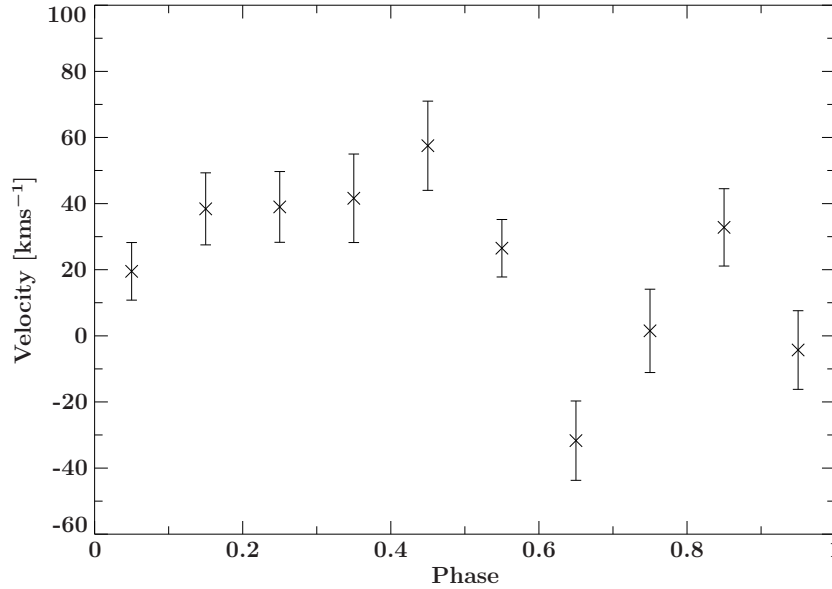
Figure 3.7: Velocity measurement of SDSS J1208 at each phase using a multi-Gaussian fit to the helium lines which show only central-spike emission (4026 Å, 4471 Å, 4921 Å, 4685 Å and 3819 Å).

with a high power spectral density (Fig. 3.6). SDSS J1642 shows a weaker bright spot leading to a less significant power spectral density. The highest peak in the periodogram was identified as the orbital period and is given in Table 3.3. A second peak with a slightly longer period shows a similar absolute power spectral density. This peak corresponds to a period of 56.35 min.

3.4.3 Radial velocities of the accretor in SDSS J1208

The central-spike feature is known to move with the accreting white dwarf and can therefore be used to measure the radial velocity curve and the real phase of the accreting white dwarf. This information in combination with the phase of the bright spot helps to establish the mass ratio of the system (Roelofs et al., 2006b; Morales-Rueda et al., 2003a; Marsh, 1999).

SDSS J1525, SDSS J0129 and SDSS J1642 show only weak or no central spikes and cannot be used to measure radial velocities of the accretor. SDSS J1208 on the other hand shows a very strong central spike with some lines strongly dominated by the central spike (e.g. He I 4471 Å, Fig. 3.8). For this line, the individual spectra were phase-binned into 10 bins and a Gaussian fit was calculated to measure the radial velocity. No periodic variations of the central spike within the error bars (Fig. 3.7) is detected, which is expected as the velocity amplitude is supposed to be $K \leq 10\,\mathrm{km\,s^{-1}}$.

3.4.4 Phase folded spectra and Doppler tomograms

A bright spot, an accretion disc and sometimes a central spike feature are visible in the phase folded spectra and Doppler tomogram of an AM CVn system. The bright spot corresponds to
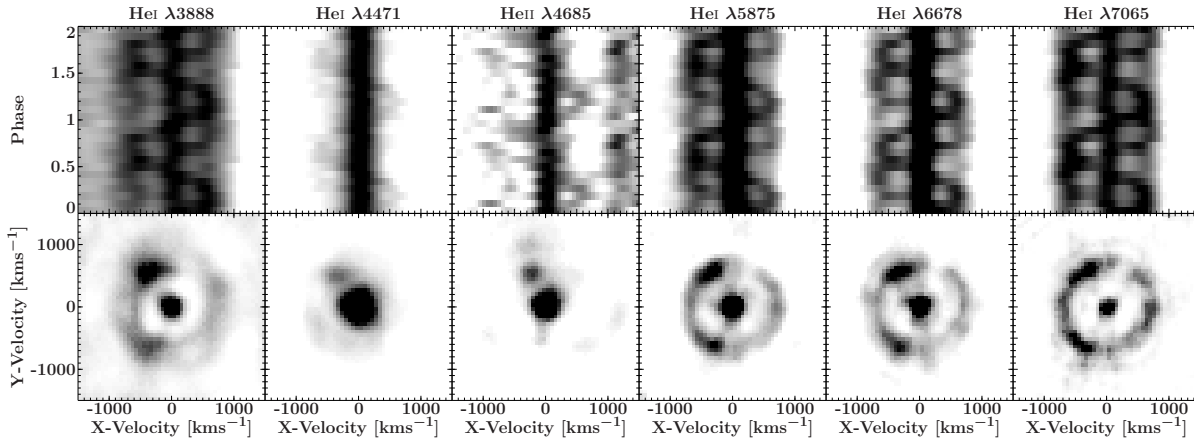
Figure 3.8: Trailed spectra (top row) and maximum-entropy Doppler tomograms (bottom row) of selected He I and He II lines of SDSS J1208. Visible is the disc, the central spike as well as both bright spots in some lines. Note that the central spike was saturated to emphasize both bright spots.
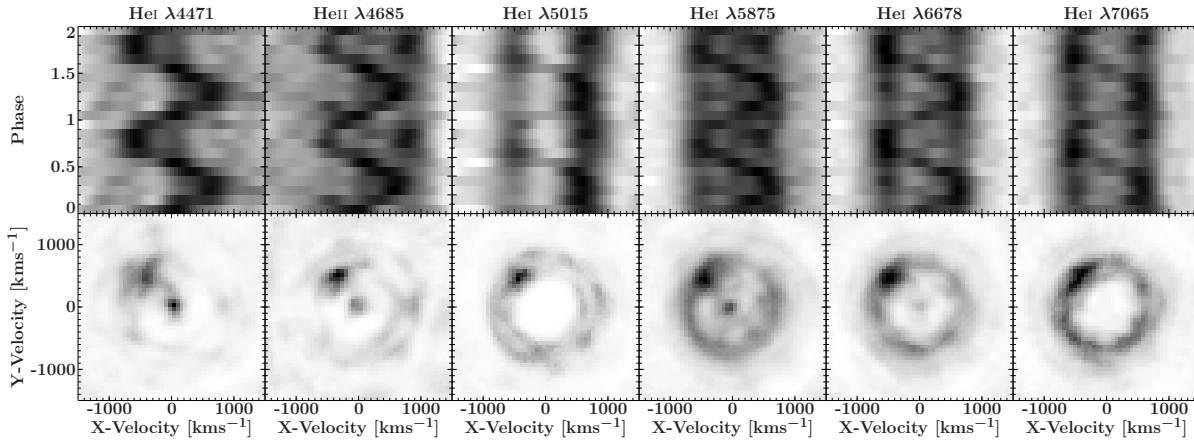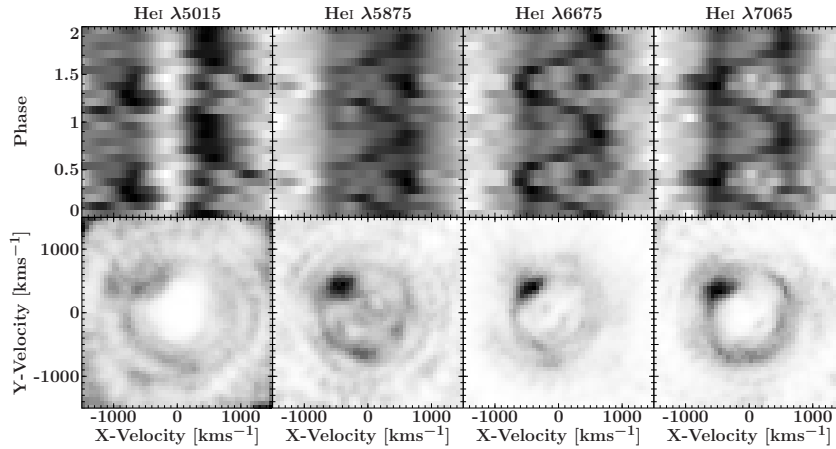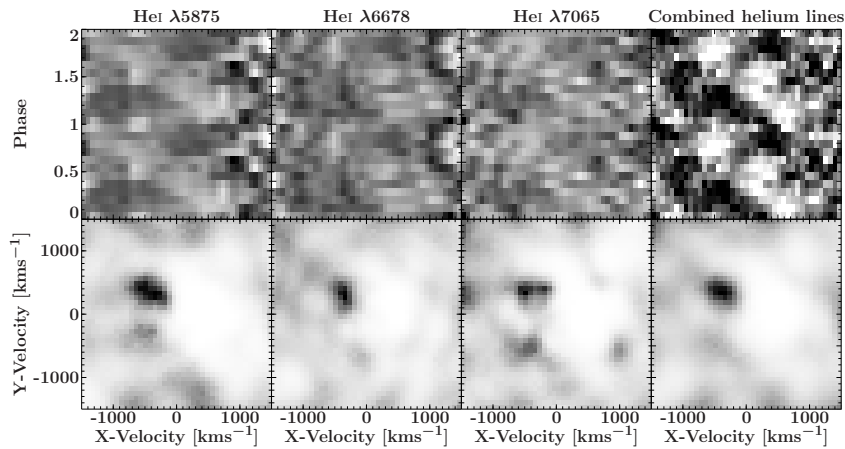

Figure 3.9: Trailed spectra (top row) and maximum-entropy Doppler tomograms (bottom row) of selected He I and He II lines of SDSS J0129. Visible is the disc, the bright spot and in some lines the central spike

the impact point where the accretion stream hits the disc. In this work the zero phase for the trailed spectra and the Doppler tomograms was set such that the bright spot is located in the upper left quarter of the Doppler tomogram and as such is arbitrary and not constrained by geometry such as could be the case in an eclipsing system.

Apart from the prominent central spike, SDSS J1208 also shows a second bright spot in most lines, best seen in He I 7065 Å (Fig 3.8). The second bright spot is discussed in more detail in Sec. 3.4.4.

SDSS J0129 and SDSS J1525 show the bright spot and disc emission in all lines not contaminated by white dwarf absorption. Only some helium lines (4471 Å, 4685 Å, 5875 Å and 6678 Å) in SDSS J0129 show the central spike, whereas there is no indication for a central spike in SDSS J1525. SDSS J0129 and SDSS J1525 also show no indication for a second bright spot (Fig 3.9, 3.10).

Figure 3.10: Trailed spectra (top row) and maximum-entropy Doppler tomograms (bottom row) of selected He I and He II lines of SDSS J1525. Visible is the disc and the bright spot.

Figure 3.11: Trailed spectra (top row) and maximum-entropy Doppler tomograms (bottom row) of selected and combined helium lines (4471 Å, 4713 Å, 4921 Å, 5015 Å, 5875 Å, 6678 Å, 7065 Å, 7281 Å) of SDSS 1642 . The average line profile has been divided out to enhance the visibility of the S-wave. Therefore, only the bright spot is visible.

SDSS J1642 is different to the previous systems. It shows strong, narrow disc emission lines (Fig. 3.11). To make the bright spot visible, each individual spectrum was divided by the grand average spectrum. Individual lines do not show the bright spot very clearly. Only a combination of all strong helium lines (4471 Å, 4713 Å, 4921 Å, 5015 Å, 5875 Å, 6678 Å, 7065 Å, 7281 Å) reveals a clear S-wave with a fairly low amplitude ($\sim$400 km s^{-1}). The strength of the S-wave is phase dependent (see Fig. 3.11). This is also seen in AM CVn itself (Nelemans et al., 2001b; Roelofs et al., 2006b) and in SDSS J0804 (Roelofs et al., 2009).

Second bright spot in SDSS J1208

A double bright-spot feature is detected in the data of SDSS J1208 as has previously been found in e.g. SDSS J1240 (Roelofs et al., 2005), GP Com and V396 Hya (Kupfer et al. sub-

Table 3.3: Overview of measured system parameters of SDSS J1208, SDSS J0129, SDSS J1642 and SDSS J1525

Object	Period (min)	T_{disc} [K]	$T_{bright\,spot}$ [K]
SDSS J1208	52.96 ± 0.40	$10\,800 \pm 400$	-
SDSS J0129	37.555 ± 0.003	$10\,600 \pm 200$	$27\,800 \pm 900$
SDSS J1642	54.20 ± 1.60	$10\,200 \pm 300$	-
SDSS	44.32 ± 0.18	-	-

mitted). These systems show the second bright spot feature at the same velocity as the first spot and, remarkably, all systems show a similar phase shift between the spots of about $120°$.

For SDSS J1208, a phase-shift between the peaks of the spots of $125° \pm 23°$ was found using the method described in Sec. 3.3.2. This result is consistent with the finding in (Roelofs et al., 2005) for SDSS J1240. All three lines show that the integrated flux of the second bright spot has a similar intensity as the first bright spot.

3.4.5   Mass ratio of SDSS J0129

A superhump period of 37.9 ± 0.2 min for SDSS J0129 was found by Shears et al. (2011) during outburst. In combination with the orbital period identified here, this leads to a period excess ($\frac{P_{sh} - P_{orb}}{P_{orb}}$) of $\epsilon = 0.0092 \pm 0.0054$. The error for the excess was estimated from the accuracy on the periods and is dominated by the error on the superhump period. Patterson et al. (2005) found an empirical relation ($\epsilon = 0.18q + 0.29q^2$) between the period excess and the mass ratio for a large number of hydrogen rich dwarf novae. Here, a mass ratio for SDSS J0129 of $q = 0.031 \pm 0.018$ using this relation is obtained.

3.4.6   Disc and bright spot temperature

To determine temperatures in the disc and bright spot the technique outlined in Sec. 3.3.2 was applied. For the disc emission, good agreement between models and observations within the error bars were found for SDSS J1208, SDSS J1642 and SDSS J0129 (see Fig. 3.12). All three systems show similar temperatures in the disc: $T_{disc} = 10\,800 \pm 400$ K for SDSS J1208, $T_{disc} = 10\,200 \pm 300$ K for SDSS J1642 and $T_{disc} = 10\,600 \pm 200$ K for SDSS J0129 (see Tab. 3.3). The spectrum of SDSS J1525 shows a strong contribution from the accreting white dwarf in all lines bluewards of He I 5015 Å (Fig. 3.3). Therefore, He I 5015 Å was excluded for the temperature estimate. SDSS J1525 is the only system that has no intersection for the flux ratio 6678/5875 in the disc region (see lower left panel in Fig. 3.12) possibly due to contamination in the spectrum from the WD.

In contrast to the disc region, only poor agreement between models and observation was found for the bright spot region. Only SDSS J0129 shows good agreement between all flux ratios and the LTE model (see Fig. 3.13): $T_{bright\,spot} = 27\,800 \pm 900$ K. SDSS J1208 has only two intersection points with the models (6678/5015 and 5875/5015) which lie between 35 000
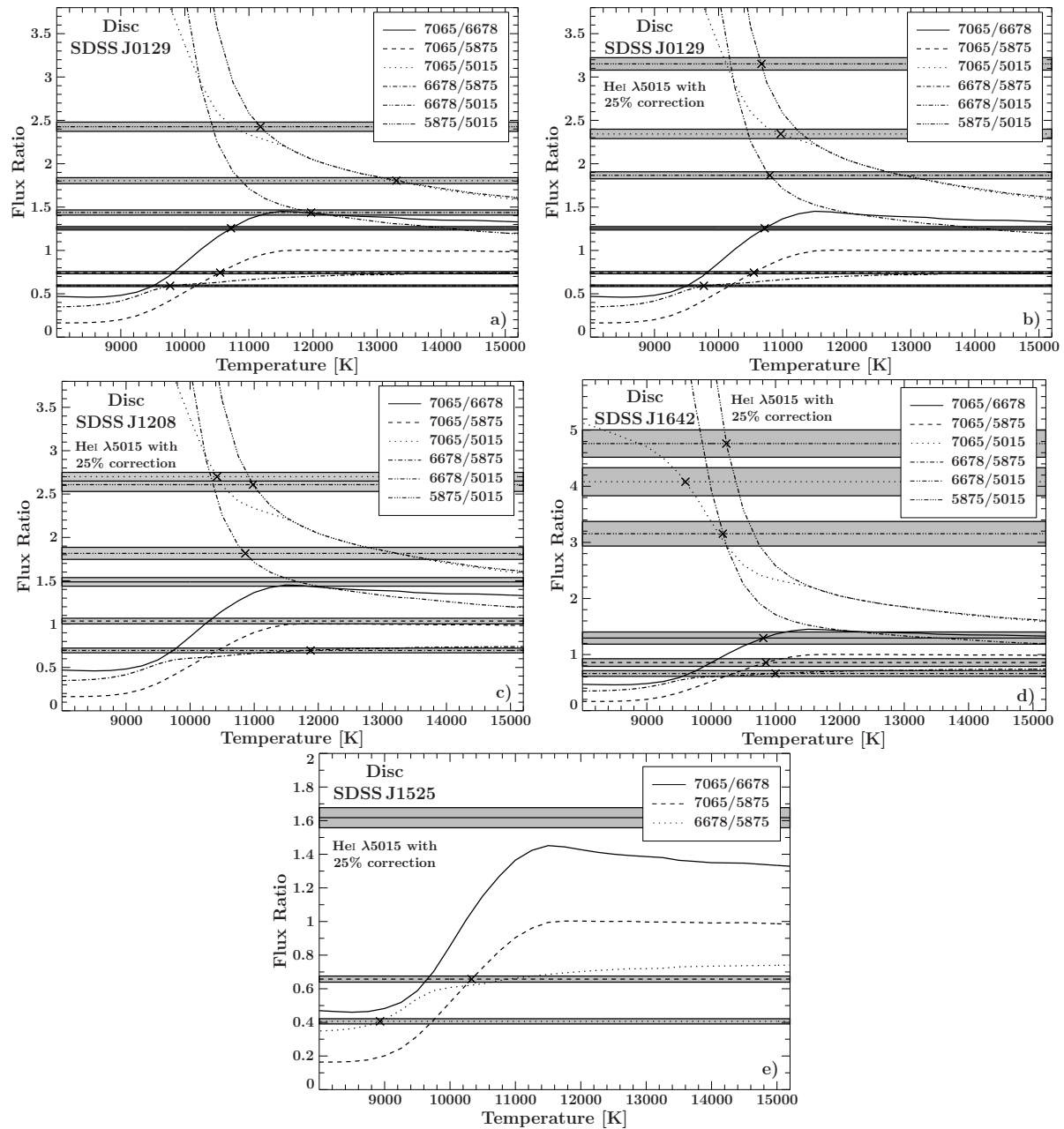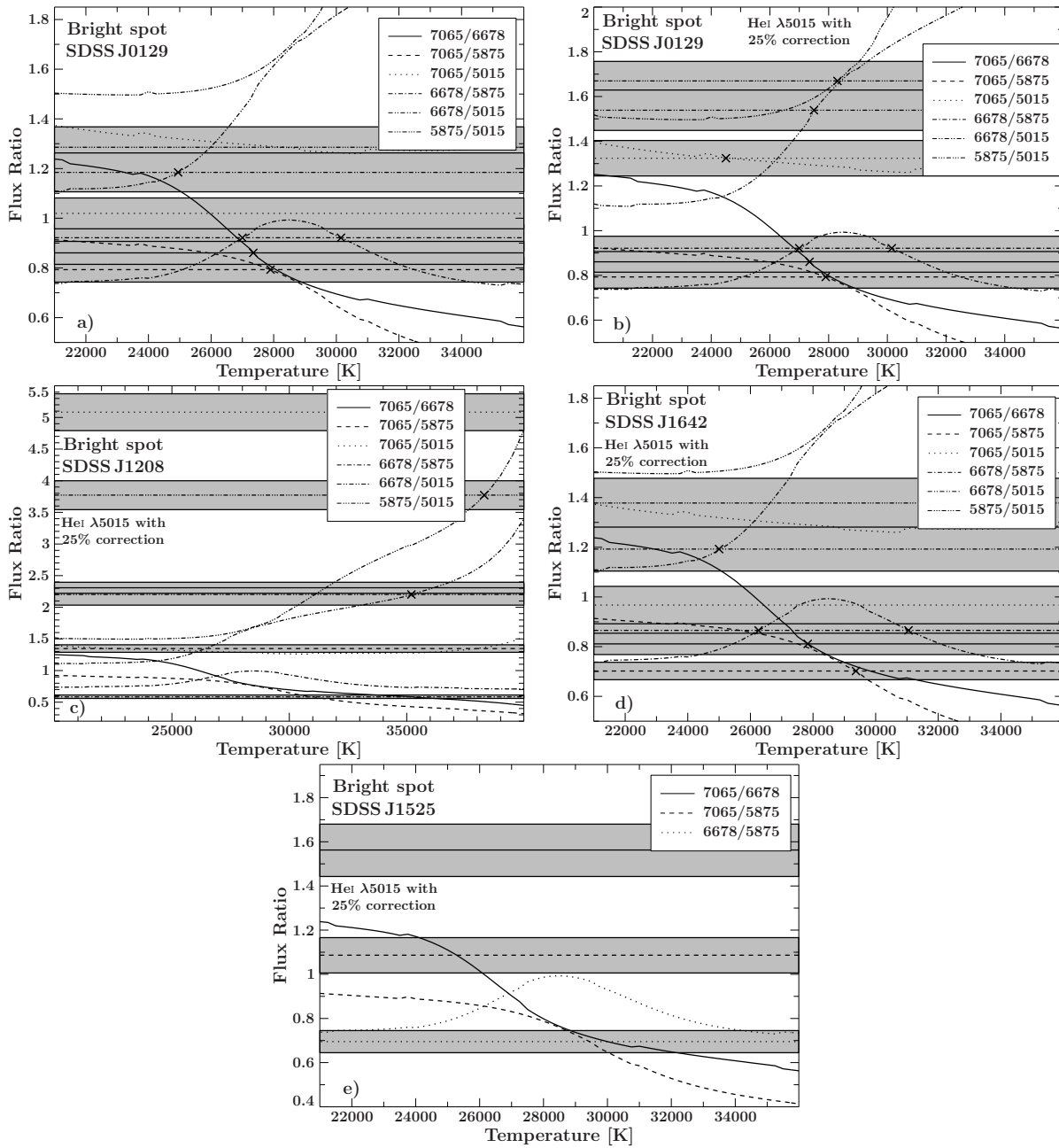
Figure 3.12: Comparison between observed disc emission (horizontal lines) and calculated flux ratios for a LTE slab model with a fixed path length of $l=10^9$cm and density of 10^{14}cm^{-1} for different helium lines of the bright spot emission region (curved lines). The horizontal lines correspond to the measured flux ratios with the error on the flux ratios shaded in grey around the horizontal line. The intersection points (x) for each line are indicated. Marsh et al. (1991) found a disagreement of 25% between observation and model for the He I 5015 Å line. In the upper right hand panel this correction was applied to the flux ratios for SDSS J0129. In the upper left hand panel the original flux ratios for SDSS J0129 are shown. A better agreement compared to other lines including the correction was found. The other three panels show the flux ratios, models with intersection for the other three systems (c) SDSS J1208 with corrected He I 5015 Å line, d) SDSS J1642 with corrected He I 5015 Å line, e) SDSS J1525 with corrected He I 5015 Å line).
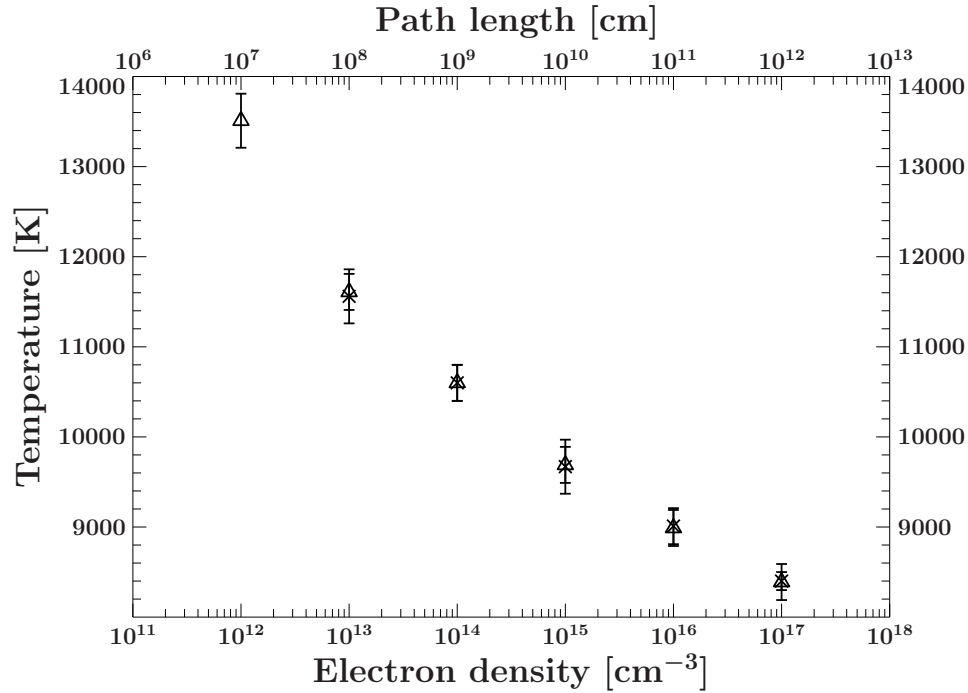
Figure 3.13: Comparison between observed bright spot emission (horizontal lines) and calculated flux ratios for a LTE slab model with a fixed path length of $l=10^9$cm and density of 10^{14}cm^{-1} for different helium lines of the bright spot emission region (curved lines). The horizontal lines correspond to the measured flux ratios with the error on the flux ratios shaded in grey around the horizontal line. The intersection points (x) for each line are indicated. Marsh et al. (1991) found a disagreement of 25% between observation and model for the He I 5015 Å line. In the upper right hand panel this correction was applied to the flux ratios for SDSS J0129. In the upper left hand panel the original flux ratios for SDSS J0129 are shown. A better agreement compared to other lines including the correction was found. The other three panels show the flux ratios, models with intersection for the other three systems (c) SDSS J1208 with corrected He I 5015 Å line, d) SDSS J1642 with corrected He I 5015 Å line, e) SDSS J1525 with corrected He I 5015 Å line).

Figure 3.14: Disc temperature estimation for SDSS J0129 with different assumptions for electron density and path length in the models. The X display the estimated temperatures with varied electron density and fixed path length (l=10^9cm). The triangles show the estimated temperatures with varied path length and fixed electron density (n_e=10^{14}cm^{-3}).

and 40 000 K (see middle left panel in Fig. 3.13). Therefore, no useful temperature estimation can be done. SDSS J1525 shows no intersection between models and observations at all. The flux ratios 7065/5015 and 5875/5015 from SDSS J1642 show discrepancy with the models. In particular, the first mentioned ratio shows a large discrepancy to the models (see middle right panel in Fig. 3.13).

3.4.7   Column density variations

To estimate systematic uncertainties on the temperatures with respect to electron density and the path length variations, two approaches were taken for SDSS J0129.

First, the temperatures were estimated by using models with a fixed path length at l=10^9cm and a variable electron density from n_e=10^{12}cm^{-3} to n_e=10^{17}cm^{-3}. All show good agreement between models and observations except for the model with n_e=10^{12}cm^{-3}.

Second, the temperature was estimated by using models with a fixed electron density n_e=10^{14}cm^{-3} and a varied path length from l=10^7cm to l=10^{12}cm. A decreasing temperature with increasing path length or electron density is found (Fig.3.14).

In both cases the column density, $n_\mathrm{e}l$, goes up, which increases the excitation of the helium lines as explained in Marsh et al. (1991). Helium lines further in the red have lower excitation energies than the helium lines in the blue. With increasing column density, the lines with lower excitation energy become stronger compared to the lines with higher excitation energies. To

compensate for this, a lower temperature for a higher column density and a higher temperature for a lower column density is needed which can be seen in Fig. 3.14. This figure shows also that changing either the path length or the electron density leads to the same change in the estimated temperatures within the errorbars. But overall the temperature obtained is not very sensitive to a change in the path length or the electron density. A change in path length or electron density with a factor of 10 000 only leads to temperature change of $\sim$3000 K.

3.5   Conclusion & Discussion

3.5.1   Metal absorption lines and spectral features

All three known systems with periods between 50 and 60 min (SDSS J1208, SDSS J1642 and SDSS J1552) display Mg absorption, whereas there is no evidence of this in the 65 min period system V396 Hya (Ruiz et al., 2001) and 46 min period system GP Com (Marsh, 1999). Metal absorption lines are well known from single white dwarf spectra but for the temperature range where Mg I is visible, also the Ca II H & K lines should be present. There is no evidence for calcium in either SDSS J1208 or SDSS J1642.

Since the composition of the accretion disc and/or the upper layer of the primary white dwarf reflects the transferred material of the secondary, any abundance anomaly will reflect the current composition and/or the nucleosynthetic history of the secondary. This means that either magnesium was enhanced and/or calcium was depleted during the evolution of the system. Another possible explanation could be element selection, such as peeling off a sedimented secondary. Three different scenarios can account for the abundance anomaly:

1) If the secondary is a degenerate white dwarf, element sedimentation took place, such that heavy elements sunk down to the center of the white dwarf. An explanation for the strong magnesium lines and the lack of calcium could be that the accreted magnesium-rich material comes from a sedimented magnesium-rich layer of the secondary. Problematic for this picture is that e.g. SDSS J1208 also shows silicon which has a higher mass than magnesium and should have sunk down closer to the center of the WD than magnesium. An added complication is that it is also not clear if the secondary is fully convective at this stage of the evolution.

2) Element selection due to selective winds from the white dwarf could separate different elements. Selective winds driven by radiation pressure are found in early B-stars and blow away metals which have large cross sections (Hempel & Holweger, 2003). However, no strong winds in the temperature range are expected for accreting white dwarfs in AM CVn systems.

3) A third possible explanation could be differential gravitational settling of various elements. Different elements have different diffusion time scales. Depending on diffusion time scales compared to the mass accretion rate, abundances of heavy elements could increase at high accretion rates or decrease at low accretion rates compared to the diffusion timescales (Koester, 2009). Bildsten et al. (2006) pointed out that for systems with periods above 40 min the nitrogen abundance will decrease in the atmosphere of the accretor because settling is faster than accretion. Therefore, systems with periods between 50-60 min which already have low accretion rates ($\sim$10^{-12}M$_\odot$yr^{-1}) could be in the stage where settling is faster than accretion

in the case of calcium, whereas for magnesium settling is slower than accretion. This would lead to a depletion of calcium and to an enhancement of magnesium in the atmosphere of the accreting WD. However, Koester (2009) showed that the diffusion time scales for calcium are only slightly shorter than for magnesium.

In a comparison, good agreement is found for three of the four systems between the measured orbital period and expected spectral features based on other systems with a similar period. The only system which shows a discrepancy between measured orbital period and expected spectral features is SDSS J1525, which has a spectrum similar to SDSS J0129 but a longer orbital period. One reason could be either a high mass accretor and/or a hot donor star because a high mass accretor is heated to a higher temperature due to compressional heating (Bildsten et al., 2006).

3.5.2   Mass ratio of SDSS J0129

Patterson et al. (2005) calibrated the relation between period excess and mass ratio ($\epsilon = 0.18q + 0.29q^2$) on a series of measurements of eclipsing Cataclysmic variables, where only KV UMa has a low ratio $q \leq 0.05$. For the extreme mass ratio regime this relation is uncertain.

In AM CVn systems, Roelofs et al. (2006b) found a large discrepancy for the mass ratio in AM CVn itself using either the empirical relation from Patterson et al. (2005) (q=0.10) or obtaining the mass ratio from the projected velocity amplitude and the phase of the accreting white dwarf ($q \geq 0.18$). Copperwheat et al. (2011) found agreement within the uncertainties in the eclipsing AM CVn system SDSS J092638.71+362402.4 between the mass ratio obtained from the phase of the white dwarf eclipse and the mass ratio obtained from the relation from Patterson et al. (2005). At this stage too few mass ratios are known to confirm or reject this relation for AM CVn systems.

3.5.3   Disc and bright spot temperatures

The single-slab LTE models with uniform density and temperature are a clear simplification of the real environment in an accretion disc. Nevertheless, the good agreement between models and observations for three out of four systems shows that the flux in the helium disc lines are well fitted with the simplified models. This leads to the assumption that the line emission possibly occurs in a small, nearly isothermal, region in the upper layers of the disc. Under the assumption of a fixed path length of $l=10^9$cm and an electron density of 10^{14}cm^{-1}, similar temperatures as Marsh et al. (1991) in GP Com are found. For the disc temperatures between 15 000 K and 25 000 K the flux ratio of the helium lines used here is rather insensitive to temperature variations. Therefore, this method can not be used for discs with temperatures within this range. Contrary to the disc region, the flux ratios from the bright spot region show good agreement between models and observations in only one system. This shows that the LTE assumption with uniform density and temperature is not completely valid in the bright spot region.

CHAPTER 4

PHASE RESOLVED SPECTROSCOPY AND *Kepler* PHOTOMETRY OF THE ULTRACOMPACT AM CVN BINARY SDSS J190817.07+394036.4

T. Kupfer, P. J. Groot, S. Bloemen, D. Levitan, D. Steeghs, T. R. Marsh, R. G. M. Rutten, G. Nelemans, T. A. Prince, F. Fürst and S. Geier

Abstract. *Kepler* satellite photometry and phase-resolved spectroscopy of the ultracompact AM CVn type binary SDSS J190817.07+394036.4 are presented. The average spectra reveal a variety of weak metal lines of different species, including silicon, sulphur and magnesium as well as many lines of nitrogen, beside the strong absorption lines of neutral helium. The phase-folded spectra and the Doppler tomograms reveal an S-wave in emission in the core of the He I 4471 Å absorption line at a period of $P_{\mathrm{orb}} = 1085.7 \pm 2.8$ sec identifying this as the orbital period of the system. The Si II, Mg II and the core of some He I lines show an S-wave in absorption with a phase offset of $170 \pm 15°$ compared to the S-wave in emission. The N II, Si III and some helium lines do not show any phase variability at all. The spectroscopic orbital period is in excellent agreement with a period at $P_{\mathrm{orb}} = 1085.108(9)$ sec detected in the three year *Kepler* lightcurve.

A Fourier analysis of the Q6 to Q17 short cadence data obtained by *Kepler* revealed a large number of frequencies above the noise level where the majority shows a large variability in frequency and amplitude. In an O-C analysis we measured a $|\dot{P}| \sim 1.0 \times 10^{-8}\,\mathrm{s\,s^{-1}}$ for some of the strongest variations and set a limit for the orbital period to be $|\dot{P}| < 10^{-10}\mathrm{s\,s^{-1}}$. The shape of the phase folded lightcurve on the orbital period indicates the motion of the bright spot. Models of the system were constructed to see whether the phases of the radial velocity

curves and the lightcurve variation can be combined to a coherent picture. However, from the measured phases neither the absorption nor the emission can be explained to originate in the bright spot.

4.1   Introduction

AM CVn systems are a small group of mass transferring ultracompact binaries with orbital periods between 5.4 and 65 minutes. AM CVn systems consist of a white dwarf (WD) primary and a WD or semi-degenerate helium star secondary (Nelemans et al., 2001a, see Solheim (2010) for a recent review). They are important as strong, low-frequency, Galactic gravitational wave sources (e.g. Nelemans et al., 2004; Roelofs et al., 2007d; Nissanke et al., 2012), the source population of the proposed â.Iaâ supernovae (Bildsten et al., 2007), and as probes of the final stages of binary evolution. Spectroscopically these systems are characterized by a deficiency of hydrogen, indicating an advanced stage of binary evolution. In the preceding binary evolution two common envelope phases or a stable Roche Lobe overflow + one common envelope formed a detached WD binary system at a period of ~hours. Gravitational wave radiation decreased the orbital separation until the low-mass secondary filled its Roche lobe and mass transfer set in at an orbital period between $3 - 10$ minutes. Some fraction of these systems survived the ensuing direct impact phase to become AM CVn systems (Nelemans et al., 2001a; Marsh et al., 2004) depending on their mass ratio and the efficiency of the angular momentum feedback. An accretion disc forms at an orbital period of ~10 min and the mass transfer stream hits the disc at the so-called bright spot. The mass-transfer-rate drops as the orbit widens and the system ends up as a more massive WD with an extremely low-mass WD (~ 0.01 M$_\odot$) at orbital periods of 40–60 min.

The number of known longer period systems ($P_{\rm orb} > 20$ min) has seen a surge in recent years due to large scale synoptic surveys such as SDSS (e.g. Anderson et al., 2005, 2008; Roelofs et al., 2005, 2009; Carter et al., 2014a), PTF (Levitan et al., 2011, 2013, 2014), and most recently Gaia (Campbell et al. in prep.). The number of known systems at the short orbital period end ($P_{\rm orb} < 20$ min) is limited to five. The most recently discovered, supposedly short period system, is SDSS J190817.07+394036.4 (hereafter SDSS J1908).

SDSS J1908 was observed in the Sloan Digital Sky Survey (SDSS) as a relatively bright ($g = 16.08$ mag) blue object. The system was labeled as a possible compact pulsator and included by the Kepler Astroseismic Science Consortium (KASC) for the survey phase at short cadence in the Kepler Space observatory (Gilliland et al., 2010; Østensen et al., 2011). A first detailed study of the object based on short cadence *Kepler* data obtained during quarter 3.3 is presented in Fontaine et al. (2011), hereafter F11, where it was concluded that SDSS J1908 is a high state AM CVn system, similar to the prototype system AM CVn itself (see e.g. Roelofs et al., 2006b). From the spectroscopic analysis F11 found that the system is seen at an inclination angle between $10°$ and $20°$. The estimated mass transfer rate lies in the range $3.5 - 8.5 \times 10^{-9}$M$_\odot$ yr^{-1} and the distance to the system is in the range $250 - 330$ pc. The luminosity variations detected by *Kepler* are dominated by a signal at a period of 938.507 s, along with its first harmonic. In addition, a second modulation with a period of 953.262 s is seen.

Table 4.1: Summary of the observations of SDSS J1908

Telescope/Date	N_{exp}	Exp. time (s)
Kepler satellite		
2010/06/24 – 2013/05/11	1.3 M	60
WHT+ISIS (R1200B/R1200R)		
2011/07/03 – 2011/07/07	1875	60
GTC+OSIRIS (R2000B)		
2011/09/15 – 2011/09/17	369	60
Keck+ESI (Echellette mode)		
2012/07/12	203	60
Keck+ESI (Echellette mode)		
2014/06/01	4	900

The lightcurve, folded on the 938.507 s period, shows a shape which is very similar to the superhump waveform found in AM CVn. In this picture the 953.262 s modulation corresponds to the orbital period, whereas the 938.507 s modulation is the superhump period.

In AM CVn itself Skillman et al. (1999) were able to explain all photometric periods in terms of only 3 basic periods that correspond to the orbital period and two additional periods, most likely due to disc precession. F11 detected 11 periods in the *Kepler* lightcurve of SDSS J1908, and could also explain all 11 periods in terms of only 3 basic periods. However, in that picture the 938.507 s modulation corresponds to the orbital period, in contradiction to finding that the waveform at that period looks similar to the superhump waveform in AM CVn. Hence, the orbital period of SDSS J1908 remains ambiguous.

A spectroscopic identification of coherent radial velocity changes is generally accepted as the most direct way of establishing the orbital period of the system. This formed the broad motivation for the present study. Additionally, the *Kepler* satellite kept SDSS J1908 as a short cadence target over the quarters Q6 to Q17, a total of 3 years: an unprecedented data set for any ultracompact binary.

4.2 Observations and Data reduction

4.2.1 Photometry

We used the Q6 to Q17 short cadence data obtained by *Kepler* with a time resolution of 58.9 sec. The original pixel data were downloaded from the Kepler Data Archive[1], resulting in 1.3 million images in the *Kepler*-band. There is a star only 5 arcsec away which contaminates the extracted flux of SDSS J1908 in the standard-pipeline. F11 identified this star as a G-star. We used point spread function (PSF) fitting as implemented in the PyKE tools provided by the NASA Kepler Guest Observer Office (Still & Barclay, 2012) to separate the lightcurves

---

[1]http://archive.stsci.edu/kepler/

of SDSS J1908 and the G-star. To correct for a linear trend caused by the instrument the lightcurve was normalised with a first order polynomial fit.

4.2.2   Spectroscopy

We obtained phase-resolved spectroscopy of SDSS J1908 over five nights on 3 – 7 July 2011 using the William Herschel telescope (WHT) and the ISIS spectrograph (Carter et al., 1993). The full data set consists of 1875 spectra taken with the R1200B grating for the blue arm and the R1200R grating in the red arm covering a wavelength range of 4300 - 5070 Å and 5580 - 6244 Å respectively. All observations were done with a 1 arcsec slit and 2×1 binning with the binning of 2 in the spatial direction. This resulted in a full-width half-maximum (FWHM) resolution of 0.92 Å for the R1200B grating and 1.04 Å for the R1200R grating. Each night an average bias frame out of 20 individual bias frames was made and a normalised flatfield frame was constructed out of 20 individual lamp flatfields. CuNeAr arc exposures were taken every hour to correct for instrumental flexure. Each exposure was wavelength calibrated by interpolating between the two closest calibration exposures. A total of 36 lines could be well fitted in each arc exposure using a Legendre function of order 4 resulting in 0.015 Å root-mean-square residuals. The best obtained signal-to-noise ratio (SNR) per spectrum was 4, whereas during July 5 we suffered from poor weather conditions and obtained only a SNR=1 per spectrum. This leads to a SNR of ∼70 in the grand average spectrum. BD+28 4211 (Oke, 1990) was used as a spectrophotometric standard to flux calibrate the spectra and correct them for the instrumental response.

SDSS J1908 was observed over three nights on 15, 16 and 17 September 2011 using the GTC and the OSIRIS spectrograph (Cepa, 1998). All observations were done with an 0.8 arcsec slit and the R2000B grating which covers a wavelength range of 3955 – 5690 Å. Every exposure was binned 2×2 on chip. This set-up results in a full-width half-maximum (FWHM) resolution of 2.65 Å. We obtained, each night, 20 bias frames to construct an average bias frame and 10 individual tungsten lamp flatfields to construct a normalised flatfield. A XeNe lamp spectrum was obtained at the beginning of the run as a master arc. About 15 lines were fitted using a Legendre function of order 5, resulting in an 0.07 Å root-mean-square residual. To save observing time, during the night about every 1.5 hr an Hg lamp spectrum was taken. This lamp has only three lines in the covered range but is good enough to account for small shifts of the spectra during the nights. Additionally, the wavelength calibration for each individual spectrum was refined using sky lines. The average SNR of the individual spectra was around 30 (for a 60 s exposure), resulting in a grand average spectrum with a SNR >200. To correct for the instrumental response L1363–3 (Oke, 1974) was used as a spectrophotometric standard. MOLLY[2] and IRAF[3] routines were used to reduce the data obtained with the WHT as well as the GTC.

---

[2]MOLLY was written by TRM and is available at http://www.warwick.ac.uk/go/trmarsh/software/

[3]IRAF is distributed by the National Optical Astronomy Observatories, which are operated by the Association of Universities for Research in Astronomy, Inc., under cooperative agreement with the National Science Foundation

To obtain both high resolution and high SNR spectra, SDSS J1908 was also observed over one night on 12 July 2012 using Keck and the ESI spectrograph in Echellette mode ($R = \frac{\lambda}{\Delta\lambda} = 8000$). The full dataset consists of 203 spectra. All observations were done with a 1.0 arcsec slit. An average flatfield frame was made out of 100 individual flatfield frames. CuAr arc exposures were taken every hour to correct for instrumental flexure. Each exposure was wavelength calibrated by interpolating between the two closest calibration exposures. MAKEE[4] was used to reduce the data. The SNR of the individual spectra was found to be around 6 (for a 60 s exposure), resulting in a grand average spectrum with a SNR around 50.

Additionally we took 4 spectra on 1 June 2014 of SDSS J1908 using Keck/ESI in Echellette mode with an exposure time of 15 min each, for the spectroscopic analysis of the average spectrum. An average flatfield frame was made out of 10 individual flatfield frames. A HgNeXeCuAr lamp spectrum was obtained at the beginning of the night as a master arc. MAKEE was used to reduce the data. The 4 spectra in combination with the data taken on 12 July 2012 result in a SNR of about 110 for the grand average spectrum.

Table 4.1 gives an overview of all observations and the instrumental set-ups.

4.3 Methods

4.3.1 Spectroscopic period determination

To determine the orbital period the violet-over-red method (V/R) described in Nather et al. (1981) was used for the spectra, following Roelofs et al. (2005, 2006a, 2007c) and Kupfer et al. (2013). To maximise the SNR the ratios of the strongest helium absorption lines (4387 Å, 4471 Å, 4921 Å and 5015 Å) were summed. Lomb-Scargle (LS) periodograms of the measured violet-over-red-ratio as a function of the barycentric date were computed. We note that all times and phases in this analysis are in barycentric times.

The uncertainty on a derived period was estimated using the bootstrap method. In a simple Monte Carlo simulation 1000 periodograms were computed and in each the highest peak was taken as the orbital period (see Kupfer et al., 2013). A number of 369 spectra were randomly picked out of the full sample of 369 spectra, allowing for a spectrum to be picked more than once. The standard deviation on the distribution of the computed orbital period is taken as a measure of the accuracy in the derived period.

4.3.2 Doppler tomography

In Doppler tomography (Marsh & Horne, 1988) phase-resolved spectra are projected onto a two-dimensional map in velocity coordinates. We refer to Steeghs (2003) and Marsh (2001) for reviews of Doppler tomography. Emission features that are stationary in the binary frame add up constructively in a Doppler tomogram while emission that is not stationary in the binary frame or moves on a period different from the orbital period will be spread out over the

---

[4]http://www.astro.caltech.edu/∼tb/ipac_staff/tab/makee/

Doppler tomogram. Therefore, Doppler tomograms are useful to separate out features that move with a different velocity and/or different phase (e.g. bright spot and central spike). In this analysis Doppler tomograms were computed using the software package DOPPLER[5] and were used to measure the systematic velocity and the velocity amplitudes of the individual lines in SDSS J1908. Absorption features were inverted to appear as emission lines in the Doppler tomogram analysis.

To measure the systematic velocity of the individual lines we followed the approach introduced by Roelofs et al. (2005). For a given trial wavelength, a feature in the spectra will appear blurred in a Doppler tomogram if the "rest" wavelength does not coincide with the trial wavelength. We thus make Doppler tomograms for a range of trial wavelengths around the rest-frame wavelength of the spectral lines and fit a 2D Gaussian to the emission feature in every Doppler tomogram. For each line the height of the fitted spot peaks strongly around a certain wavelength. The maximum of a parabolic fit to the peak heights defines the "rest" wavelength and therefore the systemic velocity. In the next step Doppler tomograms accounting for the systemic velocity were computed. The center of a 2D Gaussian fit was calculated for each line which was taken as the position of the spot.

4.3.3 Analysis of the *Kepler* lightcurve

For dynamical lightcurve analyses the discrete Fourier transform (FT) for the *Kepler* data set of our three lightcurve window were computed using a 200 days sliding window of the data. A block of 200 days of data has to be used to show a significant signal for some of the weaker periods in the FT.

Observed-minus-computed (O-C) diagrams are a powerful tool that can be used to refine the periods and search for period variations. These diagrams compare the timing of an event, which in our case is the time of phase zero in the lightcurve based on an ephemeris (observed), to when we expect such an event if it occurred at an exactly constant periodicity (computed). A linear trend in an O-C diagram corresponds to an incorrect period, whereas a parabolic trend is caused by a period derivative.

O-C diagrams were computed for the 5 strongest frequencies detected in SDSS J1908 (including the frequencies identified as possible orbital periods by F11), as well as the orbital period to search for period variations. For the three stronger periods ($90, 92$ and 184 c/d) two-week blocks of data were folded on a fixed period with a fixed zero-point. For the less strong periods ($74, 79$ and 111 c/d) two month blocks of data were folded on a fixed period with a fixed zero-point.

For the frequencies which show a sinusoidal variation in the phase folded lightcurve ($90, 92, 111, 184$ c/d), a sine curve was fitted to the folded lightcurve to obtain the phasing. For the other two frequencies ($74, 79$ c/d) a Gaussian was fitted to the phase folded lightcurve and phase of the center of the maximum was measured. In the next step, we moved one week forward in time and repeated the procedure to measure the phase. This was done for the full 1052 days of data. If the correct period is used no linear trend of the measured phase

---

[5]DOPPLER was written by TRM and is available at http://www.warwick.ac.uk/go/trmarsh/software/
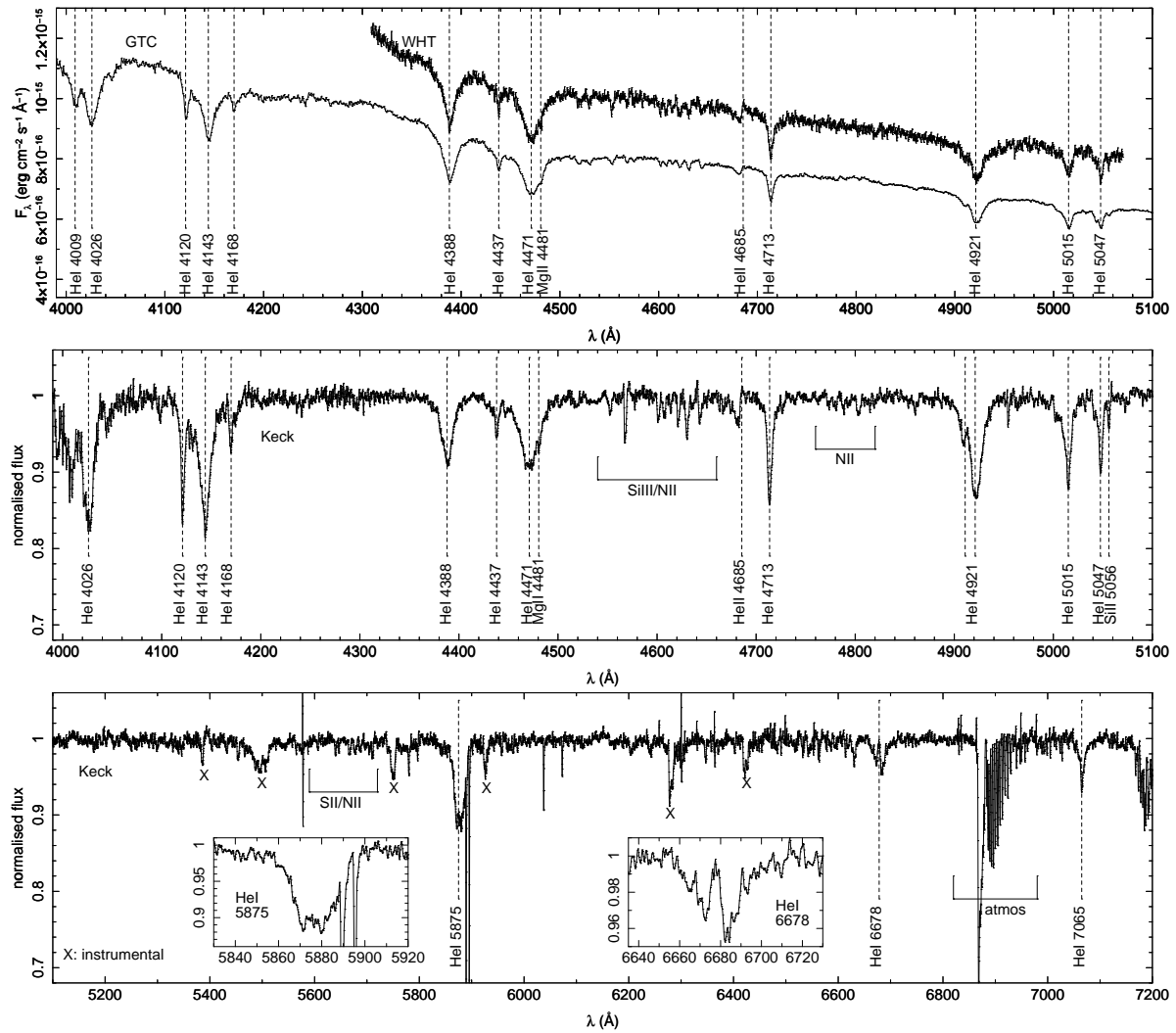
Figure 4.1: Average spectrum of SDSS J1908 obtained with the WHT, Keck and GTC. Helium absorption lines of helium are indicated. **Upper panel:** Average spectra obtained by the WHT and the GTC. **Middle and lower panel:** Gaussian smoothed normalised average spectrum obtained by Keck.
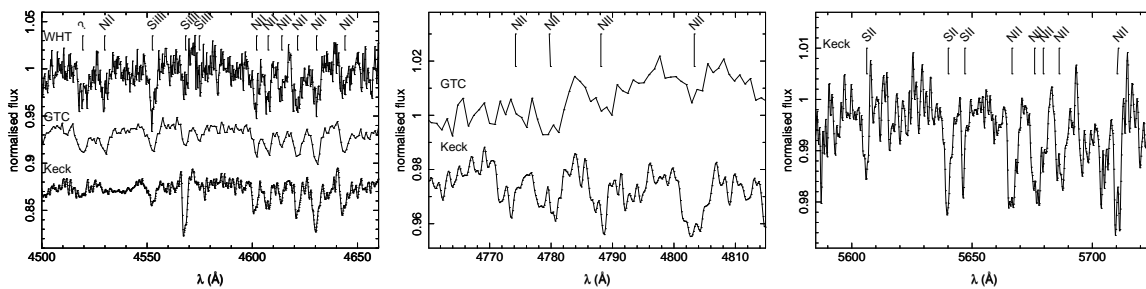

Figure 4.2: Zoomed region of the average WHT, GTC and Keck spectra around locations of various metal lines (N II, Si III and S II).
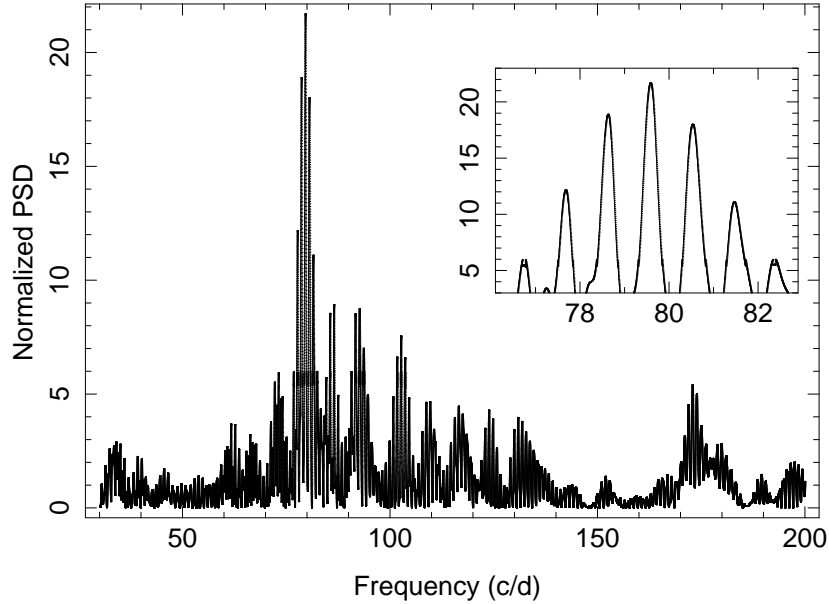
Figure 4.3: LS periodograms of the GTC data using the red over violet wing flux ratio. The strongest peak was chosen to be the correct period.

is expected. Therefore, a constant was fitted to each O-C diagram and the χ^2 value of the fit was computed. To find the best period a parabola was fitted to the computed χ^2 value and the minimum was assumed to be the best period.

Note that the Kepler lightcurve is given in barycentric Julian date (BJD). Therefore we computed BJDs for the spectroscopic data which allows us to compare the spectroscopic and the photometric datasets.

4.4   Results

4.4.1   Average spectra

Helium absorption lines

The average spectra of SDSS J1908 are shown in Fig. 4.1. The strong absorption lines of neutral helium are clearly visible. Helium absorption lines are seen in AM CVn systems during dwarf-novae type outbursts, as well as in high state systems with orbital periods < 20 min (e.g. Roelofs et al., 2007b; Levitan et al., 2013). SDSS 1908 appears very similar to the short period systems AM CVn and HP Lib (Roelofs et al., 2006b, 2007b). The He I 6678 and 5875 Å line shows an emission core which is also observed in AM CVn itself (Patterson et al., 1993). The helium emission lines in AM CVn and HP Lib are much broader than in SDSS J1908, indicating that the lines of SDSS J1908 show less rotational broadening and the system is seen under lower inclination, as also concluded by F11.
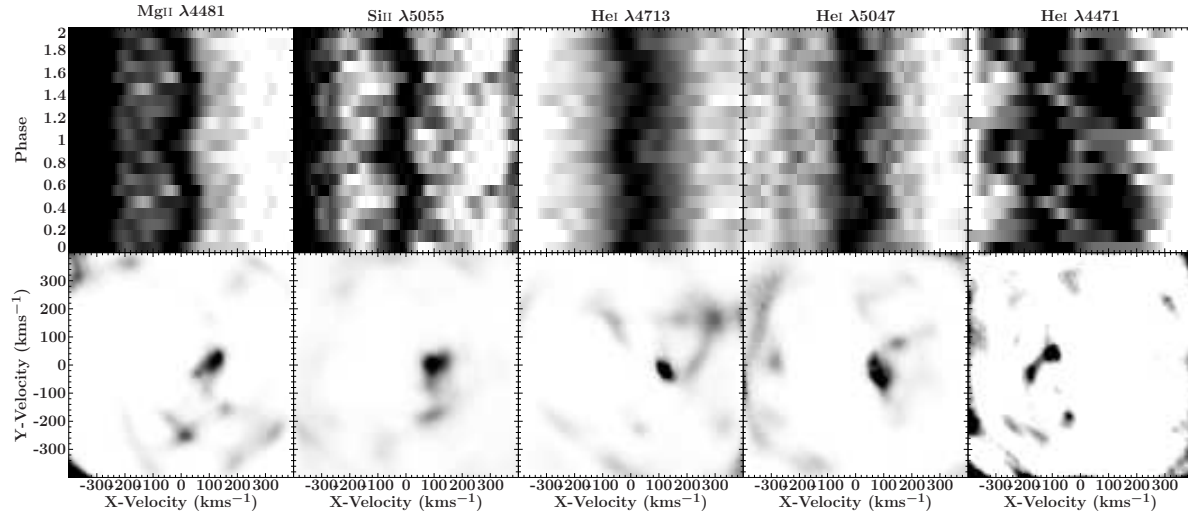
Figure 4.4: Trailed spectra (top row) and maximum-entropy Doppler tomograms (bottom row) of selected metal and He I lines of SDSS J1908. The Si II, Mg II and He I 4713/5047 Å absorption lines and the He I 4471 Å emission core is shown. Visible is a phase offset between the emission and absorption features. The average line profile has been divided out to enhance the visibility of the spot on the Doppler tomograms.

Table 4.2: Velocities of the emission and absorption lines seen in SDSS J1908

Feature	γ (km s^{-1})	K_x (km s^{-1})	K_y (km s^{-1})
Helium absorption lines			
He I 4387/4921	23.7±4.4	-	-
He I 4713	25.0±3.8	116.8±6.5	−23.3±4.5
He I 5047	10.1±5.0	84.8±9.5	−35.3±7.3
Helium emission lines			
He I 4471	15.6±5.3	−111.2±6.8	36.8±6.6
Metal absorption lines			
N II 4601 - 4643	2.3±5.0	-	-
Si III 4552/4567/4574	2.7±4.6	-	-
Mg II 4481	1.0±5.5	109.6±9.3	5.6±7.1
Si II 5041/5055	6.2±5.8	100.0±7.2	−10.4±7.6
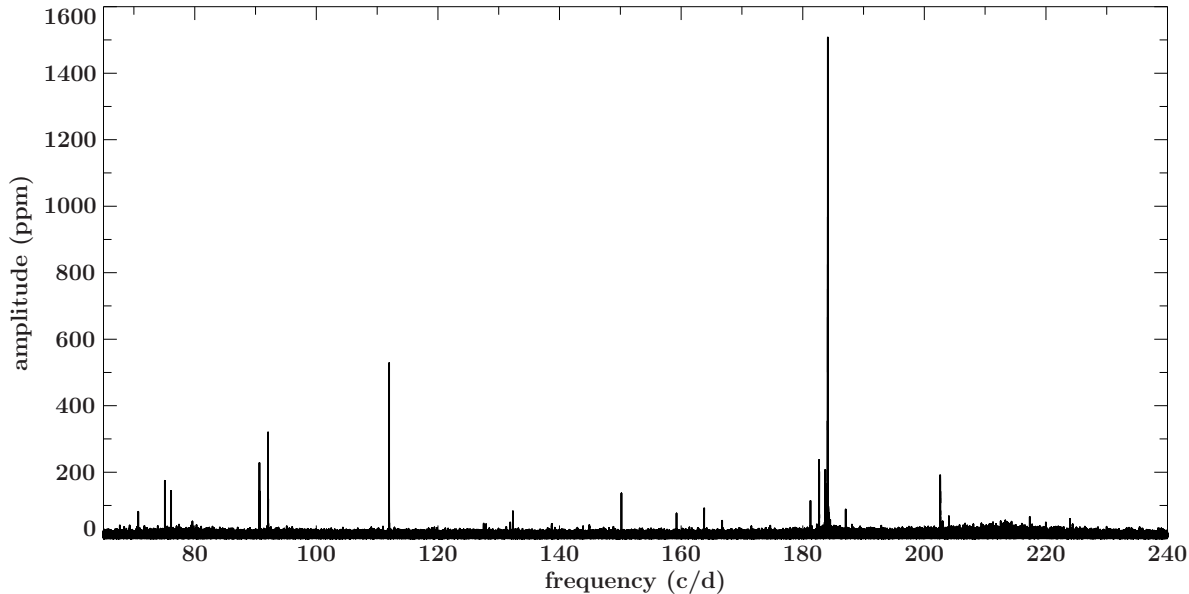
Figure 4.5: Fourier transform of the lightcurve obtained with *Kepler* of SDSS J1908.

Metal absorption lines

SDSS J1908 shows a variety of weak metal lines including a number of nitrogen lines as well as silicon and sulphur lines (see Fig. 4.2 for a selection of metal lines). In contrast to the large number of detected nitrogen lines, there is no evidence for oxygen. The strongest O I line in the optical is the triplet at 7771-7775 Å and the strongest O II lines in the optical are 4649 or 4414 Å. The strongest C II line in the optical is C II 4267 Å. This line might be visible just above the noise level in the GTC data at an equivalent width of < 0.1 Å. Table 4.9 gives an overview of the detected lines with measured equivalent widths.

4.4.2   Kinematic analysis

Spectroscopic orbital period

Using the method described in Sec. 4.3.1 the LS periodogram shows a clear peak at 1085.7 ± 2.8 sec (79.58 ± 0.20c/d, 18.095 ± 0.046 min; Fig. 4.3) in the spectroscopic data obtained with the GTC. This period is in excellent agreement with a period at $1085.10(9)$ sec detected in the *Kepler* lightcurve (see Sec. 4.5).

   To test whether this period is indeed the orbital period, the GTC and WHT spectra were phase folded on the *Kepler* period. Phase folded spectra and the Doppler tomograms were computed and analysed following Sec. 4.3.2. Phase folded spectra and Doppler tomograms are shown in Fig. 4.4. We find a weak S-wave in emission in the core of He I 4471 Å. The helium lines He I 4713/5015/5047 Å, the Si II 5041/5055 Å and the Mg II 4481 Å lines show an S-wave in absorption. The phase offset between the emission lines and the absorption lines is found to be of $170 \pm 15°$.

   No line variation was detected for He I 4387/4921 Å, Si III 4552/4567/4574 Å and N II 4601
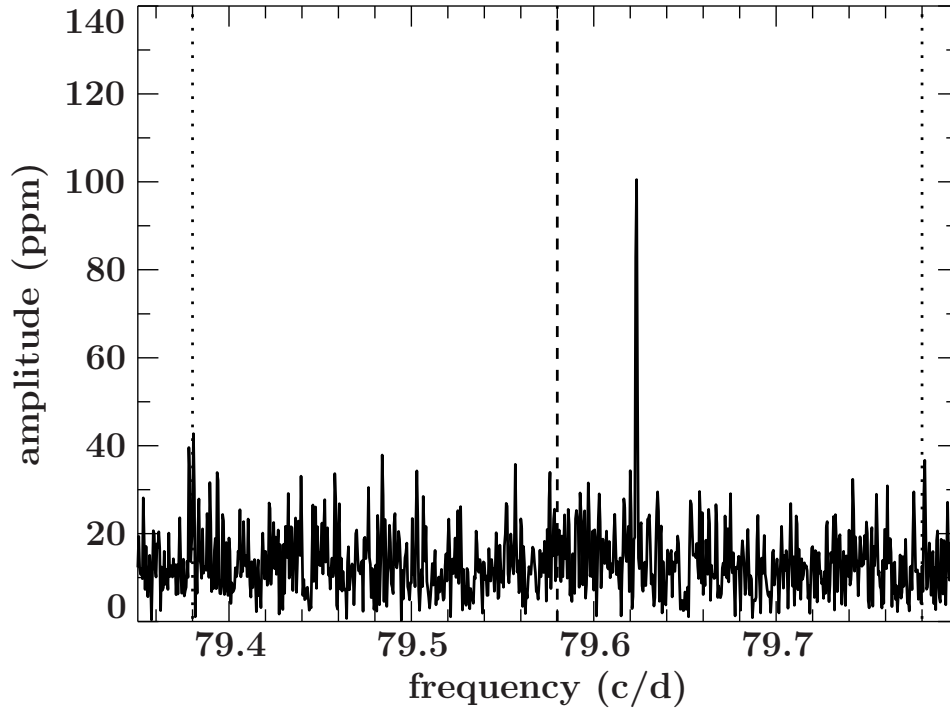
Figure 4.6: View around the peak at 79.6233 c/d in the Fourier transform of the *Kepler* lightcurve. Shown is the position of the spectroscopically determined orbital period (dashed line) with its error (dotted lines).

- 4643 Å. However, the helium lines show a different systemic velocity than the silicon and nitrogen lines. See Tab. 4.2 for an overview of the measured velocities.

The GTC and WHT data were also folded on different periods seen in the Fourier transform of the *Kepler* data. However, no variations can be seen in any other period. We therefore conclude that $1085.10(9)$ sec is the orbital period of SDSS J1908.

4.4.3   Lightcurve variations

We find no strong variation, such as dwarf novae type outbursts or superoutbursts, in the normalised lightcurve.

To determine and refine the periods in SDSS J1908, and to search for possible periodic variations in the close-by G-star, we used the disentangled 1052 days lightcurve obtained by the *Kepler* satellite. Fourier transforms (FT) of the lightcurves for both objects were computed. No periodic variations were detected in the G-star over the frequency range 0-250 c/d. This shows that even if the photometric disentangling is not perfect no influence of the position or occurrence of periods detected in SDSS J1908 is expected to come from the G-star.

Figure 4.5 shows the FT of the full lightcurve for SDSS J1908. We use the mean value of the FT amplitude spectrum of the full data set to approximate the significance on the amplitudes in Fourier space, $\sigma_{\mathrm{FTmean}} = 14\,\mathrm{ppm}$. We adopt $4\sigma_{\mathrm{FTmean}} = 52\,\mathrm{ppm}$ as the threshold of significance of the peaks in the FT amplitude spectrum. Several peaks ranging from periods
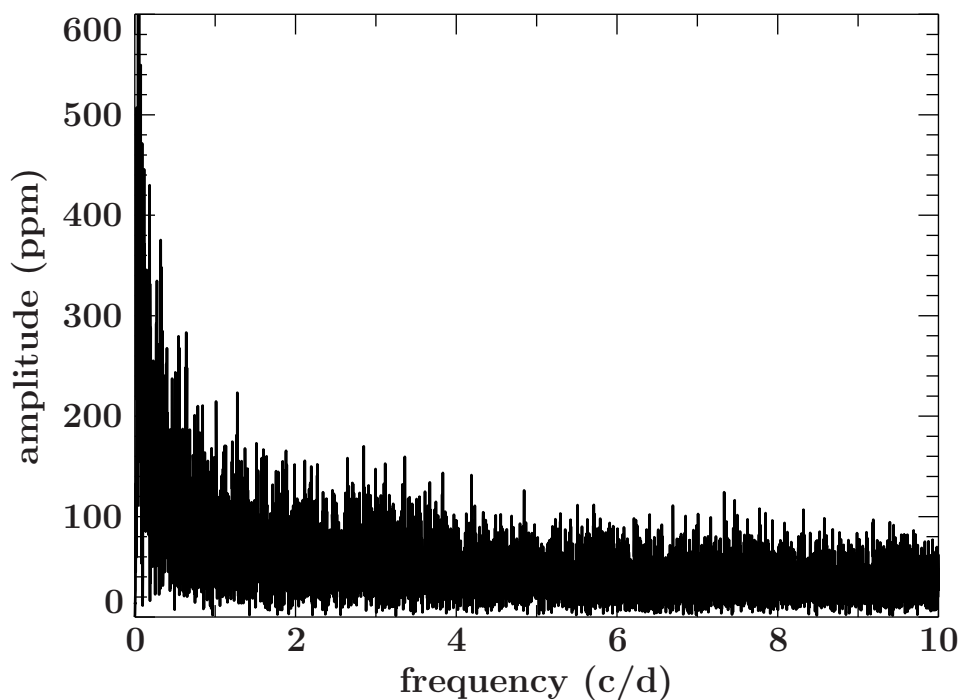
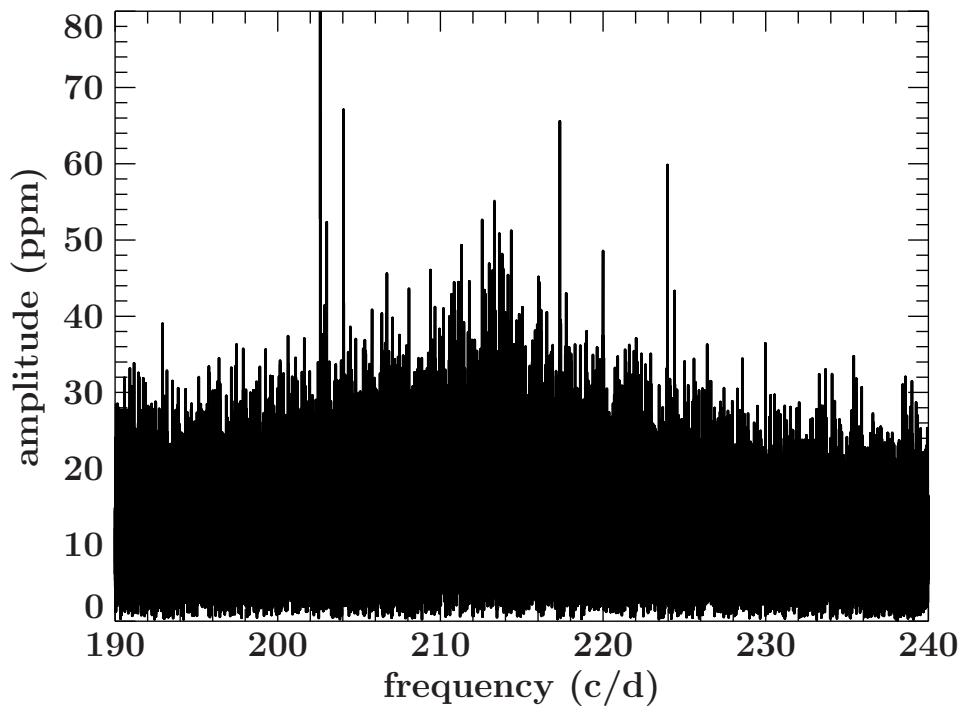**Figure 4.7:** Zoomed view on the low frequency region in the Fourier transform.

Figure 4.8: Zoomed view around the QPO in the Fourier transform.
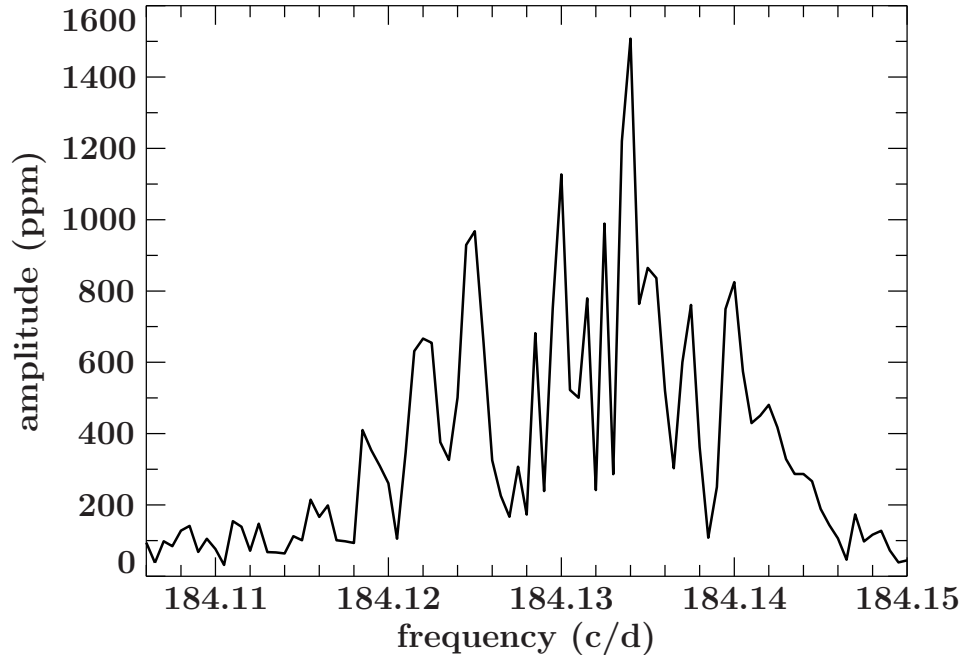
Figure 4.9: Zoomed view around the strongest peak in the Fourier transform of the *Kepler* lightcurve.

of 196 sec up to 1221 sec can be identified in the FT of the full lightcurve. We find a total of 42 signals well above the noise level in the FT amplitude spectrum.

For stable frequencies, pre-whitening the light curve by the highest peaks in a FT removes most power in that region and allows for a relatively simple extraction of the periods present in SDSS J1908. However, none of the peaks in the FT of SDSS J1908 can be pre-whitened in the standard way, because most frequencies show a variability in the frequency and therefore a pre-whitening of the strongest does not completely remove the pulse shape but leaves a new peak at slightly different frequency as the pre-whitened peak. See Sec. 4.5 for further discussion on the stability.

Figure 4.6 shows the periodogram of the *Kepler* lightcurve at the position where the spectroscopic orbital period was detected. We find a single peak at 79.6234 c/d and therefore confirm that the orbital period is also visible in the *Kepler* lightcurve.

Besides the strong periodic variations some intriguing features can be seen in the Fourier transform which were also notified by F11. Below a frequency of about 20 c/d the noise is strongly increasing as shown in Fig. 4.7. This feature is not seen in the G-star and therefore expected to be a real feature in SDSS J1908 and not caused by the satellite. Those variations are due to low-frequency variations on timescales of hours to days and are well known from cataclysmic variables and from accreting low mass X-ray binaries as a sign of accretion (van der Klis, 2005; Scaringi, 2014).

Patterson et al. (2002) discovered a quasi-periodic oscillation (QPO) in HP Lib at a frequency of $280 - 320$ c/d. We discover a similar QPO in SDSS J1908 at a frequency of about $200 - 230$ c/d corresponding to a period of $6 - 7$ min (see Fig. 4.8).
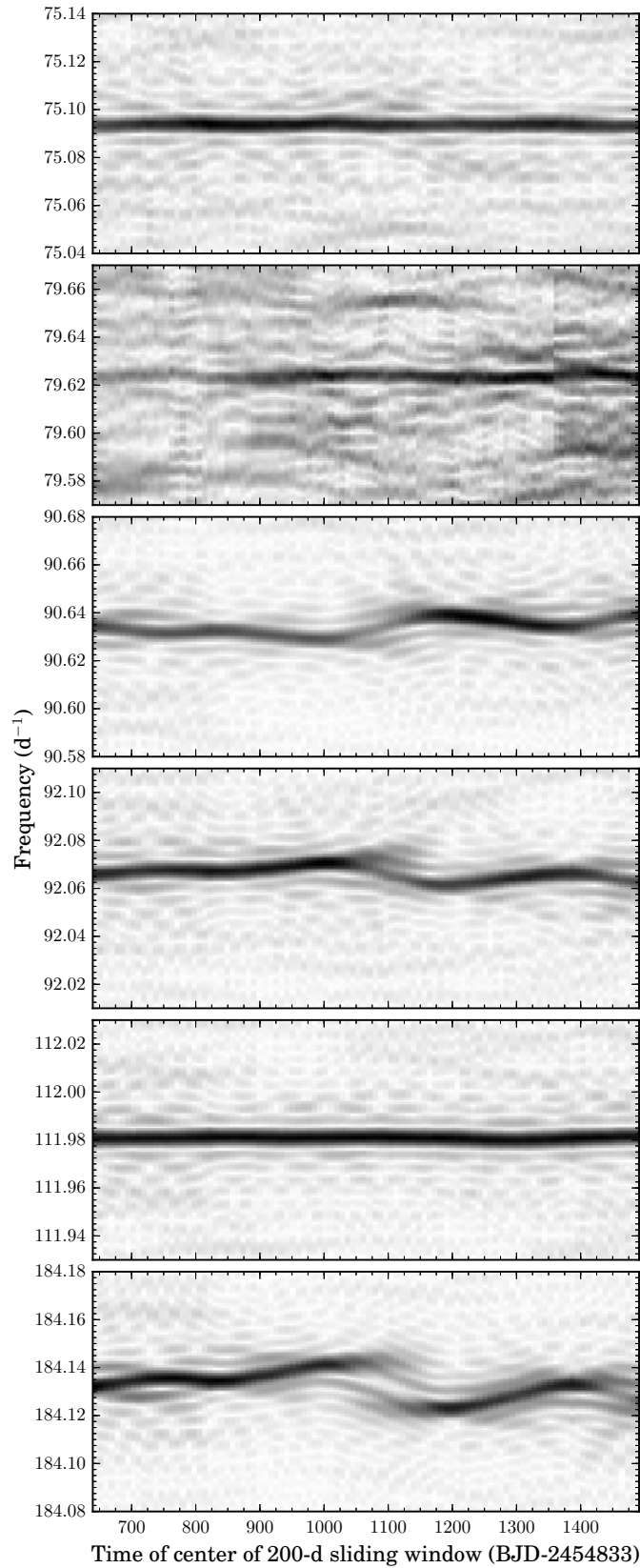
Figure 4.10: Zoomed view of the two-dimensional discrete Fourier transform for the full data set. Shown here is the amplitude vs. time and frequency for the orbital frequency and the five strongest frequencies detected in the lightcurve. We use a 200-day sliding window, and darker greyscale corresponds to higher amplitudes.

Table 4.3: Overview of the periods measured from O-C diagrams

Feature	Frequency (1/d)	Period (sec)
P_{74}	75.093(5)	1150.56(5)
P_{orb}	79.623(3)	1085.10(9)
P_{90}	90.633(5)	953.29(0)
P_{92}	92.066(1)	938.45(6)
P_{111}	111.980(5)	771.56(3)
P_{184}	184.132(6)	469.22(7)

4.5   Periodic stability

We found a large number of frequencies which show several close-by peaks in the FT. This means that the system shows either several periods with similar stable frequencies or one single frequency shows frequency variability in time (Fig. 4.9). Figure 4.9 shows the strongest variation detected in the lightcurve of SDSS J1908 at a frequency of $P = 184.1326$ c/d which shows a strong frequency variability.

Figure 4.10 shows the discrete Fourier transform amplitude spectra for the Kepler lightcurve data set, created following Sec. 4.3.3. We show the amplitude spectra for the spectroscopic orbital period as well as the five strongest peaks in the FT of the full lightcurve.

For the first half year of observations the spectroscopic period is not above the noise level in the FT. After half a year the amplitude of the orbital period increases and stays well above the noise level over the full observing period. During the last year of observations the signal strength reaches its maximum with an amplitude of ~ 150 ppm (2nd panel in Fig. 4.10). A variable strength in the signal of the orbital period in the FT is also observed in AM CVn itself (Skillman et al., 1999).

The frequencies around 75.09 c/d and 111.98 c/d (1st and 4th panel in Fig. 4.10) are visible over the full observed period with a constant strength at ~ 330 ppm for 75.09 c/d and ~ 560 ppm for 111.98 c/d. Both periods show no significant frequency variations.

The frequencies around 90.63 and 92.06 c/d show amplitude and frequency variations (3rd and 4th panel in Fig. 4.10). The frequency variations of 90.63 c/d moves opposite to the frequency variation of 92.06 c/d. The signal at 90.63 c/d becomes strongest at around BJD$-2454833 = 1200$ days and shows an amplitude of ~ 700 ppm. The signal at 90.63 c/d becomes strongest at around BJD$-2454833 = 1000$ days and reaches an amplitude of ~ 720 ppm.

The strongest frequency at around 184.13 c/d (6th panel in Fig. 4.10) shows a strong frequency and amplitude variability. After about one year the amplitude reaches its maximum with an amplitude of ~ 3350 ppm. After about another 200 days the frequency splits up and almost disappears before it reaches a large amplitude again.

In particular in the panel with the orbital period (2nd panel in Fig. 4.10), many frequencies can be seen which show a similar amplitude but are only visible for a few weeks/months and therefore are below the detection threshold in the FT of the full lightcurve. For example, in
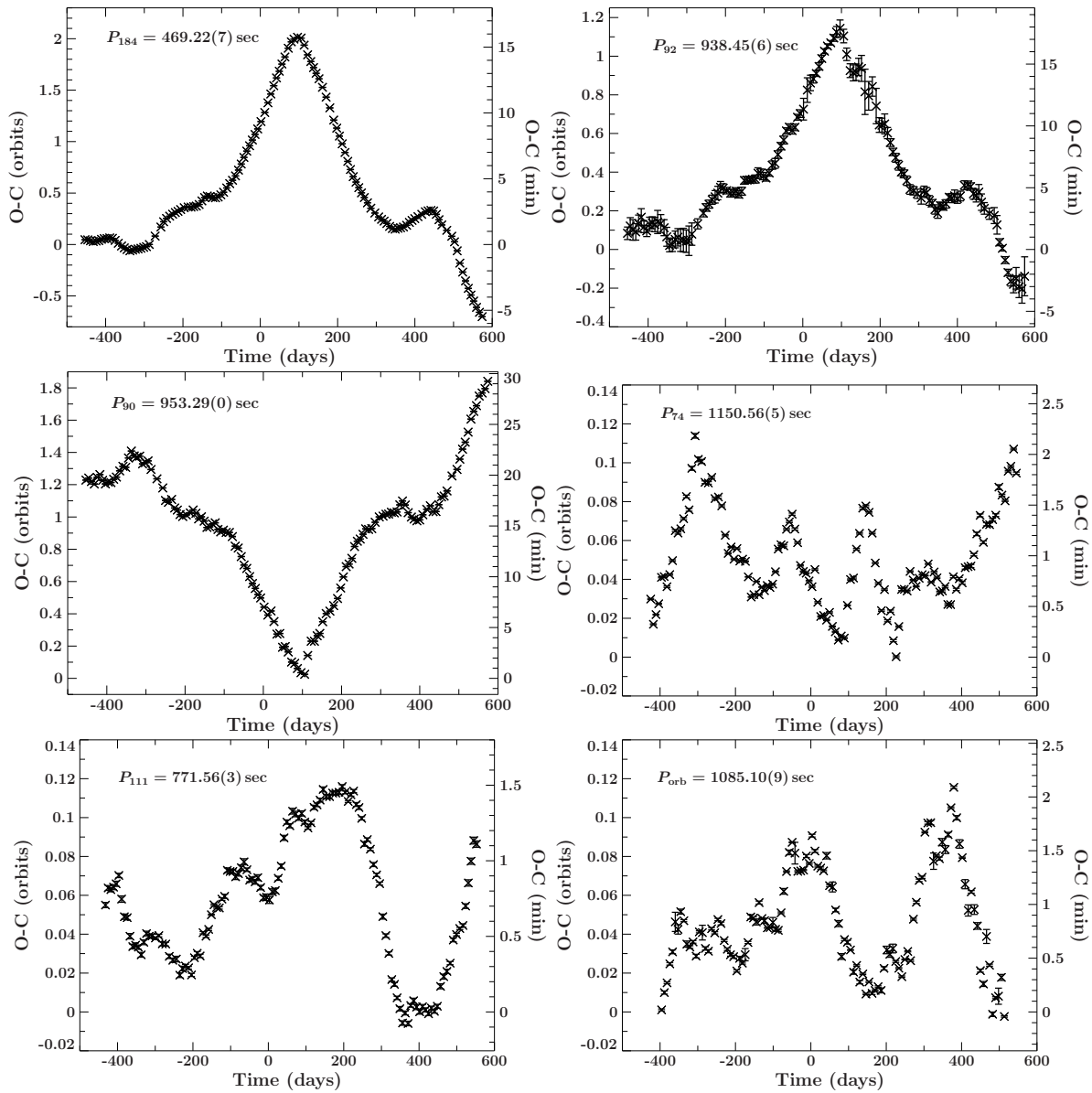
Figure 4.11: O-C diagrams of the five strongest variation in the Fourier transform as well as the spectroscopic orbital period.

the 2nd panel of Fig. 4.10 a peak starts to appear at about $BJD-2454833 = 1020$ days at a frequency of around 79.66 c/d and stays for about 150 days. This peak has a similar amplitude as the orbital period. However, because of the short duration this peak does not appear in the FT of the full lightcurve. Several more examples of frequencies which are only visible for a few weeks/months can be find over the full frequency range. Therefore, we do not provide a list of the detected frequencies but provide the de-trended full *Kepler* lightcurve in electronic form with this paper.

To refine the orbital period and derive the variability of the five strongest frequencies O-C diagrams were computed. The analysis of the O-C diagrams was done following the method outlined in Sec. 4.3.3. The O-C diagram for the peak at 184 c/d was best reproduced with a period of $P_{184} = 469.22(7)$ sec. The O-C diagrams for the lower frequency peaks at 90 and 92 c/d were best fitted with a period of $P_{92} = 938.45(6)$ sec and $P_{90} = 953.29(0)$ sec respectively. The two other frequencies detected at 74 and 111 c/d were best reproduced with a period of $P_{111} = 771.56(3)$ sec and $P_{74} = 1150.56(5)$ sec. The orbital period can be best reproduced with a period of $P_{\mathrm{orb}} = 1085.10(9)$ sec. Table 4.3 summarizes the periods measured from the O-C diagrams.

All six periods should be seen as average periods over the full observing period. Figure 4.11 shows the derived O-C diagrams. In particular three periods (P_{184}, P_{92} and P_{90}) show strong variations up to $|\dot{P}| \sim 1.0 \,\mathrm{x}\, 10^{-8}\,\mathrm{s\,s^{-1}}$ over the observed timescale of 1052 days. Skillman et al. (1999) found a similar variation with similar strength in AM CVn itself in the superhump period. The other three periods (P_{111}, P_{74} and P_{orb}) show short term variations but no strong parabolic trend over time.

4.6 Phase-folded lightcurves of the periodic signals

The *Kepler* lightcurve was phase-folded on different periods and the phase-folded lightcurve was computed. Figure 4.12 shows the phase-folded lightcurves of the five strongest variations in the FT as well as the spectroscopic orbital period. The strongest can be seen at $P_{184} = 469.22(7)$ sec. The amplitude of this variation is about 5 times stronger than the second strongest variation at $P_{111} = 771.56(3)$ sec. The variations at $P_{90} = 953.29(0)$ sec and $P_{92} = 938.45(6)$ sec also show sinusoidal variability. The latter one is superimposed with the strong first harmonic P_{184}. The period at $P_{74} = 1150.56(5)$ sec shows two maxima whereas the first one is about twice as strong as the second one. The overall shape of the phase-folded lightcurve for P_{74} looks similar to the superhump period found in HP Lib (Patterson et al., 2002).

The phase-folded lightcurve folded on the spectroscopic orbital period ($P_{\mathrm{orb}} = 1085.10(9)$ sec; Fig. 4.12, lower left panel) shows a flat part followed by an increase and decrease in luminosity covering half of the orbit. Levitan et al. (2011) presented a similar lightcurve for PTF1 J071912.13+485834.0 ($P_{\mathrm{orb}} = 1606.2 \pm 0.9$ sec). They concluded that the increase in luminosity is most likely caused by the bright spot rotating in and out of the line of sight on the side of the accretion disc. We calculated the ephemeris where the zero phase is defined as
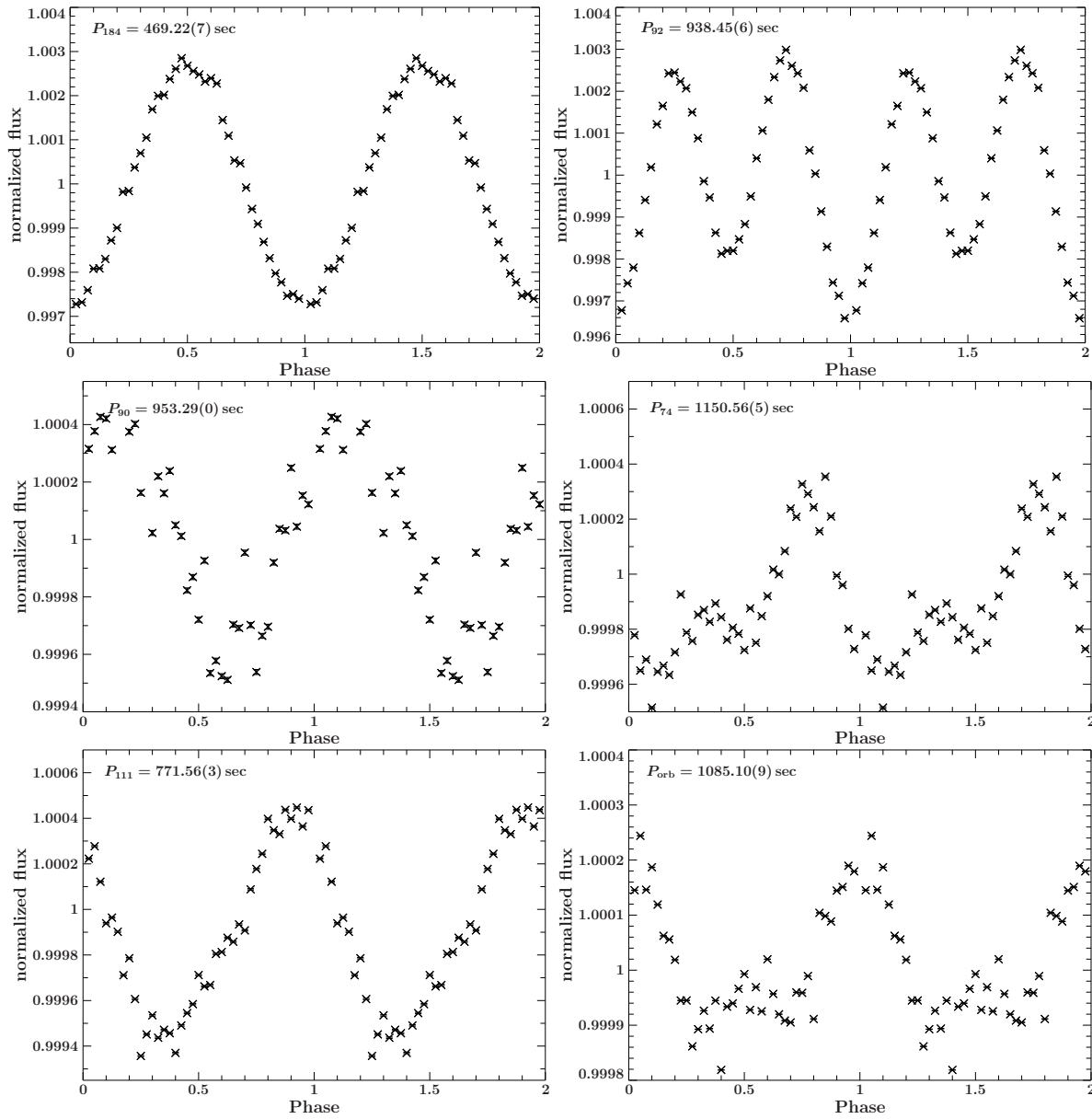
Figure 4.12: Mean folded lightcurve of the five strongest variation in the Fourier transform as well as the spectroscopic orbital period.

when the lightcurve folded on the spectroscopic orbital period reaches its flux maximum:

$$BJD_{\mathrm{max}} = 2455820.006744(2) + 0.0125591(27)\Delta E \qquad (4.1)$$

4.7   Discussion

4.7.1   Metal absorption lines

Lines of various metals, like nitrogen, oxygen or carbon can be used to trace the evolutionary history of the system. Different abundance ratios link to different donor types. A high nitrogen to carbon/oxygen ratio is expected for a helium WD donor, whereas a helium star donor is expected to show higher carbon and oxygen abundances (Nelemans et al., 2010).

Kupfer et al. (2013) discovered strong absorption lines of magnesium and silicon in the three systems known to have orbital periods between 50–60 min. In the long period system GP Com, absorption lines of nitrogen were detected as well (Kupfer et al. in prep). So far, metal absorption lines have not been observed in short period systems. SDSS J1908 is the first high state system which shows a variety of metal lines, including N II, Si II/III and S II, in absorption. Silicon as well as the sulphur lines can be used as tracer for the initial metalicity since their abundances are not supposed to be affected by nuclear synthesis processes during binary evolution. Remarkable is the detection of a large number of N II lines and the absence of oxygen and carbon lines. This might favour a helium white dwarf donor in SDSS J1908. However, this is only a qualitative statement, a detailed abundance analysis is necessary to prove the helium white dwarf nature of the donor star.

4.7.2   Change of the orbital period

AM CVn type systems that passed the period minimum are expected to show an increasing period, $\dot{P} > 0$ (Marsh et al., 2004). In an O-C diagram an increasing period shows up as parabolic trend. We do not detect an overall parabolic trend in the O-C diagram of the orbital period (Fig. 4.13) but can set a rough limit on the $\dot{P}$.

A formal fit to the data shown in Fig. 4.13, results in a $\dot{P} = 9.6 \times 10^{-11} \mathrm{s\,s^{-1}}$. For illustrative purposes we overplotted the expected signal for $\dot{P}=10^{-11}$-$10^{-09} \mathrm{s\,s^{-1}}$. A conservative estimate rules out any orbital variations $> 10^{-10} \mathrm{s\,s^{-1}}$.

4.7.3   Origin of the photometric variations

A Fourier analysis of the Q6 to Q17 short cadence data obtained by *Kepler* revealed a large number of frequencies above the noise level with most of them showing a large variability in frequency and amplitude. Some periods (e.g. 184.13 c/d) are visible over the full observing period, whereas many periods are only visible for a few weeks/months.

In combination with phase resolved spectroscopy we were able to identify the orbital period $P_{\mathrm{orb}} = 1085.10(9)$ sec. The shape of the phase folded lightcurve at the period $P_{74} = 1150.56(5)$ sec looks similar to the superhump period found in HP Lib (Patterson et al., 2002).
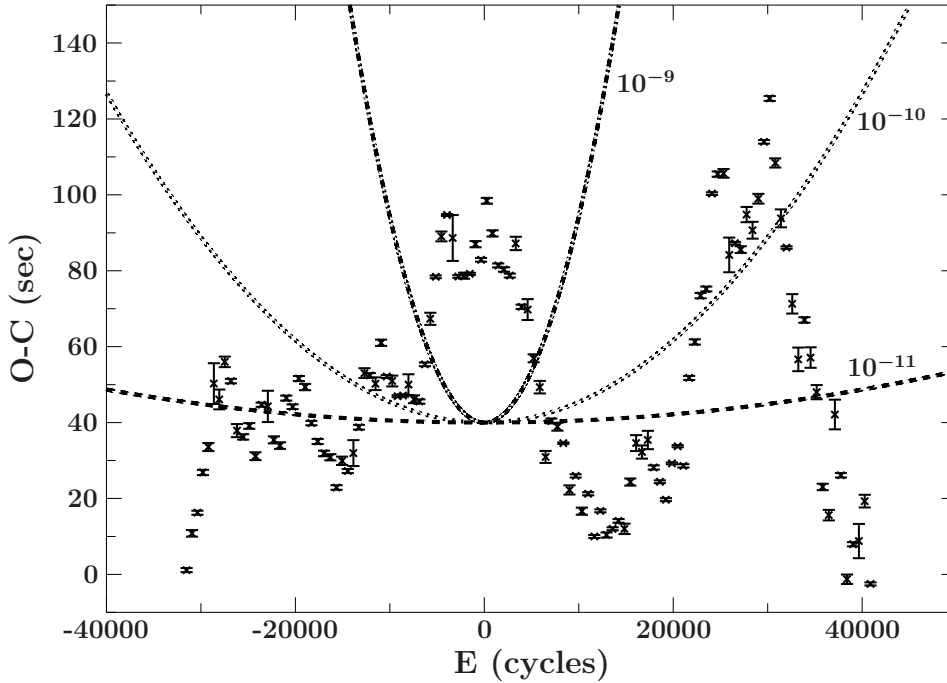
Figure 4.13: O-C diagram of the orbital evolution in SDSS J1908. Overplotted are calculated O-C diagrams for different $\dot{P}$ (dashed line: $\dot{P}=10^{-11}$ s s^{-1}, dotted line: $\dot{P}=10^{-10}$ s s^{-1}, dashed-dotted line: $\dot{P}=10^{-09}$ s s^{-1})

Therefore P_{74} corresponds most likely to the positive superhump period in SDSS J1908. This result leads to a period excess ($\epsilon = \frac{P_{\mathrm{sh}}-P_{\mathrm{orb}}}{P_{\mathrm{orb}}}$) of $\epsilon = 0.0603(2)$, which is higher than observed in AM CVn ($\epsilon = 0.0219$) and HP Lib ($\epsilon = 0.0148$). Patterson et al. (2005) found an empirical relation ($\epsilon = 0.18q+0.29q^2$) between the period excess and the mass ratio ($q = \frac{M_2}{M_1}$) for a large number of hydrogen rich dwarf novae. Here, a mass ratio for SDSS J1908 of $q=0.33$ using this relation is obtained, which is much larger than found in AM CVn itself (Roelofs et al., 2006b).

The shape of the phase folded lightcurve on the period $P_{92} = 938.45(6)$ sec and the O-C diagram looks like the variations found for the superhump period in AM CVn itself (Skillman et al., 1999). Additionally, in AM CVn the strongest variation in a FT diagram corresponds to the first harmonic of the superhump period which is also the case for the P_{92} period. If P_{92} is the negative superhump period, this would lead to a very large period excess $\epsilon = 0.1351(5)$ which was to our knowledge never observed in a system with a white dwarf accretor. Additional explanations for P_{92} with its first harmonic could be the rotational period of the white dwarf. However, it is very unlikely that the rotational period of the accreting white dwarf shows strong period variations as found in the O-C diagrams over the course of 3 years.

So far, we have only explained the origin of some of the strongest variations detected in the FT of SDSS J1908. The majority of observed frequencies in SDSS J1908 remains puzzling. Additional sources for variability which are visible over the observed period of about 3 years could be the rotational period of the accretor, pulsations in the accretor or variability in the disc. The first one can only explain a small number of additional periods detected in SDSS J1908
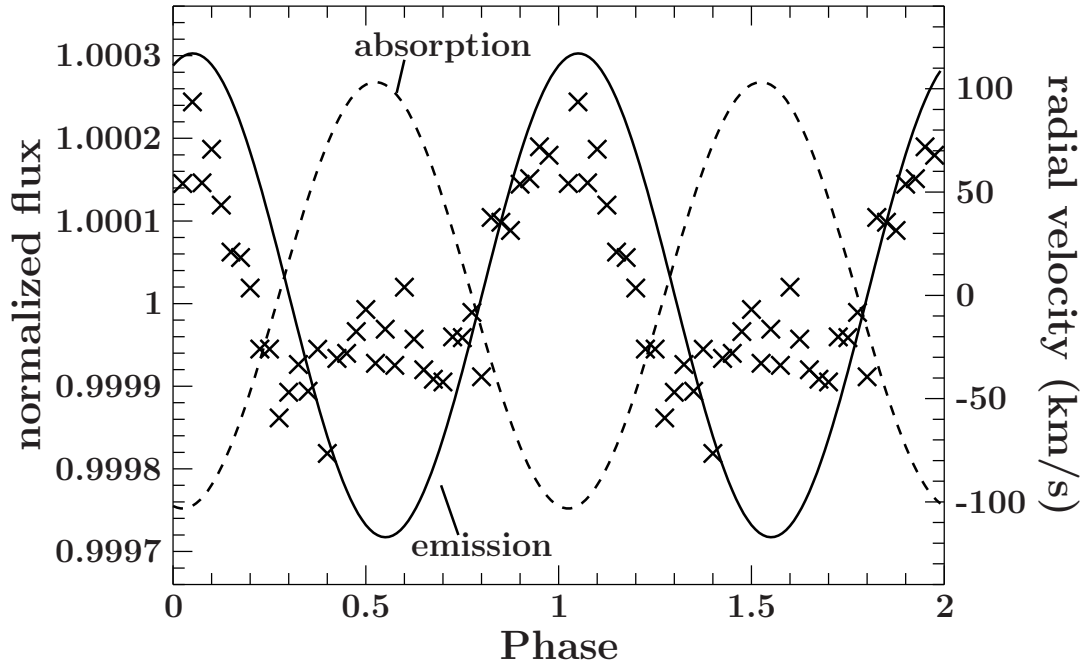
Figure 4.14: Comparison between the phase folded lightcurve at the orbital period and the velocity variations of the He I 4471 Å emission line (solid line) and the average of the absorption lines (dotted lines) using the same ephemeris

because there is only one rotational period of the accretor. The latter two could possibly explain a large number of periods as well as the appearance of frequencies which are only visible for a few weeks/months.

Hermes et al. (2014) found a large number of variations with pulsation periods between 828.2 - 1220.84 s in the pulsating DAV white dwarf GD 1212. Some pulsations in GD 1212 show a large frequency variability similar to what we find for SDSS J1908. Pulsating DB white dwarfs (V777 Herculis stars) have effective temperatures between 21 500-29 000 K and show small amplitude variations and pulsation periods between 100-1100 sec (Córsico et al., 2012). Although these systems show frequency-stable variability, all of our unexplained periods fall in that period range and therefore might be explainable with pulsations of the accretor which would be the first amongst the AM CVn systems. Alternatively, the variability of the frequencies and amplitude can be explained by variability in the disc of SDSS J1908.

4.7.4   Origin of the emission and absorption features and structure of the system

We found two different variations in the spectroscopic data. Some of the helium lines (He I 4713, 5047 Å), the Si II and the Mg II lines show a variation in absorption which moves with an offset of $170 \pm 15°$ to the emission feature seen in the core of the He I 4471 Å line.

To test whether the absorption or emission feature are caused by motion of the bright spot, the donor or the accretor we compared absorption and emission lines to the variation in the

lightcurve folded on the orbital period.

In Fig. 4.14, we present a binned, phase-folded photometric lightcurve together with the radial velocity curves of the emission from the He I 4471 Å line and the absorption lines. The radial velocity curve and the phase-folded photometric lightcurve was folded on the ephemeris given in equation 4.1. The maximum in brightness appears at the same phase when the absorption feature is most blueshifted. The maximum redshift of the He I 4471 emission feature appears just after the brightness maximum. In the following, we discuss different scenarios to see if the phase offset between the lightcurve and the radial velocity curves can be explained.

1) Bright spot: The variation in the lightcurve at the orbital period is caused by the bright spot. The maximum in brightness corresponds to the point when the bright spot is pointed to the observer. Levitan et al. (2011) found for PTF1 J071912.13+485834.0 a similar shaped photometric variation on the orbital period and showed that the maximum brightness happens when the radial velocity curve of the hot-spot crosses from blue- to redshifted, hence when the hot-spot is closest to us. Neither the emission feature nor the absorption lines are closest to us during maximum brightness and a similar explanation as for PTF1 J071912.13+485834.0 fails.

2) Reflection effect: The variation in the lightcurve at the orbital period is caused by a reflection effect of the irradiated side of the donor star. The hemisphere of a cool donor star facing the accretion disc is heated up by the significantly hotter accretion disc. This causes a variation in the lightcurve. More(less) flux is emitted if the irradiated hemisphere of the cool donor star is faced towards (away from) the observer. The maximum of brightness corresponds to the point when irradiated side of the donor star points towards to the observer.

3) Gravity darkening: The variation in the lightcurve at the orbital period is caused by gravity darkening on the highly deformed side of the donor star. The hemisphere of a cool donor star facing the accretion disc is highly deformed and the radius is much larger compared to the back side of the donor star which is not deformed. As a result, the back side of the donor star has a higher surface gravity, and thus higher temperature and brightness as well. The maximum of brightness corresponds to the point when back side of the donor star points towards to the observer.

For all three scenarios we find no satisfying solution where any obvious feature (e.g. bright spot, donor star or accretor) is expected to be seen at the observed phases for the emission and absorption lines.

Additionally, some helium lines (He I 4387, 4921 Å), the N II and the Si III lines show no variation on the orbital period at all which means that they have to originate close the center of mass. In a typical AM CVn type system, the center of mass is close to the accreting white dwarf and the inner hotter parts of the accretion disc. Indeed the excitation energy for N II and Si III is similar ($\sim$ 18-19 eV) and much higher than the excitation energy of Si II and the Mg II ($\sim$ 8-10 eV). Therefore the origin of the N II and Si III lines could be in a distinct region in the inner hotter disc where the orbital motion is below our detection limit and the origin of the Si II and the Mg II could be in a distinct region in the cooler outer region of the disc where the orbital motion is higher.

4.8   Conclusions and Summary

The average spectrum shows strong helium absorption lines, typical for an AM CVn seen in high state. Additionally, a variety of weak metal lines of different species are detected. The phase-folded spectra and the Doppler tomograms reveal radial velocity variations at a period of $P_{\mathrm{orb}} = 1085.7 \pm 2.8\,\mathrm{sec}$ which is in excellent agreement with a period at $P_{\mathrm{orb}} = 1085.10(9)\,\mathrm{sec}$ detected in the three year *Kepler* lightcurve. Therefore, we identify $P_{\mathrm{orb}} = 1085.10(9)\,\mathrm{sec}$ as the orbital period and prove the ultracompact nature of SDSS J1908.

A Fourier analysis of the Q6 to Q17 short cadence data obtained by the *Kepler* satellite revealed a large number of frequencies with strong variability in frequency and strength. In an O-C diagram we show that some periods show a strong variability similar to the superhump period of AM CVn itself. Some of the phase folded lightcurves of different periods show an overall shape similar to what is found for the superhump periods of HP Lib and AM CVn. Although some periods show very similar overall shape and variations in an O-C diagram compared to other high state systems, we are not able to identify unambiguously the negative or positive superhump in SDSS J1908.

The phase folded lightcurve on the spectroscopic orbital period shows a flat part followed by an increase and decrease in luminosity covering half of the orbit. Levitan et al. (2011) found for PTF1 J071912.13+485834.0 a similarly shaped photometric variation on the orbital period and showed that the variation is caused by the orbital period. However, in a comparison between the observed phases of the emission/absorption lines and the variation in the lightcurve we are not able to match the emission or absorption to any obvious feature in the binary such as the bright spot, the accretor or the donor star. Therefore the location of the spectroscopic variability remains undetermined.

4.9 Appendix

Table 4.4: Measured equivalent widths in (mÅ) and limits of disc emission and photospheric absorption lines

Line	EW (mÅ) WHT	EW (mÅ) GTC	EW (mÅ) Keck
He I 4009/4026	[a]	3387 ± 15	4373 ± 25
He I 4120/4143/4168	[a]	3364 ± 18	4239 ± 24
He I 4388	2511 ± 26	3031 ± 16	1437 ± 18
He I 4437/4471 Mg II 4481	4615 ± 23	4692 ± 24	2880 ± 24
Si III 4552	151 ± 14	89 ± 11	83 ± 8
Si III 4567	47 ± 8	34 ± 10	128 ± 14
Si III 4574	19 ± 7	19 ± 9	X
N II 4601	125 ± 14	128 ± 13	87 ± 9
N II 4607	102 ± 12		83 ± 10
N II 4613	83 ± 16	31 ± 9	39 ± 8
N II 4621	154 ± 18	98 ± 11	90 ± 11
N II 4630	118 ± 10	111 ± 12	146 ± 13
N II 4643	71 ± 9	65 ± 9	91 ± 14
He II 4685	-47 ± 13	-21 ± 6	-19 ± 6
He I 4713	1251 ± 24	932 ± 19	1012 ± 17
N II 4779	X	25 ± 5	57 ± 12
N II 4788	X	26 ± 6	56 ± 11
N II 4803	X	23 ± 5	92 ± 10
Si III 4828	X	31 ± 8	X
He II 4859	X	45 ± 10	[b]
He I 4910/4921	3651 ± 26	2499 ± 21	2606 ± 24
N II 5001 - 5015 He I 5015	1083 ± 23	1514 ± 24	1182 ± 19
Si II 5041/5056 He I 5047	836 ± 26	1254 ± 25	712 ± 22
S II 5606	[a]	[a]	38 ± 9
S II 5639/5640	[a]	[a]	65 ± 12
S II 5647	[a]	[a]	29 ± 8
N II 5666	[a]	[a]	87 ± 13
N II 5676/5679	[a]	[a]	92 ± 10
N II 5686	[a]	[a]	73 ± 9
N II 5710	[a]	[a]	71 ± 9
He I 5875	[a]	[a]	[c]
He I 6678	[a]	[a]	908 ± 24
He I 7065	[a]	[a]	804 ± 26
He I 7281	[a]	[a]	[d]

Lines marked with an X indicate that this line is not detectable in the spectrum obtained
[a] Spectrum does not extend to this wavelength, [b] Line present but insufficient SNR to measure, [c] Blended with Na-D lines, [d] Line present but contaminated with atmosphere.

CHAPTER 5

UVES AND X-SHOOTER SPECTROSCOPY OF THE EMISSION LINE AM CVN SYSTEMS GP COM AND V396 HYA

T. Kupfer, D. Steeghs, P. J. Groot, T. R. Marsh, G. Nelemans and G. H. A. Roelofs

Abstract. We present time-resolved spectroscopy of the AM CVn type binaries GP Com and V396 Hya. Medium-resolution spectra covering 0.3-2.5 μm were secured using the VLT/X-Shooter instrument, while the VLT/UVES echelle spectrograph provided high-resolution data. The spectra are dominated by broad helium emission lines from the accretion discs in these systems. We resolve the kinematics of the lines to $0.3\,\mathrm{km\,s^{-1}}$ accuracy, sufficient to map the kinematics of the central sharp emission components in the lines that were previously reported. We find that these spikes trace the accreting white dwarf.

A large number of nitrogen and neon lines were detected in emission and absorption. We show that the narrow emission lines of neon and nitrogen, seen in both systems, as well as the nitrogen absorption lines seen in GP Com, are also linked to the accreting white dwarf as they show the same phase and velocity amplitude as the central spikes in the helium lines.

Doppler tomograms reveal a strong accretion disc bright spot with a faint secondary bright spot at an $\sim$120-degree phase-offset to the first bright spot. From the phases and amplitudes of the central spikes and the primary bright spot, as well as the peak-to-peak velocities of the double peaked helium disc emission lines, we derive limits on the component masses and the inclination angles in both systems.

The mean velocities of the central spike show variations from line to line, ranging from -5 to $+53$ km/s. Compared to calculated line profiles that include Stark broadening we are able to explain the displacements, and the appearance of forbidden helium lines, by additional Stark broadening of emission in a helium plasma with an electron density $n_e \simeq 5 \times 10^{15}$ cm^{-3}.

In a comparison of the narrow emission lines to rotationally broadened synthetic spectra we can exclude fast rotational velocities of the accretor.

5.1   Introduction

Accretion onto white dwarfs in cataclysmic variables (CVs) commonly proceeds via Roche-lobe overflow of hydrogen-rich material from a main-sequence type donor star. A small number of systems have been identified with hydrogen-deficient, degenerate, donor stars; the AM CVn systems (see Solheim, 2010 for a recent review). These systems consist of a white dwarf (WD) primary and either a WD or significantly evolved semi-degenerate helium star companion (e.g. Nelemans et al. 2001). Observationally they are characterised by a high deficiency of hydrogen and short orbital periods (< 1 hour), indicating an advanced stage of binary evolution.

Since the identification of the prototype, AM CVn, as a semi-detached pair of degenerate dwarfs (Smak, 1967; Paczyński, 1967; Faulkner et al., 1972), over 40 additional systems and candidates have been identified. Confirmed orbital periods range from 5-65 minutes (e.g Nather et al., 1981; O'Donoghue et al., 1987, 1994; Ruiz et al., 2001; Woudt & Warner, 2003; Roelofs et al., 2005, 2006a, 2007c; Anderson et al., 2005, 2008; Roelofs et al., 2010; Levitan et al., 2011; Kupfer et al., 2013; Levitan et al., 2013; Carter et al., 2014b). AM CVn binaries are important as strong, low-frequency, Galactic gravitational wave sources (e.g. Nelemans et al., 2004; Roelofs et al., 2007d; Nissanke et al., 2012), the source population of the proposed ".Ia" supernovae (Bildsten et al., 2007), and as probes of the final stages of low-mass binary evolution.

Over the last ten years, in a large campaign using the Sloan Digital Sky Survey (SDSS; York et al. 2000) Roelofs et al. (2005, 2007c); Anderson et al. (2005, 2008); Rau et al. (2010); Carter et al. (2013) and Carter et al. (2014a) built up the population of AM CVn systems and significantly increased the number of known systems. Additionally, synoptic surveys such as the Palomar Transient Factory (PTF; Law et al., 2009) have added a similar number of systems (Levitan et al., 2011, 2013, 2014). The recent increase in the population from photometric, spectroscopic, and synoptic surveys allows the derivation of population properties such as the orbital period distribution or the presence or absence of spectral features as a function of evolutionary stage (Ramsay et al., 2012; Levitan et al., 2015). To determine the orbital period, and detect variations in the spectrum over the orbital period, phase-resolved spectroscopy is needed (e.g. Roelofs et al. 2005, 2006a; Kupfer et al. 2013), although Levitan et al. (2011) showed that the photometric period may be tied to the spectroscopic period for some systems. This is not valid for all systems. GP Com shows variability in the light curve which is not tied to the orbital motion (Morales-Rueda et al., 2003a).

Several formation channels have been proposed for these systems; a double white dwarf channel (Tutukov & Yungelson, 1979), a channel in which the donors are low-mass helium stars (Savonije et al., 1986; Tutukov & Fedorova, 1989; Yungelson, 2008), and one with evolved post-main-sequence donors (Thorstensen et al., 2002; Podsiadlowski et al., 2003). Depending on the importance of the various channels, population synthesis calculations have

suggested that the AM CVn stars could be as abundant as the hydrogen-rich CVs (Iben & Tutukov, 1991; Nelemans et al., 2001a). However, in a calibration of the space density based on the SDSS data actual numbers are much lower. The most recent works by Levitan et al. (2015) and Carter et al. (2013), building on the work by Roelofs et al. (2007d) find a space density, at the position of the Sun, of $5 \times 10^{-7}\,\mathrm{pc^{-3}}$.

In this paper we present high-resolution optical spectroscopy of the AM CVn systems GP Com (Nather et al., 1981) and V396 Hya (Ruiz et al., 2001). These two systems have relatively long orbital periods (46 and 65 minutes) and represent, evolutionary speaking, the bulk of the AM CVn systems, which should be long period, low mass-transfer-rate objects ($\sim 10^{-12} M_\odot\,\mathrm{yr^{-1}}$). In these systems, the mass-transfer-rate was thought to be below the threshold for accretion disc instabilities to occur (Hirose & Osaki, 1990), and indeed no outburst has so far been reported for GP Com or V396 Hya. However, recently three AM CVn systems with orbital periods around 48 min were discovered because of their outburst behaviour as well as their characteristic double peaked helium disc emission lines in their spectra (Woudt et al., 2013; Kato et al., 2014; Rixon et al., 2014).

GP Com has been observed extensively, and shows erratic flaring in optical, UV (Marsh et al., 1995) and X-ray (van Teeseling & Verbunt, 1994) wavebands, which is attributed to the accretion process. One of the more intriguing spectral features is the presence of sharp, low-velocity components in the optical helium emission lines. The fact that these 'central spikes' contribute to the flare spectrum and follow a low-amplitude radial velocity curve as a function of the orbital phase suggests an origin on, or near, the white dwarf accretor (Marsh, 1999; Morales-Rueda et al., 2003a). In an attempt to understand the origin of the peculiar spike, which has become ubiquitous in AM CVn stars (Roelofs et al., 2005, 2006a, 2007c) but which, for some reason,has never been observed in hydrogen-rich accretors, we secured echelle spectroscopy of GP Com and V396 Hya. High-resolution spectra allow us to fully resolve the kinematics of the line profiles in general, and their central spikes in particular. In Section 5.2 we first discuss the observations and data reduction. Section 5.3 describes the analysis of the observed kinematics of the emission lines. Section 5.4, finally, discusses the interpretation of the spikes and the physical parameters we can derive from the observed kinematics in these two binaries.

5.2 Observations and Data reduction

5.2.1 VLT/UVES observations

We employed the UV-Visual Echelle Spectrograph (UVES) mounted on the Unit 2 telescope of the ESO-VLT array at Cerro Paranal, Chile. The data were obtained in visitor mode during the night of April 7/8 2002. The instrument was configured in dichroic mode (dichroic #2) permitting simultaneous data acquisition from both the red and blue cameras. No pre-slit optics were put in the beam. Instead atmospheric dispersion was minimised by maintaining the $1''$ wide slit at the parallactic angle throughout the night. On the blue camera, a 2048x4096 pixel EEV detector covered 3826–5053Å in 29 echelle orders. The chip was read out using

Table 5.1: Summary of the observations of V396 Hya and GP Com

System	Tele./Inst.	N_{exp}	Exp. time (s)
V396 Hya			
2002-04-07	VLT/UVES	28	360
2010-02-18	VLT/X-Shooter	3f	900
GP Com			
2002-04-07	VLT/UVES	110	120
2010-02-18	VLT/X-Shooter	45	60

1 port and 2x3 on-chip binning to reduce read-out time to 22s. In this mode, a binned pixel corresponds to 4.5 km/s along the dispersion axis and a slit-limited resolution profile of 1.7 pixels. The red camera detector system consists of two 2048x4096 pixel CCD detectors, an EEV device covering 5763–7502Å in 24 orders and a red optimised MIT-LL chip covering 7760–9462Å in 15 orders. Both chips were readout in 32s using 1 port each with 2x3 on-chip binning. The pixel scale corresponds to 3.6 km/s after binning.

Frames were first de-biased using a median of 9 bias exposures. In addition, any residual bias contribution was subtracted using the overscan areas of the three CCD detectors. The orders were extracted using the ECHOMOP echelle package (Mills et al., 2014). Flat field correction was performed using the median of a series of well exposed tungsten flat field exposures obtained during the day. The individual orders were traced and profile weights were determined for optimal extraction (Horne, 1986). Target exposures were then optimally extracted after subtracting the sky background. In addition, the same profile weights were used to extract a suitable ThAr exposure as well as the median flat-field frame. The wavelength scales were determined by fitting 4-6 order polynomials to reference lines in the extracted ThAr spectrum, delivering RMS residuals of ≤0.6 km/s. The object orders were blaze corrected by division of a smoothed version of the extracted flat field spectrum. Orders were then merged into a single spectrum using inverse variance weights based on photon statistics to combine overlapping order segments. Finally, the merged spectra were flux calibrated using wide slit exposures of the B-star flux standard HD 60753.

For the red arm data, we also performed a correction for the telluric absorption features. Spectra were first aligned by cross-correlating with the telluric standard. This corrected small wavelength shifts and corrections were found to be less than 3 km/s. The telluric features in each spectrum were then removed as far as possible by adjusting the depth of the telluric template.

5.2.2 VLT/X-Shooter observations

GP Com and V396 Hya were also observed using the medium resolution spectrograph X-Shooter (Vernet et al., 2011) mounted at the Cassegrain focus on the Unit 2 telescope of the VLT array in Paranal, Chile during the night of 2010-02-18 as part of the Dutch GTO program. X-Shooter consists of 3 independent arms that give simultaneous spectra longward of the at-

mospheric cutoff (0.3 microns) in the UV (the ″UVB″ arm), optical (the ″VIS″ arm) and up to 2.5 microns in the near-infrared (the ″NIR″ arm). We used slit widths of $1.0''$, $0.9''$ and $0.9''$ in X-Shooter's three arms and binned by 2x2 in the UVB and VIS arms resulting in velocity resolutions of $14\,\mathrm{km\,s^{-1}}$, $7\,\mathrm{km\,s^{-1}}$ and $11\,\mathrm{km\,s^{-1}}$ per binned pixel for the UVB, VIS and NIR arm respectively. The reduction of the raw frames was conducted using the standard pipeline release of Reflex (version 2.3) for X-Shooter data (Freudling et al., 2013). The standard recipes were used to optimally extract and wavelength calibrate each spectrum. The instrumental response was removed by observing the spectrophotometric standard star EG 274 (Hamuy et al., 1992, 1994) and dividing it by a flux table of the same star to produce the response function.

Table 5.1 gives an overview of all observations and the instrumental set-ups.

5.3 Analysis

5.3.1 Average spectra

We present the time averaged spectra of GP Com and V396 Hya in Fig. 5.1, illustrating the striking similarity between the spectra of these two systems. The familiar triple peaked helium emission lines dominate the spectra. The high-resolution spectra obtained with UVES nicely resolve the central spike feature in both systems (lower left panel Fig. 5.1). We measured the line equivalent widths (EW) for a number of prominent lines in all spectra. In Table 5.2 and 5.3 we list the ranges of EWs observed together with their mean value. Large intrinsic EW modulations are detected in all lines throughout our observing run. In the case of GP Com, the measured EWs from UVES and X-Shooter are consistently smaller than previously reported values (e.g. Marsh et al., 1991). Thus, on top of short timescale flaring activity, GP Com also displays significant variability on longer timescales. V396 Hya shows very similar variations, with EW variations close to a factor of two for UVES. We calculate flare spectra according to the methods described in Marsh et al. (1995) and find that in both GP Com and V396 Hya the continuum as well as the disc and spike components of the lines contribute to the flaring. As discussed in Marsh (1999) and Morales-Rueda et al. (2003a), this strongly suggests that the spike originates at or near the accreting dwarf and not in an extended nebula in both of these objects.

Despite the detailed similarities between the profile shapes in GP Com and V396 Hya, a few differences can be identified in the average spectra. GP Com displays a number of sharp absorption features, most notably between 4050 Å and 4250 Å. We identify these lines as N I. No such features are present in V396 Hya (Fig. 5.2). A large number of N II absorption lines have been observed in the high state system SDSS J1908 (Kupfer et al. submitted). Morales-Rueda et al. (2003a) already reported an absorption feature near He II 4686 Å in GP Com. Indeed this feature is also present in our X-Shooter and UVES spectra but its origin remains unidentified.

In the blue spectral region the strongest N II lines are detected in absorption whereas in the red spectral region, complex N I emission dominates the spectrum. A large number of individual transitions of N I can be identified thanks to our high spectral resolution (Fig. 5.2).
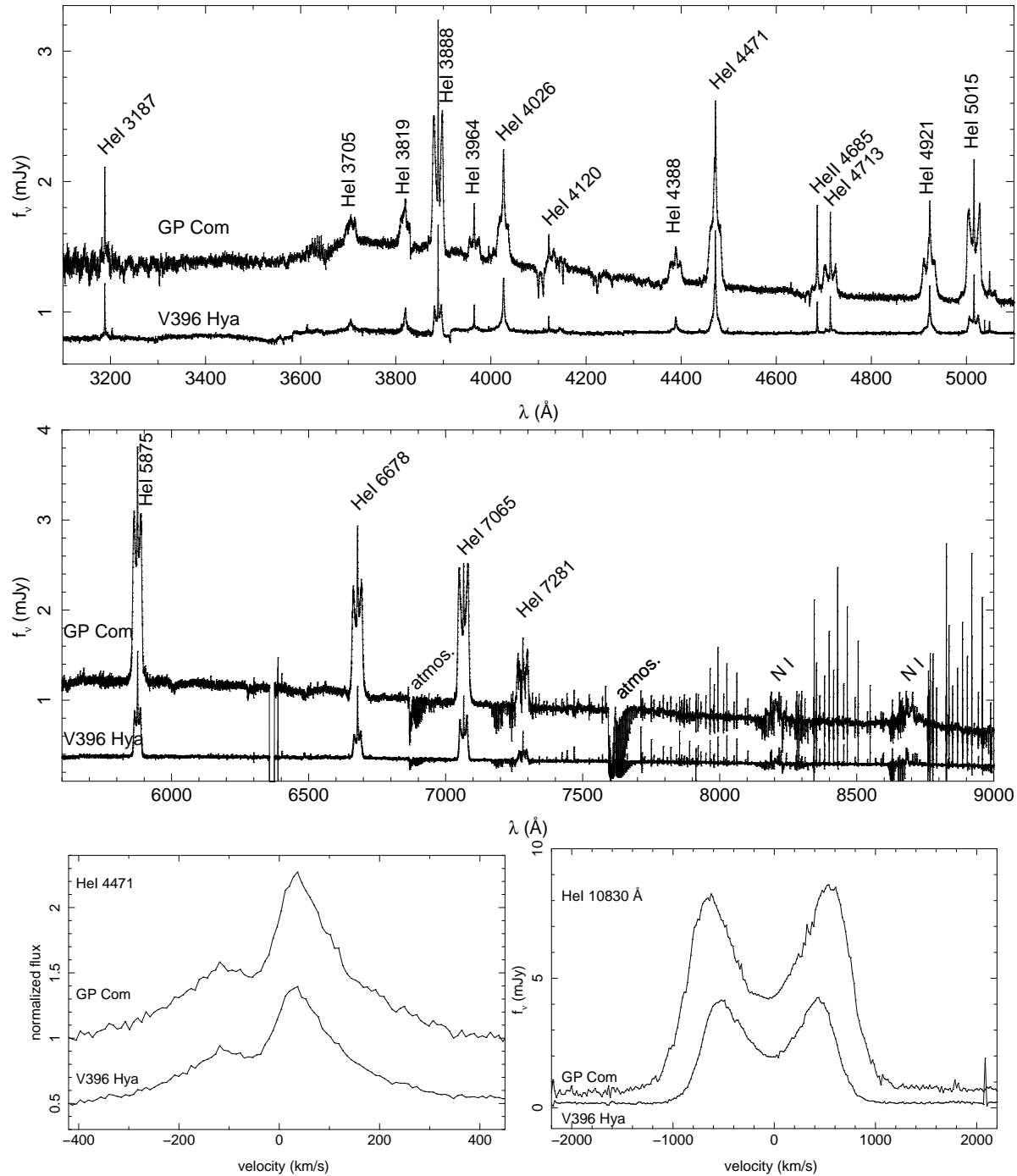
Figure 5.1: Gaussian smoothed average spectrum of GP Com and V396 Hya obtained with VLT/X-Shooter. Helium emission lines are indicated. The lower panel shows the central spike feature with its blueshifted forbidden component in He I 4471 Å observed with UVES and the strongest helium lines in the NIR arm observed with X-Shooter. The narrow spikes at wavelength > 7500 Å are residuals from the nights sky line removal.

Table 5.2: Emission line properties for GP Com

He line	UVES		X-Shooter	
	EW range (Å)	EW mean (Å)	EW range (Å)	EW mean (Å)
3187.745	-	-	0.5-1.6	1.02
3705.005	-	-	2.6-3.8	3.22
3819.607	-	-	1.7-4.0	2.96
3871.791 3888.643	$6.2\text{-}11.1^a$	8.55^a	$10.9\text{-}14.9^a$	12.62^a
3964.730	0.7-2.1	1.38	1.2-2.3	1.80
4026.191	4.6-8.7	6.56	5.2-9.5	7.29
4387.929	1.1-2.9	1.92	2.9-4.9	3.93
4471.502	8.3-14.9	11.0	11.7-20.3	14.82
4685.710 4713.170	$3.5\text{-}6.5^b$	4.9^b	$5.9\text{-}9.0^b$	7.19^b
4921.930	5.0-8.7	6.75	8.1-12.4	10.43
5015.678 5047.738	$9.9\text{-}14.8^c$	12.4^c	$17.4\text{-}22.2^c$	20.1^c
5875.661	30.4-62.7	44.1	46.7-58.8	52.41
6678.152	24.8-38.1	30.7	36.9-46.1	42.47
7065.251	35.3-51.0	41.5	47.8-56.2	51.5
7281.351	11.0-36.5	18.2	16.1-19.4	18.15
10 830.34	-	-	581.0-736.6	666.9
12 784.79	-	-	d	d
17 002.47	-	-	d	d
20 586.92	-	-	d	d

[a] Combined equivalent width of He I 3871 and He I 3888

[b] Combined equivalent width of He II 4685 and He I 4713

[c] Combined equivalent width of He I 5015 and He I 5047

[d] Line present but contaminated with atmosphere.

Table 5.3: Emission line properties for V396 Hya

He line	UVES EW range (Å)	UVES EW mean (Å)	X-Shooter EW mean (Å)
3187.745	-	-	3.8
3705.005	-	-	2.2
3819.607	-	-	5.5
3871.791 3888.643	14.0-27.9^a	20.8^a	15.9^a
3964.730	2.8-5.2	3.7	2.2
4026.191	16.4-25.4	20.94	11.0
4387.929	4.6-7.7	6.1	3.3
4471.502	24.4-39.0	31.1	18.2
4685.710 4713.170	8.1-14.4^b	11.1^b	5.8^b
4921.930	11.6-20.1	15.3	9.1
5015.678 5047.738	17.5-29.9^c	22.7^c	13.6^c
5875.661	58.3-101.8	76.4	51.5
6678.152	45.0-71.7	57.2	34.6
7065.251	54.2-89.1	70.9	50.6
7281.351	19.3-38.0	24.5	13.1
10 830.34	-	-	969.5
12 784.79	-	-	^{d}
17 002.47	-	-	^{d}
20 586.92	-	-	^{d}

^{a} Combined equivalent width of He I 3871 and He I 3888
^{b} Combined equivalent width of He II 4685 and He I 4713
^{c} Combined equivalent width of He I 5015 and He I 5047
^{d} Line present but contaminated with atmosphere.
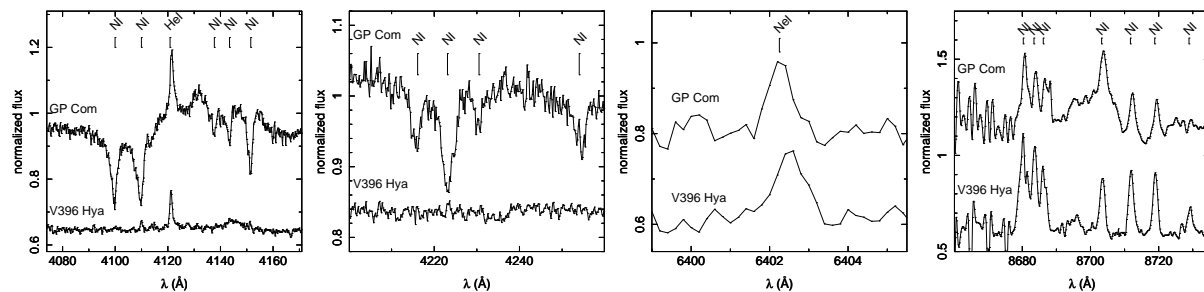
Figure 5.2: Zoomed region of the average X-Shooter spectra around locations of various metal lines in GP Com and V396 Hya.
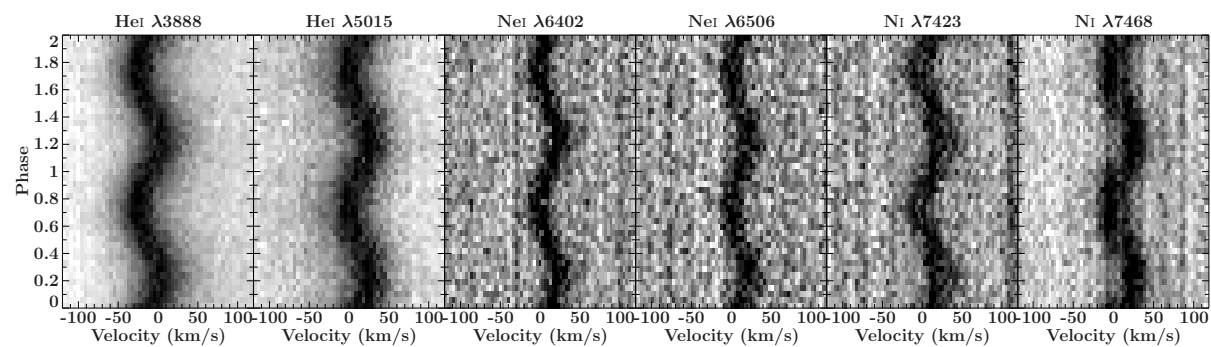
Figure 5.3: Tracing of the central spike of selected helium lines and some neon and nitrogen emission lines of GP Com from UVES data.

The equivalent widths of these blends of N I are larger in V396 Hya than in GP Com. We also identify a number of weak Ne I emission features in the spectra of both systems (see Fig. 5.2 and 5.3). See Tab. 5.6 and 5.7 for an overview of the detected lines with measured equivalent widths.

The X-Shooter spectra allow us to search for spectroscopic signatures in the near-infrared part of the spectrum. We find a strong He I 10 830Å line with an equivalent width of 666.9 Å and 969.5 Å, which is more than ten times stronger than the strongest optical helium lines. None of the helium lines in the near-infrared spectrum of GP Com and V396 Hya show a sharp central spike feature (lower right panel Fig. 5.1), a somewhat surprising difference to the optical regime. The peak-to-peak velocity of the double peaked disc emission line He I 10 830Å was found to be $1237 \pm 7\,\mathrm{km\,s^{-1}}$ for GP Com and $1069 \pm 6\,\mathrm{km\,s^{-1}}$ for V493 Hya which is significantly lower than the $1379\text{-}1414\,\mathrm{km\,s^{-1}}$ range for GP Com and the $1111\text{-}1124\,\mathrm{km\,s^{-1}}$ range for V493 Hya using the lines in the optical regime.

5.3.2 The orbital ephemeris

Marsh (1999) and Morales-Rueda et al. (2003a) have demonstrated that the central spike in GP Com shows significant radial velocity shifts as a function of the orbital phase, with an amplitude of $\sim 10 - 15$ km/s, compatible with its likely origin close to the accretor.

We perform multi-Gaussian fits to the individual line profiles, modelling the line as a com-

Table 5.4: Velocity of the central spike

| HeI line | GP Com | | V396 Hya | |
| | γ | K_1 | γ | K_1 |
(Å)	(km s^{-1})	(km s^{-1})	(km s^{-1})	(km s^{-1})
3888.643	-4.7 ± 0.2	12.7 ± 0.3	-9.9 ± 0.3	6.1 ± 0.4
3964.730	-4.1 ± 1.1	13.0 ± 1.6	-2.5 ± 1.2	5.8 ± 1.6
4387.929	14.5 ± 2.3	11.5 ± 3.2	20.1 ± 3.4	8.6 ± 4.2
4471.502	42.4 ± 0.5	11.1 ± 0.7	39.4 ± 0.6	5.4 ± 0.9
4685.710	17.4 ± 0.3	11.7 ± 0.5	16.1 ± 0.5	5.2 ± 0.6
4713.170	32.6 ± 0.3	11.1 ± 0.5	27.3 ± 0.5	4.3 ± 0.6
4921.930	52.6 ± 1.0	12.3 ± 1.6	47.8 ± 0.8	5.8 ± 1.1
5015.678	6.4 ± 0.3	12.3 ± 0.4	7.5 ± 0.4	6.0 ± 0.5
5875.661	0.4 ± 0.3	11.3 ± 0.3	2.5 ± 0.3	5.1 ± 0.5
6678.152	18.2 ± 0.2	11.6 ± 0.2	11.2 ± 0.3	6.8 ± 0.3
7065.251	23.2 ± 0.2	13.3 ± 0.3	16.0 ± 0.3	6.2 ± 0.4
7281.351	17.2 ± 0.2	8.0 ± 0.4	16.3 ± 0.4	4.1 ± 0.5
Mean		11.7 ± 0.3		5.8 ± 0.5

bination of two broad Gaussians representing the double peaked disc emission plus a narrow Gaussian for the spike. As a first step, we fit the velocities of the central spike to the individual spectra. The derived radial velocity curves are then used to determine the orbital phasing of the spike.

Although the UVES data and X-Shooter data were taken eight years apart the orbital period could not be refined because the X-Shooter data only covers about one orbit of GP Com. Therefore, for GP Com, we fix the orbital period to 46.57 minutes (Marsh, 1999). If the radial velocity curve of the spike traces the white dwarf accretor, we can define orbital phase zero as the phase of superior conjunction of the accretor (or blue to red crossing in the radial velocity curve). Individual lines give identical zero-points for the phasing, we thus fit to the three strongest helium lines simultaneously, and derive the following ephemeris for GP Com taking either the UVES or the X-Shooter data:

$$\mathrm{HJD}_{\mathrm{GP\,Com;UVES}} = 2452372.5994(2) + 0.0323386E$$

$$\mathrm{HJD}_{\mathrm{GP\,Com;X-Shooter}} = 2455245.851(2) + 0.0323386E$$

In the case of V396 Hya, the orbital period is not that well constrained, but the short duration of our observations prevents an improvement on the value of 65.1 minutes as derived by Ruiz et al. (2001). The X-Shooter data could not be used because the exposure time of the individual spectra was 15 min which covers a significant fraction of the orbit. We again use the radial velocity curve of the spike in the three strongest lines to derive the following ephemeris for V396 Hya
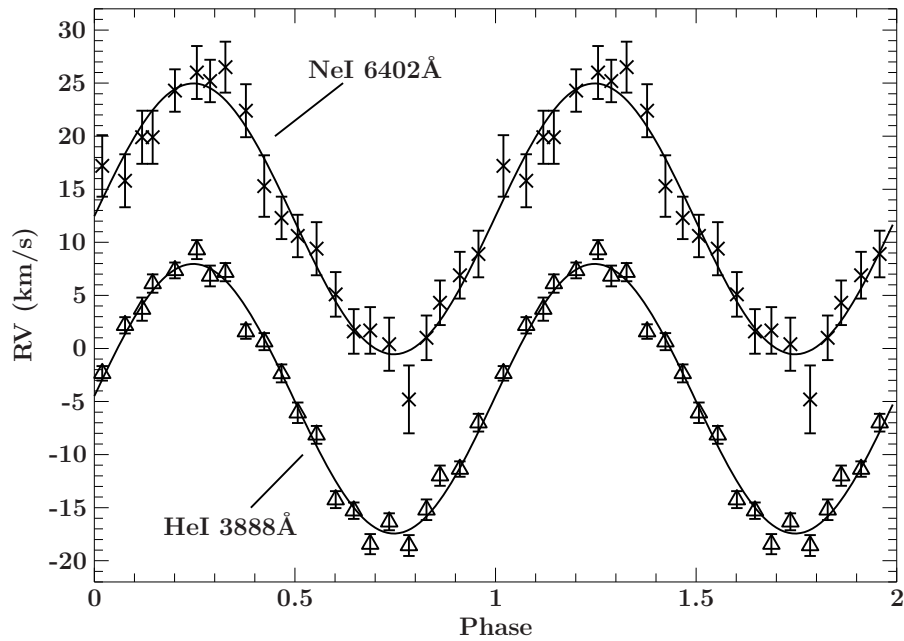
Figure 5.4: Radial velocity curves of the central spike of He I 3888 Å and the emission line Ne I 6402 Å in GP Com. Two orbits are plotted for better visualisation.
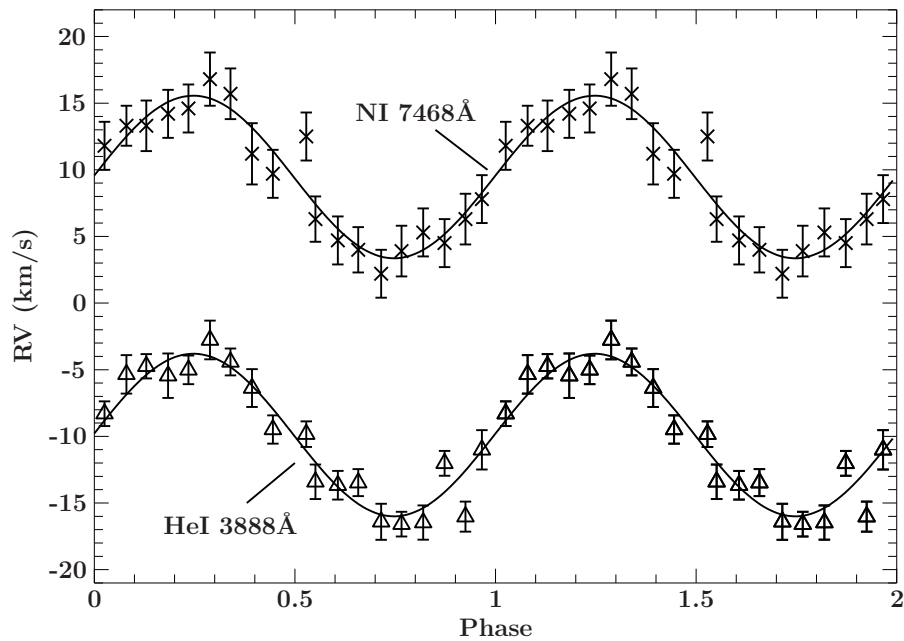

Figure 5.5: Radial velocity curves of the central spike of He I 3888 Å and the emission line N I 7468 Å in V396 Hya. Two orbits are plotted for better visualisation.
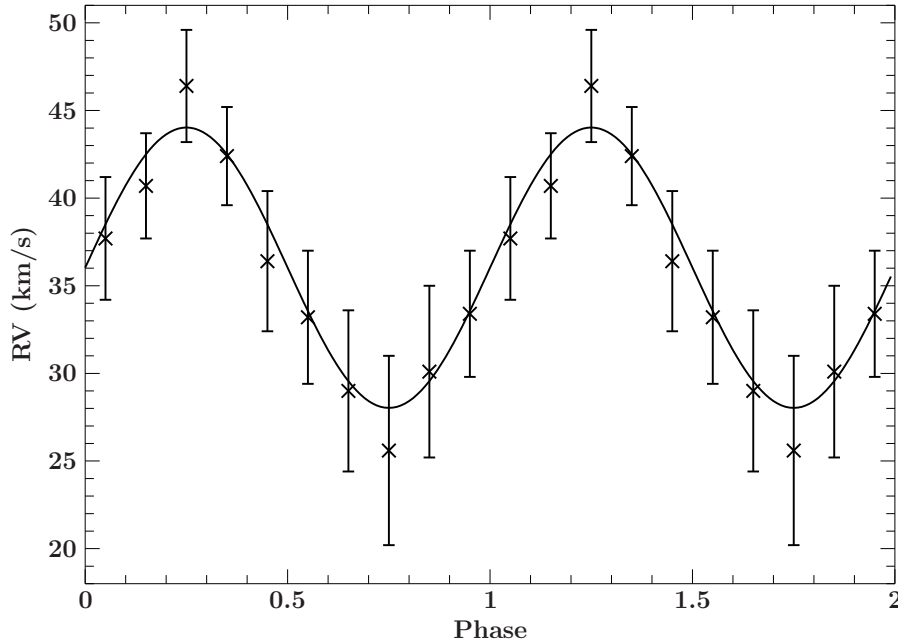
Figure 5.6: Radial velocity curve with measured velocities of the nitrogen absorption line N I 4143 Å in
GP Com. Two orbits are plotted for better visualisation.

$$\mathrm{HJD_{V396\,Hya;UVES}} = 2452372.5263(3) + 0.0452083E$$

Armed with the orbital ephemerides, we fold all spectra in order to obtain higher signal-
to-noise spectra, permitting us to derive more accurate values for the radial velocity curve of
the various emission line components. All orbital phases reported in this paper are based on
the above ephemerides.

5.3.3 The radial velocity of the central spike and the metal lines

The final radial velocity curves of the central spike components are measured by fitting to the
phase-folded spectra and fixing the period and phasing according to the derived ephemeris. A
pure sinusoid was fitted to the radial velocities to determine the mean and amplitude of the
orbital motion of the spike and their formal errors. Table 5.4 lists the properties of the spike in
all the helium lines for which a reliable fit could be made, for both our targets.

We find that all 12 usable helium lines covered by the UVES spectra are consistent with
the same radial velocity amplitude for the central spike component and thus we calculate a
weighted mean from the 12 fitted amplitudes to derive $K_{\mathrm{spike}} = 11.7 \pm 0.3\,\mathrm{km\,s^{-1}}$ for GP Com
and $K_{\mathrm{spike}} = 5.8 \pm 0.3\,\mathrm{km\,s^{-1}}$ for V396 Hya. The fact that all lines share the same phasing and
velocity amplitudes provides strong support for placing the origin of the spike at or near the
primary white dwarf, thus providing us with an accurate determination of its radial velocity
amplitude, K_1. However, the mean velocities of the central spike show variations from line to
line, from -5 to $+53\,\mathrm{km\,s^{-1}}$. The seemingly random velocity shifts reported by Marsh (1999)
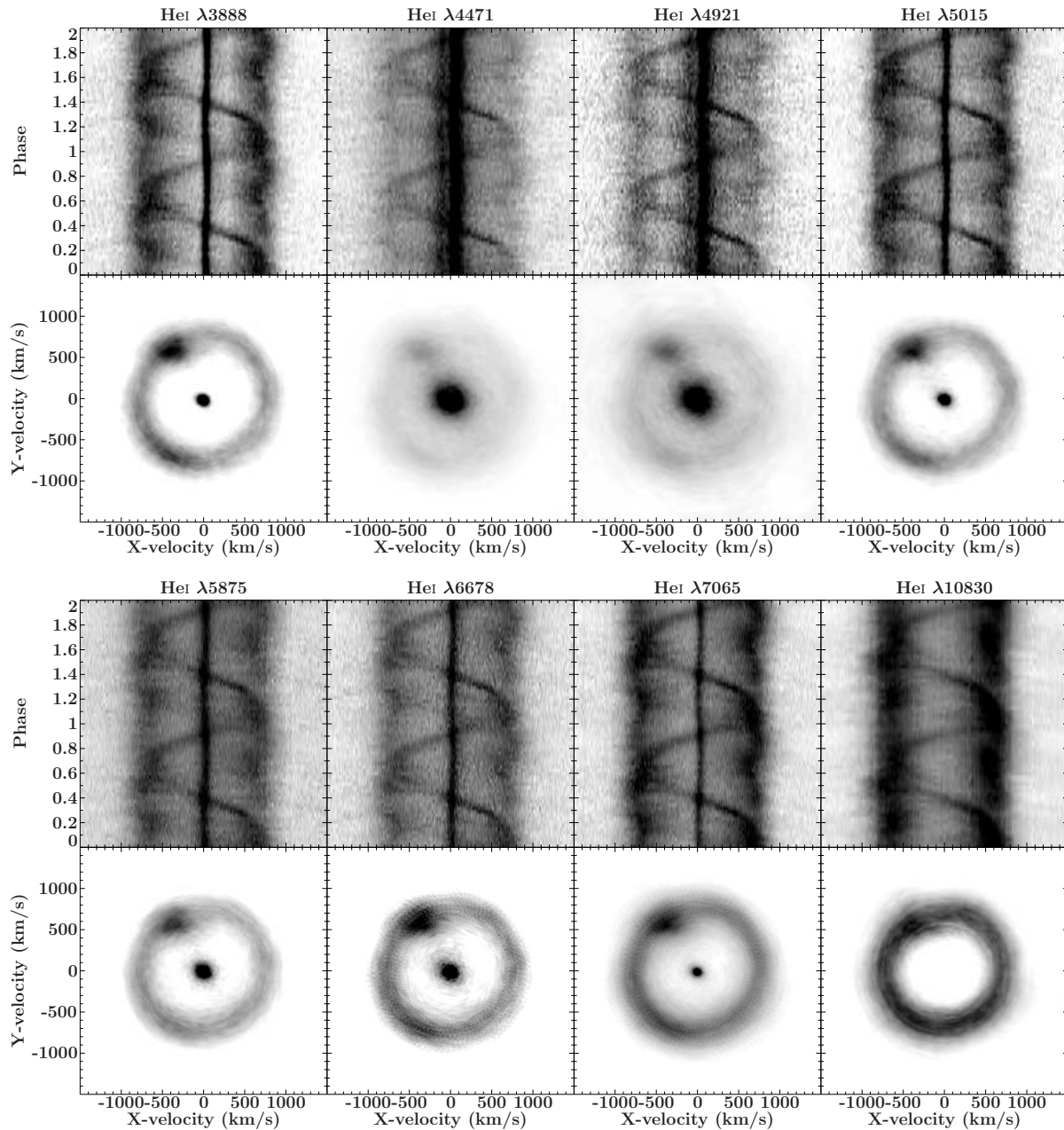
Figure 5.7: Trailed spectra and maximum-entropy Doppler tomograms of selected He I lines of GP Com obtained from XShooter data. Visible is the disc, the central spike as well as two bright spots in most lines. Note that in some lines the central spike was saturated to emphasize both bright spots.
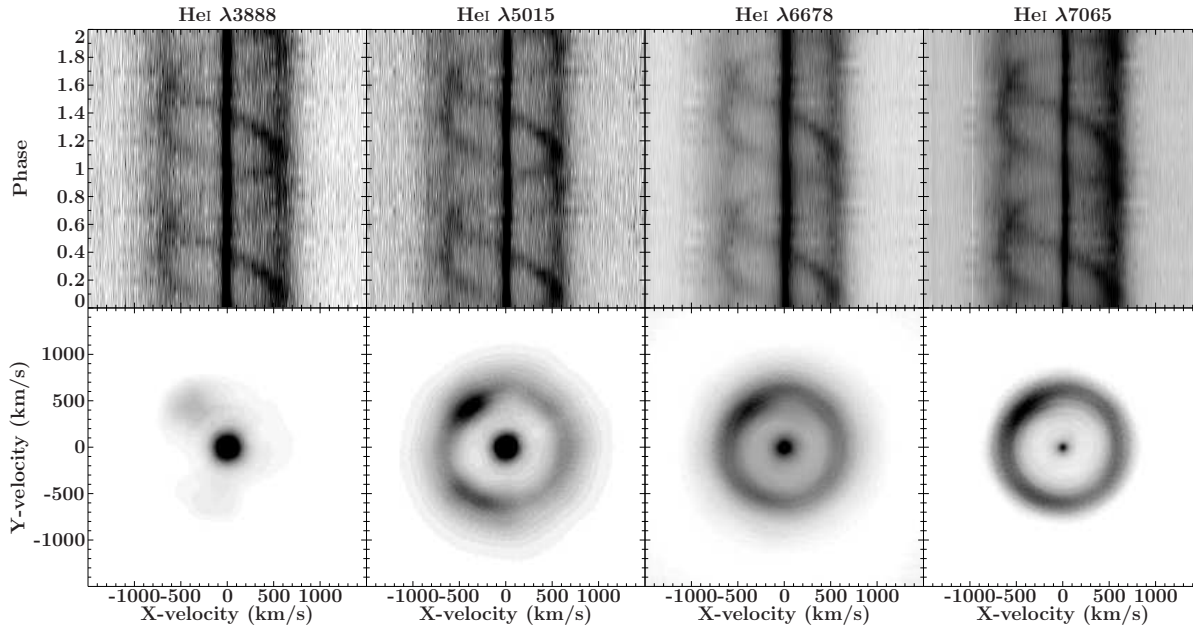
Figure 5.8: Trailed spectra and maximum-entropy Doppler tomograms of selected He I lines of V396 Hya obtained from the UVES data. Visible is the disc, the central spike as well as both bright spots in some lines. Note that in some lines the central spike was saturated to emphasize both bright spots.

and Morales-Rueda et al. (2003a) are thus confirmed in our high resolution data and extended to a larger number of lines. The shifts strongly correlate between those two stars.

Not only the central spike feature shows radial velocity variations. We find that the narrow emission lines of neon and nitrogen as well as the absorption lines in GP Com trace the motion of the central spike. Figure 5.3 shows a trailed spectrogram of the center of two strong helium emission lines as well as the two strongest nitrogen and neon emission lines in GP Com. A sinusoidal fit was made to the radial velocities of these line as obtained from the phase folded spectra. The radial velocity amplitude and phase are consistent with those of the central spike feature in the helium lines. For the co-added neon and nitrogen lines, we derive a mean amplitude $K_{\mathrm{emission}} = 12.3 \pm 0.5 \, \mathrm{km \, s^{-1}}$ and a mean velocity $\gamma = 11.88 \pm 0.9 \, \mathrm{km \, s^{-1}}$ for GP Com (Fig. 5.4) and $K_{\mathrm{emission}} = 5.6 \pm 0.8 \, \mathrm{km \, s^{-1}}$ and $\gamma = 10.2 \pm 1.6 \, \mathrm{km \, s^{-1}}$ for V396 Hya (Fig. 5.5).

The same approach was used for the N I 4143 Å absorption line in GP Com. We measure the radial velocities of the N I 4143 Å absorption line in the phase folded spectra and find a radial velocity amplitude of $K_{4143} = 8.5 \pm 2.1 \mathrm{km \, s^{-1}}$ with a mean velocity of $\gamma = 35.5 \pm 2.5 \, \mathrm{km \, s^{-1}}$. The radial velocity amplitude is consistent with the amplitude obtained for the central spikes (Fig. 5.6). Therefore, we conclude that the metal emission and absorption lines are linked to the accreting white dwarf as well.
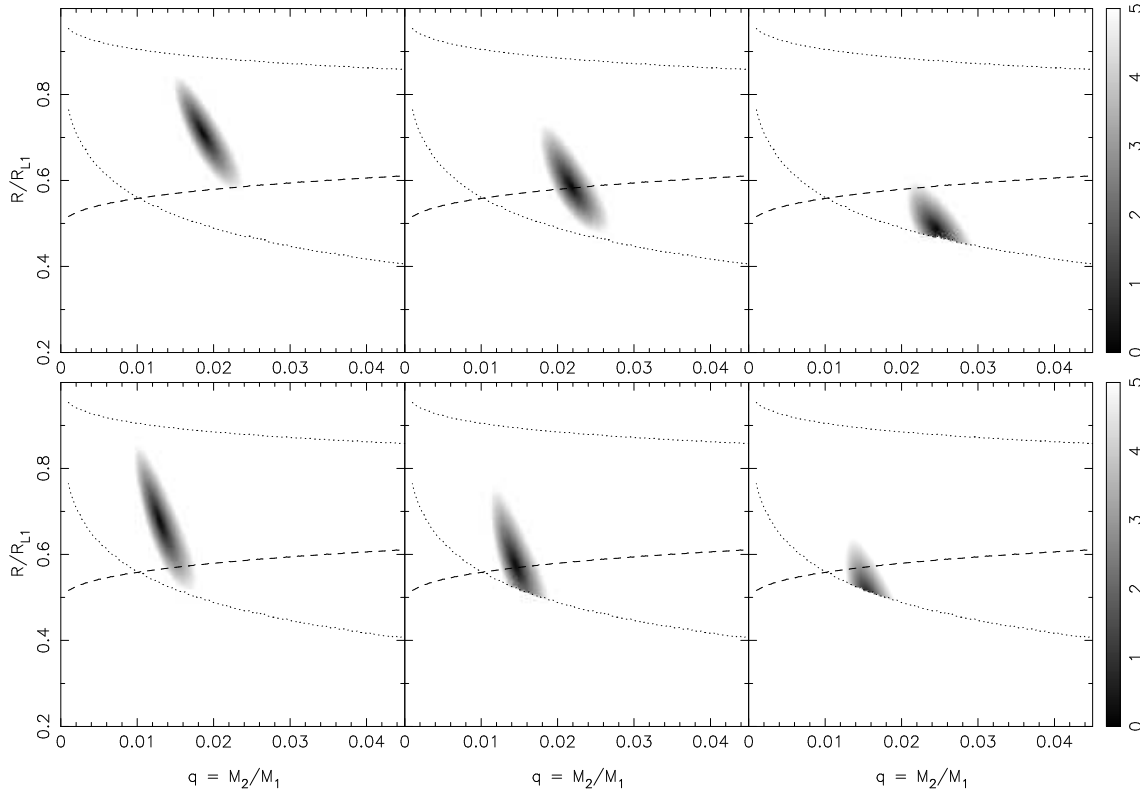
Figure 5.9: Allowed mass ratios q and effective accretion disc radii R for GP Com (top) and V396 Hya (bottom). The left panels assume ballistic accretion stream velocities in the bright spot, the right panels assume Keplerian disc velocities. Since the bright spot could be a mix of these, we show in the center panels the results for a mix of 80% ballistic stream velocities and 20% Keplerian disc velocities. The upper and lower dotted lines indicate the edge of the primary Roche lobe and the circularization radius, respectively, while the dashed line shows the 3:1 resonance radius. The gray-scale indicates the exclusion level in standard deviations.

5.3.4 System parameters via Doppler tomography

Doppler tomography (Marsh & Horne, 1988) of GP Com has been used in the past to study the properties of its accretion disc and bright spot emission (Marsh, 1999; Morales-Rueda et al., 2003a). Armed with an accurate estimate for the primary radial velocity K_1 (assuming the spike originates on or close to the accreting white dwarf), we can constrain the mass ratios by comparing gas velocities along ballistic trajectories of the accretion stream to the observed bright spot velocities in a Doppler tomogram, as has been done for several of the AM CVn stars that show a central spike (Roelofs et al., 2005, 2006a).

Fig. 5.7 and 5.8 show maximum-entropy Doppler tomograms of GP Com and V396 Hya. The central spikes are fixed to the negative Y-velocity axis, the conventional phase of the accreting white dwarf. A strong bright spot shows up near the expected accretion stream/disc impact region, with a faint secondary bright spot at $\sim$120-degree phase-offset, which was also observed in other AM CVn type systems (Roelofs et al., 2005; Kupfer et al., 2013). We assume that the strong bright spot corresponds to the first impact point of the accretion stream and the

disc, while the weaker bright spots may represent accretion stream overflow and re-impact further downstream. The latter effect has been seen in numerical simulations of accretion discs (M. Wood, in preparation; private communication).

Figure 5.9 shows the allowed mass ratios and accretion disc radii for GP Com and V396 Hya that we obtain from the phases and amplitudes of the central spikes and the primary bright spot. We solve the equation of motion for a free-falling stream of matter through the inner Lagrangian point, based on the results of Lubow & Shu (1975), and we see whether the resulting accretion stream and/or accretion disc velocities and phases at the stream-disc impact point match with the measured values. The bright spot in interacting binaries is not always observed to represent the pure ballistic stream velocities at the stream-disc impact point; the gas velocities could in principle lie anywhere between the ballistic stream velocities and the accretion disc velocities in the disc-stream impact region. We therefore consider the two limiting cases of pure ballistic stream and pure Keplerian disc velocities in the bright spot. The mass ratio and accretion disc radii (i.e., where the bright spot occurs) ranges we obtain in this way for GP Com are $0.015 < q < 0.022$ and $0.60 < R/R_{L_1} < 0.80$ assuming purely ballistic stream velocity and $0.021 < q < 0.028$ and $0.45 < R/R_{L_1} < 0.58$ assuming purely Keplerian disc velocity. For V396 Hya we find $0.010 < q < 0.016$ and $0.54 < R/R_{L_1} < 0.84$ assuming purely ballistic stream velocity and $0.013 < q < 0.018$ and $0.50 < R/R_{L_1} < 0.62$ assuming purely Keplerian disc velocity. R_{L_1} corresponds to the distance from the center of the accreting white dwarf to the inner Lagrangian point.

With the derived mass ratios and the primary velocity amplitude K_1 as well the measured disc velocities we can limit the inclination angles, the component masses and the disc sizes. Above a certain inclination angle the donor will start to eclipse the outer edges of the disc and, at high enough inclination, also the accretor. No eclipses are observed in both systems either in the lines nor in the continuum.

While these mass ratios and disc radii lie in the range where superhumps might be expected due to the $3:1$ resonance, numerical simulations indicate that the mass ratios are in fact so low that the (eccentric) accretion disc remains stationary in the binary frame (Simpson & Wood, 1998). This matches the absence of any reports of 'superhumps' in GP Com and V396 Hya.

For a given mass ratio and donor mass we calculate the expected primary velocity amplitudes. The ratio of the calculated velocity amplitudes and the measured velocity amplitudes depends only on the inclination angle. Additionally, the measured peak-to-peak (Keplerian) velocities in the double peaked lines correlate to the velocity in the outer disc, and also depend on the inclination in a similar fashion. (Horne & Marsh, 1986).

Figure 5.10 and 5.11 show the calculated inclination angles for different donor masses for GP Com assuming either purely ballistic stream or purely Keplerian velocity of the bright spot. As a lower mass limit of the donor, the mass for a Roche lobe filling zero-temperature helium object is calculated (Deloye et al., 2007). The upper limit for the donor masses are set by the Chandrasekhar mass. The dotted line in Fig. 5.10 and 5.11 corresponds to the largest allowed disc radius ($0.80\,R/R_{L_1}$ for pure ballistic stream velocities and $0.58\,R/R_{L_1}$ assuming pure Keplerian disc velocity). The largest allowed disc radius is an upper limit. The dashed-dotted line in Fig. 5.10 and 5.11 corresponds to the largest possible mass ratio ($q = 0.022$
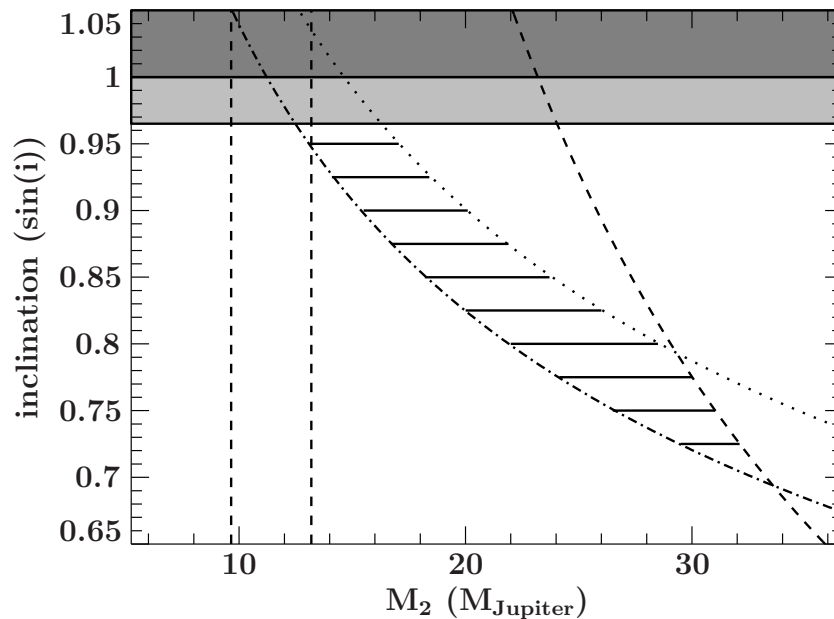
Figure 5.10: Calculated inclination angles for different donor masses for GP Com assuming purely ballistic stream velocities. The left vertical dashed line marks the zero temperature mass for the donor star, the right dashed line marks the upper limit of the donor mass found by Roelofs et al. (2007a) and the curved dashed line marks the limit when the accretor reaches the Chandrasekhar limit. The dark grey shaded area marks the region where the inclination angle exceeds 90° and the grey shaded area marks the region where the system would show eclipses assuming the largest possible disc radius. The dotted line corresponds to the largest disc radius and the dashed-dotted line to the largest mass ratio. The hatched area shows the allowed parameter range.
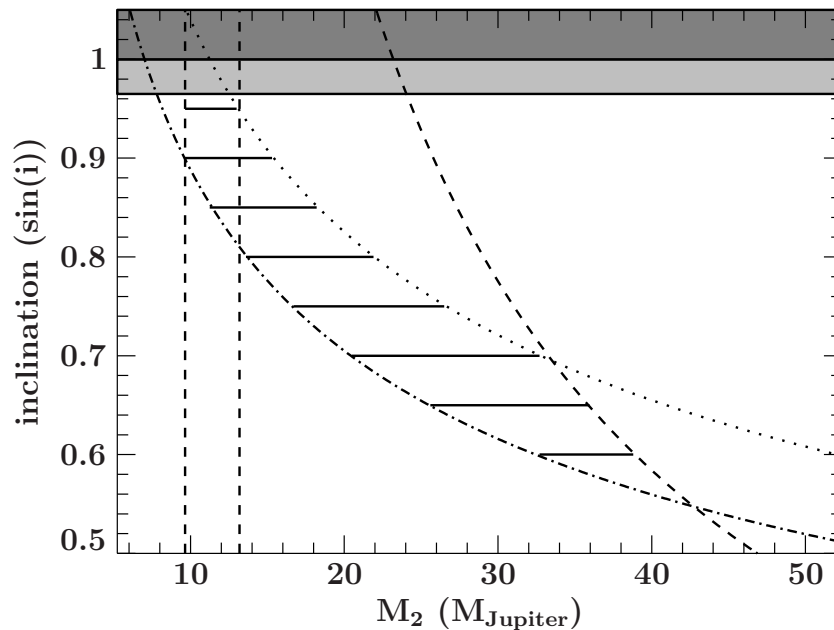
Figure 5.11: The same as for Fig. 5.10 but assuming purely Keplerian disc velocities.

for pure ballistic stream velocities and $q = 0.028$ assuming pure Keplerian disc velocities). Smaller mass ratios would shift the dashed dotted lines to right. Hence, the largest mass ratio is a lower limit. Combining these constraints leaves a small region of parameter space that is allowed.

The possible system parameters for GP Com lie in the hatched area in Fig. 5.10 and 5.11. For purely ballistic stream velocity we find a donor mass range of $12.5 < M_{2,\mathrm{GP\,Com}}/M_{\mathrm{Jupiter}} < 33.8$, a limit to the accretor mass of $M_{1,\mathrm{GP\,Com}} > 0.55\,M_\odot$, a range for the disc size of $0.68 < R/R_{L_1} < 0.80$ and a mass ratio range of $0.020 < q < 0.022$. We also derive an inclination angle range of $45° < i < 74°$. The lower limit on the inclination angle was found for the maximum accretor mass and the upper limit is set when the accretor would eclipse the outer edge of the disc. For purely Keplerian disc velocities we find a donor mass range of $9.6 < M_{2,\mathrm{GP\,Com}}/M_{\mathrm{Jupiter}} < 42.8$, a limit of the accretor mass of $M_{1,\mathrm{GP\,Com}} > 0.33\,M_\odot$, a disc size range of $0.45 < R/R_{L_1} < 0.58$ and mass ratio range of $0.024 < q < 0.028$. We derive an inclination angle range of $33° < i < 74°$.

From the mass accretion rate, Roelofs et al. (2007a) found an upper limit of $M_{2,\mathrm{GP\,Com}} = 13.2\,M_{\mathrm{Jupiter}}$ for the donor star in GP Com. If we assume this companion mass as upper limit we can set tighter constraints on the system parameter. Figure 5.10 shows that there is only a small allowed parameter range for purely ballistic stream velocities. For purely ballistic stream velocity we find a donor mass range of $12.5 < M_{2,\mathrm{GP\,Com}}/M_{\mathrm{Jupiter}} < 13.2$, a limit to the accretor mass of $0.55 < M_{1,\mathrm{GP\,Com}} < 0.59\,M_\odot$, a range for the disc size of $0.68 < R/R_{L_1} < 0.70$ and a mass ratio range of $0.0215 < q < 0.022$. We also derive an inclination angle range of $71° < i < 74°$. For purely Keplerian disc velocities (Fig. 5.11) we find an accretor mass range of $0.33 < M_{1,\mathrm{GP\,Com}} < 0.52\,M_\odot$, a disc size range of $0.45 < R/R_{L_1} < 0.58$ and mass ratio range of $0.024 < q < 0.028$. We derive an inclination angle range of $53° < i < 74°$.

Although we cannot be certain about a zero-temperature donor star in GP Com, at the orbital period of V396 Hya there should be no doubt that the donor is essentially a zero-temperature white dwarf even in the case of irradiation (Deloye et al., 2007). Therefore the mass of the donor is a fixed parameter. From the mass-radius relation for a zero-temperature helium object (equation 14 in Deloye et al., 2007), we derive a mass for the donor star in V396 Hya of $M_{2,\mathrm{V396\,Hya}} = 6.1\,M_{\mathrm{Jupiter}}$. Figure 5.12 and 5.13 show the calculated inclination angles for different donor masses in V396 Hya. Using the same approach as for GP Com we find for purely ballistic stream velocities an accretor mass range of $0.37 < M_{1,\mathrm{V396\,Hya}}/M_\odot < 0.49$, a disc size range of $0.54 < R/R_{L_1} < 0.66$ and a mass ratio range of $0.012 < q < 0.016$. We derive an inclination angle range of $51° < i < 78°$. For purely Keplerian disc velocities an accretor mass range of $0.32 < M_{1,\mathrm{V396\,Hya}}/M_\odot < 0.45$, a disc size range of $0.50 < R/R_{L_1} < 0.62$ and a mass ratio range of $0.013 < q < 0.018$ was derived. We find an inclination angle range of $47° < i < 78°$.

Table 5.5 gives an overview of the derived system parameters either assuming pure ballistic stream velocities or pure Keplerian disc velocities.
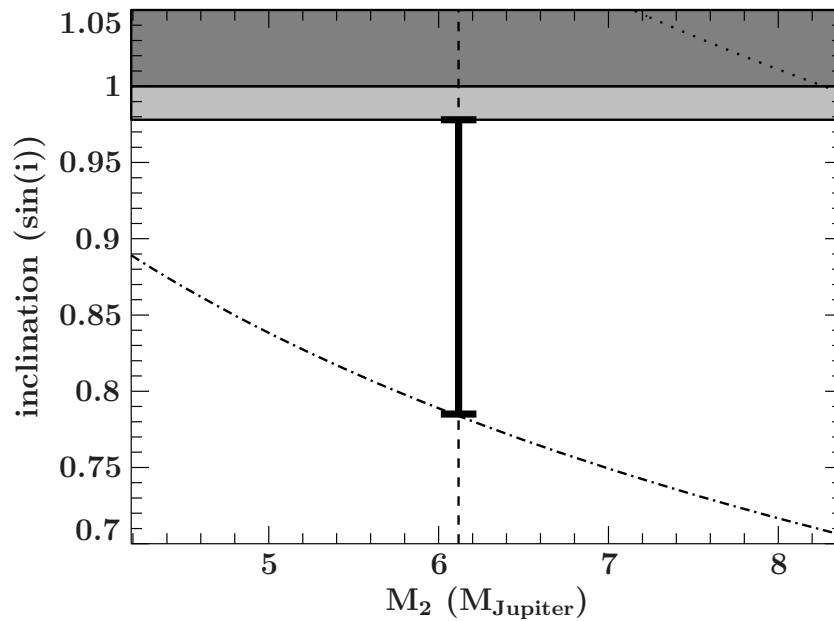
Figure 5.12: Calculated inclination angles for different donor masses for V396 Hya assuming purely ballistic stream velocities. The vertical dashed line marks the zero temperature mass for the donor star. The dark grey shaded area marks the region where the inclination angle exceeds 90° and the grey shaded area marks the region where the system would show eclipses assuming the largest possible disc radius. The dotted line corresponds to the largest disc radius and the dashed-dotted line to the largest mass ratio. The thick black line shows the allowed range on the binary inclination to the line of sight.
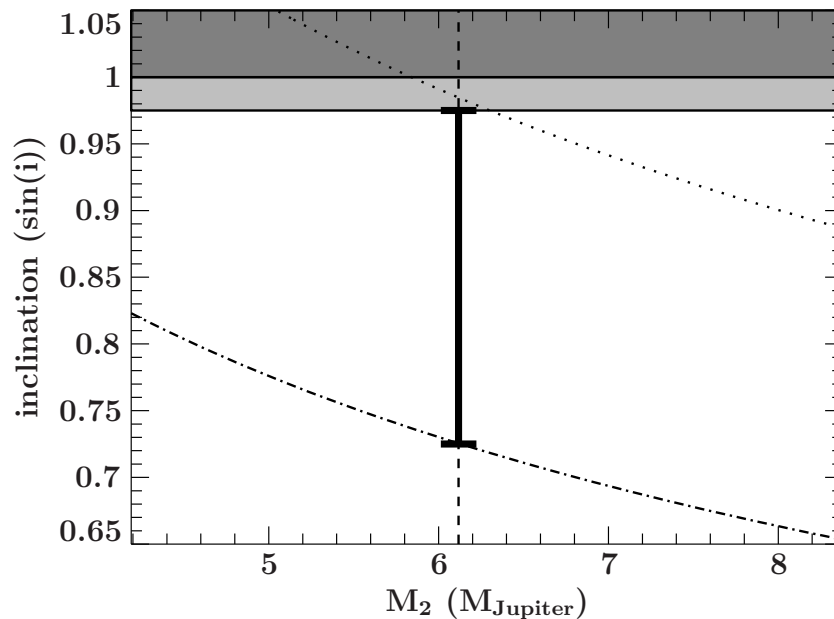

Figure 5.13: The same as for Fig. 5.12 but assuming purely Keplerian disc velocities.

Table 5.5: System parameter either assuming pure ballistic stream velocities pure Keplerian disc velocities.

	pure ballistic stream	pure Keplerian disc
GP Com (donor mass limit from Roelofs et al., 2007a)		
q	0.0215 - 0.022	0.024 - 0.028
M_1 ($M_\odot$)	0.54 - 0.59	0.33 - 0.52
M_2 (M_{Jupiter})	12.5 - 13.2	9.6 - 13.2
R/R_{L_1}	0.68 - 0.70	0.45 - 0.58
i (°)	71 - 74	53 - 74
GP Com (no restrictions for the donor mass)		
q	0.020 - 0.022	0.024 - 0.028
M_1 ($M_\odot$)	> 0.54	> 0.33
M_2 (M_{Jupiter})	12.5 - 33.8	9.6 - 42.8
R/R_{L_1}	0.68 - 0.80	0.45 - 0.58
i (°)	45 - 74	33 - 74
V396 Hya		
q	0.012 - 0.016	0.013 - 0.018
M_1 ($M_\odot$)	0.37 - 0.49	0.32 - 0.45
M_2 (M_{Jupiter})	6.1	6.1
R/R_{L_1}	0.54 - 0.66	0.50 - 0.62
i (°)	51 - 78	47 - 78

5.4 Discussion

5.4.1 Stark broadening and the behaviour of the central emission spikes

The forbidden components of neutral helium that are observed in some of the central spikes (Fig. 5.14) have led to the suggestion that the central spike profiles may be affected by Stark broadening (Morales-Rueda et al., 2003a), as modelled by Beauchamp et al. (1997) and Beauchamp & Wesemael (1998) for (single) DB white dwarfs and extreme helium (EHe) stars. Unfortunately those models appeared to predict the wrong splittings between the allowed and forbidden emission features in GP Com, such that questions remained as to whether the Stark broadening explanation was correct (Morales-Rueda et al., 2003a).

However as shown in Fig. 1 of Griem (1968), the splitting of allowed and forbidden transitions of neutral helium depends on the electron density n_e. The splittings of the absorption lines in those models are therefore relevant for those respective stellar atmospheres only. The emission lines in GP Com and V396 Hya may be caused by a single-temperature, optically thin layer of helium (see analysis by Marsh et al., 1991), such that the splittings between the allowed and forbidden transitions have a different value corresponding to the local electron density in the layer.
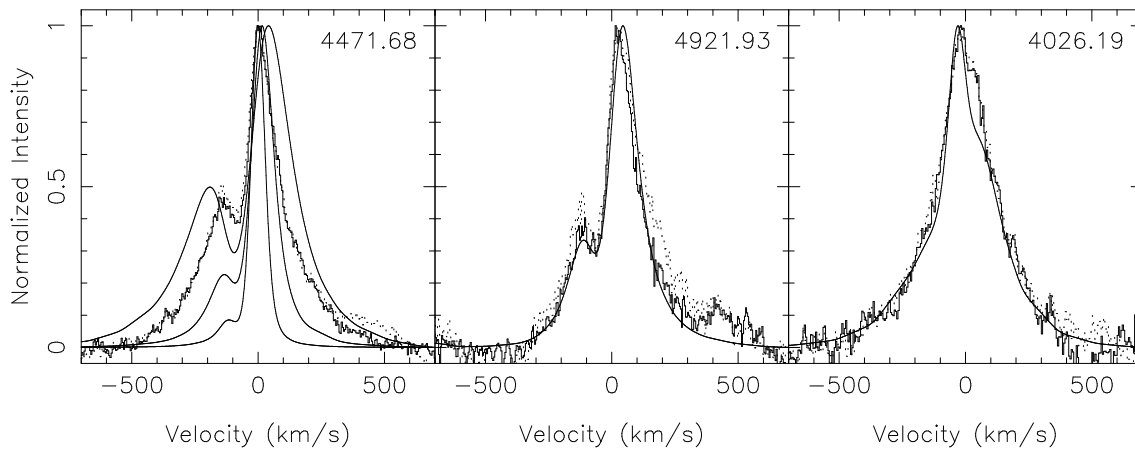
Figure 5.14: Observed spikes from the UVES spectra in GP Com (dotted histogram) and V396 Hya (solid histogram) for the three He I lines that contain observed forbidden components, together with the modelled Stark-broadened line profiles (solid line) from Beauchamp et al. (1997). The left panel shows how the amplitude and displacement of the forbidden component increases with electron density; the models shown are for electron densities of $n_e = 1 \times 10^{15}$, 3×10^{15}, and 1×10^{16} cm^{-3}. In the middle and right panel we show the model for $n_e = 3 \times 10^{15}$ cm^{-3}.

In Fig. 5.14 we show the observed profiles of the central spikes in the HeI 4471 Å and HeI 4921 Å lines in detail. Both these lines show a forbidden component blueward of the allowed transition, the strength and distance of which (relative to the allowed component) can be correctly reproduced by Stark-broadened line profile models for helium plasma with an electron density close to $n_e \simeq 5 \times 10^{15}$ cm^{-3}. The models shown in Fig. 5.14 are from Beauchamp et al. (1997), as obtained in tabular form from the stellar spectral synthesis program SPECTRUM. As an independent check, Fig. 1 in Griem (1968) points to a similar electron density.

In addition to the forbidden neutral helium lines near HeI 4471 Å and HeI 4921 Å, there is a blended forbidden component predicted blueward of HeI 4026 Å, which is confirmed by our data and can be seen in the asymmetric line profile of HeI 4026 Å (Fig. 5.14). For the other lines, assuming similar electron densities in the plasma, the models do not predict observable satellite spikes, but they do predict shifts of the emission lines by various amounts relative to their rest wavelengths. Both blueshifts and redshifts are expected, up to a few tens of km s^{-1}. Fig. 5.15 shows two helium lines where different shifts for different electron densities are expected. In Table 5.4 we see that the observed spikes are predominantly redshifted; however, the observed redshifts of the central spike can be matched reasonably well with the expected blue- and redshifts due to Stark broadening if we assume an additional, global redshift of about 15 km s^{-1} which is a combination of the systemic velocity and the gravitational redshift. The spikes shown in Fig. 5.14 were blueshifted by 15 km s^{-1}. Although, we have no possibility to measure the systemic velocity and the gravitational redshift independently, a global redshift of about 15 km s^{-1} is plausibly due to a gravitational redshift, which is conform expectations if the central spikes originate on or close to the surface of the accreting white dwarf, as suggested on the basis of their observed radial velocity amplitudes and phases (Morales-Rueda
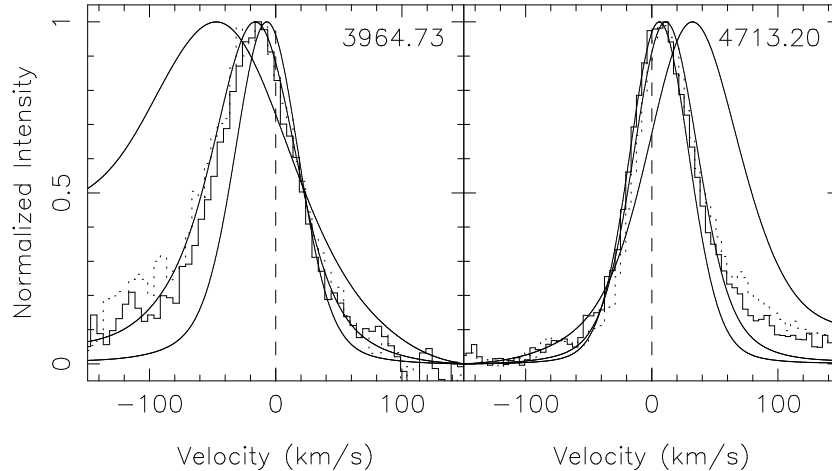
Figure 5.15: Observed spikes from the UVES spectra in GP Com (dotted histogram) and V396 Hya (solid histogram) for two more He I lines, together with the modelled Stark-broadened line profiles from Beauchamp et al. (1997). The lines were chosen for their relatively large observed shifts. The models shown are for electron densities of $n_e = 1 \times 10^{15}$, 3×10^{15}, and 1×10^{16} cm^{-3}; the broadening and shift of the lines increases with electron density. All line types are the same as in Fig. 5.14.

et al., 2003a; Marsh, 1999). Unlike the neutral helium lines, the hydrogenic He II 4686 Å line should only be broadened and *not* shifted due to the Stark effect: its measured redshift should therefore match the global redshift found in the He I lines. With a measured redshift of 17.4 ± 0.3 and 16.1 ± 0.5 km/s (Table 5.4), this is indeed the case.

Unfortunately, since there may also be red- or blueshifts due to the systemic velocities of the binaries, it is impossible to draw conclusions as to the masses of the accreting white dwarfs, even if one assumes that the spikes originate from their surfaces and that the observed (global) redshifts may thus be partially gravitational.

The emission spikes in the AM CVn stars may provide a unique view of the effects of Stark broadening on the appearance of forbidden lines of helium. Whereas such lines in DB white dwarf or EHe star atmospheres are always a convolution of an entire stellar atmosphere, the lines in the AM CVn stars appear to be produced in an optically thin slab of gas with a single density, or very narrow range of densities. Model predictions for Stark-broadened and forbidden helium lines further to the UV could be tested by our X-Shooter spectroscopy. Our fitting of the observed Stark profiles with calculated profiles is currently limited by the resolution of the grid of models available to us.

5.4.2 Metal lines

Kupfer et al. (2013) discovered strong absorption lines of magnesium and silicon in the three AM CVn systems known to have orbital periods between 50-60 min. However, they were not able to trace the origin of these lines because of the low resolution data. We show that the nitrogen absorption lines in GP Com follow the motion of the central spike. Therefore, the origin of the absorption lines are most likely photospheric absorption lines from the accretor

which is accreting material from the disc. That means that the observed abundances most likely represent the composition of the disc and therefore the donor star.

We have identified a large number of nitrogen and neon lines as well as the O I multiplet at 7771/74/75 Å in GP Com. However no evidence for iron and silicon can be found in either system. The strength of iron and silicon lines could be used to determine the initial metalicity since their abundance is not supposed to be affected by nuclear synthesis processes during binary evolution. Marsh et al. (1991) concluded that the non-detection of heavier elements such as iron and silicon shows that GP Com is a low metallicity object. The strong enhancement of nitrogen is a clear sign of CNO-processed material (Nelemans et al., 2010). This seems also to apply to V396 Hya because it does show similar spectral features as GP Com. More intriguing is the overabundance of neon which was also found in X-ray observations in GP Com (Strohmayer, 2004) because the only way to enhance neon is during helium burning which decreases the nitrogen abundance and increases the carbon and oxygen abundance.

If the observed abundances represent the composition of the donor, the overabundance of neon can only be explained through a short phase of helium burning which stopped before nitrogen is depleted and carbon and oxygen is enhanced significantly (Arnould et al., 1999). We do not see an enhanced abundance of oxygen and carbon, therefore a highly evolved helium star donor is excluded in both systems.

As an alternative scenario the observed abundances in the donor star could be affected by diffusion processes. Due to diffusion in the donor, the core of the donor star could have been enriched in ^{22}Ne (Yungelson et al., 2002). This would cause an overabundance of neon, although also here some helium burning occurred in the donor star.

5.4.3   Rotational velocity of the accretor

Before mass transfer starts the two white dwarfs in the AM CVn progenitor system have been orbiting each other for millions to billions of years. Close to the onset of mass transfer, tidal effects will have synchronized their spins with their orbits leading to rotational velocities of several hundred $\mathrm{km\,s^{-1}}$. Bildsten et al. (2006) assumed that helium is accreted onto the white dwarf with the specific angular momentum of the inner edge of the accretion disc which will spin up the accretor and lead to a minimum equatorial rotational velocity of $\sim 1250\,\mathrm{km\,s^{-1}}$. However, Marsh et al. (2004) showed that the synchronization torque between the accretor and the orbit can feed back angular momentum into the orbit which possibly spins down the accretor, stabilizes the orbit and prevents the merger of the system. This will have a positive influence on the formation rate of AM CVn systems if the synchronization timescale is short enough. To put further constraints on the synchronization timescales the rotational period of the accretor has to be compared to the orbital period of the binary. We show that the narrow emission lines of neon and nitrogen have the same phase and velocity amplitude as the central spike and conclude that the origin of these lines is also on or close to the accreting white dwarf. The strong spikes in the helium lines (e.g. He II 4686 Å) have a larger signal-to-noise ratio (SNR) compared to the neon lines but they are also broadened due to the Stark broadening. Thus despite the lower SNR, the narrow neon lines are not affected by Stark broadening and
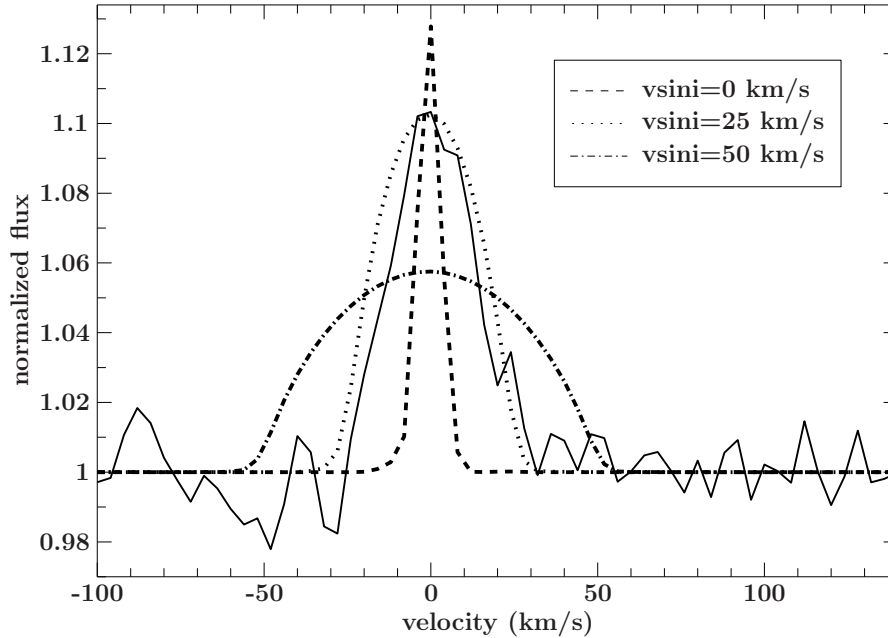
Figure 5.16: The average line profile of the narrow neon emission lines of GP Com from UVES spectra
with computed line profiles for different rotational velocities.

therefore these lines can be used to estimate the rotational velocity of the accretor.

The narrow neon and nitrogen emission lines are compared to synthetic profiles from a
single slab LTE model with uniform temperature and density which was also used by Marsh
et al. (1991) for their abundance analysis on GP Com. The computed line profile includes only
thermal broadening. Additional broadening effects like microturbulence and Stark broadening
are neglected. A synthetic model was computed using the parameters derived for GP Com
(Marsh et al., 1991). Additional rotational broadening following Gray (2008) was applied to
the synthetic models.

If the accreting white dwarf is tidally locked to the orbit, the rotational velocity of the
accretor can be calculated using the following equation:

$$v_{\text{rot}} = \frac{2\pi R_{\text{WD}}}{P_{\text{orb}}} \tag{5.1}$$

where P_{orb} corresponds to the orbital period of the system and R_{WD} to the radius of the ac-
creting white dwarf. A radius of the white dwarf accretor in both systems was found to be
$R_{\text{WD}} = 0.015\,\text{R}_\odot$ using the zero-temperature mass-radius relation of Eggleton (quoted in Ver-
bunt & Rappaport 1988) for an $0.5\,\text{M}_\odot$ white dwarf. This leads to an equatorial rotational ve-
locity of $v_{\text{rot;GPCom}} = 23.4\,\text{km\,s}^{-1}$ and $v_{\text{rot;V396Hya}} = 16.8\,\text{km\,s}^{-1}$ for the accretor in GP Com
and V396 Hya respectively. This is only an upper limit as the observed rotational velocity
depends on the inclination angle of the system.

Although we can only exclude fast rotational velocities and cannot draw a firm conclusion
whether the accretor is tidally locked, Fig. 5.16 and 5.17 shows that a broadening of $v_{\text{rot}} = 25\,\text{km\,s}^{-1}$ is needed to find good agreement between the models and the observed emission
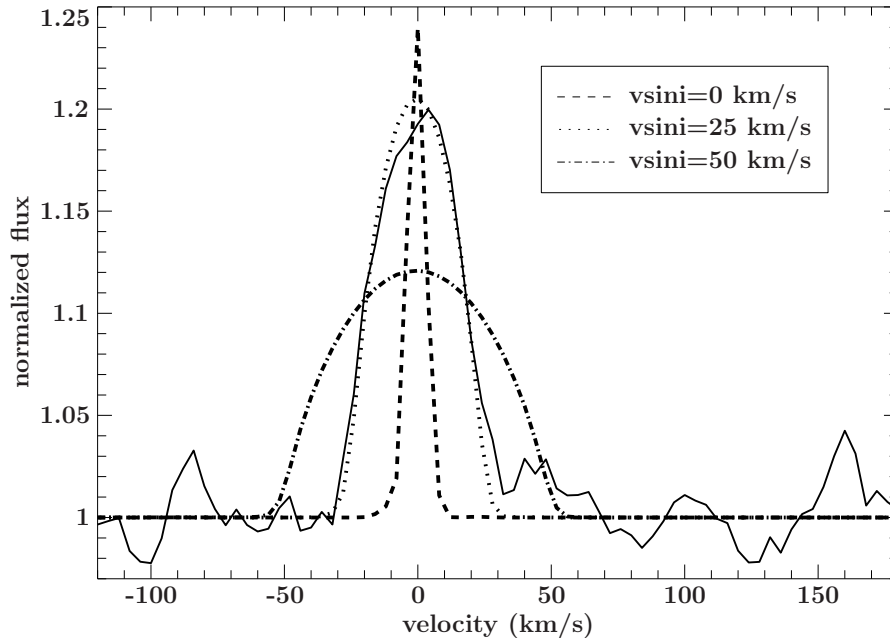
Figure 5.17: The average line profile of the narrow neon emission lines of V396 Hya from UVES spectra with computed line profiles for different rotational velocities.

lines in GP Com and V396 Hya. This value is only a lower limit and depends on the inclination angle. If the accretor mass of GP Com is close to the Chandrasekhar limit the inclination angle could be $45°$ for purely ballistic stream velocities and $33°$ for purely Keplerian disc velocities. This leads to a maximum rotational velocity of $v_{rot} < 35\,\mathrm{km\,s^{-1}}$ for the first and $v_{rot} < 46\,\mathrm{km\,s^{-1}}$ for the latter case. For V396 Hya we find a minimum inclination angle of $51°$ for purely ballistic stream velocities and $47°$ for purely Keplerian disc velocities which leads to a maximum rotational velocity of $v_{rot} < 32\,\mathrm{km\,s^{-1}}$ in the case of purely ballistic stream velocities and $v_{rot} < 34\,\mathrm{km\,s^{-1}}$ for purely Keplerian disc velocities.

Therefore, we conclude that the accretor does not rotate fast in both systems and must have spun down significantly during the evolution of GP Com and V396 Hya as AM CVn type systems.

5.5 Conclusions and summary

The average spectra of GP Com and V396 Hya reveal strong double peaked helium emission lines typical for long period AM CVn type systems. All the lines in the optical regime show, on top of the helium disc emission lines, a strong central spike feature. Interestingly, none of the helium lines in the near-infrared of GP Com and V396 Hya shows this sharp central spike feature.

Besides the strong helium lines a large number of narrow nitrogen and neon emission lines are detected in both systems. Additionally broad nitrogen absorption lines are also detected in GP Com. We show that the neon and nitrogen lines follow the motion of the central spike

and therefore have an origin on or close to the accretor with the absorption lines originating most likely in the photosphere of the accreting white dwarf. No evidence for iron and silicon was found which indicates that GP Com and V396 Hya are low metallicity objects with an overabundance of neon and nitrogen. The neon and nitrogen lines were found to be connected to the accreting white dwarf and represent the abundance pattern of the accreted material of the donor star. An enhancement of nitrogen can be explained with CNO burning whereas neon is only produced during helium burning where nitrogen is burned into carbon and oxygen. Therefore, we find no satisfying solution to explain both high neon and high nitrogen and can only exclude a highly evolved helium star donor in both systems.

Doppler tomograms reveal a strong accretion disc bright spot with a faint secondary spot at an $\sim$120-degree phase-offset to the first bright spot. From the phases and amplitudes of the central spikes and the primary bright spot as well as the peak-to-peak separation of the double peaked helium disc emission lines we limit the inclination angles and the component masses assuming that the velocity of the bright spot is either purely ballistic stream velocity or purely Keplerian disc velocity. For GP Com, we find for an accretor with a mass of $M_{1,\mathrm{GP\,Com}} > 0.55\,M_\odot$ seen under an inclination angle of $45° < i < 74°$ for purely ballistic stream velocity. For purely Keplerian disc velocity the accretor has a mass of $M_{1,\mathrm{GP\,Com}} > 0.33\,M_\odot$ and the system is seen under an inclination angle of $33° < i < 74°$. The donor in V396 Hya is expected to be a zero temperature donor star. We find a possible mass for the accretor of $0.37 < M_{1,\mathrm{V396\,Hya}}/M_\odot < 0.49$ and the system is seen under an inclination angle of $51° < i < 78°$ for purely ballistic stream velocities. For purely Keplerian disc velocities the accretor has a mass of $0.32 < M_{1,\mathrm{V396\,Hya}}/M_\odot < 0.45$ and the system is seen under an inclination angle of $47° < i < 78°$.

We find a large variation of the mean velocities of the central spike features ranging from -5 to $+53\,\mathrm{km\,s^{-1}}$ and detect forbidden components of several helium lines. Stark broadened models predict both the appearance of forbidden helium lines and the displacement for the other helium lines. Therefore, the helium lines are compared to calculated line profiles and we find that the central spike features can be correctly reproduced by Stark-broadened line profile models for helium plasma with an electron density close to $n_e \simeq 5 \times 10^{15}\,\mathrm{cm^{-3}}$.

The narrow emission lines of nitrogen and neon as well as the nitrogen absorption lines follow the motion of the central spike. Therefore, they are also connected to the accreting white dwarf and can be used to estimate the rotational velocity of the accretor. We compare the emission lines to synthetic line profiles which only include thermal and rotational broadening and neglect additional broadening mechanism such as microturbulence or Stark broadening. We show that the lines can be reproduced with a projected rotational broadening of $v_{\mathrm{rot}} \sim 25\,\mathrm{km\,s^{-1}}$ and therefore conclude that rotational velocity of the accreting white dwarf has to be $v_{\mathrm{rot}} < 46\,\mathrm{km\,s^{-1}}$ for GP Com and $v_{\mathrm{rot}} < 34\,\mathrm{km\,s^{-1}}$ which excludes a fast rotating accretor in GP Com and V396 Hya.

5.6 Appendix

Table 5.6: Equivalent widths of the nitrogen spectral lines

line	GP Com EW (Å)	V396 Hya EW (Å)
N II 3995	–0.06±0.01	–0.08±0.01
N I 4099	0.53±0.02	–0.04±0.01
N I 4109	0.40±0.02	–0.08±0.01
N I 4137	0.10±0.01	-[f]
N I 4143	0.14±0.02	–0.71±0.02[d]
N I 4151	0.32±0.02	
N I 4214/15	0.20±0.01	-
N I 4223/24	0.40±0.02	-
N I 4230	0.11±0.01	-
N I 4253	0.14±0.02	-
N I 4336	0.06±0.01	-
N I 4342	0.11±0.01	-
N I 4342	0.11±0.02	-
N I 4358	0.21±0.02	-
N II 4447	–0.03±0.01	–0.15±0.02
N II 4630	–0.06±0.01	–0.08±0.01
N I 5281	0.16±0.02	-
N I 5292	0.07±0.01	-
N I 5310	0.06±0.01	-
N I 5328	0.12±0.02	-
N I 5356	0.07±0.01	-
N II 5666	–0.05±0.01	[a]
N II 5676	–0.03±0.01	-
N II 5679	–0.10±0.01	–0.05±0.01
N II 5686	–0.02±0.01	-
N I 5999	0.15±0.02	–0.06±0.01
N I 6008	0.21±0.02	–0.07±0.01
N II 6482	[b]	–0.71±0.03[b]
N I 6644	[a]	–0.21±0.02[e]
N I 6646	[a]	
N I 7423	–0.15±0.02	–0.49±0.02
N I 7442	–0.23±0.02	–0.79±0.02
N I 7468	–0.27±0.02	–0.94±0.02
N I 7899	–0.06±0.01	–0.42±0.02
N I 8184	–0.50±0.02	–0.92±0.02
N I 8188	–0.52±0.02	–0.85±0.02

Table 5.6: continued.

line	GP Com EW (Å)	V396 Hya EW (Å)
N I 8200/01	–0.31±0.02	–0.81±0.02
N I 8210	–0.21±0.02	–0.58±0.02
N I 8216	–0.72±0.02	–1.51±0.03
N I 8223	–0.45±0.02	–0.84±0.02
N I 8242	–0.29±0.02	–0.76±0.02
N I 8567	–0.08±0.01	–0.52±0.02
N I 8594	–0.13±0.01	–0.72±0.02
N I 8629	c	c
N I 8655	c	c
N I 8680/83/86	–2.93±0.03	–4.76±0.04
N I 8703	–0.32±0.03	–1.09±0.02
N I 8711	–0.38±0.03	–1.21±0.03
N I 8718	–0.37±0.03	–1.00±0.03
N I 8728	-	-0.52±0.02
N I 8747	-	-0.21±0.02
N I 9028	–0.28±0.02	–0.69±0.02
N I 9045	–0.48±0.03	–0.99±0.02
N I 9060	–0.34±0.03	–0.88±0.02
N I 9187	–0.58±0.03	–0.86±0.02
N I 12469	-	a

[a] Line present but insufficient SNR to measure

[b] Blended with N I 6481/82/83/84 Å

[c] Line present but contaminated with atmosphere

[d] Blended with N I 4151 Å

[e] Blended with N I 6646 Å

[f] Lines marked with a - are below the detection limit of $\sim$0.01Å

Table 5.7: Equivalent widths of spectral lines other than nitrogen

line	GP Com EW [Å]	V396 Hya EW [Å]
He II 3203	−0.08±0.01	−0.34±0.03
unidentified 6460	0.09±0.01	-[b]
unidentified 6470	0.25±0.02	-
Ne I 5656	−0.03±0.01	-
Ne I 5852	-	[a]
Ne I 6074	[a]	−0.05±0.01
Ne I 6096	−0.02±0.01	−0.09±0.01
Ne I 6143	−0.04±0.01	−0.09±0.01
Ne I 6163	[a]	[a]
Ne I 6266	−0.03±0.01	−0.09±0.01
Ne I 6334	−0.03±0.01	−0.09±0.01
Ne I 6402	−0.11±0.01	−0.28±0.02
Ne I 6506	−0.06±0.01	−0.14±0.02
Ne I 6532	−0.02±0.01	−0.08±0.02
He II 6560	−0.22±0.02	−0.26±0.02
Ne I 6598	-	−0.05±0.01
Ne I 7032	−0.10±0.01	−0.09±0.01
O I 7771/74/75	−0.04±0.02	[a]
O I 8446	−0.03±0.02	-

[a] Line present but insufficient SNR to measure
[b] Lines marked with a - are below the detection limit of ∼0.01Å

CHAPTER 6

X-SHOOTER OBSERVATIONS OF ULTRACOMPACT AM CVN TYPE BINARIES

T. Kupfer, P. J. Groot, D. Steeghs, T. R. Marsh and G. Nelemans

Abstract. We present medium-resolution X-Shooter spectroscopy of the AM CVn type binaries HP Lib, V803 Cen, V406 Hya, SDSS J124058.03–015919.2, SDSS J172102.48+273301.2, SDSS J080449.49+161624.8 and SDSS J164228.08+193410.1. The spectra obtained with X-Shooter cover the full optical/near-infrared range from 0.3 - 2.5 μm and are dominated by strong helium lines, either in absorption or emission depending on whether the system is seen in high state or low state.

For the first time weak nitrogen absorption lines were detected in HP Lib. V803 Cen was observed during outburst and therefore shows broad helium absorption lines. The spectra of V406 Hya and SDSS J124058.03–015919.2 display strong nitrogen and magnesium emission lines in the far-optical-red. SDSS J080449.49+161624.8 shows more than 40 different transitions of neutral and ionized helium. In particular, the He II lines appear to be exceptionally strong. Only the He I 7065 Å line indicates a central spike feature. The overall spectral shape looks like a hydrogen-deficient magnetic CV.

Equivalent width ratios including the near-infrared He I 10830 Å line were calculated for SDSS J164228.08+193410.1 and compared with single-slab LTE models with variable electron densities and path lengths. We show that the usage of the near-infrared lines requires a more involved disc modelling than single-slab LTE models.

We present an overview of the different elements detected in the X-Shooter spectra of the various systems as well as systems from the literature. None of the systems show evidence for carbon and oxygen but almost all systems show neutral or singly ionized nitrogen. The absence of carbon and oxygen and the enrichment of nitrogen indicates that none of the observed systems had a highly evolved helium star as the progenitor of the donor.

6.1   Introduction

AM CVn systems are a small group of mass transferring ultracompact binaries with orbital periods between 5.4 and 65 minutes. AM CVn systems consist of a white dwarf (WD) primary and a WD or semi-degenerated helium star secondary (Nelemans et al., 2001a). See Solheim (2010) for a recent review. They are important as strong, low-frequency, Galactic gravitational wave sources (e.g. Nelemans et al., 2004; Roelofs et al., 2007c; Nissanke et al., 2012), the source population of the proposed â.Iaâ supernovae (Bildsten et al., 2007), and as probes of the final stages of binary evolution. Spectroscopically these systems are characterized by a deficiency of hydrogen, indicating an advanced stage of binary evolution. In the preceding binary evolution two common envelope phases have formed a detached WD binary system at a period of up to a few hours. Gravitational wave radiation decreased the orbital separation until the low-mass secondary filled its Roche lobe and mass transfer set in at an orbital period between $3 - 10$ minutes depending on the masses of both components and the entropy of the donor (Nelemans et al., 2001a; Deloye et al., 2007). Some fraction of these systems survived the ensuing direct impact phase to become AM CVn systems depending on their mass ratio and the efficiency of the angular momentum feedback (Nelemans et al., 2001a; Marsh et al., 2004). An accretion disc forms at an orbital period of $\sim$10 min and the mass transfer stream hits the disc at the so-called bright spot. The mass-transfer-rate drops as the orbit widens and the system ends up as a more massive WD with an extremely low-mass WD ($\sim$0.005 M$_\odot$; Kupfer et al. submitted) at an orbital periods above 60 min.

AM CVn systems show three phases during their lifetime based on their photometric behaviour. Systems with periods below 20 min have a high mass-transfer rate resulting in spectra that are dominated by helium absorption lines originating in the optically thick disc. Systems with periods $\gtrsim$ 40 min are in a low mass-transfer rate state and have spectra dominated by strong helium emission lines from an optically thin accretion disc. The intermediate period systems, between 20 and 40 min orbital period, undergo dwarf-nova type photometric outbursts and change their spectral behaviour from a low state, where emission lines from the disc and Stark-broadened absorption lines from the accretor dominate the spectrum, to a high state, where absorption lines from the optically thick disc dominate the spectra (Groot et al., 2001; Levitan et al., 2011; Ramsay et al., 2012; Levitan et al., 2015).

Fifteen years ago, fewer than 10 systems were known. Mainly due to two very successful surveys the known sample of AM CVn systems increased significantly. Sixteen systems were discovered by the Sloan Digital Sky Survey (e.g. Roelofs et al., 2005; Anderson et al., 2005, 2008; Rau et al., 2010; Carter et al., 2012, 2014a) and another seven systems by the Palomar Transient Factory (Levitan et al., 2011, 2013, 2014). Together with smaller scale surveys, this quadrupled the number of known systems over the last 15 years to the 43 AM CVn type binaries known today. As more systems are discovered, we are better able to understand the evolution and population characteristics of these systems.

Three different formation channels have been proposed for AM CVn type binaries; a double white dwarf channel (Tutukov & Yungelson, 1979), a channel in which the donors are low mass helium stars (Savonije et al., 1986; Tutukov & Fedorova, 1989; Yungelson, 2008), and

Table 6.1: Summary of the X-Shooter observations

System	Tele.+Instr.	N_{Exp}	Exp. time (s)
HP Lib			
2010-02-21	VLT/X-Shooter	60	20
V803 Cen			
2012-05-05	VLT/X-Shooter	37	60
2012-05-06	VLT/X-Shooter	29	60
V406 Hya			
2010-02-18	VLT/X-Shooter	3	900
SDSS J1240–0159			
2010-02-18	VLT/X-Shooter	3	900
SDSS J1721+2733			
2010-04-23	VLT/X-Shooter	36	180
SDSS J0804+1616			
2010-02-18	VLT/X-Shooter	3	900
SDSS J1642+1934			
2010-04-16	VLT/X-Shooter	48	180
2010-04-19	VLT/X-Shooter	36	180
2011-05-06	VLT/X-Shooter	22	180
2011-05-09	VLT/X-Shooter	16	180

one with evolved post-main sequence donors (Thorstensen et al., 2002; Podsiadlowski et al., 2003). A way to distinguish between these scenarios is to obtain the chemical composition of the donor, and in particular the C/O, N/O and N/C ratios, due to different levels of CNO and He burning in the progenitor of the donor (Nelemans et al., 2010). A high N/O and N/C ratio is expected for a helium white dwarf donor. Due to the enhancement of carbon and oxygen and the depletion of nitrogen during helium burning, a lower N/O and N/C ratio is expected for a semi-degenerate donor compared to the helium white dwarf donor. Although the donor has never been observed directly, the accreted material in the disc and the photosphere of the accreting white dwarf is expected to represent the composition of the donor.

The X-Shooter spectrograph covers the full optical/near-infrared range from 0.3 - 2.5 μm. The large spectral range allows to search for spectral lines of the trace elements nitrogen, oxygen and carbon to identify the nature of the donor. In this paper we present medium-resolution X-Shooter spectroscopy of 7 AM CVn type systems which cover almost the entire orbital period range of the known AM CVn type systems; HP Lib, V803 Cen, V406 Hya, SDSS J124058.03–015919.2 (hereafter SDSS J1240), SDSS J172102.48+273301.2 (hereafter SDSS J1721), SDSS J080449.49+161624.8 (hereafter SDSS J0804) and SDSSJ164228.08 +193410.1 (hereafter SDSS J1642).

6.2   Observations

The systems discussed in this paper were observed using the medium resolution spectrograph X-Shooter (Vernet et al., 2011) mounted at the Cassegrain focus on the Unit 2 telescope of the VLT array in Paranal, Chile during several nights as part of the Dutch GTO program. X-Shooter consists of 3 independent arms that give simultaneous spectra longward of the atmospheric cutoff (0.3 microns) in the UV (the ″UVB″ arm), optical (the ″VIS″ arm) and up to 2.5 microns in the near-infrared (the ″NIR″ arm). For all observations, we used slit widths of 1.0″, 0.9″ and 0.9″ in X-Shooter's three arms and binned by 2x2 in the UVB and VIS arms resulting in velocity resolutions of $14\,km\,s^{-1}$, $7\,km\,s^{-1}$ and $11\,km\,s^{-1}$ per binned pixel for the UVB, VIS and NIR arm respectively. The reduction of the raw frames was conducted using the standard pipeline release of Reflex (version 2.3) for X-Shooter data (Freudling et al., 2013). The standard recipes were used to optimally extract and wavelength calibrate each spectrum. The instrumental response was removed by observing the spectrophotometric standard star EG 274 (Hamuy et al., 1992, 1994) and dividing it by a flux table of the same star to produce the response function. x We obtain a signal-to-noise ratio (SNR) in the average spectra of the systems between ~ 76 for HP Lib and only ~ 6 for SDSS J1642 in the optical regime. In the near-infrared HP Lib has a SNR of ~ 14, V803 Cen of ~ 7 in the continuum. All the other systems have a SNR below 1 in the near-infrared continuum. Table 6.1 gives an overview of all observations.

6.3   Spectral features

6.3.1   Optical spectra

We present the time-averaged spectra of HP Lib and V803 Cen in Fig. 6.4 and 6.5. Both systems show a similar overall spectral shape. The broad helium absorption lines dominate the spectra. Helium absorption lines are seen in AM CVn systems during dwarf-novae type outbursts, as well as in high state systems with orbital periods $< 20\,min$ (e.g. Roelofs et al., 2007b; Levitan et al., 2013). HP Lib and V803 Cen appear very similar to the short period systems AM CVn and SDSS J1908 (Kupfer et al. submitted). V803 Cen is known to have an orbital period of 26.6 min and shows helium lines in emission during quiescence and broad helium absorption lines during outburst (Roelofs et al., 2007b). Therefore, our X-Shooter observations of V803 Cen were conducted during an outburst. Besides the broad absorption lines of helium, we find evidence for weak absorption lines of nitrogen in HP Lib (see Fig. 6.4). No such feature can be seen in V803 Cen. Roelofs et al. (2007b) found nitrogen absorption lines in high signal-to-noise ratio spectra during outburst in V803 Cen. HP Lib shows a series of absorption features between 3100 and 3300 Å. We are not able to identify the origin of these lines. We cannot exclude that they originate from poor data extraction in the UV (e.g. fringing).

Figure 6.6 and 6.7 show the averaged X-Shooter spectrum of V406 Hya and SDSS J1240. Roelofs et al. (2006a) found that both systems show broad helium absorption lines from a DB white dwarf which we also detect. On top of that, the spectra show strong double peaked
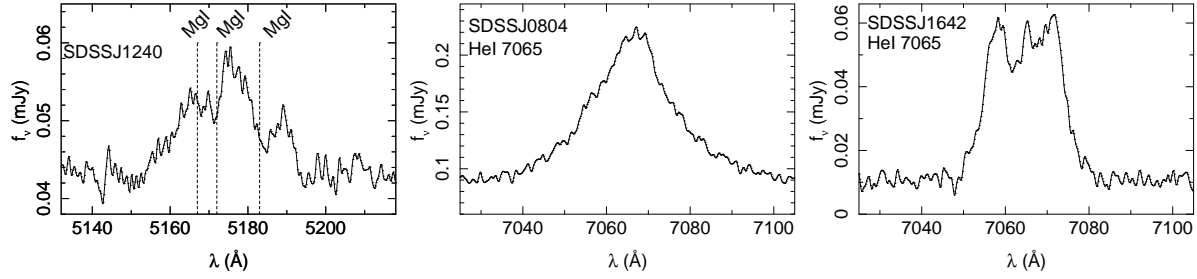
Figure 6.1: Zoomed region of the average X-Shooter spectra around the emission feature at 5170 Å in SDSS J1240. Profile of the He I 7065 Å line in SDSSJ0804 and SDSSJ1642.
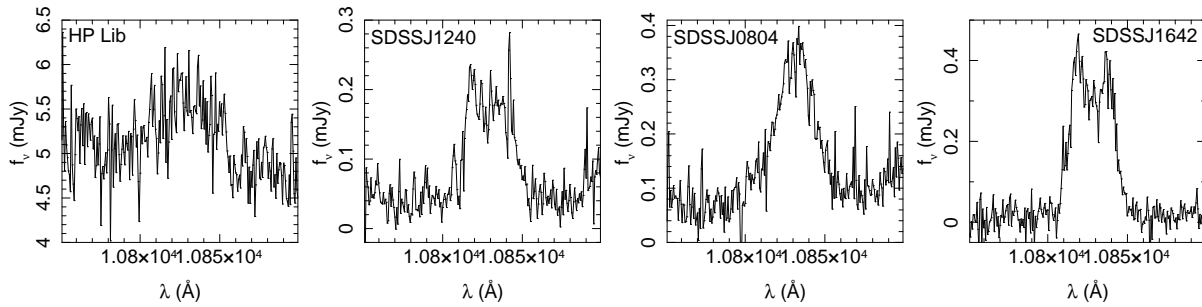

Figure 6.2: Zoomed region of the average X-Shooter spectra around the near-infrared He I 10 830.34 Å line in HP Lib, SDSSJ1240, SDSSJ0804 and SDSSJ1642.

helium emission lines from an optically thin, helium-dominated accretion disc. Additionally, Roelofs et al. (2006a) noticed also emission lines of silicon, iron and nitrogen in both systems. The largest difference is the presence of strong double peaked Ca II H&K disc emission lines in V406 Hya. Such strong calcium emission lines have only been observed in two other AM CVn type systems (Levitan et al., 2013). Thanks to our higher resolution X-Shooter spectra we identify in both systems a strong Mg II multiplet in the far-red at around 9218 Å as well as the Mg II 4481 Å line in the red wing of He I 4471 Å. Roelofs et al. (2006a) identified a broad emission feature around 5170 Å as iron emission. The higher resolution reveals that the emission around 5170 Å can be better explained with a double peaked Mg I triplet originating in the disc, although we cannot exclude that the magnesium emission is superimposed with some iron emission (left panel in Fig. 6.1).

SDSS J1721 was discovered during a spectroscopic survey of color-selected objects from the Sloan Digital Sky Survey (Rau et al., 2010). Figure 6.8 shows the average spectrum of SDSS J1721. The blue part of the spectrum is dominated by broad helium absorption lines from the accretor, whereas the red part of the spectrum is dominated by double-peaked helium disc emission lines. Unfortunately, the low signal-to-noise ratio (~ 10) average spectrum does not allow us to search for additional weak spectral features of different species.

Figure 6.9 shows the average spectrum of the remarkable system SDSS J0804. Roelofs et al. (2009) revealed single-peaked helium emission lines with an unusually strong series of ionized helium and speculated that SDSS J0804 is the first magnetic AM CVn star. The large

Table 6.2: Overview of the detected elements.

System	He I	He II[b]	N I	N II	N III	C I/II	O I	Ne I	Mg I	Mg II	Si I	Si II	Si III	S II	Ca II	Fe II
HM Cnc[i]	e[o]	e	x[q]	-[r]	e	-	x	x	-	-	-	-	-	x	-	-
AM CVn[j]	a[p]	-	x	-	-	-	x	x	-	a	-	-	-	x	-	-
SDSSJ1908[h]	a	-	-	a	-	-	-	-	-	a	-	a	a	a	-	-
HP Lib	a	-	-	a	-	-	-	-	-	-	-	-	-	-	-	-
V803 Cen	e	-	-	-[c]	-	-	-	-	-	-	-	-	-	-	-	-
PTF1 J0719[k]	e	-	e	-	-	-	-	-	-	-	-	e	-	-	-	e
PTF1 J0943[l]	e	-	e	-	-	-	-	-	-	-	-	e	-	-	e	e
V406 Hya	e	e	e	-	-	-	-	-	e[d]	-	-	e	-	-	e	e[e]
PTF1 J0435[l]	e	-	-	-	-	-	-	-	-	-	-	e	-	-	e	e
SDSSJ1730[f]	e	e	x	e	-	-	x	e	-	-	-	e	-	-	-	e
SDSSJ1240	e	e	e	-	-	-	-	-	e[d]	-	-	e	-	-	-	e[e]
SDSSJ0129[g]	e	-	-	-	-	-	-	-	-	-	-	e	-	-	-	e
SDSSJ1721	e	-	e	-	-	-	-	-	-	-	-	-	-	-	-	-
SDSSJ1525[g]	e	-	x	-	-	-	-	-	-	-	-	e	-	-	-	e
SDSSJ0804	e	e	e	e	-	-	-	-	e	e	-	e	-	-	-	e
GP Com[a]	e	e	e/a	e	-	-	e	e	-	-	-	-	-	-	-	-
SDSSJ1208[g]	e	-	e	-	-	-	-	-	a	-	a	e	-	-	-	-
SDSSJ1642	e	-	e	-	-	-	-	-	a	-	-	-	-	-	-	-
SDSSJ1552[m]	e	-	-	-	-	-	-	-	a	-	-	-	-	-	-	-
SDSSJ1137[n]	e	-	e	-	-	-	-	-	-	-	-	-	-	-	-	-
V396 Hya[a]	e	e	e	e	-	-	-	e	-	-	-	-	-	-	-	-
SDSSJ1505[n]	e	-	e	-	-	-	-	-	-	-	-	-	-	-	-	-
PTF1 J2219[l]	e	-	e	-	-	-	-	-	-	-	-	e	-	-	-	e
PTF1 J0857[l]	e	-	e	-	-	-	-	-	-	-	-	-	-	-	-	-
PTF1 J1523[l]	e	-	e	-	-	-	-	-	-	-	-	e	-	-	-	e

[a] Kupfer et al. (submitted); [b] He II lines other than 4686 Å; [c] Roelofs et al. (2007b) found N II; [d] possibly Fe II; [e] possibly Mg I; [f] Carter et al. (2014b); [g] Kupfer et al. (2013); [h] Kupfer et al. (submitted); [i] Roelofs et al. (2010); [j] Roelofs et al. (2006b); [k] Levitan et al. (2011); [l] Levitan et al. (2013); [m] Roelofs et al. (2007c); [n] Carter et al. (2014a); [o] e: emission lines; [p] a: absorption lines; [q] x: not covered by the spectra; [r] -: not detected

spectral range allows us to identify more than 40 individual transitions of neutral and ionized helium. In particular, the large number and strength of ionized helium lines is remarkable and can act as a benchmark to identify these lines in other systems. We find indications of a weak central spike feature in the He I 7065 Å line (middle panel in Fig. 6.1). Additionally, strong N II emission lines as well as iron and silicon emission lines are detected over the full optical range.

Kupfer et al. (2013) detected strong helium emission lines in the average spectrum of SDSS J1642 and measured an orbital period of 54.2 min. Additionally, SDSS J1642 is one of the three known systems to show absorption lines of Mg I (Kupfer et al., 2013). Figure 6.10 shows the average spectrum obtained with X-Shooter. The spectrum resolves the helium emission lines and reveals the typical double peaked disc profile with a central spike on top (right panel in Fig. 6.1). For the first time the far-red part of the spectrum can be inspected for spectral features. We identify broad nitrogen emission lines in the far-red. Unfortunately, the signal-to-noise ratio is not high enough to clearly confirm the magnesium absorption lines around 3850 Å.

Table 6.2 gives an overview of the detected elements in the systems observed with X-Shooter as well as in other systems from the literature.

6.3.2   Near-infrared lines

X-Shooter spectroscopy allows us to search for spectroscopic signatures in the near-infrared part of the spectrum. Kupfer et al. (submitted) found strong double-peaked helium emission lines in the near-infrared of GP Com and V396 Hya. None of these lines show a strong central spike feature.

Fig. 6.2 shows He I 10 830Å of the systems where the lines are detectable. Again, none of the lines show a central spike feature. In the optical, high state systems show helium lines in absorption and can be well distinguished from the low state systems which show the lines from neutral helium in emission. All systems of our sample show the He I 10 830Å line in emission, which was expected for the low state systems. However, for the high state system, HP Lib, this a rather surprising result. Table 6.3 gives an overview of the measured equivalent widths of He I 10 830 Å.

6.4   Disc temperature of SDSS J1642

Kupfer et al. (2013) computed flux ratios of optical helium lines from Doppler tomograms to estimate the temperatures of the disc and the bright spot of four AM CVn systems. The obtained flux ratios were compared to a single slab LTE model with uniform temperature and density. They found good agreement between data and the model in three out of four systems for the disc region. SDSS J1642 was found to have a disc temperature of T_{disc}=10 200 $\pm$ 300 K (Kupfer et al., 2013).

We extend this analysis for SDSS J1642 by including the near-infrared He I 10830 Å line. An equivalent width (EW) ratio of EW(5875 Å)/EW(10830 Å)= 6.88 $\pm$ 0.35 is calculated
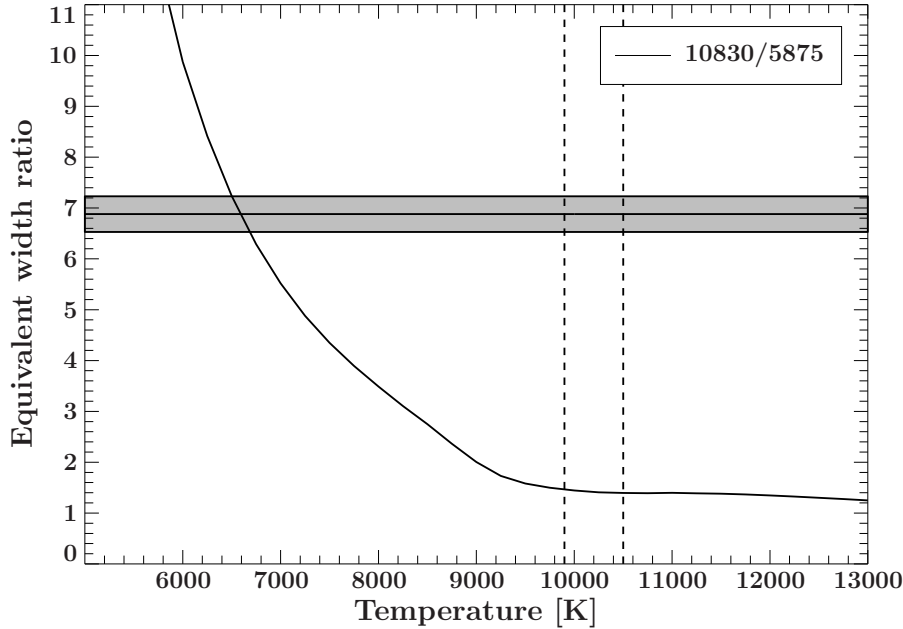
Figure 6.3: Comparison between observed disc emission (horizontal lines) and calculated equivalent width ratio for a LTE slab model with a fixed path length of $l=10^9$cm and density of 10^{14}cm^{-1} for the equivalent width ratio of the disc emission region (curved line). The horizontal line corresponds to the measured equivalent width ratio with the error shaded in grey around the horizontal line. The vertical dotted lines mark the region of the disc temperature found by Kupfer et al. (2013).

and compared to a single slab LTE model. Figure 6.3 shows that the equivalent ratio can be explained with a disc temperature of T_{disc}=6600 $\pm$ 100 K which is inconsistent with the result of Kupfer et al. (2013). To match their result an EW ratio of 1.43 ± 0.05 is required. Therefore, a full usage of the near-infrared lines requires a more involved disc modelling than has been used so far for the optical regime.

6.5 Limits on the primary mass and inclination

We measure the peak-to-peak velocity in the double-peaked emission profile for those systems where this feature is present by fitting a double Gaussian (see Tab. 6.3). The peak separation is an indicator of the (Keplerian) disc velocity of gas in the outer ranges of the accretion disc (Horne & Marsh, 1986).

Groot et al. (2001) put limits on the primary mass and the inclination angle of the CP Eri from the half of the measured peak-to-peak velocities. They assumed a disc size which extends to 70 % of the primary Roche lobe. Using the same assumption on the disc size and equation 4 from Groot et al. (2001), we derive a relation of the primary mass and the inclination angle for our systems with a measured orbital period and peak-to-peak velocity.

$$M_{1,\text{V406 Hya}} = 0.152 \sin^{-3}(i) \, M_\odot \tag{6.1}$$

Table 6.3: Measured peak-to-peak velocities and equivalent widths of He I 10830 Å.

System	outer disc vel. (km s^{-1})	EW (10830Å) (Å)
HP Lib	-^{a}	–6.5±0.4
V803 Cen	-^{a}	–4.0±0.6
V406 Hya	1400±36	-^{a}
SDSS J1240	742±12	–140.7±2.6
SDSS J1721	1805±65	-^{a}
SDSS J0804	-^{a}	–114.1±1.8
SDSS J1642	615±26	–497.4±9.1

^{a} not detectable

$$M_{1,\text{SDSS J1240}} = 0.025 \, \sin^{-3}(i) \, M_\odot \tag{6.2}$$

$$M_{1,\text{SDSS J1642}} = 0.021 \, \sin^{-3}(i) \, M_\odot \tag{6.3}$$

None of the systems show (grazing) eclipses. Therefore, we set an upper limit on the inclination angle of $i \lesssim 70°$ and derive a lower limit of the accretor mass of $M_{1,\text{V406 Hya}} > 0.183 \, M_\odot$, $M_{1,\text{SDSS J1240}} > 0.030 \, M_\odot$ and $M_{1,\text{SDSS J1642}} > 0.025 \, M_\odot$ for V406 Hya, SDSS J1240 and SDSS J1642 respectively. In particular the accretor mass limit of the latter two systems is not very strict, which is a result of the small peak-to-peak separations. The mass of the accretor has to be below $1.4 \, M_\odot$ which sets a lower limit on the inclination angle. We find $i_{\text{V406 Hya}} > 28°$, $i_{\text{SDSS J1240}} > 15°$ and $i_{\text{SDSS J1642}} > 14°$ for V406 Hya, SDSS J1240 and SDSS J1642 respectively.

6.6   Discussion

6.6.1   Helium lines

All spectra of our sample of AM CVn type binaries are dominated by strong helium lines. Systems with orbital periods below 20 min and during dwarf-novae type outbursts show absorption lines in their spectra. HP Lib and V803 Cen show broad helium absorption lines, confirming that V803 Cen was observed during outburst.

In the mid-period range ($P_{\text{orb}} \sim 30\text{-}40$ min) V406 Hya, SDSS J1240 and SDSS J1721 show broad absorption lines of the accreting white dwarf and, on top of the absorption lines, double-peaked helium emission lines of the accretion disc. V406 Hya, SDSS J1240 and SDSS J1721 have orbital periods of 33.8 min, 37.4 min and 38.1 min respectively (Roelofs et al., 2005, 2006a, Augusteijn, T, private communication), which is well in agreement with the observed spectral features.

Table 6.4: Strongest expected lines of various metals

Element	Spectral line (Å)	Comments
C I	8335, 9100, 9405,	not detected in an AM CVn
C II	4267, 6578, 6582	not detected in an AM CVn
N I	4099, 4109	in the blue spectral range
N I	7450, 8200, 8700	in the red spectral range
N II	4630, 5680	
O I	7774, 8446	
O II	4349, 4414, 4649	not detected in an AM CVn
Ne I	6402, 6506	
Mg I	5167, 5172, 5183	blended with Fe II
Mg II	7896, 9218, 4481	4481 blended with He I 4471
Si I	3905	
Si II	4130, 5056, 6347	
Si III	4552, 4567, 4574	
S II	5606, 5639	
Ca II	3933, 3964	Ca H&K
Fe II	5169, 5317	5169 blended with Mg I

On the long-period end ($P_{orb} > 40$ min) SDSS J0804 and SDSS J1642 have spectra which are dominated by strong helium disc emission lines. SDSS J1642 shows the typical double-peaked helium emission lines with a strong central spike feature. SDSS J0804 is a remarkable system because the system is dominated by only broad single-peaked lines without a central spike. Only the He I 7065 Å line displays a weak central spike feature. Additionally, the system shows exceptional strong He II lines. Roelofs et al. (2009) found that the spectrum of SDSS J0804 looks like a hydrogen deficient copy of magnetic CVs and speculated that the exceptional spectrum of SDSS J0804 can be explained if the system is magnetic. Our medium-resolution spectroscopy confirms this result and we conclude that SDSS J0804 is a good candidate to be the first magnetic AM CVn type binary.

6.6.2 Metal lines

Since the composition of the accretion disc and/or the upper layer of the primary white dwarf reflects the transferred material of the secondary, the observed abundances are expected to represent the composition of the donor star. Marsh et al. (1991) predicted Si II emission at 6346 Å and 6371 Å and Fe II emission at 5169 Å to be the strongest metal lines in helium-dominated optically-thin accretion discs. In principle, the strength of these lines can be used

to determine the initial metalicity since their abundance is not supposed to be affected by nuclear synthesis processes during binary evolution.

About half of the systems in Tab. 6.2 show clear evidence of silicon. The Fe II emission at 5169 Å is superimposed with Mg I. At least for V406 Hya and SDSS J1240 we find evidence of strong Mg II lines in the far-red and therefore conclude that the emission feature at 5169 Å can at least be partly caused by Mg I. Strong magnesium lines were also detected in the three systems which show orbital periods between 50-60 min, although in absorption. Therefore, we find a significant number of systems showing strong magnesium lines. An overabundance of magnesium cannot be explained by any nuclear burning processes expected to have occurred in these systems.

Table 6.4 gives an overview of the strongest detected metal lines in AM CVn type systems and for carbon and oxygen the strongest expected lines.

6.6.3 Implications on the formation history

During the main-sequence phase of the donor, hydrogen burning occurs through the CNO cycle. The bottleneck reaction in the CNO cycle is nitrogen to oxygen which increases the nitrogen abundance and depletes the carbon and oxygen abundance. If the CNO cycle is somehow interrupted (e.g. through mass-loss) the system is expected to be left with an overabundance of nitrogen. If the object reaches the helium burning phase, helium is burned through the triple-alpha process which produces carbon. Additionally alpha captures on nitrogen produce oxygen. Therefore, the helium burning phase increases the abundance of oxygen and carbon and decreases the abundance of nitrogen. That means that a helium white dwarf donor will show enhanced nitrogen and depleted oxygen and carbon, whereas a semi-degenerate helium star will show increased carbon and oxygen compared to nitrogen (Nelemans et al., 2010).

None of our objects show evidence for carbon and only GP Com shows weak oxygen lines. In contrast, almost all stars of the sample presented in Tab. 6.2 show nitrogen lines which are expected to represent the accreted material from the donor star. Although we cannot constrain the exact donor type without an accurate abundance measurement, the absence of carbon and oxygen indicates that none of the systems have a highly evolved helium star donor.
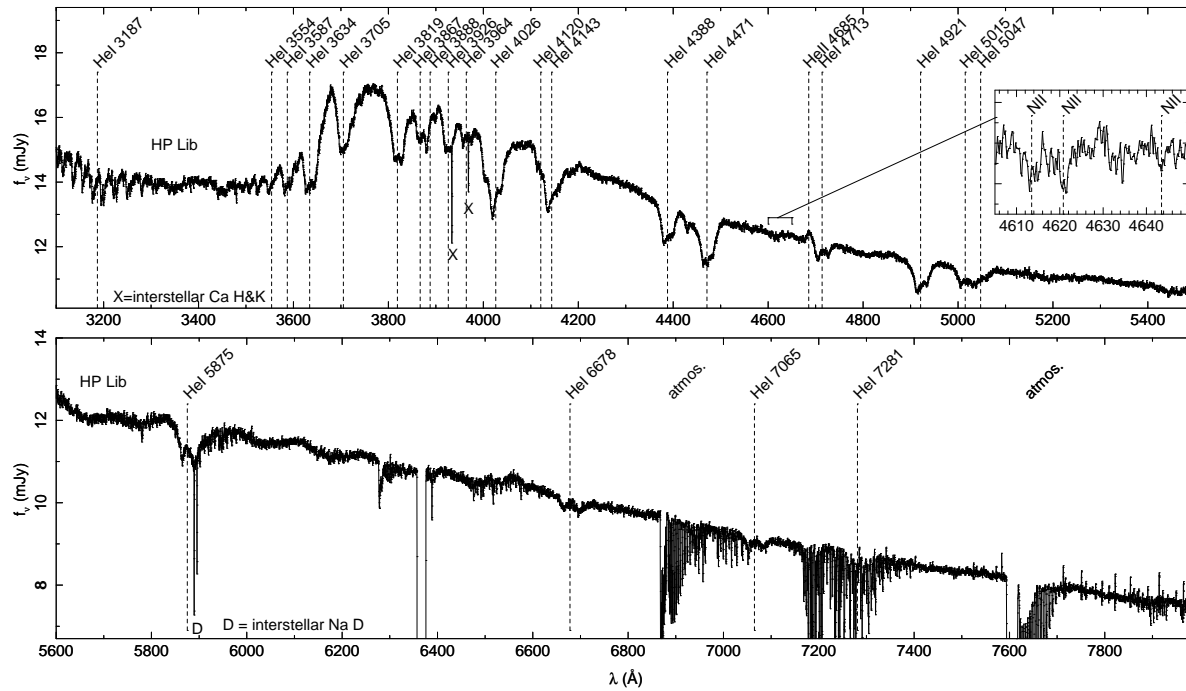
6.7 Appendix

Figure 6.4: Gaussian smoothed average spectrum of HP Lib obtained with VLT/X-Shooter. Prominent lines are indicated.
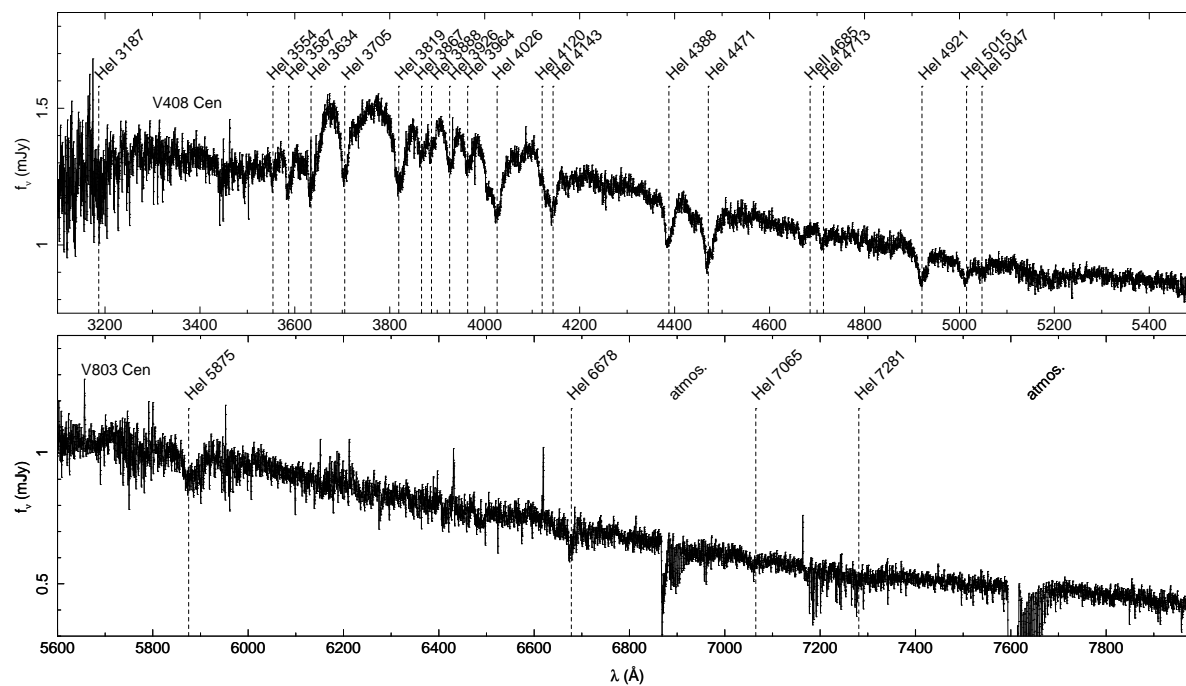
Figure 6.5: Gaussian smoothed average spectrum of V803 Cen obtained with VLT/X-Shooter. Prominent lines are indicated.
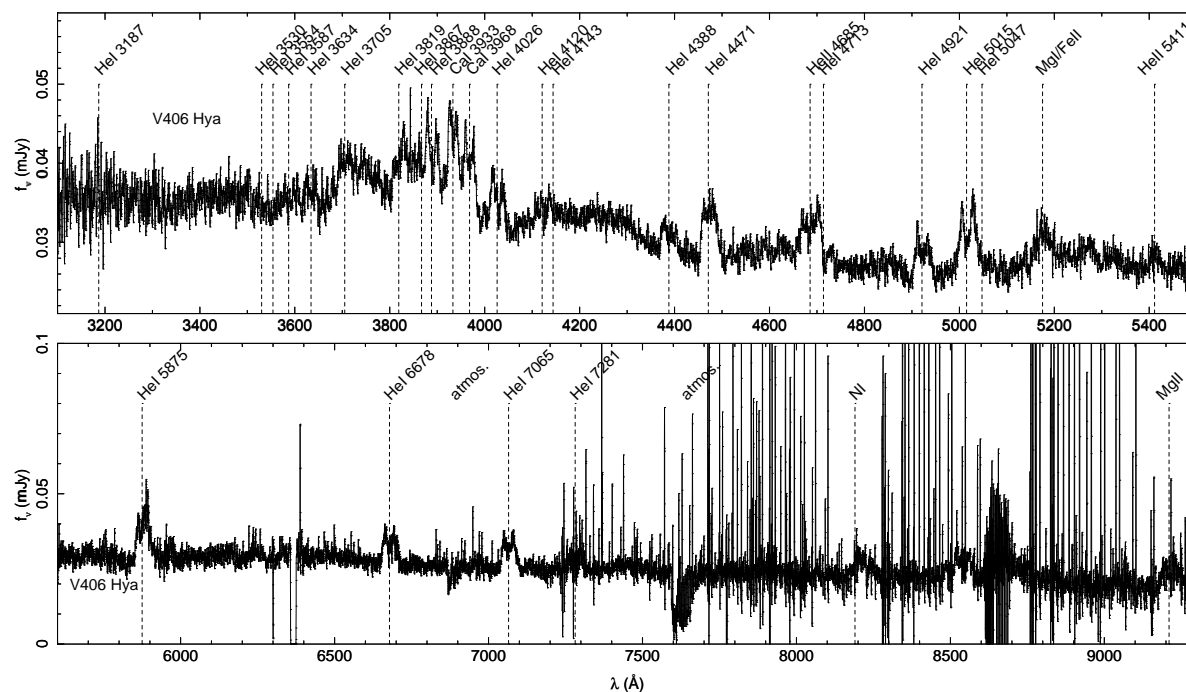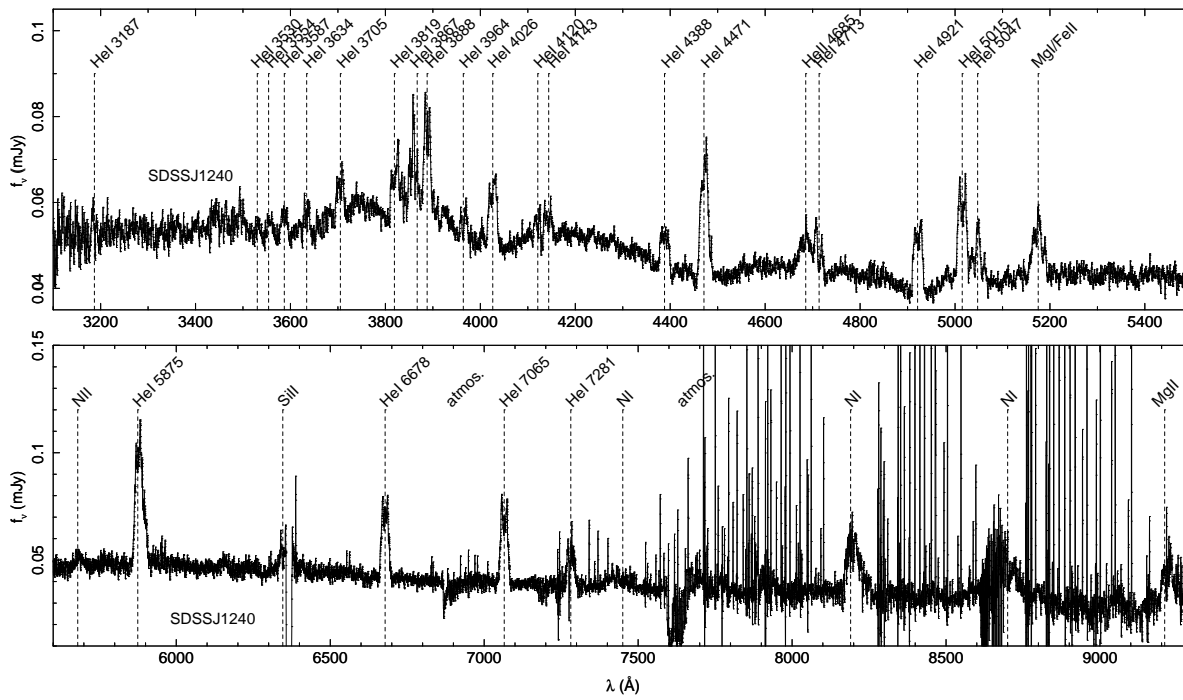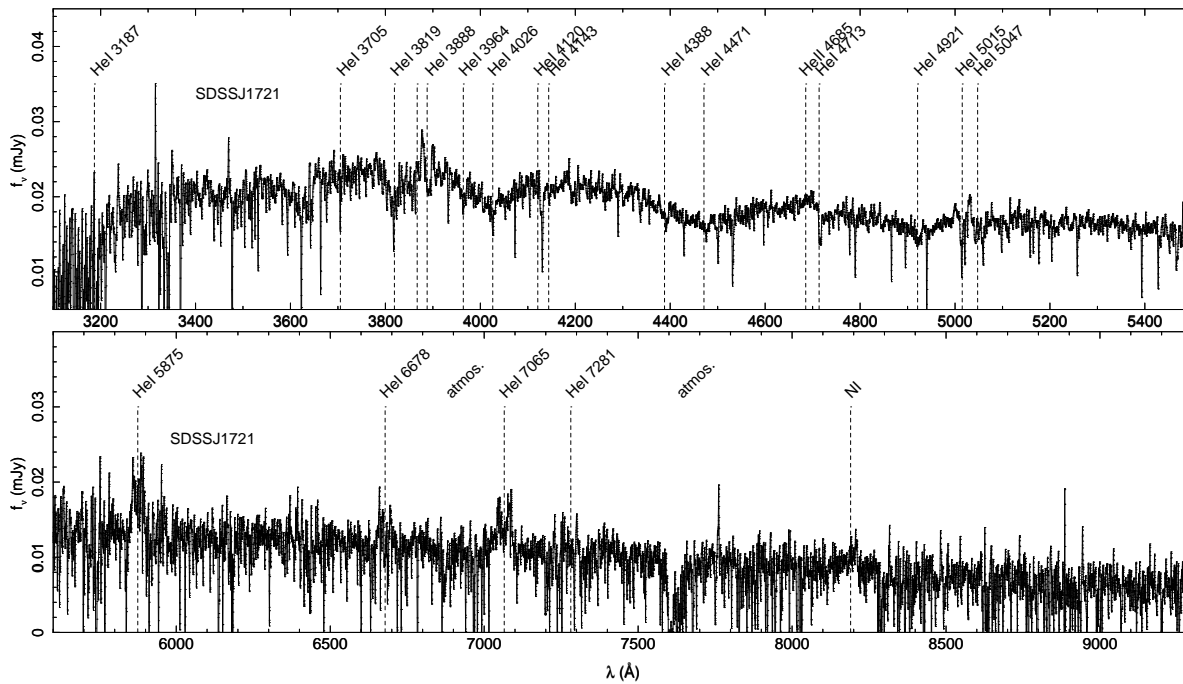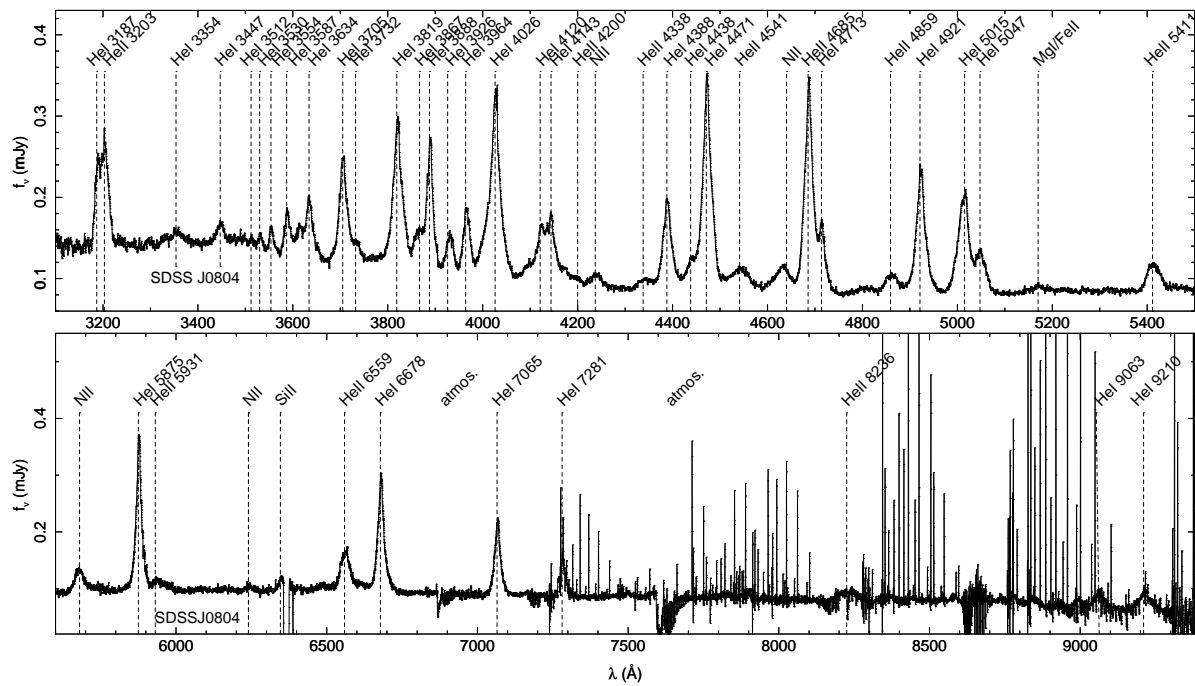

Figure 6.6: Gaussian smoothed average spectrum of V406 Hya obtained with VLT/X-Shooter. Prominent lines are indicated. The forest of narrow emission lines in the red part of the spectrum ($> 7500\,\text{Å}$) are residuals from the sky-line removal.
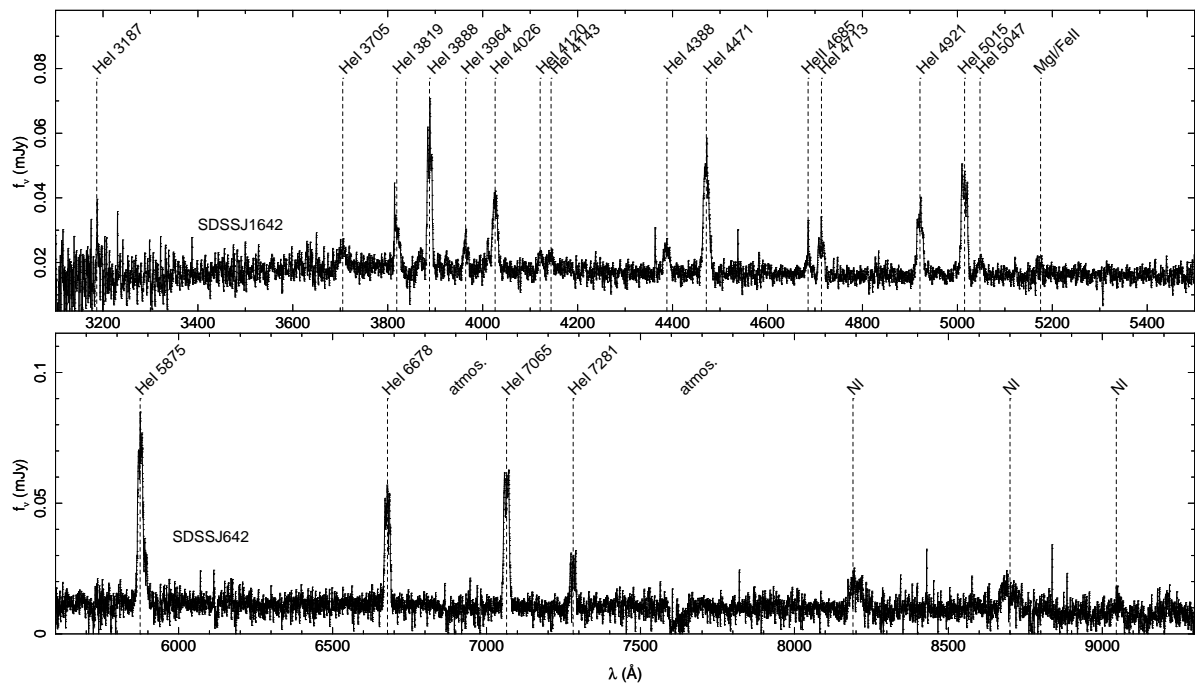
Figure 6.7: Gaussian smoothed average spectrum of SDSS J1240 obtained with VLT/X-Shooter. Prominent lines are indicated. The forest of narrow emission lines in the red part of the spectrum ($> 7500\,\text{Å}$) are residuals from the sky-line removal.

Figure 6.8: Gaussian smoothed average spectrum of SDSS J1721 obtained with VLT/X-Shooter. Prominent lines are indicated. The large number of narrow absorption lines is due to the low signal-to-noise ratio.

Figure 6.9: Gaussian smoothed average spectrum of SDSS J0804 obtained with VLT/X-Shooter. Prominent lines are indicated. The forest of narrow emission lines in the red part of the spectrum ($> 7500\,\text{Å}$) are residuals from the sky-line removal.

Figure 6.10: Gaussian smoothed average spectrum of SDSS J1642 obtained with VLT/X-Shooter. Prominent lines are indicated.

REFERENCES

Almeida, L. A., Jablonski, F., Tello, J., & Rodrigues, C. V. 2012, *A photometric and spectroscopic study of NSVS 14256825: the second sdOB+dM eclipsing binary*, MNRAS, 423, 478

Anderson, S. F. et al. 2005, *Ultracompact AM Canum Venaticorum Binaries from the Sloan Digital Sky Survey: Three Candidates Plus the First Confirmed Eclipsing System*, AJ, 130, 2230

Anderson, S. F. et al. 2008, *Two More Candidate AM Canum Venaticorum (am CVn) Binaries from the Sloan Digital Sky Survey*, AJ, 135, 2108

Arnould, M., Goriely, S., & Jorissen, A. 1999, *Non-explosive hydrogen and helium burnings: abundance predictions from the NACRE reaction rate compilation*, A&A, 347, 572

Barlow, B., Wade, R., Liss, S., & Stark, M. 2014, *Resolved, but Unresolved: A Trio of Triple- and Quadruple-Star Hot Subdwarf Systems*, in Astronomical Society of the Pacific Conference Series, Vol. 481, Astronomical Society of the Pacific Conference Series, ed. V. van Grootel, E. Green, G. Fontaine, & S. Charpinet, 301

Barlow, B. N., Dunlap, B. H., & Clemens, J. C. 2011, *Radial Velocity Confirmation of a Binary Detected from Pulse Timings*, ApJL, 737, L2

Barlow, B. N., Kilkenny, D., Drechsel, H., et al. 2013, *EC 10246-2707: an eclipsing subdwarf B + M dwarf binary*, MNRAS, 430, 22

Beauchamp, A. & Wesemael, F. 1998, *The Optical Spectrum of Extreme Helium Stars: A Hotbed of Forbidden Components of Neutral Helium*, ApJ, 496, 395

Beauchamp, A., Wesemael, F., & Bergeron, P. 1997, *Spectroscopic Studies of DB White Dwarfs: Improved Stark Profiles for Optical Transitions of Neutral Helium*, ApJS, 108, 559

Bildsten, L., Shen, K. J., Weinberg, N. N., & Nelemans, G. 2007, *Faint Thermonuclear Supernovae from AM Canum Venaticorum Binaries*, ApJL, 662, L95

Bildsten, L., Townsley, D. M., Deloye, C. J., & Nelemans, G. 2006, *The Thermal State of the Accreting White Dwarf in AM Canum Venaticorum Binaries*, ApJ, 640, 466

Bloemen, S., Marsh, T. R., Østensen, R. H., et al. 2011, *Kepler observations of the beaming binary KPD 1946+4340*, MNRAS, 410, 1787

Breedt, E., Gänsicke, B. T., Drake, A. J., et al. 2014, *1000 cataclysmic variables from the Catalina Real-time Transient Survey*, MNRAS, 443, 3174

Breedt, E., Gänsicke, B. T., Marsh, T. R., et al. 2012, *CSS100603:112253-111037: a helium-rich dwarf nova with a 65 min orbital period*, MNRAS, 425, 2548

Brown, W. R., Kilic, M., Allende Prieto, C., Gianninas, A., & Kenyon, S. J. 2013, *The ELM Survey. V. Merging Massive White Dwarf Binaries*, ApJ, 769, 66

Brown, W. R., Kilic, M., Allende Prieto, C., & Kenyon, S. J. 2010, *The ELM Survey. I. A Complete Sample of Extremely Low-mass White Dwarfs*, ApJ, 723, 1072

Carter, D. et al. 1993, *ISIS USERS MANUAL*

Carter, P. J., Gänsicke, B. T., Steeghs, D., et al. 2014a, *Two new AM Canum Venaticorum binaries from the Sloan Digital Sky Survey III*, MNRAS, 439, 2848

Carter, P. J., Marsh, T. R., Steeghs, D., et al. 2012, *A search for the hidden population of AM CVn binaries in the Sloan Digital Sky Survey*, MNRAS, 392

Carter, P. J., Marsh, T. R., Steeghs, D., et al. 2013, *A search for the hidden population of AM CVn binaries in the Sloan Digital Sky Survey*, MNRAS, 429, 2143

Carter, P. J., Steeghs, D., Marsh, T. R., et al. 2014b, *The AM Canum Venaticorum binary SDSS J173047.59+554518.5*, MNRAS, 437, 2894

Cepa, J. 1998, *OSIRIS Imaging and Spectroscopy for the GTC*, Astrophysics and Space Science, 263, 369

Charpinet, S., Van Grootel, V., Reese, D., et al. 2008, *Testing the forward modeling approach in asteroseismology. II. Structure and internal dynamics of the hot B subdwarf component in the close eclipsing binary system PG 1336-018*, A&A, 489, 377

Clausen, D., Wade, R. A., Kopparapu, R. K., & O'Shaughnessy, R. 2012, *Population Synthesis of Hot Subdwarfs: A Parameter Study*, ApJ, 746, 186

Coenen, T., van Leeuwen, J., & Stairs, I. H. 2011, *A search for radio pulsations from neutron star companions of four subdwarf B stars*, A&A, 531, A125

Copperwheat, C. M., Marsh, T. R., Littlefair, S. P., et al. 2011, *SDSS J0926+3624: the shortest period eclipsing binary star*, MNRAS, 410, 1113

Córsico, A. H., Althaus, L. G., Miller Bertolami, M. M., & Bischoff-Kim, A. 2012, *Asteroseismology of the Kepler V777 Herculis variable white dwarf with fully evolutionary models*, A&A, 541, A42

Deca, J., Marsh, T. R., Østensen, R. H., et al. 2012, *PG 1018-047: the longest period subdwarf B binary*, MNRAS, 421, 2798

Deloye, C. J., Taam, R. E., Winisdoerffer, C., & Chabrier, G. 2007, *The thermal evolution of the donors in AM Canum Venaticorum binaries*, MNRAS, 381, 525

Dorman, B., Rood, R. T., & O'Connell, R. W. 1993, *Ultraviolet Radiation from Evolved Stellar Populations. I. Models*, ApJ, 419, 596

Downes, R. A. 1986, *The KPD survey for galactic plane ultraviolet-excess objects Space densities of white dwarfs and subdwarfs*, ApJs, 61, 569

Drechsel, H., Heber, U., Napiwotzki, R., et al. 2001, *HS 0705+6700: A new eclipsing sdB binary*, A&A, 379, 893

Dufour, P., Kilic, M., Fontaine, G., et al. 2012, *Detailed Compositional Analysis of the Heavily Polluted DBZ White Dwarf SDSS J073842.56+183509.06: A Window on Planet Formation?*, ApJ, 749, 6

Edelmann, H. 2008, *HW Vir's Companion: an M-type Dwarf, or maybe a Giant Rotating Spherical Mirror?*, in Astronomical Society of the Pacific Conference Series, Vol. 392, Hot Subdwarf Stars and Related Objects, ed. U. Heber, C. S. Jeffery, & R. Napiwotzki, 187

Edelmann, H., Heber, U., Altmann, M., Karl, C., & Lisker, T. 2005, *High resolution spectroscopy of bright subdwarf B stars. I. Radial velocity variables*, A&A, 442, 1023

Edelmann, H., Heber, U., Lisker, T., & Green, E. M. 2004, *Radial velocity curves of nine sdB binary stars*, Astrophysics and Space Science, 291, 315

Edelmann, H., Heber, U., Napiwotzki, R., Reid, I. N., & Saffer, R. A. 1999, *Spectral analysis of the binary sdB star Feige 36*, in Astronomical Society of the Pacific Conference Series, Vol. 169, 11th European Workshop on White Dwarfs, ed. S.-E. Solheim & E. G. Meistas, 546

Eggleton, P. 2006, Evolutionary Processes in Binary and Multiple Stars

Eggleton, P. P. 1983, *Approximations to the radii of Roche lobes*, ApJ, 268, 368

Espaillat, C., Patterson, J., Warner, B., & Woudt, P. 2005, *The Helium-rich Cataclysmic Variable ES Ceti*, PASP, 117, 189

Faulkner, J., Flannery, B. P., & Warner, B. 1972, *Ultrashort-Period Binaries. II. HZ 29 (=AM CVn): a Double-White Semidetached Postcataclysmic Nova?*, ApJL, 175, L79

Ferdman, R. D., Stairs, I. H., Kramer, M., et al. 2010, *A Precise Mass Measurement of the Intermediate-Mass Binary Pulsar PSR J1802 - 2124*, ApJ, 711, 764

Fontaine, G., Brassard, P., Charpinet, S., et al. 2012, *A preliminary look at the empirical mass distribution of hot B subdwarf stars*, A&A, 539, A12

Fontaine, G. et al. 2011, *Discovery of a New AM CVn System with the Kepler Satellite*, ApJ, 726, 92

For, B.-Q., Edelmann, H., Green, E. M., et al. 2008, *KBS 13 – a Rare Reflection Effect sdB Binary with an M Dwarf Secondary*, in Astronomical Society of the Pacific Conference Series, Vol. 392, Hot Subdwarf Stars and Related Objects, ed. U. Heber, C. S. Jeffery, & R. Napiwotzki, 203

For, B.-Q., Green, E. M., Fontaine, G., & Shaw, S. 2010, *A rare reflection effect eclipsing sdB+dM binary: 2M 1533+3759*, Astrophysics and Space Science, 329, 87

For, B.-Q., Green, E. M., O'Donoghue, D., et al. 2006, *First Attempt at Spectroscopic Detection of Gravity Modes in the Long-Period Pulsating Subdwarf B Star PG 1627+017*, ApJ, 642, 1117

Freudling, W., Romaniello, M., Bramich, D. M., et al. 2013, *Automated data reduction workflows for astronomy. The ESO Reflex environment*, A&A, 559, A96

Geier, S., Classen, L., Brünner, P., et al. 2012a, *Low-mass Stellar and Substellar Companions to sdB Stars*, in Astronomical Society of the Pacific Conference Series, Vol. 452, Fifth Meeting on Hot Subdwarf Stars and Related Objects, ed. D. Kilkenny, C. S. Jeffery, & C. Koen, 153

Geier, S., Heber, U., Edelmann, H., et al. 2013a, *Hot subdwarf stars in close-up view. IV. Helium abundances and the ^{3}He isotopic anomaly of subdwarf B stars*, A&A, 557, A122

Geier, S., Heber, U., Kupfer, T., & Napiwotzki, R. 2010a, *Binaries discovered by the SPY project . V. GD 687 - a massive double degenerate binary progenitor that will merge within a Hubble time*, A&A, 515, A37

Geier, S., Heber, U., Podsiadlowski, P., et al. 2010b, *Hot subdwarf stars in close-up view. I. Rotational properties of subdwarf B stars in close binary systems and nature of their unseen companions*, A&A, 519, A25

Geier, S., Hirsch, H., Tillich, A., et al. 2011a, *The MUCHFUSS project - searching for hot subdwarf binaries with massive unseen companions. Survey, target selection and atmospheric parameters*, A&A, 530, A28

Geier, S., Karl, C., Edelmann, H., Heber, U., & Napiwotzki, R. 2006, *Spectroscopic Analyses of subluminous B stars in binaries*, in International Symposium on Nuclear Astrophysics - Nuclei in the Cosmos

Geier, S., Kupfer, T., Heber, U., et al. 2015, *The catalogue of radial velocity variable hot subluminous stars from the MUCHFUSS project*, , 577, A26

Geier, S., Marsh, T. R., Wang, B., et al. 2013b, *A progenitor binary and an ejected mass donor remnant of faint type Ia supernovae*, A&A, 554, A54

Geier, S., Maxted, P. F. L., Napiwotzki, R., et al. 2011b, *Massive unseen companions to hot faint underluminous stars from SDSS (MUCHFUSS). Analysis of seven close subdwarf B binaries*, A&A, 526, A39

Geier, S., Napiwotzki, R., Heber, U., & Nelemans, G. 2011c, *Binaries discovered by the SPY survey. VI. Discovery of a low mass companion to the hot subluminous planetary nebula central star EGB 5 - a recently ejected common envelope?*, A&A, 528, L16

Geier, S., Nesslinger, S., Heber, U., et al. 2007, *The hot subdwarf B + white dwarf binary KPD 1930+2752. A supernova type Ia progenitor candidate*, A&A, 464, 299

Geier, S., Nesslinger, S., Heber, U., et al. 2008, *Tidal synchronisation of the subdwarf B binary PG 0101+039*, A&A, 477, L13

Geier, S., Østensen, R. H., Heber, U., et al. 2014, *Orbital solutions of eight close sdB binaries and constraints on the nature of the unseen companions*, A&A, 562, A95

Geier, S., Schaffenroth, V., Drechsel, H., et al. 2011d, *Binaries Discovered by the MUCH-FUSS Project: SDSS J08205+0008An Eclipsing Subdwarf B Binary with a Brown Dwarf Companion*, ApJL, 731, L22

Geier, S., Schaffenroth, V., Hirsch, H., et al. 2012b, *MUCHFUSS - Massive Unseen Companions to Hot Faint Underluminous Stars from SDSS*, Astronomische Nachrichten, 333, 431

Gianninas, A., Dufour, P., Kilic, M., et al. 2014, *Precise Atmospheric Parameters for the Shortest-period Binary White Dwarfs: Gravitational Waves, Metals, and Pulsations*, ApJ, 794, 35

Gilliland, R. L. et al. 2010, *Initial Characteristics of Kepler Short Cadence Data*, ApJL, 713, L160

Gokhale, V., Peng, X. M., & Frank, J. 2007, *Evolution of Close White Dwarf Binaries*, ApJ, 655, 1010

Gray, D. F. 2008, The Observation and Analysis of Stellar Photospheres

Green, E. M., Fontaine, G., Hyde, E. A., Charpinet, S., & Chayer, P. 2006, *Subdwarf B Star Evolutionary Systematics, Conundrums and Cautionary Remarks*, Baltic Astronomy, 15, 167

Green, E. M., Fontaine, G., Hyde, E. A., For, B.-Q., & Chayer, P. 2008, *Systematics of Hot Subdwarfs Obtained from a Large Low Resolution Survey*, in Astronomical Society of the Pacific Conference Series, Vol. 392, Hot Subdwarf Stars and Related Objects, ed. U. Heber, C. S. Jeffery, & R. Napiwotzki, 75

Green, E. M., For, B., Hyde, E. A., et al. 2004, *Companions of Post-Common Envelope sdB Binaries*, Astrophysics and Space Science, 291, 267

Green, E. M., For, B.-Q., & Hyde, E. A. 2005, *The Secondary Companions in Short-Period sdB Binaries*, in Astronomical Society of the Pacific Conference Series, Vol. 334, 14th European Workshop on White Dwarfs, ed. D. Koester & S. Moehler, 363

Green, R. F., Schmidt, M., & Liebert, J. 1986, *The Palomar-Green catalog of ultraviolet-excess stellar objects*, ApJs, 61, 305

Greenstein, J. L. 1954, *New features in the spectra of white dwarfs.*, AJ, 59, 322

Greenstein, J. L. & Matthews, M. S. 1957, *Studies of the White Dwarfs. I. Broad Features in White Dwarf Spectra.*, ApJ, 126, 14

Griem, H. R. 1968, *Calculated Electron and Ion Stark Broadening of the Allowed and Forbidden 2^3P-4 ^3P, ^3D, ^3F Transitions in Neutral Helium*, ApJ, 154, 1111

Groot, P. J., Nelemans, G., Steeghs, D., & Marsh, T. R. 2001, *The Quiescent Spectrum of the AM Canum Venaticorum Star CP Eridani*, ApJL, 558, L123

Hagen, H.-J., Groote, D., Engels, D., & Reimers, D. 1995, *The Hamburg Quasar Survey. I. Schmidt observations and plate digitization.*, A&A, 111, 195

Hamuy, M., Suntzeff, N. B., Heathcote, S. R., et al. 1994, *Southern spectrophotometric standards, 2*, PASP, 106, 566

Hamuy, M., Walker, A. R., Suntzeff, N. B., et al. 1992, *Southern spectrophotometric standards.*, PASP, 104, 533

Han, Z., Podsiadlowski, P., Maxted, P. F. L., & Marsh, T. R. 2003, *The origin of subdwarf B stars - II*, MNRAS, 341, 669

Han, Z., Podsiadlowski, P., Maxted, P. F. L., Marsh, T. R., & Ivanova, N. 2002a, *The origin of subdwarf B stars - I. The formation channels*, MNRAS, 336, 449

Han, Z., Podsiadlowski, P., & Tout, C. A. 2002b, *Criterion for Dynamical Instability of Mass Transfer in Binary Evolution*, in Astronomical Society of the Pacific Conference Series, Vol. 279, Exotic Stars as Challenges to Evolution, ed. C. A. Tout & W. van Hamme, 297

Heber, U. 1986, *The atmosphere of subluminous B stars. II - Analysis of 10 helium poor subdwarfs and the birthrate of sdB stars*, A&A, 155, 33

Heber, U. 2009, *Hot Subdwarf Stars*, Annual Review of Astronomy Astrophysics, 47, 211

Heber, U., Drechsel, H., Østensen, R., et al. 2004, *HS 2333+3927: A new sdB+dM binary with a large reflection effect*, A&A, 420, 251

Heber, U., Edelmann, H., Lisker, T., & Napiwotzki, R. 2003, *Discovery of a helium-core white dwarf progenitor*, A&A, 411, L477

Heber, U., Moehler, S., Napiwotzki, R., Thejll, P., & Green, E. M. 2002, *Resolving subdwarf B stars in binaries by HST imaging*, A&A, 383, 938

Heber, U., Reid, I. N., & Werner, K. 2000, *Spectral analysis of multi mode pulsating sdB stars. II. Feige 48, KPD 2109+4401 and PG 1219+534*, A&A, 363, 198

Hempel, M. & Holweger, H. 2003, *Abundance analysis of late B stars. Evidence for diffusion and against weak stellar winds*, A&A, 408, 1065

Hermes, J. J., Charpinet, S., Barclay, T., et al. 2014, *Precision Asteroseismology of the Pulsating White Dwarf GD 1212 Using a Two-wheel-controlled Kepler Spacecraft*, ApJ, 789, 85

Hirose, M. & Osaki, Y. 1990, *Hydrodynamic simulations of accretion disks in cataclysmic variables - Superhump phenomenon in SU UMa stars*, PASJ, 42, 135

Høg, E., Fabricius, C., Makarov, V. V., et al. 2000, *The Tycho-2 catalogue of the 2.5 million brightest stars*, A&A, 355, L27

Horne, K. 1985, *Images of accretion discs. I - The eclipse mapping method*, MNRAS, 213, 129

Horne, K. 1986, *An optimal extraction algorithm for CCD spectroscopy*, PASP, 98, 609

Horne, K. & Marsh, T. R. 1986, *Emission line formation in accretion discs*, MNRAS, 218, 761

Humason, M. L. & Zwicky, F. 1947, *A Search for Faint Blue Stars.*, ApJ, 105, 85

Iben, Jr., I. & Tutukov, A. V. 1991, *Helium star cataclysmics*, ApJ, 370, 615

Ivanova, N., Justham, S., Chen, X., et al. 2013, *Common envelope evolution: where we stand and how we can move forward*, The Astronomy and Astrophysics Review, 21, 59

Jester, S., Schneider, D. P., Richards, G. T., et al. 2005, *The Sloan Digital Sky Survey View of the Palomar-Green Bright Quasar Survey*, AJ, 130, 873

Kaltenegger, L. & Traub, W. A. 2009, *Transits of Earth-like Planets*, ApJ, 698, 519

Kaplan, D. L., Bhalerao, V. B., van Kerkwijk, M. H., et al. 2013, *A Metal-rich Low-gravity Companion to a Massive Millisecond Pulsar*, ApJ, 765, 158

Kaplan, D. L., Bildsten, L., & Steinfadt, J. D. R. 2012, *Orbital Evolution of Compact White Dwarf Binaries*, ApJ, 758, 64

Karl, C., Heber, U., Jeffery, S., Napiwotzki, R., & Geier, S. 2006, *Spectroscopic Analysis of Sdb Binaries from the Spy Project*, Baltic Astronomy, 15, 151

Kato, T., Hambsch, F.-J., & Monard, B. 2015, *ASASSN-14cc: A likely helium analog of RZ Leonis Minoris*, PASJ, 67, L2

Kato, T., Nogami, D., Baba, H., Hanson, G., & Poyner, G. 2000, *CR Boo: the 'helium ER UMa star' with a 46.3-d supercycle*, MNRAS, 315, 140

Kato, T., Ohshima, T., Denisenko, D., et al. 2014, *Superoutburst of SDSS J090221.35+381941.9: First measurement of mass ratio in an AM CVn-type object using growing superhumps*, PASJ, 66, L7

Kato, T., Stubbings, R., Monard, B., et al. 2004, *V803 Centauri: Helium Dwarf Nova Mimicking a WZ Sge-Type Superoutburst*, PASJ, 56, 89

Kawka, A., Pigulski, A., O'Toole, S., et al. 2012, *Binary Properties of Subdwarfs Selected in the GALEX Survey*, in Astronomical Society of the Pacific Conference Series, Vol. 452, Fifth Meeting on Hot Subdwarf Stars and Related Objects, ed. D. Kilkenny, C. S. Jeffery, & C. Koen, 121

Kilic, M., Brown, W. R., Allende Prieto, C., et al. 2012, *The ELM Survey. IV. 24 White Dwarf Merger Systems*, ApJ, 751, 141

Kilkenny, D., O'Donoghue, D., Koen, C., Stobie, R. S., & Chen, A. 1997, *The Edinburgh-Cape Blue Object Survey - II. Zone 1 - the North Galactic CAP*, MNRAS, 287, 867

Kirchhoff, G. 1860, *Ueber das Verhältniss zwischen dem Emissionsvermögen und dem Absorptionsvermögen der Körper für Wärme und Licht*, Annalen der Physik, 185, 275

Kleinman, S. J., Kepler, S. O., Koester, D., et al. 2013, *SDSS DR7 White Dwarf Catalog*, ApJs, 204, 5

Klepp, S. & Rauch, T. 2011, *On the sdOB primary of the post common-envelope binary AA Doradus (LB 3459)*, A&A, 531, L7

Koen, C., Orosz, J. A., & Wade, R. A. 1998, *KPD 0422+5421: a new short-period subdwarf B/white dwarf binary*, MNRAS, 300, 695

Koester, D. 2009, *Accretion and diffusion in white dwarfs. New diffusion timescales and applications to GD 362 and G 29-38*, A&A, 498, 517

Kopal, Z. 1959, Close binary systems

Kraus, A. L. & Hillenbrand, L. A. 2007, *The Stellar Populations of Praesepe and Coma Berenices*, AJ, 134, 2340

Kupfer, T., Geier, S., McLeod, A., et al. 2014, *Finding Compact Hot Subdwarf Binaries in the Galactic Disc*, in Astronomical Society of the Pacific Conference Series, Vol. 481, Astronomical Society of the Pacific Conference Series, ed. V. van Grootel, E. Green, G. Fontaine, & S. Charpinet, 293

Kupfer, T., Groot, P. J., Levitan, D., et al. 2013, *Orbital periods and accretion disc structure of four AM CVn systems*, MNRAS, 432, 2048

Lada, C. J. 2006, *Stellar Multiplicity and the Initial Mass Function: Most Stars Are Single*, ApJL, 640, L63

Landolt, A. U. 2007, *UBVRI Photometric Standard Stars around the Sky at -50° Declination*, AJ, 133, 2502

Landolt, A. U. 2009, *UBVRI Photometric Standard Stars Around the Celestial Equator: Updates and Additions*, AJ, 137, 4186

Law, N. M., Kulkarni, S. R., Dekany, R. G., et al. 2009, *The Palomar Transient Factory: System Overview, Performance, and First Results*, PASP, 121, 1395

Levitan, D., Fulton, B. J., Groot, P. J., et al. 2011, *PTF1 J071912.13+485834.0: An Outbursting AM CVn System Discovered by a Synoptic Survey*, ApJ, 739, 68

Levitan, D., Groot, P. J., Prince, T. A., et al. 2015, *Long-term photometric behaviour of outbursting AM CVn systems*, MNRAS, 446, 391

Levitan, D., Kupfer, T., Groot, P. J., et al. 2013, *Five new outbursting AM CVn systems discovered by the Palomar Transient Factory*, MNRAS, 430, 996

Levitan, D., Kupfer, T., Groot, P. J., et al. 2014, *PTF1 J191905.19+481506.2-a Partially Eclipsing AM CVn System Discovered in the Palomar Transient Factory*, ApJ, 785, 114

Lisker, T., Heber, U., Napiwotzki, R., et al. 2005, *Hot subdwarfs from the ESO Supernova Ia Progenitor Survey. I. Atmospheric parameters and cool companions of sdB stars*, A&A, 430, 223

Lubow, S. H. & Shu, F. H. 1975, *Gas dynamics of semidetached binaries*, ApJ, 198, 383

Malmquist, K. G. 1936, *Investigations on the stars in high galactic latitudes II. Photographic magnitudes and colour indices of about 4500 stars near the north galactic pole.*, Stockholms Observatoriums Annaler, 12, 7

Marsh, T. R. 1999, *Kinematics of the helium accretor GP COM*, MNRAS, 304, 443

Marsh, T. R. 2001, *Doppler Tomography*, in Lecture Notes in Physics, Berlin Springer Verlag, Vol. 573, Astrotomography, Indirect Imaging Methods in Observational Astronomy, ed. H. M. J. Boffin, D. Steeghs, & J. Cuypers, 1

Marsh, T. R. & Horne, K. 1988, *Images of accretion discs. II - Doppler tomography*, MNRAS, 235, 269

Marsh, T. R., Horne, K., & Rosen, S. 1991, *Evidence for CNO processed material in the accretion disk of GP Comae*, ApJ, 366, 535

Marsh, T. R., Nelemans, G., & Steeghs, D. 2004, *Mass transfer between double white dwarfs*, MNRAS, 350, 113

Marsh, T. R., Wood, J. H., Horne, K., & Lambert, D. 1995, *The discovery of high-velocity flares in NV and the detection of carbon in the double degenerate binary GP COM*, MNRAS, 274, 452

Maxted, P. f. L., Heber, U., Marsh, T. R., & North, R. C. 2001, *The binary fraction of extreme horizontal branch stars*, MNRAS, 326, 1391

Maxted, P. F. L., Marsh, T. R., Heber, U., et al. 2002, *Photometry of four binary subdwarf B stars and the nature of their unseen companion stars*, MNRAS, 333, 231

Maxted, P. F. L., Marsh, T. R., & North, R. C. 2000a, *KPD 1930+2752: a candidate Type Ia supernova progenitor*, MNRAS, 317, L41

Maxted, P. F. L., Moran, C. K. J., Marsh, T. R., & Gatti, A. A. 2000b, *Orbital periods of the binary sdB stars PG0940+068 and PG 1247+554*, MNRAS, 311, 877

Maxted, P. F. L., Serenelli, A. M., Miglio, A., et al. 2013, *Multi-periodic pulsations of a stripped red-giant star in an eclipsing binary system*, , 498, 463

Mengel, J. G., Norris, J., & Gross, P. G. 1976, *Binary Hypothesis for the Subdwarf B Stars*, ApJ, 204, 488

Mereghetti, S., Campana, S., Esposito, P., La Palombara, N., & Tiengo, A. 2011, *Search for X-ray emission from subdwarf B stars with compact companion candidates*, A&A, 536, A69

Mereghetti, S., La Palombara, N., Esposito, P., et al. 2014, *Constraints on the winds of hot subdwarf stars from X-ray observations of two sdB binaries with compact companions: CD -30° 11223 and PG 1232-136*, MNRAS, 441, 2684

Mereghetti, S., Tiengo, A., Esposito, P., et al. 2009, *An Ultramassive, Fast-Spinning White Dwarf in a Peculiar Binary System*, Science, 325, 1222

Mermilliod, J.-C. 1992, *Archives of photometric data*, Highlights of Astronomy, 9, 725

Mills, D., Webb, J., Clayton, M., & Gray, N. 2014, *ECHOMOP: Echelle data reduction package*, Astrophysics Source Code Library

Morales-Rueda, L., Marsh, T. R., Steeghs, D., et al. 2003a, *New results on GP Com*, A&A, 405, 249

Morales-Rueda, L., Maxted, P. F. L., Marsh, T. R., North, R. C., & Heber, U. 2003b, *Orbital periods of 22 subdwarf B stars*, MNRAS, 338, 752

Moran, C., Maxted, P., Marsh, T. R., Saffer, R. A., & Livio, M. 1999, *The orbital parameters of three new subdwarf B binaries*, MNRAS, 304, 535

Müller, S., Geier, S., & Heber, U. 2010, *The cool companion of AA Doradus–Brown dwarf or late M star?*, Astrophysics and Space Science, 329, 101

Napiwotzki, R., Christlieb, N., Drechsel, H., et al. 2001a, *Search for progenitors of supernovae type Ia with SPY*, Astronomische Nachrichten, 322, 411

Napiwotzki, R., Edelmann, H., Heber, U., et al. 2001b, *Binaries discovered by the SPY project. I. HE 1047-0436: A subdwarf B + white dwarf syste*, A&A, 378, L17

Napiwotzki, R., Karl, C. A., Lisker, T., et al. 2004a, *Close binary EHB stars from SPY*, Astrophysics and Space Science, 291, 321

Napiwotzki, R., Yungelson, L., Nelemans, G., et al. 2004b, *Double degenerates and progenitors of supernovae type Ia*, in Astronomical Society of the Pacific Conference Series, Vol. 318, Spectroscopically and Spatially Resolving the Components of the Close Binary Stars, ed. R. W. Hilditch, H. Hensberge, & K. Pavlovski, 402–410

Naslim, N., Geier, S., Jeffery, C. S., et al. 2012, *The helium-rich subdwarf CPD-20°1123: a post-common-envelope binary evolving on to the extended horizontal branch*, MNRAS, 423, 3031

Nather, R. E., Robinson, E. L., & Stover, R. J. 1981, *The twin-degenerate interacting binary G61-29*, ApJ, 244, 269

Nebot Gómez-Morán, A., Gänsicke, B. T., Schreiber, M. R., et al. 2011, *Post common envelope binaries from SDSS. XII. The orbital period distribution*, A&A, 536, A43

Nelemans, G. 2005, *AM CVn stars*, in Astronomical Society of the Pacific Conference Series, Vol. 330, The Astrophysics of Cataclysmic Variables and Related Objects, ed. J.-M. Hameury & J.-P. Lasota, 27

Nelemans, G. 2010, *Population synthesis of Galactic subdwarf B stars*, Astrophysics and Space Science, 329, 25

Nelemans, G., Portegies Zwart, S. F., Verbunt, F., & Yungelson, L. R. 2001a, *Population synthesis for double white dwarfs. II. Semi-detached systems: AM CVn stars*, A&A, 368, 939

Nelemans, G., Steeghs, D., & Groot, P. J. 2001b, *Spectroscopic evidence for the binary nature of AM CVn*, MNRAS, 326, 621

Nelemans, G., Yungelson, L. R., & Portegies Zwart, S. F. 2004, *Short-period AM CVn systems as optical, X-ray and gravitational-wave sources*, MNRAS, 349, 181

Nelemans, G., Yungelson, L. R., van der Sluys, M. V., & Tout, C. A. 2010, *The chemical composition of donors in AM CVn stars and ultracompact X-ray binaries: observational tests of their formation*, MNRAS, 401, 1347

Németh, P., Kawka, A., & Vennes, S. 2012, *A selection of hot subluminous stars in the GALEX survey - II. Subdwarf atmospheric parameters*, MNRAS, 427, 2180

Nissanke, S., Vallisneri, M., Nelemans, G., & Prince, T. A. 2012, *Gravitational-wave Emission from Compact Galactic Binaries*, ApJ, 758, 131

O'Donoghue, D., Kilkenny, D., Chen, A., et al. 1994, *EC:15330-1403 and the Am-Canum Stars*, MNRAS, 271, 910

O'Donoghue, D., Kilkenny, D., Koen, C., et al. 2013, *The Edinburgh-Cape Blue Object Survey - III. Zone 2; galactic latitudes -30° > b > -40°*, MNRAS, 431, 240

O'Donoghue, D., Menzies, J. W., & Hill, P. W. 1987, *Photometry and spectroscopy of the interacting binary white dwarf V803 CEN (AE-1)*, MNRAS, 227, 347

Oke, J. B. 1974, *Absolute Spectral Energy Distributions for White Dwarfs*, ApJS, 27, 21

Oke, J. B. 1990, *Faint spectrophotometric standard stars*, AJ, 99, 1621

Oke, J. B. & Gunn, J. E. 1982, *An Efficient Low Resolution and Moderate Resolution Spectrograph for the Hale Telescope*, PASP, 94, 586

Orosz, J. A. & Wade, R. A. 1999, *Confirmation of eclipses in KPD 0422+5421, a binary containing a white dwarf and a subdwarf B star*, MNRAS, 310, 773

Østensen, R., Oreiro, R., Drechsel, H., et al. 2007, *HS 2231+2441: A New Eclipsing sdB Binary of the HW Vir Type*, in Astronomical Society of the Pacific Conference Series, Vol. 372, 15th European Workshop on White Dwarfs, ed. R. Napiwotzki & M. R. Burleigh, 483

Østensen, R. H., Geier, S., Schaffenroth, V., et al. 2013, *Binaries discovered by the MUCH-FUSS project. FBS 0117+396: An sdB+dM binary with a pulsating primary*, A&A, 559, A35

Østensen, R. H., Green, E. M., Bloemen, S., et al. 2010a, *2M1938+4603: a rich, multimode pulsating sdB star with an eclipsing dM companion observed with Kepler*, MNRAS, 408, L51

Østensen, R. H., Silvotti, R., Charpinet, S., et al. 2010b, *First Kepler results on compact pulsators - I. Survey target selection and the first pulsators*, MNRAS, 409, 1470

Østensen, R. H., Telting, J. H., Reed, M. D., et al. 2014, *Asteroseismology revealing trapped modes in KIC 10553698A*, A&A, 569, A15

Østensen, R. H. & Van Winckel, H. 2012, *Radial-velocity Monitoring of Long-period Hot-subdwarf + Main-sequence Binaries with HERMES@Mercator*, in Astronomical Society of the Pacific Conference Series, Vol. 452, Fifth Meeting on Hot Subdwarf Stars and Related Objects, ed. D. Kilkenny, C. S. Jeffery, & C. Koen, 163

Østensen, R. H. et al. 2011, *First Kepler results on compact pulsators - VI. Targets in the final half of the survey phase*, MNRAS, 414, 2860

O'Toole, S. J. & Heber, U. 2006, *Abundance studies of sdB stars using UV echelle HST/STIS spectroscopy*, A&A, 452, 579

O'Toole, S. J., Heber, U., & Benjamin, R. A. 2004, *Detection of a companion to the pulsating sdB Feige 48*, A&A, 422, 1053

O'Toole, S. J., Napiwotzki, R., Heber, U., et al. 2006, *NGC 6121-V46: a Low-Mass Double Degenerate Ellipsoidal Variable in a Globular Cluster*, Baltic Astronomy, 15, 61

Paczyński, B. 1967, *Gravitational Waves and the Evolution of Close Binaries*, Acta Astronomica, 17, 287

Paczyński, B. 1971, *Evolutionary Processes in Close Binary Systems*, Annual Review of Astronomy and Astrophysics, 9, 183

Paczynski, B. 1976, *Common Envelope Binaries*, in IAU Symposium, Vol. 73, Structure and Evolution of Close Binary Systems, ed. P. Eggleton, S. Mitton, & J. Whelan, 75

Parsons, S. G., Marsh, T. R., Gänsicke, B. T., et al. 2012, *The shortest period detached white dwarf + main-sequence binary*, MNRAS, 419, 304

Patterson, J., Fried, R. E., Rea, R., et al. 2002, *Superhumps in Cataclysmic Binaries. XXI. HP Librae (=EC 15330-1403)*, PASP, 114, 65

Patterson, J., Halpern, J., & Shambrook, A. 1993, *Evidence for Accretion Disk Precession in the Cataclysmic Binary AM Canum Venaticorum*, ApJ, 419, 803

Patterson, J., Kemp, J., Shambrook, A., et al. 1997, *Superhumps in Cataclysmic Binaries. XII. CR Bootis, a Helium Dwarf Nova*, PASP, 109, 1100

Patterson, J., Walker, S., Kemp, J., et al. 2000, *V803 Centauri: A Helium-rich Dwarf Nova*, PASP, 112, 625

Patterson, J. et al. 2005, *Superhumps in Cataclysmic Binaries. XXV. q_{crit}, $\epsilon(q)$, and Mass-Radius*, Publications of the Astronomical Society of the Pacific, 117, 1204

Pfahl, E., Rappaport, S., & Podsiadlowski, P. 2003, *The Galactic Population of Low- and Intermediate-Mass X-Ray Binaries*, ApJ, 597, 1036

Piro, A. L. 2011, *Tidal Interactions in Merging White Dwarf Binaries*, ApJL, 740, L53

Podsiadlowski, P., Han, Z., & Rappaport, S. 2003, *Cataclysmic variables with evolved secondaries and the progenitors of AM CVn stars*, MNRAS, 340, 1214

Podsiadlowski, P., Rappaport, S., & Pfahl, E. D. 2002, *Evolutionary Sequences for Low- and Intermediate-Mass X-Ray Binaries*, ApJ, 565, 1107

Postnov, K. A. & Yungelson, L. R. 2014, *The Evolution of Compact Binary Star Systems*, Living Reviews in Relativity, 17, 3

Pyrzas, S., Gänsicke, B. T., Brady, S., et al. 2012, *Post-common envelope binaries from SDSS - XV. Accurate stellar parameters for a cool 0.4 $M_\odot$ white dwarf and a 0.16 $M_\odot$ M dwarf in a 3 h eclipsing binary*, MNRAS, 419, 817

Raghavan, D., McAlister, H. A., Henry, T. J., et al. 2010, *A Survey of Stellar Families: Multiplicity of Solar-type Stars*, ApJs, 190, 1

Ramsay, G., Barclay, T., Steeghs, D., et al. 2012, *The long-term optical behaviour of helium-accreting AM CVn binaries*, MNRAS, 419, 2836

Ramspeck, M., Heber, U., & Edelmann, H. 2001, *Early type stars at high galactic latitudes. II. Four evolved B-type stars of unusual chemical composition*, A&A, 379, 235

Rau, A., Roelofs, G. H. A., Groot, P. J., et al. 2010, *A Census of AM CVn Stars: Three New Candidates and One Confirmed 48.3-Minute Binary*, ApJ, 708, 456

Reed, M. D. & Stiening, R. 2004, *A Search for Main-Sequence Companions to Subdwarf B Stars Using the Two Micron All Sky Survey*, PASP, 116, 506

Rixon, G., Fraser, M., Koposov, S., et al. 2014, *Gaia Alerts classified at the William Herschel Telescope*, The Astronomer's Telegram, 6593, 1

Roelofs, G. H. A., Groot, P. J., Benedict, G. F., et al. 2007a, *Hubble Space Telescope Parallaxes of AM CVn Stars and Astrophysical Consequences*, ApJ, 666, 1174

Roelofs, G. H. A., Groot, P. J., Marsh, T. R., et al. 2005, *SDSS J124058.03-015919.2: a new AM CVn star with a 37-min orbital period*, MNRAS, 361, 487

Roelofs, G. H. A., Groot, P. J., Marsh, T. R., Steeghs, D., & Nelemans, G. 2006a, *Phase-resolved spectroscopy of the helium dwarf nova 'SN 2003aw' in quiescence*, MNRAS, 365, 1109

Roelofs, G. H. A., Groot, P. J., Nelemans, G., Marsh, T. R., & Steeghs, D. 2006b, *Kinematics of the ultracompact helium accretor AM Canum Venaticorum*, MNRAS, 371, 1231

Roelofs, G. H. A., Groot, P. J., Nelemans, G., Marsh, T. R., & Steeghs, D. 2007b, *On the orbital periods of the AM CVn stars HP Librae and V803 Centauri*, MNRAS, 379, 176

Roelofs, G. H. A., Groot, P. J., Steeghs, D., Marsh, T. R., & Nelemans, G. 2007c, *The long-period AM CVn star SDSS J155252.48+320150.9*, MNRAS, 382, 1643

Roelofs, G. H. A., Groot, P. J., Steeghs, D., et al. 2009, *SDSSJ080449.49+161624.8: a peculiar AM CVn star from a colour-selected sample of candidates*, MNRAS, 394, 367

Roelofs, G. H. A., Nelemans, G., & Groot, P. J. 2007d, *The population of AM CVn stars from the Sloan Digital Sky Survey*, MNRAS, 382, 685

Roelofs, G. H. A., Rau, A., Marsh, T. R., et al. 2010, *Spectroscopic Evidence for a 5.4 Minute Orbital Period in HM Cancri*, ApJL, 711, L138

Ruiz, M. T., Rojo, P. M., Garay, G., & Maza, J. 2001, *CE 315: A New Interacting Double-Degenerate Binary Star*, ApJ, 552, 679

Saffer, R. A., Bergeron, P., Koester, D., & Liebert, J. 1994, *Atmospheric parameters of field subdwarf B stars*, ApJ, 432, 351

Savonije, G. J., de Kool, M., & van den Heuvel, E. P. J. 1986, *The minimum orbital period for ultra-compact binaries with helium burning secondaries*, A&A, 155, 51

Scaringi, S. 2014, *A physical model for the flickering variability in cataclysmic variables*, MNRAS, 438, 1233

Schaffenroth, V., Geier, S., Barbu-Barna, I., et al. 2014a, *New HW Virginis Systems from the MUCHFUSS Project*, in Astronomical Society of the Pacific Conference Series, Vol. 481, Astronomical Society of the Pacific Conference Series, ed. V. van Grootel, E. Green, G. Fontaine, & S. Charpinet, 253

Schaffenroth, V., Geier, S., Drechsel, H., et al. 2013, *A new bright eclipsing hot subdwarf binary from the ASAS and SuperWASP surveys*, A&A, 553, A18

Schaffenroth, V., Geier, S., Heber, U., et al. 2014b, *Binaries discovered by the MUCHFUSS project. SDSS J162256.66+473051.1: An eclipsing subdwarf B binary with a brown dwarf companion*, A&A, 564, A98

Schlafly, E. F. & Finkbeiner, D. P. 2011, *Measuring Reddening with Sloan Digital Sky Survey Stellar Spectra and Recalibrating SFD*, ApJ, 737, 103

Shears, J., Brady, S., Koff, R., Goff, W., & Boyd, D. 2011, *Superhumps and post-outburst rebrightening episodes in the AM CVn star SDSS J012940.05+384210.4*, ArXiv e-prints

Silvotti, R., Østensen, R. H., Bloemen, S., et al. 2012, *Orbital properties of an unusually low-mass sdB star in a close binary system with a white dwarf*, MNRAS, 424, 1752

Simpson, J. C. & Wood, M. A. 1998, *Time Series Energy Production in Smoothed Particle Hydrodynamics Accretion Disks: Superhumps in the AM Canum Venaticorum Stars*, ApJ, 506, 360

Skidmore, W., Mason, E., Howell, S. B., et al. 2000, *Investigating the structure of the accretion disc in WZ Sge from multiwaveband time-resolved spectroscopic observations - I*, MNRAS, 318, 429

Skillman, D. R., Patterson, J., Kemp, J., et al. 1999, *Superhumps in Cataclysmic Binaries. XVII. AM Canum Venaticorum*, PASP, 111, 1281

Smak, J. 1967, *Light variability of HZ 29*, Acta Astronomica, 17, 255

Solheim, J. E. 2010, *AM CVn Stars: Status and Challenges*, Publications of the Astronomical Society of the Pacific, 122, 1133

Stark, M. A. & Wade, R. A. 2003, *Single and Composite Hot Subdwarf Stars in the Light of 2MASS Photometry*, AJ, 126, 1455

Steeghs, D. 2003, *Doppler Tomography of Accreting Binaries*, in IAU Joint Discussion, Vol. 9, IAU Joint Discussion

Steeghs, D., Marsh, T. R., Barros, S. C. C., et al. 2006, *GEMINI Spectroscopy of the Ultra-compact Binary Candidate V407 Vulpeculae*, ApJ, 649, 382

Still, M. & Barclay, T. 2012, *PyKE: Reduction and analysis of Kepler Simple Aperture Photometry data*, Astrophysics Source Code Library

Stobie, R. S., Kilkenny, D., O'Donoghue, D., et al. 1997, *The Edinburgh-Cape Blue Object Survey - I. Description of the survey*, MNRAS, 287, 848

Stroeer, A., Heber, U., Lisker, T., et al. 2007, *Hot subdwarfs from the ESO supernova Ia progenitor survey. II. Atmospheric parameters of subdwarf O stars*, A&A, 462, 269

Strohmayer, T. E. 2004, *Detection of Nitrogen and Neon in the X-Ray Spectrum of GP Comae Berenices with XMM/Newton*, ApJL, 608, L53

Telting, J. H., Baran, A. S., Nemeth, P., et al. 2014, *KIC 7668647: a 14 day beaming sdB+WD binary with a pulsating subdwarf*, A&A, 570, A129

Telting, J. H., Østensen, R. H., Baran, A. S., et al. 2012, *Three ways to solve the orbit of KIC 11 558 725: a 10-day beaming sdB+WD binary with a pulsating subdwarf*, A&A, 544, A1

Thorstensen, J. R., Fenton, W. H., Patterson, J. O., et al. 2002, *1RXS J232953.9+062814: A Dwarf Nova with a 64 Minute Orbital Period and a Conspicuous Secondary Star*, ApJ, 567, L49

Tillich, A., Heber, U., Geier, S., et al. 2011, *The Hyper-MUCHFUSS project: probing the Galactic halo with sdB stars*, A&A, 527, A137

Tsugawa, M. & Osaki, Y. 1997, *Disk Instability Model for the AM Canum Venaticorum Stars*, PASJ, 49, 75

Tutukov, A. & Yungelson, L. 1996, *Double-degenerate semidetached binaries with helium secondaries: cataclysmic variables, supersoft X-ray sources, supernovae and accretion-induced collapses*, MNRAS, 280, 1035

Tutukov, A. V. & Fedorova, A. V. 1989, *Formation and Evolution of Close Binary Stars Containing Helium Donors*, Soviet Astronomy, 33, 606

Tutukov, A. V., Fedorova, A. V., Ergma, E. V., & Yungelson, L. R. 1985, *Evolution of Low-Mass Close Binaries - the Minimum Orbital Period*, Soviet Astronomy Letters, 11, 52

Tutukov, A. V. & Yungelson, L. R. 1979, *On the influence of emission of gravitational waves on the evolution of low-mass close binary stars*, Acta Astronomica, 29, 665

Tutukov, A. V. & Yungelson, L. R. 1981, *Evolutionary Scenario for Close Binary Systems of Low and Moderate Masses*, Nauchnye Informatsii, 49, 3

Udalski, A., Szymanski, M., Kubiak, M., et al. 2002, *The Optical Gravitational Lensing Experiment. BVI Maps of Dense Stellar Regions. III. The Galactic Bulge*, Acta Astronomica, 52, 217

van der Klis, M. 2005, *The QPO phenomenon*, Astronomische Nachrichten, 326, 798

van Teeseling, A. & Verbunt, F. 1994, *ROSAT X-ray observations of ten cataclysmic variables*, A&A, 292, 519

Vennes, S., Kawka, A., O'Toole, S. J., Németh, P., & Burton, D. 2012, *The Shortest Period sdB Plus White Dwarf Binary CD-30 11223 (GALEX J1411-3053)*, ApJL, 759, L25

Verbeek, K., Groot, P. J., Scaringi, S., et al. 2012, *Spectroscopic follow-up of ultraviolet-excess objects selected from the UVEX survey*, MNRAS, 426, 1235

Verbunt, F. & Rappaport, S. 1988, *Mass transfer instabilities due to angular momentum flows in close binaries*, ApJ, 332, 193

Vernet, J., Dekker, H., D'Odorico, S., et al. 2011, *X-shooter, the new wide band intermediate resolution spectrograph at the ESO Very Large Telescope*, A&A, 536, A105

Vos, J., Østensen, R. H., Degroote, P., et al. 2012, *The orbits of subdwarf B + main-sequence binaries. I. The sdB+G0 system PG 1104+243*, A&A, 548, A6

Vos, J., Østensen, R. H., Németh, P., et al. 2013, *The orbits of subdwarf-B + main-sequence binaries. II. Three eccentric systems; BD+29°3070, BD+34°1543 and Feige 87*, A&A, 559, A54

Vučković, M., Aerts, C., Östensen, R., et al. 2007, *The binary properties of the pulsating subdwarf B eclipsing binary PG 1336-018 (NY Virginis)*, A&A, 471, 605

Wang, B., Justham, S., & Han, Z. 2013, *Producing Type Iax supernovae from a specific class of helium-ignited WD explosions*, A&A, 559, A94

Webbink, R. F. 1984, *Double white dwarfs as progenitors of R Coronae Borealis stars and Type I supernovae*, ApJ, 277, 355

Wesemael, F., Fontaine, G., Bergeron, P., Lamontagne, R., & Green, R. F. 1992, *Studies of hot B subdwarfs. VIII - Stromgren photometry of hot, hydrogen-rich subdwarf candidates in the Palomar-Green and Kitt Peak-Downes surveys*, AJ, 104, 203

Wisotzki, L., Koehler, T., Groote, D., & Reimers, D. 1996, *The Hamburg/ESO survey for bright QSOs. I. Survey design and candidate selection procedure.*, A&AS, 115, 227

Wood, J. H. & Saffer, R. 1999, *Spectroscopy of the post-common envelope binary HW Virginis*, MNRAS, 305, 820

Wood, M. A., Casey, M. J., Garnavich, P. M., & Haag, B. 2002, *Superhumps in the helium dwarf nova KL Draconis*, MNRAS, 334, 87

Woudt, P. A. & Warner, B. 2003, *The new AM CVn star in Hydra*, MNRAS, 345, 1266

Woudt, P. A., Warner, B., & Motsoaledi, M. 2013, *CSS121123:045020-093113: A WZ Sge-type dwarf nova amongst the AM CVn systems*, The Astronomer's Telegram, 4726, 1

Woudt, P. A., Warner, B., & Rykoff, E. 2005, *2QZ J142701.6-012310*, IAU Circ., 8531, 3

Yoon, S.-C. & Langer, N. 2004, *Helium accreting CO white dwarfs with rotation: Helium novae instead of double detonation*, A&A, 419, 645

York, D. G. et al. 2000, *The Sloan Digital Sky Survey: Technical Summary*, AJ, 120, 1579

Yungelson, L. R. 2008, *Evolution of low-mass helium stars in semidetached binaries*, Astronomy Letters, 34, 620

Yungelson, L. R., Nelemans, G., & van den Heuvel, E. P. J. 2002, *On the formation of neon-enriched donor stars in ultracompact X-ray binaries*, A&A, 388, 546

Yungelson, L. R. & Tutukov, A. V. 2005, *A Model for the Population of Helium Stars in the Galaxy: Low-Mass Stars*, Astronomy Reports, 49, 871

Zorotovic, M., Schreiber, M. R., & Gänsicke, B. T. 2011, *Post common envelope binaries from SDSS. XI. The white dwarf mass distributions of CVs and pre-CVs*, A&A, 536, A42

SUMMARY & CONCLUSIONS

The majority of stars are born in binary stars. If the initial period of the system is short enough ($P_{\mathrm{orb}} \lesssim 30\,\mathrm{yr}$) both components can come into contact and the systems possibly end up as (ultra-)compact binaries with orbital periods of a few minutes up to several hours, consisting of at least one degenerate object. Although many different large scale surveys increased the number of known (ultra-)compact binaries significantly of the last years, many open questions remain. What happens during the common envelope phase? Which evolutionary paths are preferred for different mass ratios? What fraction of systems merge and what kind of object is formed during the merger? How many systems prevent the merger? What is the effect of angular momentum transfer in the system? How do the different individual populations of (ultra-)compact binaries fit in the whole family of (ultra-)compact binaries? A detailed observational study of the different populations as well as a precise parameter study of individual systems is crucial to address these questions.

Population of compact hot subdwarf binaries

Compact hot subdwarf binaries (sdBs) are binaries with periods between one hour and a few days consisting of a core helium burning hot subdwarf star and a low mass main sequence (dM) or white dwarf companion. In chapter 2 we present orbital and atmospheric parameters and put constraints on the nature of the companions of 12 close hot subdwarf star binaries, leading to the 142 known systems of hot subdwarf binaries with orbital periods less than 30 days and measured mass functions. For the first time, a detailed population study of the known population of compact hot subdwarf binaries was carried out.

We present an analysis of the companion mass distribution and show that it is bimodal. One peak around $0.1\,\mathrm{M}_\odot$ corresponds to the low-mass main-sequence (dM) and substellar companions. The other peak around $0.4\,\mathrm{M}_\odot$ corresponds to the white dwarf companions. The derived masses for the white dwarf companions are significantly lower than the average mass for single carbon-oxygen white dwarfs. In a $T_{\mathrm{eff}} - \log g$ diagram of sdB+dM companions we find signs that the sdB components are more massive compared to the rest of the sample.

The formation of low mass helium white dwarf (WD) binaries with masses $< 0.45\,\mathrm{M}_\odot$ and WD companions is expected to occur in a similar way as the formation of sdB+WD binaries with the difference that the low mass helium white dwarf looses so much mass during the common envelope phase that it is not massive enough to ignite helium in the core. Compact WD+dM binaries are also the product of common envelope evolution and so we might expect

173

that the properties of these binaries are similar to the sdB+dM binaries. Indeed, some WD+dM systems may have been created as hot subdwarf stars with dM companions where the sdB primaries since evolved to become white dwarfs with masses close to $0.47\,\mathrm{M_\odot}$. Both samples show a significantly different companion mass distribution indicating either different selection effects or different evolutionary paths.

Sixteen systems were identified where the dM companion will fill its Roche lobe within a Hubble time due to the orbital shrinkage and which will eventually evolve into a cataclysmic variable; two of them will have a brown dwarf as donor star. Twelve systems with confirmed WD companions will merge within a Hubble time where the majority (8 systems) have a mass ratio such that they most likely will merge and form RCrB stars or massive C/O white dwarfs. KPD1930+2752 and CD-30°11223 have massive WD companion with masses $>\ 0.7\,\mathrm{M_\odot}$ and are therefore potential supernova Ia progenitors. The remaining two systems have a very low mass ratio and most likely prevent the merger and evolve into a stable AM CVn type binary.

The properties of ultracompact AM CVn type binaries

AM CVn systems are semi-detached ultracompact binaries. These systems show orbital periods between 5.4 - 65 min and consist of a degenerate primary and (semi-)degenerate secondary.

Chapter 3 presents a full analysis of phase resolved spectroscopy of four recently discovered AM CVn type binaries. We measured the orbital periods of all four systems and identified distinctive features in the grand average spectra as well as the phase folded spectra. SDSS J1208 shows two bright spots with a phase offset of $125° \pm 23°$ a feature that has already been observed in SDSS J1240 and shows up in GP Com and V396 Hya (chapter 4).

We discovered that three of the systems have orbital periods between 50 and 60 min. Only those show strong absorption lines of Mg I and sometimes Si I/II. No AM CVn system at other orbital periods show these lines. There is no evidence of these lines in the 65 min period system V396 Hya. The 46 min period system GP Com shows only nitrogen in absorption (chapter 4). We measured no significant radial velocity variations for these lines, likely indicating that these lines originate on or very close to the accreting white dwarf. Metal absorption lines are well known from single white dwarf spectra but, for the temperature range where Mg I is visible, also the Ca II H & K lines should be present. There is no evidence for calcium in either of the systems and we discuss three different scenarios to explain this abundance anomaly.

As Doppler tomography remaps line intensities from the wavelength-time domain to the velocity frame, the technique can also be used to derive line intensities of specific regions in the binary system. We extracted the flux ratios for several helium lines for the disc and bright spot region and compared them with single-slab LTE models with variable electron densities and path lengths to estimate the disc and bright spot temperature structure in the disc. This technique was used for the first time to limit the characteristics of the accretion disc and bright spot regions under the assumption of an LTE slab model in AM CVn type binaries. Of course, the single-slab LTE models with uniform density and temperature are a simplification of the real environment in an accretion disc. Nevertheless, we found good agreement between data and the model in three out of four studied systems for the disc region. All three systems show

similar disc temperatures of $\sim 10\,500$ K whereas no agreement between the models and the observations was found for the bright spot region.

Kepler satellite photometry and phase-resolved spectroscopy of the ultracompact AMCVn type binary SDSS J1908 is presented in chapter 4. SDSS J1908 is an AM CVn system of particular interest because it is in the Kepler field and was observed with Kepler over almost 3 years continuously which results in an unprecedented data set for any ultracompact binary. Keck, GranTeCan and the William Herschel telescope were used for follow-up phase-resolved spectroscopic observations of SDSS J1908 to better understand the properties of this system. The phase-folded spectra and the Doppler tomograms reveal an S-wave in emission in the core of the He I 4471 Å absorption line. The Si I,II, Mg II and the core of some He I lines show an S-wave in absorption with a phase offset of $170 \pm 15°$ compared to the S-wave in emission. We measured the orbital period to be $P_{\rm orb} = 1085.108(9)$ min, confirming the AM CVn type nature of the system. We find that SDSS J1908 is the first high state system, which shows a large number of metal lines, including silicon, sulphur and magnesium as well as many lines of nitrogen. Such lines help to constrain the evolutionary background of SDSS J1908. The detection of nitrogen and the absence of carbon and oxygen indicates CNO processed material which favours a helium white dwarf donor in SDSS J1908.

Additionally, in a Fourier transform of the three years of consecutive *Kepler* observations we find 42 different periods in the system well above the noise. Most of the periods show large amplitude and frequency variations. Additionally a large number of peaks were detected in the Fourier transform which are only visible for a few weeks/months. Using O-C diagrams, we showed that some periods show that some of the strongest variations show a variability of $|\dot{P}| \sim 1.0 \times 10^{-8}\,{\rm s\,s^{-1}}$ likely to occur in the superhump phenomenon. We also set a limit on the orbital period derivative of $|\dot{P}| < 10^{-10}{\rm s\,s^{-1}}$. The shape of the phase folded lightcurve on the orbital period indicates the motion of the bright spot moving in and out of the line of sight. However, in a comparison between the observed phases of the emission/absorption lines and the variation in the lightcurve we are not able to match the emission or absorption components to any obvious feature in the binary system such as the bright spot, the accretor or the donor star. Therefore the location of the spectroscopic variability remains undetermined.

High-resolution phase-resolved spectroscopy allows a measurement of the velocity in the observed systems accurately. Chapter 5 presents high- and medium-resolution UVES and X-Shooter phase-resolved spectroscopy of the well known AM CVn type binaries GP Com and V396 Hya. The spectra obtained with X-Shooter cover the full optical/near-infrared range from 0.3 - 2.5 μm. All the helium lines in the optical regime show, on top of the disc emission, a strong central spike feature. Interestingly, none of the helium lines in the near-infrared of GP Com and V396 Hya shows this sharp central spike feature which is a rather surprising result. A large number of weak nitrogen and neon emission lines were detected in both systems as well as nitrogen in absorption in GP Com. The overabundance of nitrogen can be explained with CNO burning whereas neon is only produced during helium burning. We find two possible solutions. One explanation is that some helium burning occurred in the donor which increased the neon abundance but stopped early enough to not deplete the nitrogen abundance. Another explanation would be that little helium burning occurred in the donor and due to diffu-

sion processes the neon abundance in the core of the donor was enhanced and what we see now is accretion of the core where only very little helium was burned but which was additionally enriched with neon due to diffusion.

The high-resolution spectroscopy allowed us to measure the radial velocity variations of the central spike features and the metal lines accurately. We show that the neon and nitrogen lines follow the motion of the central spike and are therefore also linked to the accreting white dwarf. Doppler tomograms reveal a second bright spot in both systems. From the phases and amplitudes of the central spikes and the primary bright spot as well as the peak-to-peak separation of the double peaked helium disc emission lines we limit the inclination angles and the component masses assuming that the velocity of the bright spot is either purely ballistic stream velocity or purely Keplerian disc velocity. For GP Com, we find an accretor with a mass of $M_{1,\mathrm{GP\,Com}} > 0.55\,\mathrm{M}_\odot$ seen under an inclination angle of $45° < i < 74°$ for purely ballistic stream velocity. For purely Keplerian disc velocity the accretor has a mass of $M_{1,\mathrm{GP\,Com}} > 0.33\,\mathrm{M}_\odot$ and the system is seen under an inclination angle of $33° < i < 74°$. The donor in V396 Hya is expected to be a zero temperature donor star. We find a possible mass for the accretor of $0.37 < M_{1,\mathrm{V396\,Hya}}/M_\odot < 0.49$ and the system is seen under an inclination angle of $51° < i < 78°$ for purely ballistic stream velocity. For purely Keplerian disc velocity the accretor has a mass of $0.32 < M_{1,\mathrm{V396\,Hya}}/M_\odot < 0.45$ and the system is seen under an inclination angle of $47° < i < 78°$.

The spectra show forbidden helium lines as well as a large variability of the mean velocities of the central spike features. Stark broadened models predict both of these features. For the first time the central spikes were compared to computed Stark profiles and we find good agreement between the Stark broadened models and the observed profiles for an electron density around $n_e \simeq 5 \times 10^{15}\,\mathrm{cm}^{-3}$.

The high-resolution spectra resolve the weak and narrow neon and nitrogen lines. Therefore, these lines are well suited to estimate the rotational velocity of the accreting white dwarf. The emission lines were compared to synthetic line profiles which only include thermal and rotational broadening. We show that the lines do not allow fast projected rotational velocities; $v_{\mathrm{rot}} < 46\,\mathrm{km\,s}^{-1}$ for GP Com and $v_{\mathrm{rot}} < 34\,\mathrm{km\,s}^{-1}$ and conclude that the accretor is most likely in agreement to being tidally locked to the orbit.

As part of the Dutch GTO program, X-shooter was used to observe seven AM CVn type binaries. These systems cover almost the entire range of the known population of AM CVn type systems with a period range of 18 min up to 44 min. The results of the analysis of this homogeneous sample is presented in chapter 6.

For the first time weak nitrogen absorption lines were detected in HP Lib and the spectra of V406 Hya and SDSS J124058.03–015919.2 display strong nitrogen and magnesium emission lines in the far-red. SDSS J080449.49+161624.8 shows more than 40 different transitions of neutral and ionized helium. In particular, the He II lines appear to be exceptional strong. The overall spectrum looks like a hydrogen deficient copy of a magnetic CV and we speculate that the exceptional spectrum of SDSS J080449.49+161624.8 can be explained if the system is magnetic. All systems of our sample show the He I 10 830Å line in emission, which was expected for the low state systems. However, for the high state system, HP Lib, this a rather

surprising result.

In chapter 3 flux ratios of the optical helium lines were used to estimate the temperatures of the disc and the bright spot of four AM CVn systems. The obtained flux ratios were compared to a single slab LTE model with uniform temperature and density and we found good agreement between data and the model in three out of four systems for the disc region. In chapter 6, we extend this analysis for SDSS J1642 by including the near-infrared He I 10 830 Å line and show that the usage of the near-infrared lines require a more involved disc modelling than single-slab LTE models.

We measured the separation of the double-peaked helium emission profile for those systems where this feature is present. Because the peak separation is an indicator of the (Keplerian) disc velocity of gas in the outer ranges of the accretion disc we are able to put limits on the primary mass and the inclination angle. A lower limit of the accretor mass of $M_{1,\text{V406 Hya}} > 0.183\,M_\odot$, $M_{1,\text{SDSS J1240}} > 0.030\,M_\odot$ and $M_{1,\text{SDSS J1642}} > 0.025\,M_\odot$ for V406 Hya, SDSS J1240 and SDSS J1642 respectively was found. In particular the accretor mass limit of the latter two systems is not very strict, which is a result of the small peak-to-peak separations. For the inclination angle, we find $i_{\text{V406 Hya}} > 28°$, $i_{\text{SDSS J1240}} > 15°$ and $i_{\text{SDSS J1642}} > 14°$ for V406 Hya, SDSS J1240 and SDSS J1642 respectively.

Additionally, we present an overview of detected elements in a large number of AM CVn type systems. A remarkable result is, that almost all systems show nitrogen lines, whereas none of the systems show carbon and only GP Com shows weak oxygen. As already described earlier, nitrogen is enhanced during hydrogen burning through the CNO cycle. If in the following evolution helium ignites, carbon is produced through the triple-alpha process and oxygen is enhanced by alpha captures of nitrogen which decreases the nitrogen abundance. Therefore, a pure helium white dwarf where no helium burning occurred is expected to show a large overabundance of nitrogen, whereas a semi-degenerate helium white dwarf will show increased carbon and oxygen and decreased nitrogen abundances. Although we cannot constrain the donor type of the studied systems without an accurate abundance measurement, the absence of carbon and oxygen indicates that none of the systems has a highly evolved helium star donor.

Nederlandse Samenvatting

De meerderheid van de sterren wordt geboren in dubbelster systemen. Als de initiële baanperiode van het systeem kort genoeg is, dan kunnen beide componenten in contact komen en kan het systeem eindigen als een (ultra-)compacte dubbelster met een baanperiode van enkele minuten tot een paar uur, met tenminste één gedegenereerd object, de uitgebrande kern van een ster. Ondanks het feit dat verschillende grote 'surveys' de laatste jaren het aantal bekende (ultra-)compacte dubbelster systemen beduidend heeft toe doen nemen, zijn er nog veel open vragen. Wat gebeurt er tijdens een 'common-envelope' fase? Hoe hangt de massaverhouding samen met evolutionaire geschiedenis van het systeem? Welke fractie van systemen versmelten en wat voor object ontstaat er tijdens een samensmelting? Hoeveel systemen voorkomen een samensmelting? Wat is het effect van overdracht van draaiimpuls? Hoe passen de individuele (ultra-)compacte dubbelsterren in de populatie van (ultra-)compacte dubbelsterren? Een gedetailleerd onderzoek naar de verschillende populaties, zowel als onderzoek naar de precieze parameters van individuele systemen zijn cruciaal om al deze vragen te beantwoorden.

Populatie van compacte, hete subdwerg dubbelsterren

Compacte, hete subdwerg dubbelsterren (sdBs) zijn dubbelsterren met baanperiodes van 1 uur tot een paar dagen waarin de zwaardere van de twee sterren een ster is die helium in de kern verbrand. De tweede ster in het systeem is of een witte dwerg of een lage massa hoofdreeksster. In hoofdstuk 2 presenteren we de baanperiodes en atmosferische parameters en stellen limieten aan de aard van de begeleiders van 12 nauwe hete subdwerg dubbelsterren. Dit brengt het totaal op 142 bekende systemen van hete subdwerg dubbelsterren met een baanperiode minder dan 30 dagen en een bekende massafunctie. De massafunctie is een combinatie van waarneembare parameters die een onderlimiet geeft aan de massa van de (ongeziene) begeleider in het systeem.

We laten zien dat de massadistributie van de begeleiders bimodaal is. Een piek rond de $0.1\,M_\odot$ komt overeen met lage massa hoofdreeks sterren (dM) en bruine dwergen. De andere piek rond $0.4\,M_\odot$ komt overeen met witte dwergen als begeleider. De gemeten massa's voor de witte dwergen zijn beduidend lager dan de gemiddelde massa van een koolstof-zuurstof witte dwerg. In een temperatuur-oppervlakte zwaartekracht diagram van sdB+dM sterren zien we tekenen dat de sdB componenten zwaarder zijn dan de rest van de sdB sterren.

De vorming van lage massa helium witte dwerg (WD) dubbelsterren met massa's $< 0.45\,M_\odot$

en een witte dwerg begeleider is vergelijkbaar met de vorming van sdB+WD dubbelsterren, met het verschil dat de lage massa helium witte dwerg te veel massa verliest tijdens de 'common envelope' fase zodat deze niet zwaar genoeg is om heliumfusie in de kern op te starten. Compacte WD+dM dubbelsterren zijn ook het product van een 'common envelope' evolutie en dus is het te verwachten dat de eigenschappen van deze dubbelsterren vergelijkbaar zijn met de sdB+dM dubbelsterren. Dit lijkt het geval te zijn. Sommige WD+dM systemen zouden gemaakt kunnen zijn als hete subdwerg ster met een dM begeleider waarbij de subdwerg ster vervolgens evolueert tot een witte dwerg met een massa rond de $0.47\,M_\odot$. Beide groepen hebben een beduidend verschillende begeleider-massa verdeling wat aangeeft dat de ene groep makkelijker te vinden is dan de andere of dat de evolutie verschillend voor beide groepen.

We hebben zestien systemen gevonden waarbij de dM begeleider zijn Rochevolume vult binnen de Hubbletijd doordat de baanperiode afneemt. Deze systemen zullen dus evolueren naar een cataclysmische variabele, waarbij twee van deze systemen een bruine dwerg begeleider hebben. Twaalf systemen met witte dwerg begeleiders zullen binnen de Hubbletijd samensmelten waarbij de meerderheid (acht systemen) een massaverhouding heeft zodat ze waarschijnlijk een RCrB ster vormen of een zware C/O witte dwerg. KPD1930+2752 en CD-30°11223 hebben een zware WD begeleider met een massa van $> 0.7\,M_\odot$ en zijn dus mogelijk voorlopers van een type Ia supernova. De overgebleven twee systemen hebben een zeer lage massaverhouding en zullen waarschijnlijk niet samensmelten maar een stabiele AM CVn type dubbelster vormen.

De eigenschappen van ultracompacte AM CVn type dubbelsterren

AM CVn systemen zijn ultracompacte dubbelsterren waarbij een van de twee sterren zijn Rochevolume vult. Deze systemen hebben baanperiodes tussen de 5.4 tot 65 minuten en bestaan uit een gedegenereerde ster en een (semi-)gedegenereerde begeleider.

In hoofdstuk 3 beschrijven we de analyse van fase opgeloste spectroscopie van vier recent ontdekte AM CVn dubbelsterren. We meten de baanperiode van alle vier de systemen en identificeren karakteristieke eigenschappen in zowel de gemiddelde van de spectra als de opfase-gevouwen-spectra. SDSS J1208 heeft twee 'bright spots' afkomstig van de accretieschijf met een baan fase verschil van $125° \pm 23°$, een eigenschap die ook al waargenomen was in SDSS J1240, GP Com and V396 Hya (hoofdstuk 4).

We hebben 3 systemen ontdekt met een baanperiode tussen de 50 en 60 minuten. Alleen deze systemen vertonen sterke absorptie lijnen van Mg I en soms Si I/II. Geen AM CVn systeem met een andere baanperiode vertoont deze lijnen. Deze lijnen zijn ook niet te zien in het 65 min periode systeem V396 Hya. Het systeem met een baanperiode van 46 minuten, GP Com, vertoont alleen stikstoflijnen in absorptie (hoofdstuk 4). We meten geen significante radiale snelheidsvariaties in deze lijnen, wat waarschijnlijk betekent dat ze door de witte dwerg of door de accretieschijf dichtbij de witte dwerg worden uitgezonden. Metaal-absorptielijnen

zijn bekend in witte dwerg spectra maar voor het temperatuurbereik waarover Mg I zichtbaar is, zouden ook de Ca II H & K lijnen zichtbaar moeten zijn. In geen enkele van deze systemen zijn de calciumlijnen te zien en we bespreken drie mogelijke scenario's die dit kunnen verklaren.

Doppler tomografie transformeert de spectra van een golflengte-tijd weergave naar een snelheidsweergave. De techniek kan daarom gebruikt worden om de lijnintensiteiten te meten van specifieke plaatsen in het dubbelstersysteem. We meten de intensiteitsverhoudingen van de verschillende heliumlijnen van de schijf en de 'bright spot' en vergelijken dit met enkele-schijf-LTE modellen met variabele elektronendichtheden en padlengtes om temperatuur van de schijf en 'bright spot' af te schatten. Dit is de eerste keer dat deze techniek gebruikt wordt om de schijf- en 'bright spot' eigenschappen te meten in AM CVn systemen onder aanname van lokaal thermisch evenwicht (LTE). Deze modellen zijn natuurlijk een simplificatie van de werkelijkheid. Desondanks vinden we een goede overeenkomst tussen de metingen en de modellen in drie van de vier bestudeerde systemen. De schijftemperaturen van deze drie systemen vertonen een vergelijkbare temperatuur van $\sim$10 500 K, maar er is geen goede overeenkomst tussen de metingen en modellen van de 'bright spot'.

Fotometrische data van de *Kepler* satelliet en fase opgeloste spectroscopie van het ultra-compacte AMCVn systeem SDSS J1908 wordt besproken in hoofdstuk 4. SDSS J1908 is een AM CVn systeem dat bijzonder is omdat het in het Kepler-veld staat en dus bijna 3 jaar lang ononderbroken waargenomen is door de satelliet, wat een dataset oplevert die niet te vergelijken is. Keck, GranTeCan en William Herschel telescopen zijn gebruikt om fase-opgeloste spectroscopische waarnemingen te doen van SDSS J1908 om de eigenschappen van het systeem beter te kunnen begrijpen. De op-fase-gevouwen spectra en de Doppler tomografie diagrammen tonen een duidelijke S-golf in emissie in de kern van de He I 4471 Å absorptie lijn. De Si I,II, Mg II en de kern van sommige He I lijnen laten ook een S-golf in absorptie zien met een fase-verschil van $170 \pm 15°$ vergeleken met de S-golf in emissie. De baanperiode van het systeem is $P_{\mathrm{orb}} = 1085.108(9)$ min, wat bevestigt dat het een AM CVn systeem is. We stellen vast dat SDSS J1908 het eerste 'high state' systeem dat een groot aantal metaallijnen vertoond, onder ander silicium, sulfaat en magnesium en ook veel stikstoflijnen. Deze lijnen zeggen iets over welke evolutie het systeem wel (en niet) heeft doorlopen. De aanwezigheid van stikstof en het afwezig zijn van zuurstof en stikstof duid op dat de CNO cyclus heeft plaats gevonden, waardoor het waarschijnlijk is dat de begeleider in het systeem SDSS J1908 een helium witte dwerg is.

In een Fourieranalyse van de 3 jaar aan *Kepler* data vinden we 42 verschillende periodes duidelijk boven het ruisniveau. De meeste van de periodes hebben grote variaties in amplitude en frequentie ondergaan. Ook is er een groot aantal pieken in het Fourier spectrum dat er maar een paar weken tot maanden zichtbaar zijn. Door de gemeten en verwachte baanfasen tegen elkaar uit te zetten in een diagram (een 'O-C diagram'), zien we dat sterkste variatie $|\dot{P}| \sim 1.0 \, \mathrm{x} \, 10^{-8} \, \mathrm{s \, s^{-1}}$ waarschijnlijk veroorzaakt wordt door 'superhumps'. We hebben ook een limiet gesteld aan de afname van de baanperiode $|\dot{P}| < 10^{-10} \mathrm{s \, s^{-1}}$. De vorm van de op fase van de baanperiode gevouwen lichtcurve duidt er op dat de 'bright spot' in en uit het gezichtsveld van de waarnemer beweegt. We vergelijken vervolgens de lichtcurve variabiliteit

en de variabiliteit in de emissie- en absorptie lijnen, maar het is niet mogelijk om de lijnen te koppelen aan een van de componenten van de dubbelster. De oorzaak van de variabiliteit in de emissie en absorptie lijnen is dus niet bekend.

Met hoge-resolutie, fase opgeloste spectroscopie is het mogelijk om de snelheid van het systeem nauwkeurig te meten. In hoofdstuk 5 tonen we fase opgeloste, hoge en gemiddelde resolutie spectra van de meest bekende AM CVn-type dubbelsterren GP Com and V396 Hya, opgenomen met de UVES en X-Shooter spectrografen. De spectra verkregen met X-Shooter beslaan het volledige optische en nabij-infrarode deel van het spectrum, met een golflengte bereik van 0.3 - 2.5 μm. Alle heliumlijnen in het optische deel van het spectrum vertonen, samen met emissie van de schijf, sterke, gecentreerde emissie pieken. Interessant is dat geen van de heliumlijnen in het nabij-infrarood van GP Com en V396 Hya een centrale piek vertonen, een verrassend resultaat. Een groot aantal zwakke stikstof- en neon emissielijnen zijn ook zichtbaar in beide systemen, evenals stikstof in absorptie in GP Com. De grote hoeveelheid aan stikstof kan verklaard worden door de CNO cyclus fusie, terwijl neon alleen geproduceerd wordt tijdens helium fusie. Er zijn twee oplossingen voor dit probleem. Eén verklaring is dat er een beetje helium fusie heeft plaatsgevonden in de donor waardoor de hoeveelheid neon toeneemt, maar dat deze fusie snel genoeg stopte om niet alle stikstof te vernietigen. Een andere verklaring is dat er geen heliumverbranding plaatsvond in de donor maar dat vroeg in de evolutie van de donor neon naar de kern is gezakt. Wat we nu zien is massa overdracht van de kern waar maar een beetje helium fusie heeft plaats gevonden, maar met extra neon door diffusie.

Door de hoge resolutie van de spectra zijn we instaat om de radiale snelheid van de centrale pieken en de metaallijnen nauwkeurig te meten. De neon- en stikstoflijnen vertonen dezelfde beweging als de centrale piek en zijn dus ook afkomstig van de accreterende witte dwerg. Doppler tomogrammen laten een tweede 'brightspot' zien in beide systemen. Uit de fase en amplitude van de centrale pieken en de voornaamste 'brightspot', en de piek-tot-piek scheiding van de dubbel gepiekte helium lijnen van de accretie schijf, stellen we limieten aan de inclinatie en massaverhouding, aangenomen dat de 'bright spot' in een ballistische baan of een Keplerbaan beweegt. Voor GP Com vinden we een accretor massa van $M_{1,\mathrm{GP\,Com}} > 0.55\,\mathrm{M_\odot}$ en een inclinatiehoek van $45° < i < 74°$, aangenomen dat de baan puur balistisch is. Als we aannemen dat de baan een Keplerbaan is, dan vinden we een accretor massa van $M_{1,\mathrm{GP\,Com}} > 0.33\,\mathrm{M_\odot}$ en een inclinatiehoek van $33° < i < 74°$. De donor van V396 Hya is waarschijnlijk een 'zero-temperature' donor. Het massa bereik van de accretor van $0.37 < M_{1,\mathrm{V396\,Hya}}/M_\odot < 0.49$ en de inclinatie van het systeem is $51° < i < 78°$ voor puur balistische baansnelheden. Voor baansnelheden van de schijf met een pure Keplerbaan is de accretor massa $0.32 < M_{1,\mathrm{V396\,Hya}}/M_\odot < 0.45$ en ligt de inclinatiehoek tussen $47° < i < 78°$.

De spectra vertonen verboden heliumlijnen en ook een grote variabiliteit van de gemiddelde snelheid van de centrale pieken in de heliumlijnen. Stark-verbreding-modellen voorspellen deze beide effecten. Voor de eerste keer zijn de centrale pieken vergeleken met berekende Stark profielen en we vinden een goede overeenkomst tussen de Stark-verbrede modellen en de waargenomen profielen voor een elektronendichtheid van $n_e \simeq 5 \times 10^{15}\ \mathrm{cm}^{-3}$.

Omdat in de hoge-resolutiespectra de zwakke en smalle neon- en stikstoflijnen goed te zien zijn, is het mogelijk om hieruit de rotatiesnelheid van de witte dwerg te bepalen. We vergelijken emissielijnen met synthetische lijnprofielen die alleen thermische en rotationele verbreding in acht nemen. Hieruit volgt dat de geprojecteerde rotationele snelheid niet hoger kan zijn dan $v_{\rm rot} < 46\,{\rm km\,s^{-1}}$ voor GP Com en $v_{\rm rot} < 34\,{\rm km\,s^{-1}}$, en we concluderen dat de accretor waarschijnlijk gesynchroniseerd wordt met de baan.

Als onderdeel van het Nederlandse GTO programma (gegarandeerde tijd omdat Nederland meegebouwd heeft aan X-Shooter) hebben we X-Shooter gebruikt om zeven AM CVn systemen te observeren. Deze systemen bestrijken het hele bereik aan mogelijke periodes, tussen de 18 min tot 44 min. Het resultaat van de analyse van deze homogene steekproef wordt beschreven in hoofdstuk 6.

Voor de eerste keer hebben we zwakke stikstoflijnen waargenomen in het systeem HP Lib en in de spectra van V406 Hya en SDSS J124058.03–015919.2 zien we sterke stikstof en magnesium emissie lijnen in het ver-infrarood. In het spectrum van SDSS J080449.49+161624.8 zijn meer dan 40 verschillende overgangen van neutral en geioniseerd helium te zien. Vooral de He II lijnen zijn buitengewoon prominent. Het algehele spectrum lijkt op een magnetische cataclysmische variabele zonder waterstof en we speculeren dan ook dat SDSS J080449.49+ 161624.8 een systeem is waarbij het magneetveld de accretie domineerd. Alle systemen die we waargenomen hebben vertonen de He I 10 830Å lijn in hun spectrum, iets wat we verwachten in 'low state' systemen. Maar voor het 'high state' systeem HP Lib was dit een verrassende vondst.

In hoofdstuk 3 gebruikten we de flux verhoudingen van de optische heliumlijnen om de temperatuur van de schijf en de 'bright spot' in vier AM CVn te bepalen. De fluxverhoudingen werden vergeleken met enkele-schijf-LTE modellen met een uniforme dichtheid en temperatuur en we vonden een goede overeenkomst tussen de data en de modellen in drie van de vier systemen. In hoofdstuk 6 breiden we de analyse van SDSS J1642 verder uit door ook de nabij infrarood lijnen He I 10 830 Å te gebruiken en laten zien dat voor het modelleren van de infrarood lijnen een uitgebreider model nodig is dan een enkele-schijf-LTE modellen met een uniforme dichtheid en temperatuur.

We meten de scheiding van de dubbel-gepiekte helium emissie profiel voor de systemen waarin we dit profiel waarnemen. Omdat de piek scheiding een indicator is van rotatie snelheid van de (Kepler) schijf, kunnen we hiermee limieten stellen aan de massa van de accretor en de inclinatiehoek. Een onderlimiet aan de massa van de accretors V406 Hya, SDSS J1240 en SDSS J1642 is $M_{1,\rm V406\,Hya} > 0.183\,M_\odot$, $M_{1,\rm SDSS\,J1240} > 0.030\,M_\odot$ en $M_{1,\rm SDSS\,J1642} > 0.025\,M_\odot$. Het limiet van de laatste twee systemen is niet heel erg strikt omdat de piek-tot-piek afstand niet heel groot was. Voor de inclinatiehoek van de systemen vinden we $i_{\rm V406\,Hya} > 28°$, $i_{\rm SDSS\,J1240} > 15°$ en $i_{\rm SDSS\,J1642} > 14°$ voor de systemen V406 Hya, SDSS J1240 and SDSS J1642.

Ook geven we een overzicht van de waargenomen elementen in een groot aantal van de AM CVn systemen. Een opmerkelijk resultaat is dat bijna alle systemen stikstoflijnen vertonen, maar geen van de systemen vertoond koolstof en alleen in GP Com zijn zuurstoflijnen te zien. Zoals eerder genoemd, neemt de hoeveelheid stikstof toe door de CNO fusie cyclus.

Als tijdens de volgende evolutionaire stap helium ontbrandt, wordt er koolstof geproduceerd door het 'triple-alfa' proces. Stikstof vangt deze alfadeeltjes en wordt daarbij omgezet tot zuurstof, waardoor de hoeveelheid stikstof dus afneemt. Hieruit volgt dat een pure helium witte dwerg waar geen heliumverbranding heeft plaatsgevonden een grote hoeveelheid stikstof bevat, terwijl een semi-gedegenereerde witte dwerg juist veel koolstof en zuurstof bevat. Ook al kunnen we het donortype van de bestudeerde systemen niet bepalen zonder nauwkeurig de samenstelling van de donor te meten, de afwezigheid van koolstof en zuurstof geeft wel aan dat geen van de systemen een er geëvolueerde helium ster als donor heeft.

Deutsche Zusammenfassung

Diese Arbeit zeigt eine detaillierte Studie verschiedener kompakter und ultrakompakter Doppelsternsysteme. Das Ziel ist es die Evolutionsgeschichte dieser Doppelsternsysteme besser zu verstehen um ein klareres Bild von der Sternenspätentwicklung zu gewinnen. Die genannten Systeme bestehen aus zwei alten Sternen, die sich umkreisen. Die dabei erreichte Umlaufperiode reicht von wenigen Minuten bis hin zu maximal wenigen Tagen.

Benedetto Castelli gelang es als erste Person im Jahr 1617 ein Doppelsternsystem mit einem Teleskop zu beobachten und dieses in seine beiden Komponenten aufzulösen. Heute wissen wir, dass die Mehrheit der Sterne nicht als Einzelsterne geboren werden, sondern in Doppel- oder gar Mehrfachsystemen auftreten. Die wichtigsten Parameter, die die Evolution der beiden Komponenten in einem Doppelsternsystem beschreiben, sind deren Massen sowie die Umlaufperiode. Je weiter die beiden Sterne voneinander entfernt sind, desto länger ist ihre Umlaufperiode. Bei den meisten Doppelsternsystemen ist diese so lang, dass die Entwicklungen der beiden stellaren Komponenten unabhängig voneinander ablaufen, d.h. beide Sterne werden niemals in Kontakt treten.

Ist die Orbitalperiode allerdings kurz genug ($\lesssim 30$ Jahre), können beide Komponenten im Laufe ihrer Entwicklung vom Hauptreihenstern zum weißen Zwerg in Kontakt treten und es kann zu einem Massenaustausch kommen. Dieser Massentransfer verringert den Drehimpuls, was zur Folge hat, dass sich beide Komponenten näher kommen und somit die Umlaufperiode kleiner wird. Am Ende dieser Entwicklung können die Umlaufperioden dieser Systeme nur noch wenige Minuten bis maximal wenige Tage betragen. Die Systeme bestehen jetzt aus zwei weißen Zwergen oder einem weißen Zwerg und einem Heliumstern. Weiße Zwerge stellen für fast alle Sterne das Endstadium der Sternentwicklung dar. Sie erzeugen keine Energie mehr, sind in etwa so groß wie die Erde und haben ca. die Masse einer halben Sonne. Auch unsere Sonne wird, sobald ihr Energievorrat verbraucht ist, als weißer Zwerg enden. Heliumsterne bilden eine Vorstufe zum weißen Zwerg. Sie erzeugen Energie in Form von Kernfusion, bei der sie in ihrem Inneren Helium zu Kohlenstoff fusionieren. Sobald das Heliumreservoir verbraucht ist, entwickeln sie sich direkt zu einem weißen Zwerg.

In der folgenden Entwicklung des engen Doppelsternsystems verliert das System durch Abstrahlung von Gravitationswellen weiter an Energie. Dadurch schrumpft der Abstand des Systems weiter und die Umlaufperiode wird noch kürzer. Gravitationswellen wurden von Albert Einstein in der allgemeinen Relativitätstheorie postuliert, sind aber bis heute nicht direkt beobachtet worden. In vielen Fällen hat die Abstrahlung von Gravitationswellen keinen messbaren Effekt. Wenn die Umlaufperiode des Doppelsternsystems allerdings kurz genug

ist ($\lesssim$ wenige Stunden), dann kann die Abstrahlung von Gravitationswellen dazu führen, dass sich beide Komponenten auch messbar immer näher kommen. Hieraus können sich drei verschiedene Varianten ergeben. Entweder berühren sich beide Komponenten und verschmelzen zu einem Einzelstern oder sie verschmelzen und explodieren als sog. Supernova Ia. Als dritte Alternative kann das Verschmelzen vermieden werden und das System kann nach der Berührung ein stabiles masseakretierendes System, ein sogenanntes AM Canum Venaticorum (AM CVn) Doppelsternsystem, bilden. Offene Fragestellungen bis heute sind: Welcher Entwicklungsweg wird von verschiedenen Doppelsternsystemen bevorzugt? Welche Systeme vermeiden das Verschmelzen und welche Systeme formen stabile AM CVn Doppelsterne und wie sehen diese Systeme im Detail aus?

Die Population von heißen unterleuchtkräftigen Sternen

Heiße unterleuchtkräftige Sterne oder hot subdwarfs (in diesem Kapitel kurz sdBs genannt) sind Heliumsterne, die im Kern Helium zu Kohlenstoff fusionieren und ca. 0.5 Sonnenmassen haben. Sie besitzen nur noch eine dünne Wasserstoffhülle um den Heliumkern. Im Regelfall besitzen helium-fusionierende Sterne eine dicke Wasserstoffhülle. Am unteren Rand dieser Wasserstoffhülle befindet sich eine Schicht in der Wasserstoff zu Helium fusioniert wird (sogenannte Horizontalaststerne). Die Struktur der sdBs unterscheidet sich hierbei signifikant von den Horizontalaststernen, da deren Wasserstoffhülle zu dünn ist um eine Wasserstofffusion zu ermöglichen. Sobald im Kern das Helium zu Kohlenstoff fusioniert ist, entwickeln sich sdBs direkt zu weißen Zwergen.

Die wichtigste offene Frage im Zusammenhang mit sdBs betrifft ihre Entstehung. Die Frage stellt sich wie sdBs ihre dicke Wasserstoffhülle verlieren. Der Massentransfer zwischen einem sdBs und seinem Begleiterstern könnte dabei eine wichtige Rolle spielen. Dies zeigten bereits frühere Studien, in welchen gezeigt wurde, dass sich ca. die Hälfte aller sdBs in kompakten Doppelsternsystemen mit Umlaufperioden von weniger als ~ 10 Tagen befinden. Dies kann bereits ein Hinweis darauf sein, dass der sdB während eines Massentransfers seine dicke Wasserstoffhülle verliert.

In Kapitel 2 werden die Parameter von zwölf sdB Doppelsternsystemen, die von uns entdeckt wurden, beschrieben. Dies führt mit den 130 vorher gelisteten Systemen zu einer Gesamtzahl von 142 bekannten kompakten sdB Doppelsternsystemen deren Umlaufperioden weniger als 30 Tage betragen. Im Zuge dieser Arbeit wurde zum ersten Mal eine detaillierte Populationsanalyse der bekannten kompakten sdB Doppelsternsysteme durchgeführt.

Als Begleitertypen konnten zum einen kühle Hauptreihensterne mit Massen von ca. 0.1 Sonnemassen und zum anderen weiße Zwerge mit Massen von ca. 0.4 Sonnenmassen identifiziert werden. Die gefundene Masse für die weißen Zwerge liegt deutlich unter der durchschnittlichen Masse, die ein allein auftretender weißer Zwerg (ca. 0.6 Sonnenmassen) besitzt. Dies deutet darauf hin, dass weiße Zwerge einen beträchtlichen Teil ihrer Masse während ihrer Entwicklung in einem Doppelsternsystem verlieren.

Mithilfe der bestimmten Begleitertypen, Begleitermassen und Umlaufperioden haben wir Rückschlüsse daraus gezogen was passiert, wenn der sdB und sein Begleiter in Kontakt treten.

Aufgrund der relativ niedrigen Masse der weißen Zwerg-Begleiter, wird die Mehrheit der Systeme dabei verschmelzen und einen neuen Einzelstern formen, einen sogenannten RCrB Stern. Lediglich zwei der 142 bekannten Doppelsternsysteme werden wahrscheinlich als Supernova Ia explodieren. Zwei weitere Systeme haben Umlaufperioden und Begleitermassen, sodass sie wahrscheinlich ein stabiles ultrakompaktes AM CVn Doppelsternsystem bilden.

Die Eigenschaften von ultrakompakten AM CVn Doppelstern-systemen

Ein spezieller Objekttyp, der in dieser Arbeit diskutiert wird, sind die AM CVn Doppelsterne, benannt nach dem Prototyp AM Canum Venaticorum (AM CVn). Der Prototyp wurde als variabler Stern in der Konstellation Canum Venatici (Jagdhund) gefunden. In den ersten Beobachtungen von AM CVn fiel auf, dass das System nur Helium und keinen Wasserstoff aufweist. Dies deutete bereits auf ein weitentwickeltes System hin. Als zweite Auffälligkeit wurde eine Helligkeitsvariation mit einer Periode von ca. 18 min entdeckt, welche sich später als Umlaufperiode herausstellte.

Heute wissen wir, dass AM CVn Systeme ultrakompakte Doppelsterne mit Umlaufperioden zwischen 5.4 und 65 Minuten sind. Sie bestehen aus einem weißen Zwerg mit einer Masse von ca. 0.5-1.0 Sonnenmassen. Der Begleiter ist entweder auch ein weißer Zwerg oder ein Heliumstern. Beide Sterne sind sich so nah, dass Material vom Begleiter auf den weißen Zwerg überfließt. Das Material trifft dabei in fast allen Systemen nicht direkt auf die Oberfläche des weißen Zwerges sondern sammelt sich in einer Scheibe um diesen (eine sogenannte Akkretionsscheibe) und fällt dann langsam auf jenigen herab. Der Auftreffpunkt des Materiestroms in der Akkretionsscheibe erzeugt einen heißen Punkt am Rand, der heller leuchtet als der Rest der Akkretionsscheibe. Diesen Punkt nennt man 'bright spot'. Anstatt zu verschmelzen haben es diese Systeme geschafft, ein stabiles akkretierendes Doppelsternsystem zu bilden. Im Laufe ihrer Entwicklung entfernen sich beide Komponenten wieder langsam voneinander bis sie nach mehreren Milliarden Jahren am Ende ihrer Entwicklung eine Umlaufperiode von ca. einer Stunde haben.

Bis heute ist noch nicht bekannt welcher Begleitertyp, ob weißer Zwerg oder Heliumstern, wie stark zur Population von AM CVn Doppelsternsystemen beiträgt. Jedoch zeigen beide Begleitertypen unterschiedliche Elementhäufigkeiten. So wurde in einem weißen Zwerg-Begleiter lediglich Wasserstoff zu Helium fusioniert. Bei diesem Prozess dient unter anderem Stickstoff als Katalysator und wird im Zuge der Kernfusion angereichert. Ist der Begleiter jedoch ein Heliumstern wird das Helium zu Kohlenstoff, bzw. der Stickstoff zu Sauerstoff fusioniert. Daher erwartet man eine Anreicherung von Kohlenstoff und Sauerstoff sowie ein Abbau von Stickstoff in den Systemen mit Heliumstern-Begleiter zu finden.

Besonders interessant sind diese Systeme im Hinblick auf ihre Gravitationswellenstrahlung. Aufgrund ihre Kompaktheit und kurzen Umlaufperioden bilden sie die stärksten und zahlenmäßig häufigsten Quellen für kurzwellige Gravitationswellenstrahlung in unserer Galaxis.

Zur Jahrtausendwende waren weniger als zehn AM CVn Systeme bekannt. Aufgrund

neuer Beobachtungstechniken konnte die Zahl der bekannten Systeme über die letzten 15 Jahre zu 43 Systemen vervierfacht werden. Im Zuge dieser Neuentdeckungen wurden bestimmte Eigenschaften der AM CVn Population sichtbar. Ziel dieser Arbeit ist es Charakteristiken individueller Systeme zu bestimmen um ein homogenes Bild der bekannten Population von AM CVn Doppelsternsystemen zu erhalten. Dies hilft uns deren Evolutionsgeschichte zu bestimmen und sie in den vielfältigen Zoo von (ultra-)kompakten Doppelsternsystemen einzuordnen.

In Kapitel 3 wird eine detaillierte Analyse von vier erst kürzlich entdeckten AM CVn Systemen beschrieben. Hierbei haben wir entdeckt, dass die drei bekannten Systeme, die Umlaufperioden zwischen 50 und 60 Minuten haben, Signaturen von Magnesium im akkretierenden weißen Zwerg zeigen. Kein anderes bekanntes System zeigt diese Signaturen. Verschiedene Szenarien welche das Magnesium in diesen Systemen erklären könnten, werden in diesem Kapitel diskutiert.

Zum ersten Mal wurden Mithilfe von Dopplertomographie verschiedene Regionen der vier AM CVn Systeme getrennt und die Temperatur der Akkretionsscheiben bestimmt. Die Akkretionsscheibe wurde hierbei als dünne Scheibe mit einheitlicher Temperatur und Dichte modelliert. Dies stellt eindeutig eine Approximation an die tatsächlichen Bedingungen in einer Akkretionsscheibe dar. Überraschenderweise fanden wir trotzdem eine gute Übereinstimmung zwischen Beobachtung und Modell in drei der vier beobachteten Systeme und haben dabei eine ähnliche Temperatur von ca. $\sim 10\,500$ Kelvin für die Akkretionsscheiben gemessen.

Kapitel 4 beschreibt die Analyse eines besonders interessanten ultrakompakten AM CVn Doppelsternsystems mit dem Katalognamen SDSS J1908. Dieses System wurde ca. drei Jahre am Stück vom Kepler Satellit beobachtet. Der Kepler Satellit misst die Helligkeit von Sternen mit hoher Präzission in einem kleinen, immer gleichen Bereich des Himmels und wurde in erster Linie zur Detektion von Exoplaneten gebaut. Zufällig liegt SDSS J1908 im Gesichtsfeld des Satelliten, sodass wir einen einzigartigen Datensatz von Helligkeitsmessungen eines AM CVn Systems zur Auswertung zur Verfügung hatten.

Neben der Umlaufperiode (18.085 Minuten) konnten wir eine Reihe verschiedener Elemente im System identifizieren. Unter anderem wurde Stickstoff entdeckt, jedoch gibt es keinen Hinweis auf Kohlenstoff, was darauf hindeutet, dass der Begleiter in diesem System ein weißer Zwerg ist. In einer genauen Analyse der Daten des Kepler Satelliten konnten wir neben der Umlaufperiode 41 weitere Perioden entdecken, die höchstwahrscheinlich von Helligkeitsvariationen in der Akkretionsscheibe kommen. Die Umlaufperiode war über den beobachteten Zeitraum weitestgehend stabil. Jedoch konnten wir Mithilfe der Daten ein Limit an der zu erwarteten Gravitationswellenstrahlung bestimmen. Einige andere Perioden zeigen eine deutliche Frequenzvariation, sprich die Periode war über den dreijährigen Beobachtungszeitraum nicht stabil. Verschiedene Erklärungsmöglichkeiten für die Variation werden innerhalb des Kapitels diskutiert.

Zwei bekannte AM CVn Systeme, GP Com und V396 Hya, wurden mit dem Very Large Teleskop (VLT) in Chile beobachtet, womit uns hochwertige Daten zur Auswertung zur Verfügung standen. Die Resultate werden in Kapitel 5 präsentiert. Die Daten erlauben zum einen eine genaue Vermessung der Bewegungen in beiden Systemen, zum anderen konnte zum er-

sten Mal der nahe Infrarotbereich in einem AM CVn Doppelsternsystem analysiert werden. Stickstoff und Neon konnte in beiden Systemen identifiziert werden. Die überdurchschnittliche Häufigkeit von Stickstoff deutet auch in diesen Systemen auf einen weißen Zwerg als Begleiter hin. Jedoch entsteht Neon nur als Nebenprodukt während der Fusion von Helium, was wiederum auf einen Heliumstern als Begleiter hindeutet. Im Moment haben wir noch keine zufriedenstellende Erklärungsmöglichkeit für diese Beobachtung.

Die hohe Qualität der Daten erlaubt uns die Geschwindigkeit des akkretierenden weißen Zwerges sowie des 'hot-spots' zu messen. Dadurch sind wir in der Lage Rückschlüsse auf die Massen des akkretierenden weißen Zwerges sowie des Begleiters zu ziehen. Des Weiteren war es uns möglich eine langsame Rotationsgeschwindigkeit des akkretierenden weißen Zwerges in beiden Systemen zu bestimmen. Im Vergleich zu ihrer, bei Entstehung des Systems, schnellen Rotationsgeschwindigkeit kann darauf geschlossen werden, dass sie während ihrer Entwicklung höchstwahrscheinlch deutlich an Geschwindigkeit verloren haben. Dieser Effekt hat eine stabilisierende Wirkung auf das System, die von der Zeitdauer abhängig ist, die der weiße Zwerg benoitigt, um Rotationsgeschwindigkeit zu verlieren. Zusätzlich wirkt sich dies positiv auf die Bildung von ultrakompakten AM CVn Systemen aus, sprich je schneller der akkretierende weiße Zwerg an Rotationsgeschwindigkeit verliert, desto weniger Systeme verschmelzen sondern bilden stattdessen AM CVn Doppelsternsysteme. Die Rotationsgeschwindigkeit konnte zum ersten Mal innerhalb der Geschichte dieser Systeme im Zuge dieser Arbeit gemessen werden.

Sieben weitere bekannte AM CVn Doppelsternsysteme wurden mit dem VLT beobachtet. Die Systeme überdecken fast den kompletten Bereich von Umlaufperioden der bekannten Population von ultrakompakten Doppelsternsystemen. Die Resultate der Analyse dieser homogenen Stichprobe sind in Kapitel 6 beschrieben.

Verschiedene Elemente wurden in den Systemen identifiziert. Hierbei fällt SDSS J0804 besonders auf. Die Daten deuten auf ein Magnetfeld innerhalb des Systems hin. Dies wäre das erste bekannte AM CVn Doppelsternsystem mit einem Magnetfeld. In drei der sieben Systeme haben wir Untergrenzen für die Masse des akkretierenden weißen Zwerges bestimmt.

Zusätzlich präsentieren wir eine Übersichtstabelle mit den detektierten Elementen in verschiedenen bekannten AM CVn Doppelsternsystemen. Besonders auffallend ist, dass fast alle Systeme Stickstoff zeigen, jedoch kein einziges System Kohlenstoff und lediglich ein einziges System Sauerstoff zeigt. Da dieses Ergebnis rein qualitativ ist, können wir keine konkrete Aussage über den Begleitertyp treffen. Sicher können wir sagen, dass keines der diskutierten Systeme einen weitentwickelten Heliumstern besitz, da diese sonst deutliche Anzeichen für Kohlenstoff und Sauerstoff zeigen müssten. Dieses Ergebnis hilft uns die Entstehungsgeschichte dieser exotischen Systeme besser zu verstehen.

LIST OF PUBLICATIONS

Refereed publications:

1. Hot subdwarf binaries from the MUCHFUSS project - Analysis of 10 new systems and a population study of all known short period hot subdwarf binaries
Kupfer, T., Geier, S., Heber, U. et al. 2015, A&A, 576, 44

2. Orbital periods and accretion disc structure of four AM CVn systems
Kupfer, T., Groot, P. J., Levitan, D. et al. 2013, MNRAS, 432, 2048

3. Phased resolved spectroscopy and *Kepler* photometry of the ultracompact AM CVn system SDSS J190817.07+394036.4
Kupfer, T., Groot, P. J., Bloemen, S. et al., 2015, MNRAS, submitted

4. UVES and X-Shooter spectroscopy of the emission line AM CVn systems GP Com and V396 Hya
Kupfer, T., Steeghs, D., Groot, P. J., et al., in prep.

5. X-Shooter observations of ultracompact AM CVn type binaries
Kupfer, T., Groot, P. J., Marsh, T. et al., in prep

Unrefereed publications:

1. Finding compact hot subdwarf binaries in the Galactic disc
Kupfer, T., Geier, S., McLeod, A. F. et al. 2014, Astronomical Society of the Pacific Conference Series, 481, 293

2. GTC observations of ultracompact AM CVn binaries
Kupfer, T., Groot, P. J. and Rutten, R G. M. 2013, Revista Mexicana de Astronomia y Astrofisica Conference Series, 42, 102

3. Extreme Helium Stars: Model Atmospheres and a NLTE analysis of BD+10°2179
Kupfer, T., Heber, U., Przybilla, N. et al. 2010, American Institute of Physics Conference Series, 1273, 209-212

Refereed publications (Co-Author):

1. The catalogue of radial velocity variable hot subluminous stars from the MUCHFUSS project
   Geier, S., **Kupfer, T.**, Heber, U. et al. 2015, A&A, 577, 26

2. The fastest unbound star in our Galaxy - Ejected by a thermonuclear supernova
   Geier, S., Fürst, F., Ziegerer, E., **Kupfer, T.** et al. 2015, Science, 347, 1126

3. KIC7668647: a 14 day beaming sdB+WD binary with a pulsating subdwarf
   Telting, J. H., Baran, A. S., Nemeth, P., Østensen, R. H., **Kupfer, T.** et al. 2014, A&A, 570, 129

4. The Second Data Release of the INT Photometric Halpha Survey of the Northern Galactic Plane (IPHAS DR2)
   Barentsen, G., Farnhill, H. J., Drew, J. E., ...**Kupfer, T.** ... et al. 2014, MNRAS, 444, 3230

5. Two new AM Canum Venaticorum binaries from the Sloan Digital Sky Survey III
   Carter, P. J., Gänsicke, B. T., Steeghs, D., ...**Kupfer, T.**... et al. 2014, MNRAS, 439, 2848

6. PTF1 J191905.19+481506.2 - A Partially Eclipsing AM CVn System Discovered in the Palomar Transient Factory
   Levitan, D., **Kupfer, T.**, Groot, P. J. et al. 2014, ApJ, 785, 114

7. The AM CVn binary SDSS J173047.59+554518.5
   Carter, P. J., Steeghs, D., Marsh, T. R., **Kupfer, T.** et al. 2014, MNRAS, 437, 2894

8. A progenitor binary and an ejected mass donor remnant of faint type Ia supernovae
   Geier, S., Marsh, T. R., Wang, B., ...**Kupfer, T.** ... et al. 2013, A&A, 554, 54

9. The helium-rich cataclysmic variable SBSS 1108+574
   Carter, P. J., Steeghs, D., de Miguel, E., ...**Kupfer, T.** ... et al. 2013, MNRAS, 431, 372

10. Five New Outbursting AM CVn systems discovered by the Palomar Transient Factory
    Levitan, D., **Kupfer, T.**, Groot, P. J. et al. 2013, MNRAS, 430, 996

11. A search for the hidden population of AM CVn binaries in the Sloan Digital Sky Survey
    Carter, P. J., Marsh, T. R., Steeghs, D., ...**Kupfer, T.** ... et al. 2013, MNRAS, 429, 2143

12. Discovery of a stripped red giant core in a bright eclipsing binary system
    Maxted, P. F. L., Anderson, D. R., Burleigh, M. R., ...**Kupfer, T.** ... et al. 2011, MNRAS, 418, 1156

13. Binaries discovered by the MUCHFUSS project SDSS J082053.53+000843.4 – An eclipsing subdwarf B binary with brown dwarf companion
    Geier, S., Heber, U., Schaffenroth, V., ...**Kupfer, T.** ... et al. 2011, APJL, 731, L22+

14. Massive unseen companions to hot faint underluminous stars from SDSS (MUCHFUSS). Analysis of seven close subdwarf B binaries
Geier, S., Maxted, P. F. L., Napiwotzki, R., ...**Kupfer, T.** ... et al. 2011, A&A, 526, A39+

15. Hot subdwarfs in binary systems and the nature of their unseen companions
Geier, S., Heber, U., Tillich, A., ...**Kupfer, T.** ... et al. 2010a, Ap&SS, 329, 91-99

16. Hot subdwarf stars in close-up view. I. Rotational properties of subdwarf B stars in close binary systems and nature of their unseen companions
Geier, S., Heber, U., Podsiadlowski, P., ...**Kupfer, T.** ... et al. 2010c, A&A, 519, A25+

17. Binaries discovered by the SPY project. V. GD 687 – a massive double degenerate binary progenitor that will merge within a Hubble time
Geier, S., Heber, U., **Kupfer, T.**, & Napiwotzki, R. 2010b, A&A, 515, A37+

Unrefereed publications (Co-Author):

1. New HW Virginis Systems from the MUCHFUSS Project
Schaffenroth, V., Geier, S., Barbu-Barna, I, ...**Kupfer, T.**... et al. 2014, Astronomical Society of the Pacific Conference Series, 481, 253

2. MUCHFUSS: Status and Highlights
Geier, S., **Kupfer, T.**, Barlow, B. et al. 2014, Astronomical Society of the Pacific Conference Series, 481, 243

3. The Second Eclipsing AM CVn Star
Levitan, D. B., Groot, P. J., **Kupfer, T.** et al. 2014, AAS Meeting #223, #154.16

4. The Search for AM CVn Systems with the Palomar Transient Factory
Levitan, D. B., Kulkarni, S. R., Prince, T. A., ...**Kupfer, T.** ... et al. 2013, AAS Meeting #221, #401.01

5. Discovery of the Closest Hot Subdwarf Binary with White Dwarf Companion
Geier, S., Marsh, T. R., Dunlap, B. H., ...**Kupfer, T.** ... et al. 2013, Astronomical Society of the Pacific Conference Series, 469, 373

6. Discovery of a Stripped Red-giant Core in a Bright Eclipsing Binary Star
Maxted, P. F. L., Anderson, D. R., Burleigh, M. R., ...**Kupfer, T.** ... et al. 2012, Astronomical Society of the Pacific Conference Series, 452, 137

7. The MUCHFUSS Project: Searching for the Most Massive Companions to Hot Subdwarf Stars in Close Binaries and Finding the Least Massive Ones
Geier, S., Schaffenroth, V., Hirsch, H., ...**Kupfer, T.** ... et al. 2012, Astronomical Society of the Pacific Conference Series, 452, 129

8. MUCHFUSS - Massive Unseen Companions to Hot Faint Underluminous Stars from SDSS
   Geier, S., Schaffenroth, V., Hirsch, H., ...**Kupfer, T.** ... et al. 2012, Astronomische Nachrichten, 333, 431

9. Analysis of Two Eclipsing Hot Subdwarf Binaries with a Low Mass Stellar and a Brown Dwarf Companion
   Schaffenroth, V., Geier, S., Heber, U., ...**Kupfer, T.** ... et al. 2011, American Institute of Physics Conference Series, 1331, 174-181

10. Substellar companions and the formation of hot subdwarf stars
    Geier, S., Heber, U., Tillich, A., ...**Kupfer, T.** ... et al. 2011, American Institute of Physics Conference Series, 1331, 163-169

11. Analysis of two eclipsing hot subdwarf binaries with a low mass stellar and a brown dwarf companion
    Schaffenroth, V., Geier, S., Heber, U., ...**Kupfer, T.** ... et al. 2010, American Institute of Physics Conference Series, 1273, 243-246

12. The MUCHFUSS project – Searching for massive compact companions to hot subdwarf stars
    Geier, S., Heber, U., Tillich, A., ...**Kupfer, T.** ... et al. 2010, AIP Conference Proceedings, 1314, 67-72

13. Massive Unseen Companions to Hot Faint Underluminous Stars from SDSS (MUCHFUSS) – Status report
    Geier, S., Heber, U., Tillich, A., ...**Kupfer, T.** ... et al. 2010, American Institute of Physics Conference Series, 1273, 263-268

14. Analysis of two eclipsing hot subdwarf binaries with a low mass stellar and a brown dwarf companion
    Schaffenroth, V., Geier, S., Heber, U., ...**Kupfer, T.** ... et al. 2010, American Institute of Physics Conference Series, 1273, 243-246

15. Hot subdwarf binaries – Masses and nature of their heavy compact companions
    Geier, S., Heber, U., Edelmann, H., ...**Kupfer, T.** ... et al. 2009, Journal of Physics Conference Series, 172, 012008

ACKNOWLEDGEMENTS

The Netherlands Research School of Astronomy (NOVA) who supported my work and travels financially. The Leids Kerkhoven-Bosscha Fonds for their financial support of my travel and printing of this thesis.

The members of the reading committee for their effort in reading and judging my thesis.

Ein Dankeschön geht an meine Freunde zu Hause, dem JRK Eismannsberg, den Kirwaboum Happurg, der Fußballmannschaft des SC Happurg sowie dem Posaunenchor Happurg und ganz besonders Otti und Jessi. Ihr habt mir immer gezeigt, dass es auch ein Leben neben der Astronomie gibt. Thomas, vielen Dank fürs Korrekturlesen.

Für eure Unterstützung möchte ich mich auch bei meinen Eltern, sowie meiner Oma und meinen Geschwistern bedanken. Besonderer Dank gilt meinem Onkel Gerald und meinem Opa Heinz, dafür dass ihr mich immer meinen eigenen Weg habt gehen lassen, auch wenn ihr leider das Ende dieser Arbeit nicht mehr erleben durftet.

Moni, vielen Dank für deine bedingungslose Unterstützung über all die Jahre. Dafür, dass du mich in jeder Sekunde unterstützt hast, ohne dass du etwas zurückerwartet hast, auch wenn uns oft viele Kilometer getrennt haben oder der Laptop mal wieder bis sehr spät in die Nacht gelaufen ist. Ganz besonders in den Momenten in denen ich nicht lachen konnte hast du mich wieder zum Lachen gebracht. Ich hoffe sehr, dass wir so eng verbunden bleiben wie es die AM CVn Systeme sind und unsere Liebe mindestens genauso lange hält wie die Sterne am Himmel leuchten.

CURRICULUM VITAE

I was born in Grimma in the German Democratic Republic on 1st April 1984. At this time nobody could have imagined that I will ever be allowed the cross the border to West-Germany and even further to the Netherlands to do a PhD in astrophysics. But thank god it came different and a few smart politicians ended the cold war. After the Wall came down and Germany was finally reunified we moved to the beautiful village Happurg in Bavaria.

I finished school after grade 10 and started an apprenticeship as industrial mechanic at Demag ergotech GmbH in Schwaig, Germany which I successfully finished after three years. After those very interesting years I decided to go back to school to obtain my high school degree followed by a 5 year undergraduate study of physics at the university of Erlangen-Nuremberg as the last but one class with Diploma as degree before the system was changed to Bachelor and Master.

My enthusiasm in astronomy started early in my study. Already as a 2nd year undergraduate student I joined the group of Prof. Dr. Ulrich Heber at the Remeis observatory in Bamberg as student assistent working on data reduction and analysis of Echelle spectra obtained with the ESO-2.2m/Feros and HET/High-resolution spectrograph. During my undergraduate study I conducted two observing runs at the Calar Alto observatory, Spain and at La Silla observatory, Chile. As ERASMUS student I spent 3 months at Armagh observatory, Northern Ireland to work with Prof. Dr. Simon Jeffery on an abundance analysis of extreme helium stars which I continued as Diploma thesis supervised by Prof. Dr. Uli Heber and Prof. Dr. Norbert Przybilla with the title *Extreme Helium Stars: Model atmospheres and a NLTE abundance analysis of BD+10° 2179*. Finally in October 2010 I received my Diploma in physics with material science as minor subject.

In May 2011 I started my doctorate at the Department of Astrophysics at the Radboud University Nijmegen on ultracompact AM CVn type binaries supervised by Prof. Dr. Paul Groot. During the sabbatical of my supervisor I had the privilege to spent about two months in total at the California Institute of Technology, USA.

I was teaching assistent for several Bachelor classes including Kaleidoskop, Interstellar Medium, Progammeren I and observational astronomy. For the latter I was responsible coordinator over two years. I conducted several training sessions for the staff at the 35 cm telescope on the roof of the Huygensgebouw.

Over the years I had the possibility to obtain data for my research at various observatories, including the William Herschel telescope, the Isaac Newton telescope, the Gran Telescopio de Canarias, the 3.5 m telescope at Calar Alto observatory, the Keck telescope, the Hale telescope at Palomar observatory as well as the Shane telescope at Lick observatory.

I presented my work with posters or oral presentations at several seminars and national and international conferences in Nordwijkhout, Lommel (Netherlands), Warwick (UK), Garching, Erlangen (Germany), Lake Louise (Canada), Santa Cruz de la Palma (Spain) , Boston, Milwaukee, Tucson, Pasadena and Santa Cruz (USA).

After this very successful doctorate in Nijmegen I received a Caltech postdoctoral fellowship for astrophysics research working with PTF/ZTF which I will start in September 2015 at the California Institute of Technology, USA.